Conference Proceedings of the Society for Experimental Mechanics Series

François Barthelat · Pablo Zavattieri · Chad S. Korach
Barton C. Prorok · K. Jane Grande-Allen *Editors*

Mechanics of Biological Systems and Materials, Volume 4

Proceedings of the 2013 Annual Conference on Experimental and Applied Mechanics

Springer

Conference Proceedings of the Society for Experimental Mechanics Series

Series Editor
Tom Proulx
Society for Experimental Mechanics, Inc.,
Bethel, CT, USA

For further volumes:
http://www.springer.com/series/8922

François Barthelat • Pablo Zavattieri • Chad S. Korach
Barton C. Prorok • K. Jane Grande-Allen
Editors

Mechanics of Biological Systems and Materials, Volume 4

Proceedings of the 2013 Annual Conference on Experimental and Applied Mechanics

Springer

Editors
François Barthelat
McGill University
Montreal, QC
Canada

Chad S. Korach
State University of New York
Stony Brook, NY
USA

K. Jane Grande-Allen
Rice University
Houston, TX
USA

Pablo Zavattieri
Purdue University
West Lafayette, IN
USA

Barton C. Prorok
Auburn University
Auburn, AL
USA

ISSN 2191-5644 ISSN 2191-5652 (electronic)
ISBN 978-3-319-00776-2 ISBN 978-3-319-00777-9 (eBook)
DOI 10.1007/978-3-319-00777-9
Springer Cham Heidelberg New York Dordrecht London

Library of Congress Control Number: 2013945400

Printed on acid-free paper

Springer is part of Springer Science+Business Media (www.springer.com)

Preface

Mechanics of Biological Systems and Materials, Volume 4: Proceedings of the 2013 Annual Conference on Experimental and Applied Mechanics represents one of eight volumes of technical papers presented at the SEM 2013 Annual Conference & Exposition on Experimental and Applied Mechanics organized by the Society for Experimental Mechanics and held in Lombard, IL, June 3–5, 2013. The complete Proceedings also includes volumes on: *Dynamic Behavior of Materials; Challenges in Mechanics of Time-Dependent Materials and Processes in Conventional and Multifunctional Materials; Advancement of Optical Methods in Experimental Mechanics; MEMS and Nanotechnology; Experimental Mechanics of Composite, Hybrid, and Multifunctional Materials; Fracture and Fatigue; Residual Stress, Thermomechanics & Infrared Imaging, Hybrid Techniques and Inverse Problems.*

Each collection presents early findings from experimental and computational investigations on an important area within Experimental Mechanics, the Mechanics of Biological Systems and Materials being one of these areas.

This volume summarizes the exchange of ideas and information among scientists and engineers involved in the research and analysis of how mechanical loads interact with the structure, properties, and function of living organisms and their tissues. The scope includes experimental, imaging, numerical, and mathematical techniques and tools spanning various length and time scales. Establishing this symposium at the Annual Meeting of the Society for Experimental Mechanics provides a venue where state-of-the-art experimental methods can be leveraged in the study of biomechanics. A major goal of the symposium was for participants to collaborate in the asking of fundamental questions and the development of new techniques to address bio-inspired problems in society, human health, and the natural world. The organizers would like to thank all the speakers and staff at SEM for enabling a successful program.

Montreal, QC, Canada — François Barthelat
West Lafayette, IN, USA — Pablo Zavattieri
Stony Brook, NY, USA — Chad S. Korach
Auburn, AL, USA — Barton C. Prorok
Houston, TX, USA — K. Jane Grande-Allen

Contents

Chapter 1
Study of the Transient Response of Tympanic Membranes Under Acoustic Excitation

Morteza Khaleghi, Ivo Dobrev, Ellery Harrington, Cosme Furlong, and John J. Rosowski

Abstract Characterization of the transient response of the human Tympanic Membrane (TM) subjected to impulse acoustic excitation is important in order to further understand the mechanics of hearing. In this paper, we present results of our initial investigations of the transient response of an artificial fully-constrained circular membrane as a simplified model of the TM. Two different optical methods used in our investigations are Laser Doppler Vibrometery (LDV) and Pulsed Double-Exposure Digital Holography (PDEDH) for single-point and full-field-of-view measurements of displacements, respectively. Applying Hilbert Transformation methods to the measured displacements allows determination of the transient characteristics of the membrane, including damping ratios and time constants, which are also computed and compared with corresponding FEM models. We expect to use this method in the investigation of the transient response of TM of specific species.

Keywords Transient response • Laser Doppler Vibrometry (LDV) • Digital holography • Hilbert transform • Tympanic membrane

1.1 Introduction

The ear is responsible for translating variations in air pressure, whether from music, speech, or other sources, into the neural activity necessary for our perception and interpretation of sound [1]. The *auditory periphery* can be broken into three functionally and anatomically distinct components: external, middle, and inner ear, as shown in Fig. 1.1. The primary role of the external and middle ear is to pass the sound stimulus from the environment to the inner ear. The sound wave is diffracted and scattered by the body, head, and ear, and some fraction of the incident sound energy is gathered at the entrance to the ear canal. That sound is transformed as it travels down the roughly cylindrical ear canal to the Tympanic Membrane (TM). The sound acting on the TM sets the ossicles (malleus, incus, and stapes) into motion. The mechanical motion of the ossicles produces a sound pressure and volume velocity of the stapes, in the oval window, at the entrance to the lymph-filled inner ear. The sound pressure and volume velocity in the lymphs within the vestibule

M. Khaleghi (✉) • I. Dobrev • E. Harrington
Center for Holographic Studies and Laser micro-mechaTronics (CHSLT)

Mechanical Engineering Department, Worcester Polytechnic Institute, Worcester, MA 01609, USA
e-mail: mkm@wpi.edu

C. Furlong
Center for Holographic Studies and Laser micro-mechaTronics (CHSLT)

Mechanical Engineering Department, Worcester Polytechnic Institute, Worcester, MA 01609, USA

Eaton-Peabody Laboratory, Massachusetts Eye and Ear Infirmary, Boston, MA, USA

Department of Otology and Laryngology, Harvard Medical School, Boston, MA, USA

J.J. Rosowski
Eaton-Peabody Laboratory, Massachusetts Eye and Ear Infirmary, Boston, MA, USA

Department of Otology and Laryngology, Harvard Medical School, Boston, MA, USA

F. Barthelat et al. (eds.), *Mechanics of Biological Systems and Materials, Volume 4*,
Conference Proceedings of the Society for Experimental Mechanics Series,
DOI 10.1007/978-3-319-00777-9_1,

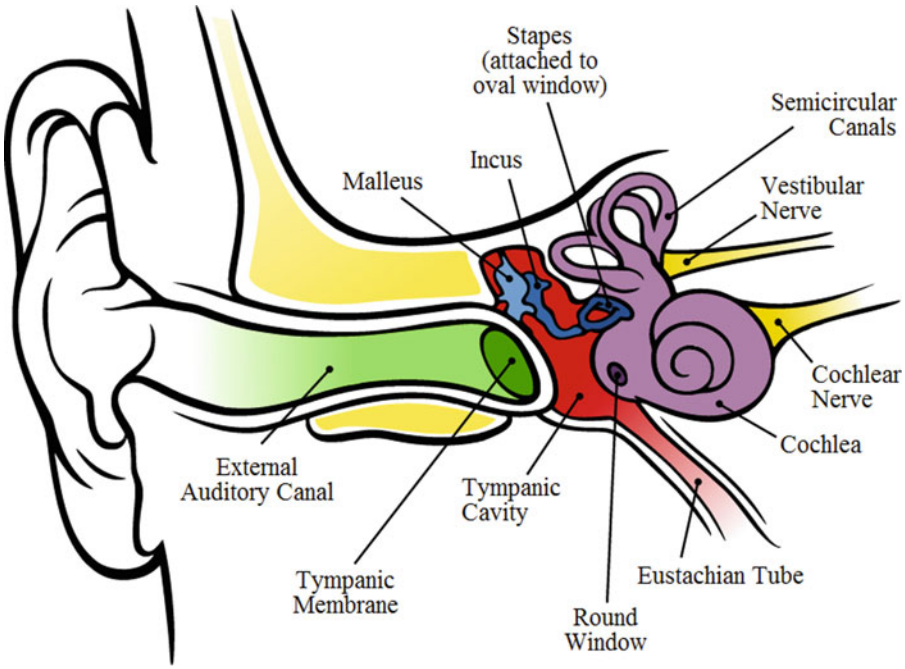

Fig. 1.1 Schematic of auditory system with its primary components [3]

(or entrance) of the inner ear stimulate the cochlear partition, resulting in motion of the partition's basilar membrane and mechanical stimulation of the hair cells within the partition. The hair cells produces graded electrical signals that are sent to the brain for further interpretation [2].

Therefore, acoustically-induced vibrations of the TM play a primary role in the hearing process, in that these motions are the initial mechanical response of the ear to airborne sound [4, 5]. Characterization of these displacements, which are in the nanometer scale, is important for a better understanding of the secrets of hearing. Several research groups have been studying these sound-induced displacements resulted from tone stimuli [6–8], however, transient response of the TM, e.g., the behavior of the eardrum excited by a short pulse (as opposed to tone) needs further investigations. In this paper, the transient response of an artificial membrane is studied by two different optical techniques. Pulsed Double-Exposure Digital Holography (PDEDH) is used to measure and quantify in full-field-of-view, while, Laser Doppler Vibrometery (LDV) is used to monitor these displacements pointwise in order to extract damping ratios and time-constants of the membrane. The amplitude of the oscillation varies slowly with time, and the shape of the slow time-variation is called *envelope* [9]. The envelope often contains important information about the signal. By using the Hilbert Transform (HT), the rapid oscillations can be removed from the signal to produce a direct representation of the envelope alone.

1.2 Methods

1.2.1 Acquisition System Overview

The digital holography system is capable of operating in time-averaged and stroboscopic modes [8, 10, 11]. The time-averaged mode is used for rapid, real-time identification of resonant frequencies of the vibrating samples and their corresponding mode shapes. The stroboscopic mode is used to quantify the magnitude and phase of the TM's entire surface at a nanometer scale [11]. As shown in Fig. 1.2, our holographic system contains several subsystems. *Measurement subsystem* includes an interferometer that recombines the reference and back-scattered object beams, and permits these two wave fields to interfere at the CCD sensor. *Laser delivery subsystem* includes laser light sources, with a central wavelength of 532 nm, an acousto-optic modulator (AOM), mirrors, and laser to fiber coupler which provide coherent light source for measurements. *Computer and control subsystem* controls the recording parameter such as sound-excitation level and frequency, phase shifting, synchronizations for stroboscopic measurements and all the acquisition parameters. Also, *positioning subsystem* locates the measurement system (otoscope head) at appropriate position.

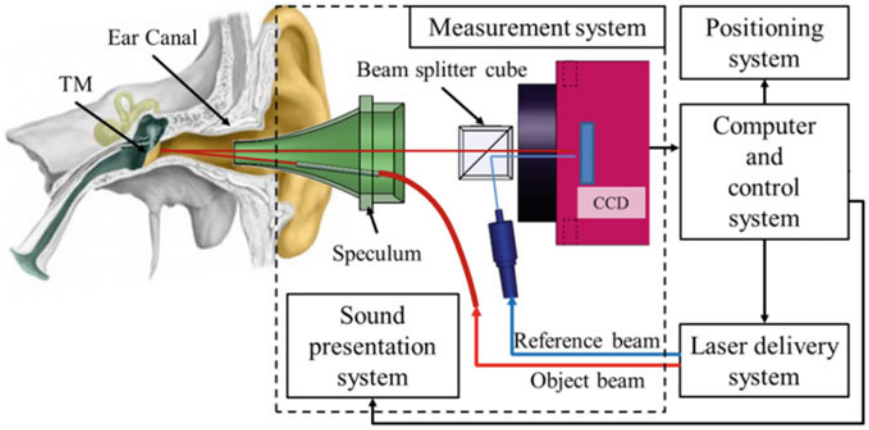

Fig. 1.2 Schematic illustration of the measuring system. The measurement and sound presentation systems are combined within the head of the otoscope. *TM* tympanic membrane, or eardrum, *CCD* charge-coupled device [12]

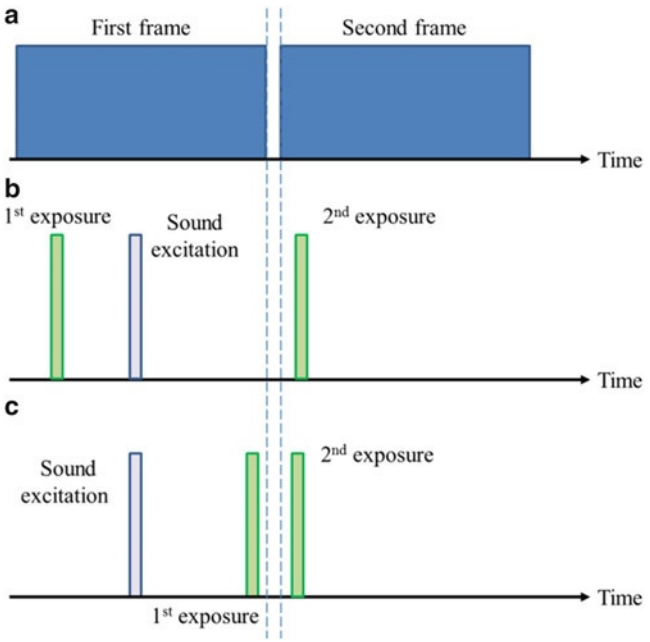

Fig. 1.3 Schematic illustration of the pulsed double exposure acquisition method: (**a**) two consecutive frames of the camera with an interframe time between any two frames; (**b**) sound presentation system is triggered at the first frame between the 1st and 2nd exposures of the camera. This situation is for the absolute displacement measurement in which the first exposure (reference state) is at an unstressed state; and (**c**) sound presentation system is triggered before the first exposure of the camera. This situation is for the purpose of comparative studies of two consecutive frames where the first exposure (reference) is also at a stressed state

1.2.2 Pulsed Double Exposure Acquisition Technique

The basic idea behind pulsed double exposure acquisition is that the sound stimuli and the two exposures of the camera are controlled with respect to each other. As shown in Fig. 1.3, the exposures of the camera are set to be relatively short (in our experiments 20 μs) by means of an Acousto-Optic Modulator (AOM). Sound presentation system is always triggered at the first frame and depending on the purpose of the study, the position of the first exposure is adjusted to be before or after the sound stimuli. In order to capture the transient events, the second exposure always is set to be early in the second frame. To capture the absolute displacement in a transient manner, the timing of the system is set as shown in Fig. 1.3b, whereas to

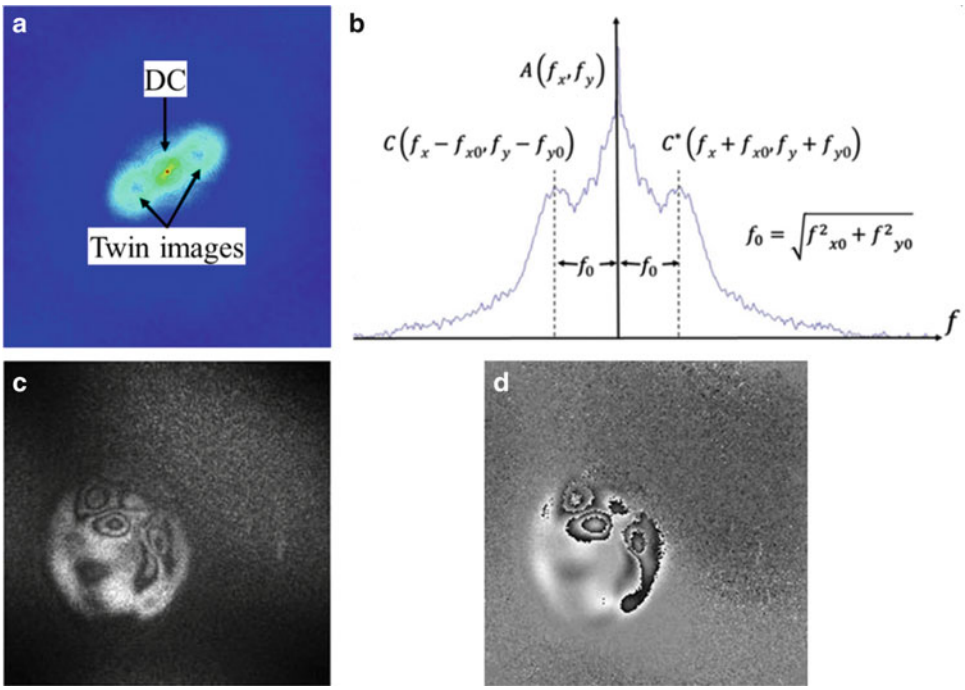

Fig. 1.4 Frequency components of a hologram: (**a**) 2D Fourier transform spectrum of a hologram showing the DC and the twin images; (**b**) 2D cross-section of frequency domain of FFT spectrum of a hologram with a carrier frequency f_0. The DC and the twin images components are also shown; (**c**) numerically-reconstructed hologram showing the object as well is its twin image; and (**d**) optical phase of the hologram

capture the relative displacement between any two consecutive exposures, the timing is adjusted as configured in Fig. 1.3c. By this technique, the *simulated* frame rate of acquisition system can be increased to over 50,000 fps, while the regular frame rate of the camera is 60 fps.

1.2.3 Single Frame Lensless Digital Holography

The spatial phase shifting method is realized by adding a high spatial carrier frequency into the signal of the hologram. Taking a Fast Fourier Transform (FFT) of such a hologram [13, 14] results in

$$H(f_x,f_y) = A(f_x,f_y) + C(f_x - f_{x0},f_y - f_{y0}) + C^*(f_x + f_{x0},f_y + f_{y0}), \tag{1.1}$$

where A is the DC term, C and C^* are the complex distribution of the twin images components that mathematically are described as complex conjugates of one another, f_{x0} and f_{y0} denote the spatial carrier frequency in x and y direction correspondingly. As shown in Fig. 1.4, since the spatial variations of the components of the interferogram are slower compared to the carrier frequency, the twin image components will be separated in the frequency domain. By masking the undesired regions of the Fourier spectra, we isolate only the relevant information for the object of interest.

Additionally, the DC component can be mathematically removed from the hologram by recognizing that the DC component in the Fourier space is due to the low-frequency amplitude spatial variation in the hologram and it can be isolated by applying a high-pass filter. This is computationally efficiently achieved by subtracting the local average of the interferogram obtained by convolution of the interferogram with a low-pass kernel. The optical phase of the interferogram is obtained by taking the Inverse Fourier Transform (IFFT) of the masked, shifted spectra in the frequency domain.

1.2.4 High-Speed Imaging Measurements

To evaluate the accuracy of our developed, high-speed resembled system (pulsed double exposure holographic system), the transient response of the membrane is also captured by means of a high-speed camera. Some distinguished advantages of the

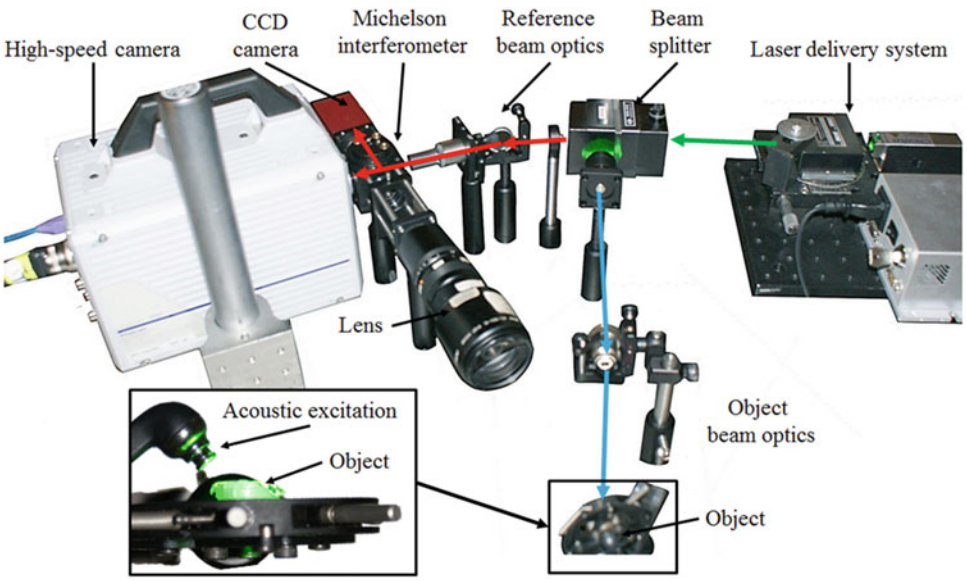

Fig. 1.5 Overview of a prototype high-speed digital holographic system setup. The system includes a high-speed camera (>25,000 fps) and a CCD camera (60 fps). The CCD camera allows for dynamic feedback of the image quality through live processing with custom holographic software prior to high-speed measurements

system are temporal resolution less than 1 μs, single frame acquisition less than 10 μs, high framerate acquisition of 25,000 fps at 512 × 512 pixels, which can be increased to 87,500 fps at 256 × 256 pixel (Fig. 1.5).

1.3 Results

1.3.1 Experimental Results Obtained by PDEDH

The transient response of a human TM subjected to a pulse acoustic stimulus is shown in Fig. 1.6. The output of a solid state green laser (COHERENT, Compass 315 M-50) with a power of 50 mW is coupled into a fiber and the object is illuminated with the light coming out of this fiber. In this series of experiments, the output power of the fiber is 17 mW which allow us to have an exposure time of 20 μs. Also, frame rate of the acquisition system is 10,000 fps. As shown in Fig. 1.6, the transient response of the surface of the human TM is faster that the sampling rate (every 100 μs). Therefore, in order to capture Rayleigh waves, higher sampling rate are necessary.

1.3.2 Experimental Results Obtained by High-Speed Camera

As shown in Fig. 1.5, a high-speed camera (Photron Fastcam SA5) is mounted on the measurement system. In this series of experiments, the frame rate of the camera is 87,500 fps with an interframe time of 11 μs. The output power of the object beam of the laser is 20 mW, which allows us to have 10 μs exposure time. The sound source is a 50 μs pulse wave that is mounted 10 mm away from the membrane at an angle of 45 deg relative to the membrane surface normal. As illustrated in Fig. 1.7, three distinguished stages of *initiation*, *propagation*, and *reflection* can be observed. Initiation of the traveling wave occurs at the boundaries that are closer to the sound source. Propagation of the traveling waves, which defines the group velocity of the surface wave; and Reflection of the traveling wave from the farther boundaries.

1.3.3 Experimental Results Obtained by LDV

A Polytec LDV with a helium neon laser light is used [15]. One of the fundamental considerations in doing LDV measurements is that the point of interest should not be a node of vibration at the driving frequency. To ensure that the

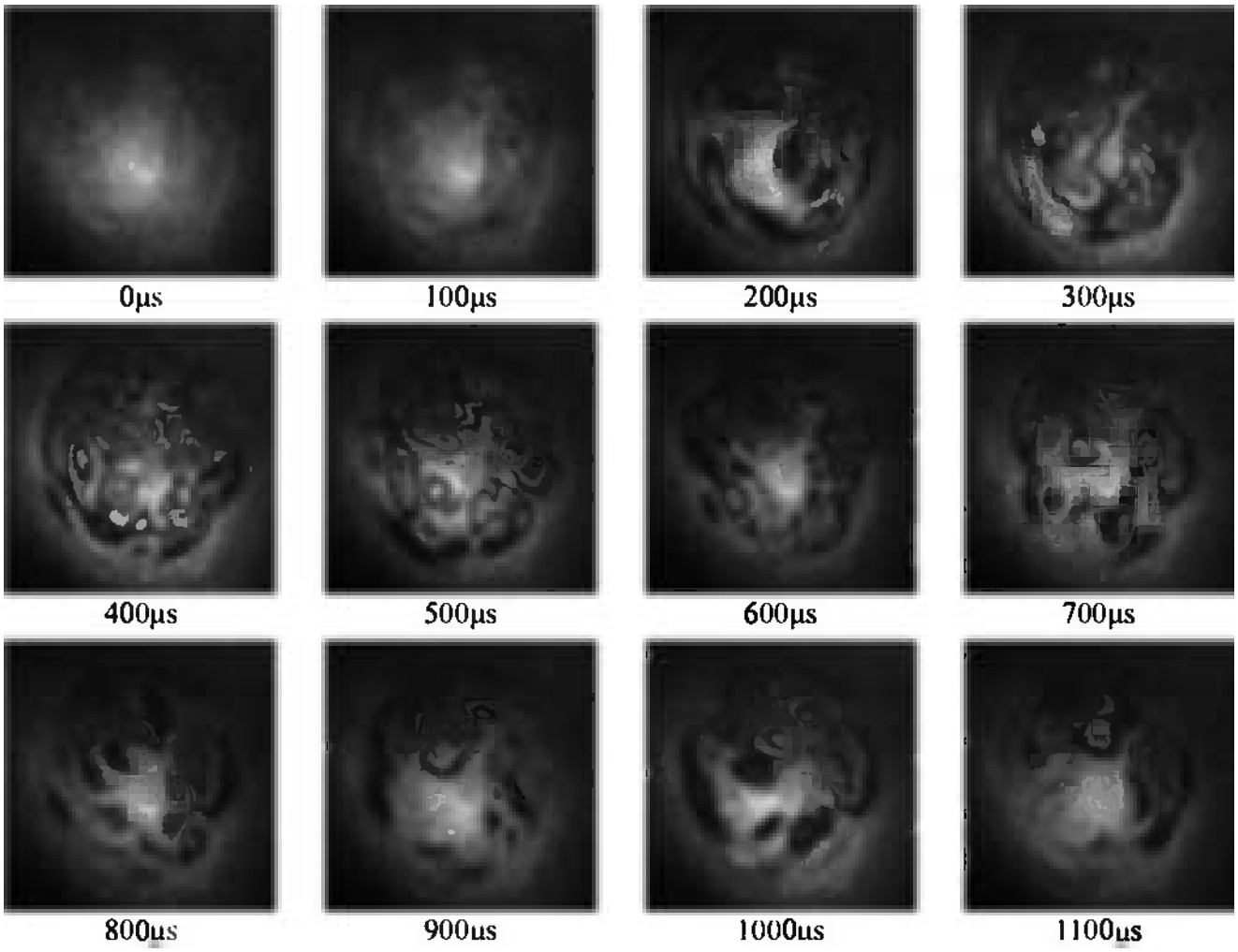

Fig. 1.6 Results of transient response of a human TM due to a pulse acoustic stimulus obtained by the PDEDH system. The time stamp shown is referenced with respect to the beginning of the acoustic stimulus. The temporal resolution shown is 100 μs

selected point is an antinode, an Eigen frequency FEM analysis is performed and the results are shown in Fig. 1.8. Based on the FEM results, the laser beam of the LDV is adjusted at the center point of the membrane and the results are shown in Fig. 1.9. Our LDV captures a time-varying signal containing a rapidly-oscillating component, which is characterized by a time-constant of 140 ms. The logarithmic decrement and damping ratio are calculated by Eqs. 1.2 and 1.3, respectively.

$$\delta = \frac{1}{n}\ ln\frac{x(t)}{x(t+nT)} \tag{1.2}$$

$$\zeta = \frac{1}{\sqrt{1+\left(\frac{2\pi}{\delta}\right)^2}} \tag{1.3}$$

1.3.4 Transient Response Simulated by FEM

As the preliminary step in analyzing the transient response of the interaction of impulse acoustic loads with the membrane, the transient propagation of sound wave in air is modeled. Figure 1.10 illustrates the first 100 μs of impulse-generated sound propagation wave. Three point sources with Gaussian impulse acoustic source with a peak time of 8 μs are introduced at the right boundary of the membrane.

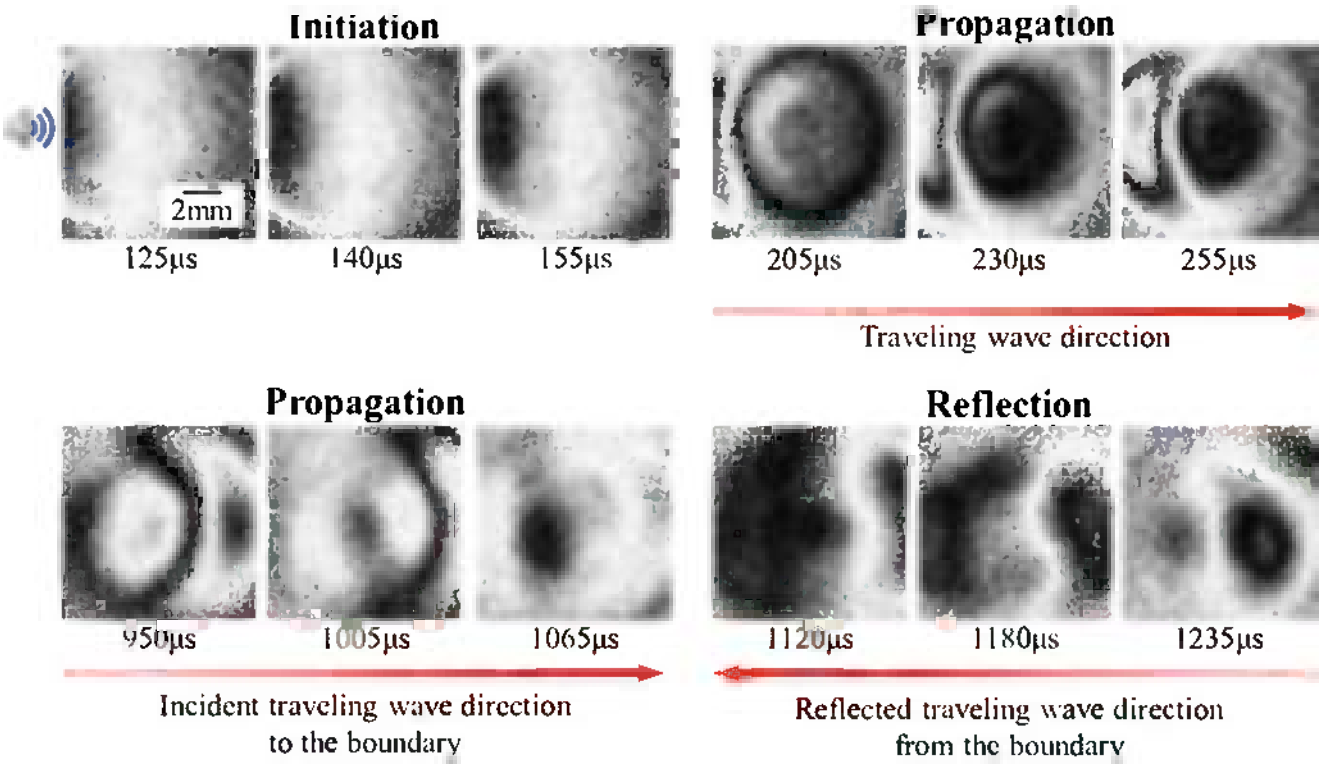

Fig. 1.7 Results of transient response of a circular latex membrane with 10 mm diameter. Measurements have duration of 1.2 ms. Sample is excited by an impulse acoustic stimulus positioned on the *left* of the membrane that triggers surface waves to initiate, propagate, and reflect across the sample. Time stamps are referenced to the beginning of the pulsed acoustic excitation

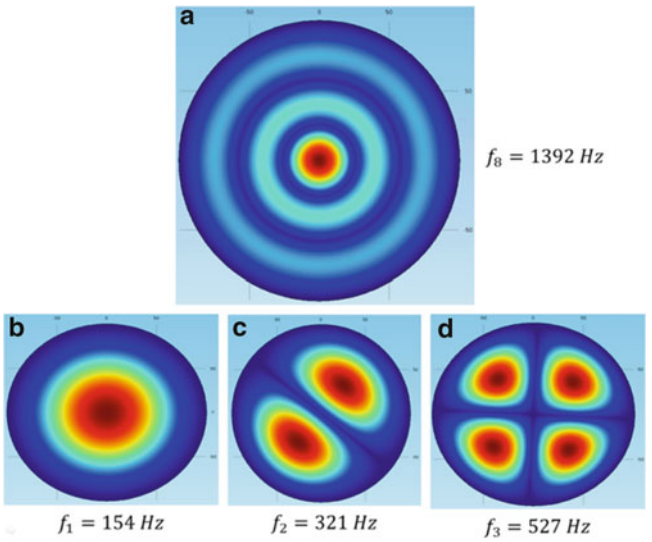

Fig. 1.8 Results of Eigen-frequency analysis performed on a circular latex membrane with a radius of 10 mm and thickness of 100 μm: (**a**) the 8th mode of vibration which is close to the driving tone frequency in the LDV measurements; (**b**) the 1st mode of vibration; (**c**) the 2nd mode of vibration; (**d**) the 3rd mode of vibration

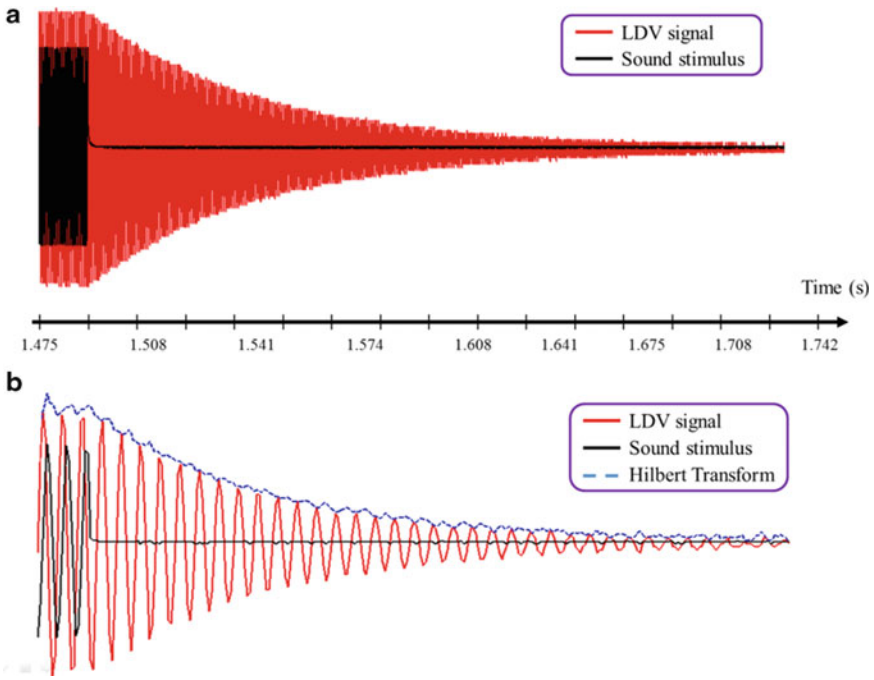

Fig. 1.9 Transient response of the center point of a circular latex membrane subjected to a tone of 1,402 Hz: (**a**) the original signals of LDV and sound stimuli; and (**b**) the sub-sampled signals of LDV, sound stimuli and Hilbert Transform applied on the LDV signal to extract the envelope of the LDV signal. The results show a time constant of 140 ms

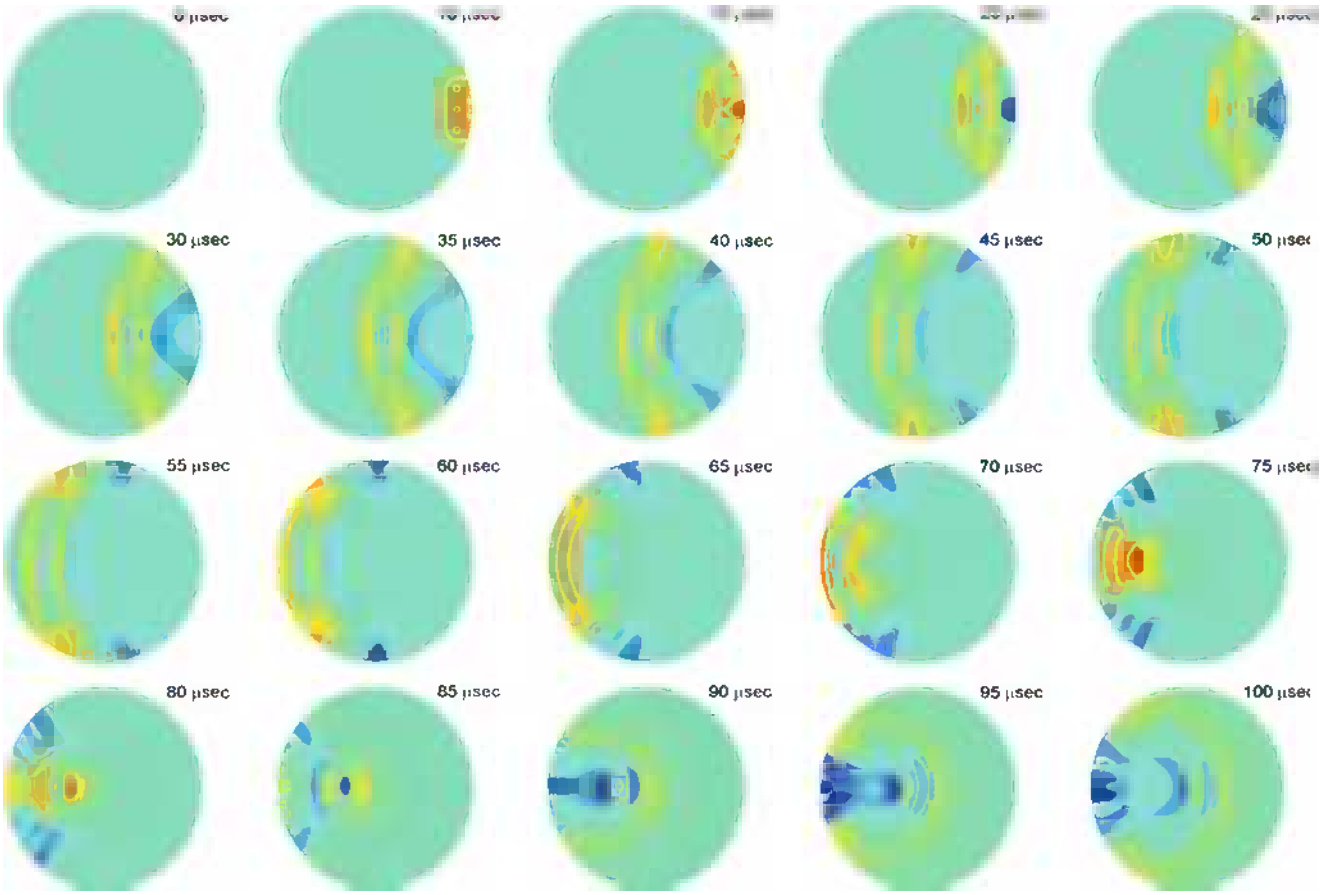

Fig. 1.10 Transient response of a circular shell subjected to a Gaussian pulse acoustic wave field. Radius of the disk is 10 mm and thickness is 0.1 mm (100 μm). Computed wave speed is 338 m/s, which is within 1 % of the theoretical speed of sound in air under standard pressure and temperature

1.4 Conclusions and Future Work

Understanding the transient response of Tympanic Membrane (TM) under acoustic impulses is a crucial step in decoding the secrets of hearing. In this paper, transient response of a circular latex membrane subjected to acoustic impulse was studies by several techniques. In full-field measurements, the fleeting propagation of traveling wave was captured by high-speed interferometric techniques. In addition, to obtain the damping ratio and time constant of the membrane, single-point measurements were performed by LDV. Our high-speed full-field interferometric system is also capable to measure the damping parameters at every point on the surface of the membrane, so that we can generate a 2D map of damping ratios and time-constants for every particular point of the surface of the membrane. Results will be presented in future publications.

Acknowledgements This work has been funded by the National Institute on Deafness and Other Communication Disorders (NIDCD), the National Institute of Health (NIH), the Massachusetts Eye and Ear Infirmary (MEEI), and the Mittal Fund. The authors also gratefully acknowledge the support of the NanoEngineering, Science, and Technology (NEST) program at the Mechanical Engineering Department, Worcester Polytechnic Institute.

References

1. Geisler CD (1998) From sound to synapse, physiology of the mammalian ear. Oxford University Press, New York
2. Rosowski JJ (2010) External and middle ear function, Oxford handbook of auditory science: the ear, chapter 3. doi:10.1093/oxfordhb/9780199233397.013.0003
3. Chittka L, Brockmann A (2005) Perception space-the final frontier. PLoS Biol 3(4):e137. doi:10.1371/journal.pbio.0030137, 564-568
4. Rosowski JJ, Dobrev I, Khaleghi M, Lu W, Cheng JT, Harrington E, Furlong C (2013) Measurements of three-dimensional shape and sound-induced motion of the chinchilla tympanic membrane. Hear Res 301:44–52. doi:10.1016/j.heares.2012.11.022
5. Khaleghi M, Lu W, Dobrev I, Cheng JT, Furlong C, Rosowski JJ (2013) Digital holographic measurements of shape and three-dimensional sound-induced displacements of tympanic membrane. Opt Eng 52(10), 2013
6. Furlong C, Dobrev I, Harrington EJ, Hefti P, Khaleghi M (2012)_ Miniaturization as a key factor to the development and application of advanced metrology systems. Proc SPIE 8413. doi:10.1117/12.981668, 84130T-1:12
7. Solis SM, Santoyo FM, Hernandez-Montes S (2012) 3D displacement measurements of the tympanic membrane with digital holographic interferometry. Opt Express 20(5):5613–5621. doi:10.1364/OE.20.005613
8. Rosowski JJ, Cheng JT, Ravicz ME, Hulli N, Harrington EJ, Hernandez-Montes MS, Furlong C (2009) Computer-assisted time-averaged holography of the motion of the surface of the tympanic membrane with sound stimuli of 0.4 to 25 kHz. Hear Res 253:83–96
9. Thrane N, Wismer J, Konstantin-Hansen H, Gade S (2013) Practical use of the Hilbert transform, technical note, Brüel&Kjær, Denmark
10. Stetson KA, Brohinsky WR (1988) Fringe-shifting technique for numerical analysis of time-average holograms of vibrating objects. J Opt Soc Am A 5(9):1472–1476
11. Cheng JT, Aarnisalo AA, Harrington EJ, Hernandez-Montes MS, Furlong C, Merchant SN, Rosowski JJ (2010) Motion of the surface of the human tympanic membrane measured with stroboscopic holography. Hear Res 263(1–2):66–77
12. Furlong C, Dobrev I, Rosowski JJ, Cheng JT (2013) Assessing eardrum deformation by digital holography. SPIE News Room J Biomed Opt Med Imag. doi:10.1117/2.1201212.004612
13. Takeda M, Ina H, Kobayashi S (1982) Fourier-transform method of fringe-pattern analysis for computer-based topography and interferometry. J Opt Soc Am 72:156–160
14. Dobrev I, Furlong C, Cheng JT, Rosowski JJ (2013) Optimization of a digital holographic otoscope system for in-vivo measurements. Opt Las Eng (in-preparation)
15. Polytec GmbH (2013) Single point vibrometer. http://www.polytec.com

Chapter 2
Directional Failure of Tendons in the Presence of a Notch Defect

Gregory A. Von Forell, Peter S. Hyoung, and Anton E. Bowden

Abstract Ligaments and tendons have been hypothesized to be highly resistant to tear propagation. However, alterations to ligament material response in the presence of tears have yet to be reported. The purpose of this research was to identify the variation in mechanical behavior at distinct fiber angles in tendon both with and without an intentional notch defect (mode I fracture toughness). Seventy two porcine tendon specimens were tested in uniaxial tension. Twety four specimens were pulled along the fiber direction (90°), 24 specimens along the matrix direction (0°), and 24 specimens had a fiber orientation of approximately 45°. In each group of specimens, half (12) were notched approximately 1/4 of the dimension transverse to the loading direction. Tendon tissues containing defects demonstrated a phenomenal resistance to tear propagation, regardless of loading direction. No observable crack propagation occurred in any of the specimens. Also, no significant differences were found in the strength and stiffness of specimens between the groups that had the defects and the ones that didn't.

Keywords Tendon • Ligament • Failure • Tear • Biomechanics

2.1 Introduction

Ligaments and tendons are commonly torn or ruptured [1], however, our current understanding of what level of injury warrants continued use versus rest or even surgical intervention is almost exclusively empirical in nature. Ligaments and tendons have been hypothesized to be highly resistant to tear propagation [2], however specific values for fracture toughness have yet to be reported. A tissue's ability to resist further propagation once it has been torn has been recently investigated in soft biological tissues not including tendons and ligaments [2–8]. These results have provided a backdrop for initiating a preliminary study exploring the directional fracture toughness in tendons and ligaments.

Ligaments are soft fibrous tissues that are made of elastin and collagen fibers and attach one bone to another across a joint. Tendons are similar in structure, but connect muscle to bone. Due to the structure of the ligaments and tendons, their mechanical responses are anisotropic with their nonlinear elastic properties being much higher along the direction of the collagen fibers when compared to the matrix direction. Ligaments and tendons are highly resistant to tension but buckle quickly in compression due to geometric effects (i.e., their "sheet-like" organization).

Although efforts have been made to characterize the fracture toughness various fiber orientations in structural materials [9], there are no reports of these characterizations being made in biological tissues. Based on experience with polymer matrix composites [10], we hypothesized that the fracture toughness is likely to be the highest when the crack is perpendicular to the fibers and lowest when it is parallel to the fibers. However, the specifics describing variation of fracture toughness with fiber angle have not been reported. The purpose of this research was to identify the variation in mechanical behavior at distinct fiber angles in tendon both with and without an intentional notch defect (mode I fracture toughness).

G.A. Von Forell • P.S. Hyoung • A.E. Bowden (✉)
Brigham Young University, 435 Crabtree Building, Provo, UT, USA 84602,
e-mail: abowden@byu.edu

F. Barthelat et al. (eds.), *Mechanics of Biological Systems and Materials, Volume 4*,
Conference Proceedings of the Society for Experimental Mechanics Series,
DOI 10.1007/978-3-319-00777-9_2,

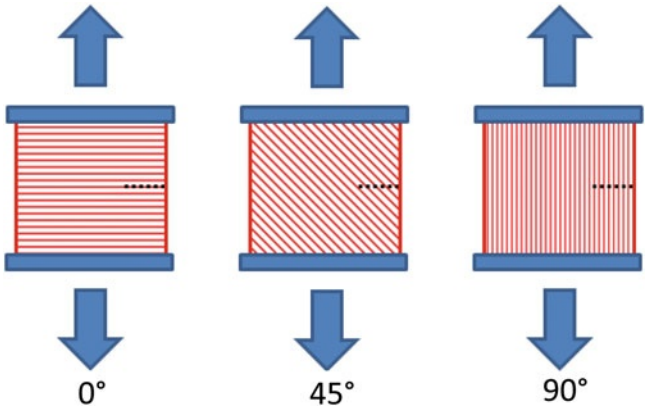

Fig. 2.1 Representation of the three groups of specimens pulled in tension. The *arrows* show the direction of tension. The *lines* show the direction of the tendon fibers. The *dotted line* shows the location of the notches that were created in half of the testing specimens

2.2 Methods and Materials

Freshly dissected porcine tendon was obtained from a local abattoir and stored at −20°C until testing. Testing specimens were cut to a uniform thickness of 0.5 mm using a cryotome, and were approximately 1 cm by 0.5 cm. A total of 72 specimens were tested in uniaxial tension. Twenty four specimens were pulled along the fiber direction (90°), 24 specimens along the matrix direction (0°), and 24 specimens had a fiber orientation of approximately 45°. In each group, half of the specimens were notched approximately 1/4 of the dimension transverse to the loading direction using a microtome blade while frozen, while a control group remained unnotched. Figure 2.1 shows a representation of an example from each group where the specimens have been notched. All specimens were pulled in tension using an Instron Model 3342 (Instron, Norwood, MA) at a rate of 10 mm/min. Specimens were held in grips with fresh sand paper super glued to the surface. Specimens were kept hydrated by periodic spritzing of PBS solution throughout testing. The order of testing was randomized over 2 days of testing. Individual specimen dimensions were quantified using calibrated optical microscopy. Analysis of the dimensions of each specimen including length, width, thickness and crack length (if present) was done using Analyze 8.1 (Mayo Clinic, Rochester MN).

2.3 Results

Figure 2.2 shows typical failures of the tendons from each of the groups with and without notches. Surprisingly, no observable crack propagation occurred in any of the specimens (indicating a virtually infinite mode I fracture toughness!) No visible difference in failure mode was seen between groups with and without notches when being pulled at the same angle. Stresses and strains were calculated for all of the specimens. For the specimens that contained defects, the stresses were calculated based on the width of the specimen minus the crack length to determine whether the crack tip induced stress concentrations that would reduce the strength of the specimen. Results for Young's Modulus and ultimate tensile strength and their corresponding standard deviations are shown in Fig. 2.3. No significant difference was found between similar groups with and without notches when being pulled at the same angle.

2.4 Discussion

The tendon tissue showed a very high resistance to tear propagation, primarily due to dramatic increase in crack dimension (e.g., crack tip blunting). There were no significant differences found in the strength and stiffness of specimens with and without defects. Figure 2.4 shows the crack tip blunting that occurred for specimens with fiber directions oriented both parallel to the notch direction (A) and perpendicular to the fiber direction (B). Although crack tip blunting geometrically reduces the stresses around the crack tip, the results shown in this research suggest the blunting doesn't fully explain the tendon's high fracture toughness. Other published research shows that tears in soft tissues can still propagate even when

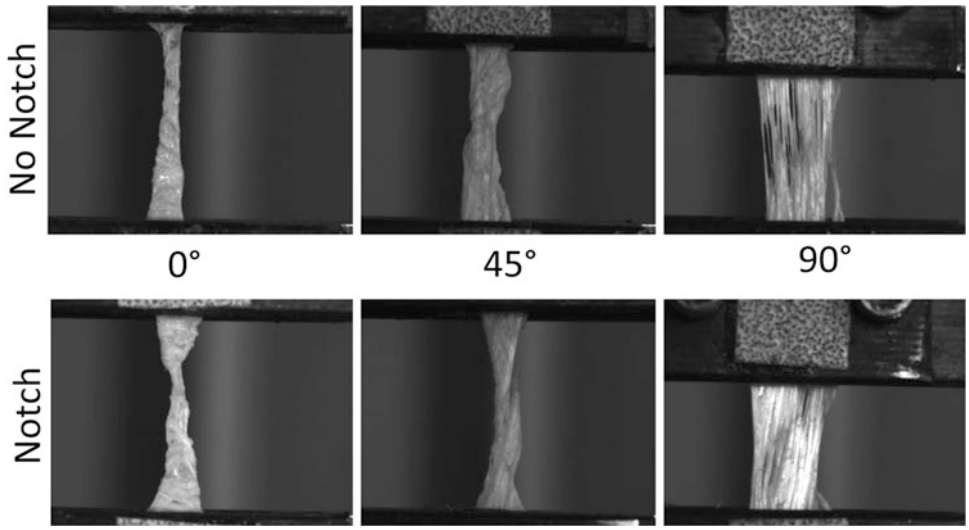

Fig. 2.2 Photographs of a typical failure of the tendons for all three groups with and without notches

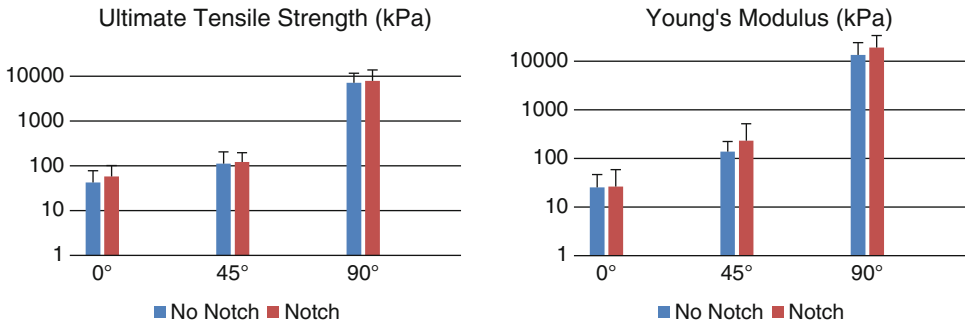

Fig. 2.3 Ultimate tensile strength and Young's Modulus for all three groups with and without notches

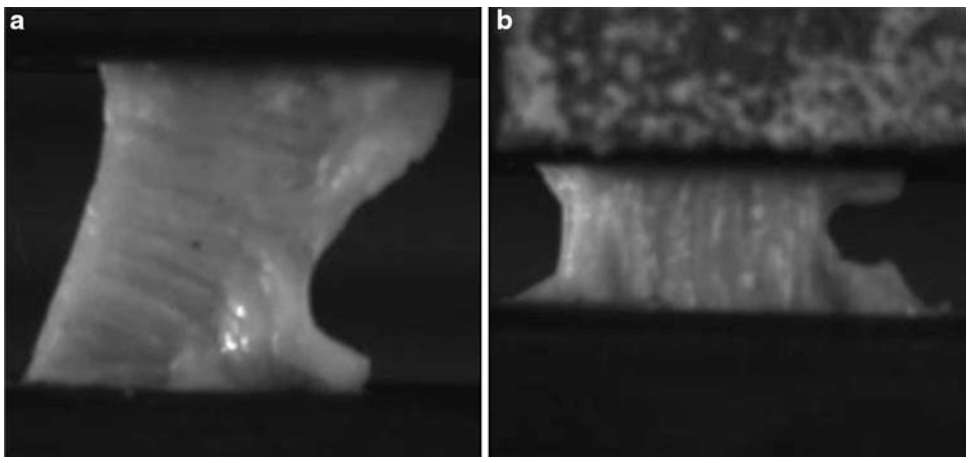

Fig. 2.4 Examples of crack tip blunting for 0° (**a**) and 90° (**b**)

crack tip blunting is substantial [8].zhe high fracture toughness results in the fiber direction (90°) are likely explained by the high energy required for the fibers to fail which would be required for the crack to propagate. This effect is exaggerated by the large difference in stiffness between the matrix and fiber direction that exists in the porcine tendon.

However, we were surprised to find that the angle between the tear and fiber direction showed no difference in the tendon's fracture toughness. This behavior seems to be driven by the unique constitutive response of the matrix (i.e., concave down, virtually flat stress–strain response at higher strains). Thus, there is virtually no stress concentration at the crack tip. Unlike traditional engineering materials, which share load with material in the crack region at the expense of a stress concentration at the crack tip, the tissue above and below the crack do not contribute to the mechanical stiffness of the tissue. Thus, the tissue sacrifices a stronger material response, but with the benefit of strong crack growth inhibition.

The strength and stiffness of the tissue at the various angles followed of the expected behavior of standard composite materials. However, only three angles were tested, and more angles would need to be tested to show that the patterns follow a "rule of mixtures".

2.5 Conclusion

The results of this study show that ligaments and tendons have an incredibly high ability to resist further tearing after an initial tear. This high fracture toughness is even higher than shown previously in other soft tissues such as muscle. Therefore, after an initial tear, the largest concern comes from the tendon or ligament lower strength due to a smaller cross section and not from any stress risers that may occur from geometric effects of a tear.

Acknowledgements Funding for this project was provided by the National Science Foundation (CMMI-0952758). Any opinions, findings, and conclusions or recommendations expressed in this material are those of the authors and do not necessarily reflect the views of the National Science Foundation.

References

1. Clayton RA, Court-Brown CM (2008) The epidemiology of musculoskeletal tendinous and ligamentous injuries. Injury 39(12):1338–1344
2. Taylor D et al (2012) The fracture toughness of soft tissues. J Mech Behav Biomed Mater 6:139–147
3. Purslow PP (1985) The physical basis of meat texture – observations on the fracture-behavior of cooked bovine M-semitendinosus. Meat Sci 12(1):39–60
4. Stok K, Oloyede A (2007) Conceptual fracture parameters for articular cartilage. Clin Biomech (Bristol, Avon) 22(6):725–735
5. Chin-Purcell MV, Lewis JL (1996) Fracture of articular cartilage. J Biomech Eng 118(4):545–556
6. Oyen-Tiesma M, Cook RF (2001) Technique for estimating fracture resistance of cultured neocartilage. J Mater Sci Mater Med 12(4):327–332
7. Koombua K, Pidaparti RM, Beatty MW (2006) Fracture toughness estimation for the TMJ disc. J Biomed Mater Res A 79(3):566–573
8. Wu KS et al (2006) Graded delamination behavior of human stratum corneum. Biomaterials 27(34):5861–5870
9. Chou I (1998) Effect of fiber orientation and moisture absorption on the interlaminar fracture toughness of CFRP laminates. Adv Comp Mater 7(4):377–394
10. Norman DA, Robertson RE (2003) The effect of fiber orientation on the toughening of short fiber-reinforced polymers. J Appl Polym Sci 90 (10):2740–2751

Chapter 3
Age and Regional Dependence of Collagen Crimp in Heart Valves

Jennifer M. Kreuz, Kendra N. Erskine, Alicia A. Blancas, and K. Jane Grande-Allen

Abstract The hierarchical structure and organization of collagen plays an integral role in the mechanical behavior of heart valve tissues, but with few exceptions the degree of collagen fiber crimp has not been extensively quantified. Given our recent demonstration of age-dependent and region-dependent variations in mechanical behavior of heart valves, this study quantified crimp period and amplitude in all four heart valves as a function of orientation (circumferential vs. radial), age (6 week, 6 month, and 6 year old pigs), and region (mitral anterior leaflet center vs. free edge). Polarized light microscopy of picrosirius red stained sections revealed that collagen crimp was generally consistent between the circumferential and radial directions, although for the pulmonary valve there was a greater crimp period circumferentially than radially. Comparing all valves and orientations showed that the crimp period was greatest circumferentially in the center of the mitral anterior leaflet. With respect to age, crimp period was lowest in the 6 month old aortic valve (matching previously reported patterns of aortic valve leaflet extensibility) and highest in the 6 month old mitral anterior leaflet center. Interestingly, the differences in magnitudes of crimp amplitude mimicked the crimp period data, suggesting a scaling phenomenon in collagen fiber crimping.

Keywords Heart valve • Collagen • Crimp • Extracellular matrix • Soft tissue mechanics

3.1 Introduction

The hierarchical structure and organization of collagen plays an integral role in the mechanical behavior of heart valve tissues and thus in the efficiency of valve function [1–3]. It is widely appreciated that collagen fibers within heart valves demonstrate crimp, as they do in many other connective tissues, but with a few notable exceptions the degree of collagen crimp in native valves has not been extensively quantified. Collagen within the chordae tendineae of mitral valves has received the most quantitative analysis. For example, Liao and Vesely reported that there was a correlation between the magnitude of crimp period in collagen in chordae and the extensibility of these same tissues [4]. More recently, Vidal Bde and Mello employed a Fast Fourier Transform method to measure the birefringence of collagen crimp in chordae, which allowed them to quantify the amount of collagen fiber alignment and also demonstrated the helical structure of collagen fibers [5]. As for the heart valve leaflets, it has been reported in several studies of collagen crimp in aortic valves subjected to different fixation pressures that as pressure increased, there was an increase in the period of the crimp and a decrease in total amount of visibly crimped collagen [6, 7]. Joyce et al. reported that for 8–9 month old pigs, the period of collagen crimp was similar between the aortic and pulmonary valve leaflets fixed at pressure of 0 mm Hg, and was in the range of 10–20 μm [3]. Although Aikawa et al. showed that the overall alignment of collagen within the semilunar valves increases with age [8], there has not been a quantitative analysis of the variation in crimp amplitude and period with age. It is also unknown whether crimp patterns vary amongst the different anatomic regions of the heart valves, or between collagen fibers oriented circumferentially or radially. It appears to be a common assumption in models of valve biomechanics that crimp patterns do not vary, even though it was previously demonstrated crimp period does vary among different types of chordae [4].

J.M. Kreuz • K.N. Erskine • A.A. Blancas • K.J. Grande-Allen (✉)
Department of Bioengineering, Rice University, 6100 Main St., MS 142, Houston, TX 77005, USA
e-mail: grande@rice.edu

F. Barthelat et al. (eds.), *Mechanics of Biological Systems and Materials, Volume 4*,
Conference Proceedings of the Society for Experimental Mechanics Series,
DOI 10.1007/978-3-319-00777-9_3,

A recent study from our group characterized the age-related changes in the mechanical properties of aortic and mitral valves [9]. The ages of pigs used in this study were 6-week, 6-month, and 6-year, which correspond to human ages of pediatric, young adult, and older adult. With increasing age, the general findings were corresponding increases in the pre-transition and post-transition stiffnesses and reductions in extensibility. Interestingly, the circumferentially oriented strips from the 6-month old aortic valves were the least extensible and showed the highest pre-transition stiffness, compared with the 6-week and 6-year old age groups. It was noted in performing that study that the transition regions of the stress–strain curves changed with age and orientation of the section. Therefore, a new parameter was created, termed the radius of transition curvature (RTC), to describe this region; RTC was measured by fitting a circle to the transition region and measuring the radius of the circle. The RTC was significantly different between the radially and circumferentially sections for both the aortic and mitral valves, and increased with age for circumferentially oriented sections of the free edge of the mitral anterior leaflet and for mitral leaflet radial sections. We speculated that the degree of collagen crimp may have been a contributing factor to the age-dependent and region/valve-dependent variations in material behavior, particularly those related to the first portion of the stress–strain curve, namely pre-transition stiffness, extensibility, and RTC.

Therefore, the purpose of this study was to investigate collagen crimp period and amplitude in radially and circumferentially oriented strips of heart valve tissue. Two studies were performed. In the first study, we built upon the previous mechanical testing work [9] by using picrosirius red staining to characterize collagen crimp in aortic and mitral valves from 6 week, 6 month, and 6 year old pigs. In the second study, w investigated collagen crimp in leaflets from all four valves from 6 month old pigs.

3.2 Methods

3.2.1 Tissue Sample Procurement

For the first study, the aortic valve (AV) and mitral valve (MV) were obtained from at least three hearts from each age group of pigs (6 week, 6 month, and 6 year, Table 3.1). Porcine hearts were obtained from abattoirs (Fisher Ham and Meat, Spring, TX, for 6 week-old and 6 month-old pigs; Animal Technologies, Tyler, TX, for 6 year-old pigs). Because the anterior leaflet of the MV demonstrates heterogeneous stiffness [10] and ECM composition [11], these leaflets were divided into circumferentially oriented sections from the anterior center (MVAC) and the free edge (MVF) (Fig. 3.1). Several radially oriented sections were also collected for visual comparison with the circumferential sections.

Table 3.1 Number of hearts used in the first study. All analyzed samples were circumferentially oriented

	6 week	6 month	6 year
Mitral valve	–	–	–
Anterior leaflet free edge	3	3	3
Anterior leaflet center	3	3	3
Aortic valve	3	8	3

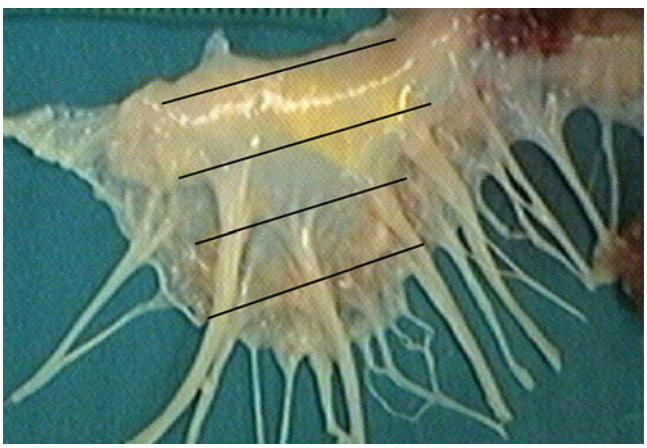

Fig. 3.1 The mitral anterior leaflet was divided into two circumferentially oriented sections, the center region (MVAC) and the free edge region (MVF)

Table 3.2 Number of hearts used in the second study

	Circumferential	Radial
Mitral valve		
Anterior leaflet free edge	3	–
Anterior leaflet center	3	–
Anterior leaflet	–	3
Posterior leaflet	3	3
Aortic valve	8	7
Tricuspid valve	6	6
Pulmonary valve	6	6

For the second study, the MV, AV, tricuspid valve (TV), and pulmonary valve (PV) were obtained from at least 3 hearts from 6 month old pigs (Table 3.2). The valves were fixed in 10 % formalin overnight, cut into 5 mm wide segments oriented in either the circumferential or radial direction of the heart valve, and embedded in paraffin. The valves were then cut into 5 μm sections. One to three sections per valve segment were then mounted on slides depending on the study. For the first study, all segments were circumferentially oriented and 2–3 sections were prepared from each segment. For the second study, samples were analyzed in both the circumferential and radial directions. A greater number of valves were analyzed in the second study, thus only one section was prepared per valve segment.

3.2.2 Picrosirius Red Staining and Microscopy

Valve sections were dewaxed with xylene, rehydrated using a series of graded alcohols, and stained with picrosirius red (0.1 % Sirius red in saturated aqueous picric acid) for 1 h. The slides were then were rinsed in two rounds of 0.5 % acetic acid in ddH_2O, dehydrated, and mounted with cover slips. Sections were viewed under polarized light using a microscope with a 40× or 63× objective. Two matched groups of images were captured using the polarizer set either for complete extinction of light or to allow transmission of light. In both cases the wavy crimping pattern of the collagen fibers was evident, however in the latter case the entire sample appeared reddish pink against a white background and in former case the birefringent collagen fibers were visible as red-orange banded structures against a black background. Furthermore, within each group (birefringent or white light background), there were multiple images captured from each slide to demonstrate the collagen crimp within the valvular fibrosa layer.

3.2.3 Measuring Crimp Characteristics

Crimp period and amplitude were measured from the polarized light images using ImageJ (NIH, Bethesda, MD). Three straight lines were drawn across the image at approximately 25 %, 50 %, and 75 % of the distance from the top (Fig. 3.2), and any sections of crimped collagen fibers that intersected the line were measured. Multiple individual collagen fibers were analyzed for each image.

Period was measured from the images of birefringent collagen (black blackground), in which the peaks and troughs of the crimp pattern were apparent as dark bands. To perform the measurement, lines were drawn across sections of visible banding that intersected with the 25 %, 50 %, or 75 % lines described above. Since each band represents either a peak or a trough, the distance between two bands represented a single crimp period. The period was calculated by dividing the length of the line (shown in yellow in Fig. 3.2) by half the number of bands intersecting the line (indicated by the white arrows in Fig. 3.2).

Amplitude was measured from the polarized light images with the white background; these images better showed individual fibers than did the birefringent images. The amplitude was measured by drawing a line across two peaks of the same fiber (yellow lines in Fig. 3.2). Another line was drawn perpendicular from the peak-to-peak line down to the bottom of the trough of the same fiber as shown by the green line in Fig. 3.2. Amplitude was calculated by dividing the length of the green line by two.

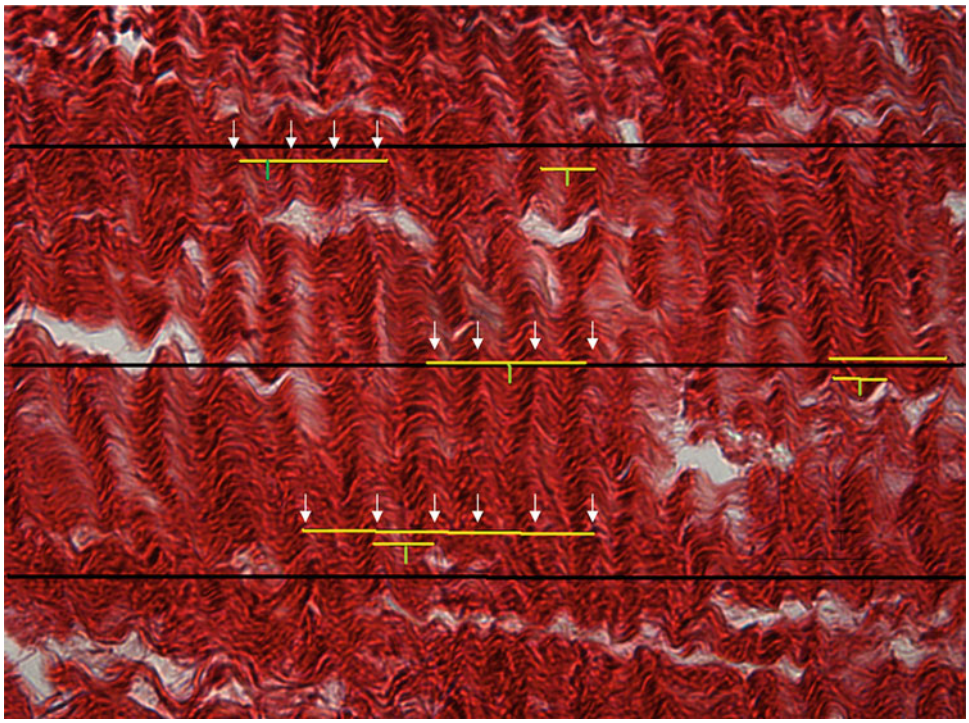

Fig. 3.2 Method for measuring wavelength (*arrows* and *yellow lines*) and amplitude (*green lines*) (color figure in online)

3.2.4 Data and Statistical Analysis

Descriptive statistics (mean and standard deviation) were determined for the data for each direction, age, and valve or valve region, depending upon the study. Single factor analysis of variance (ANOVA) with post-hoc Tukey tests were used to determine whether differences between factors were statistically significant at a level of 0.05. All statistical tests were performed using SigmaStat (SPSS, Chicago, IL).

3.3 Results

3.3.1 Study 1: Effect of Age

In the first study, we measured period and amplitude of collagen crimp in circumferentially oriented sections of AV, MVAC, and MVF, and found significant differences between the 6 week, 6 month, and 6 year age groups. Upon initial visual analysis, it was immediately apparent that there was more crimp aligned in the circumferential direction (Figs. 3.3 and 3.4). Both orientations show a higher amount of collagen organized on the edges of the valve than the center. Due to the low organization of collagen in the radial direction, the wavelength and amplitude were not able to be measured accurately in that orientation and thus the data analysis was limited to the circumferential sections. Initial visual analysis appears to show smaller waves in the 6 month age group circumferentially (Fig. 3.3).

In the AV, the crimp period was largest in the 6 week age group and smallest at 6 months (both $p < 0.05$, Fig. 3.5). The crimp period at 6 years was larger than at 6 months AV ($p < 0.0001$) but smaller than at 6 weeks ($p < 0.0001$). Crimp amplitude in the AV was similarly the lowest for the 6 month age group ($p \leq 0.015$), but there was no difference between the crimp amplitude at 6 weeks and 6 years ($p = 0.144$, Fig. 3.6).

In the MVAC, crimp period at 6 weeks was significantly smaller than the period at 6 months ($p \leq 0.001$). There was no significant difference in crimp period between 6 week and 6 month old samples. Crimp amplitude in the 6 month valves was higher than for both the 6 week and 6 year old valves ($p < 0.05$), but the 6 week and 6 year old valves were not different from each other. In the MVF, crimp period in the 6 week old valves was again significantly smaller than in

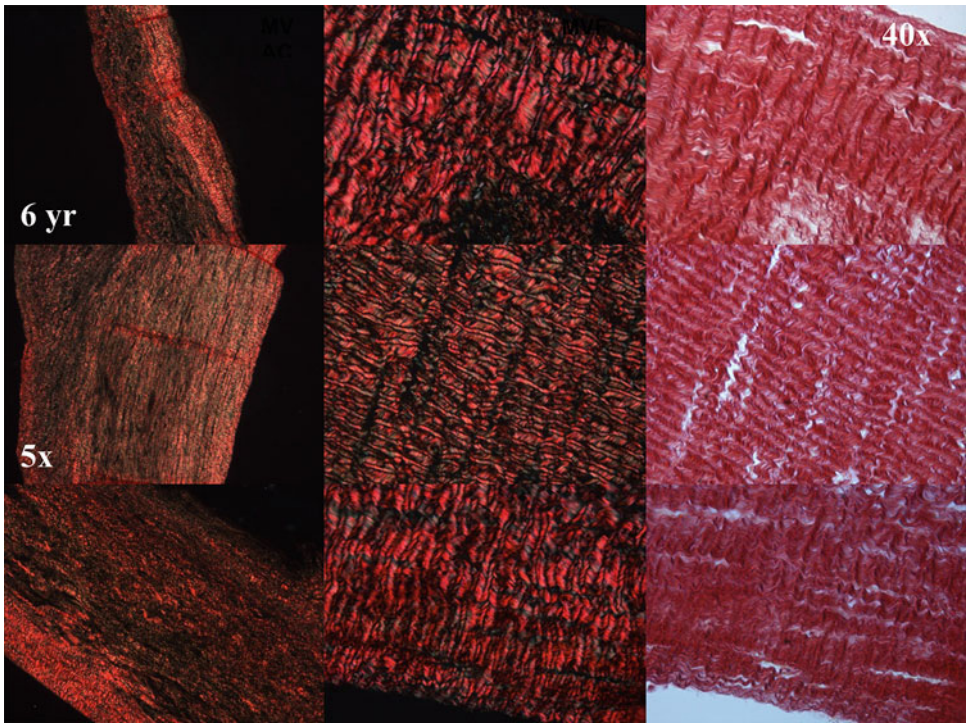

Fig. 3.3 Circumferential Sections. Rows are 6 week, 6 month and 6 year age groups. Columns are 5× polarized with *dark* background, 40× polarized with dark background, and 40× polarized with *white* background

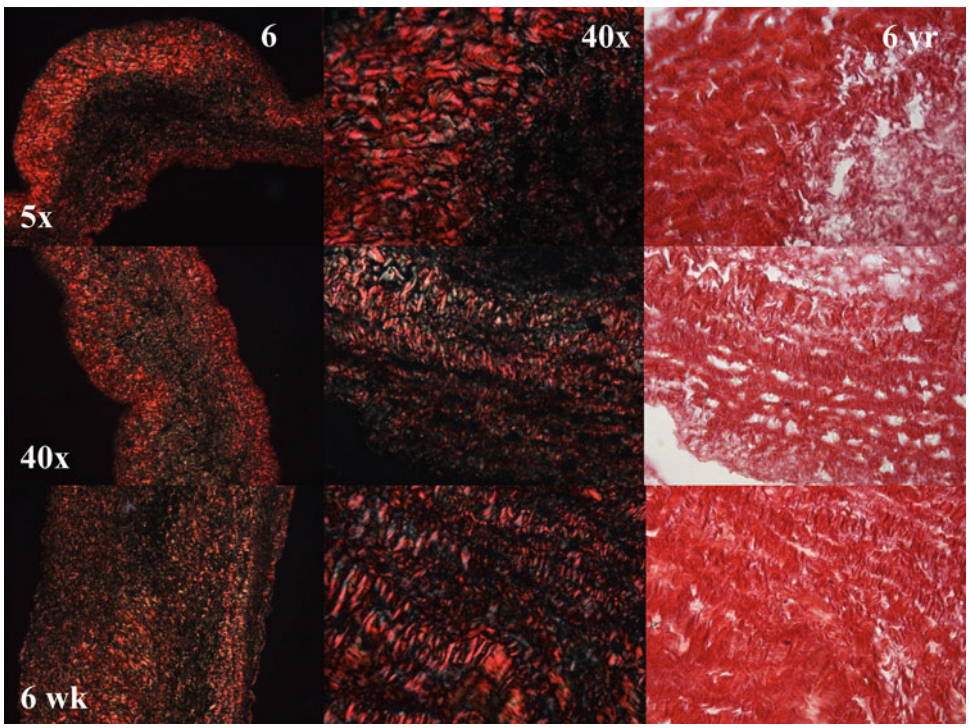

Fig. 3.4 Radial sections. Rows are 6 week, 6 month, and 6 year. Columns are 5× polarized with *dark* background, 40× polarized with dark background, and 40× polarized with *white* background

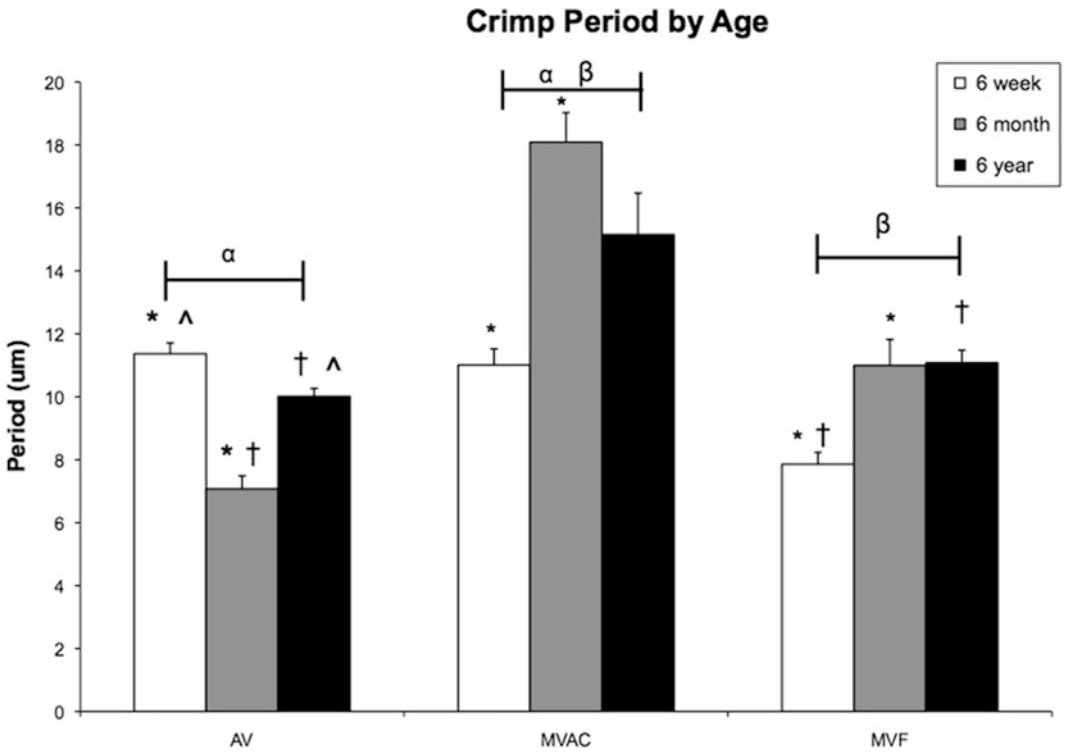

Fig. 3.5 Crimp period by age. α, β signify statistical difference between valve types. *, ^, † signify statistical difference between ages within each valve type

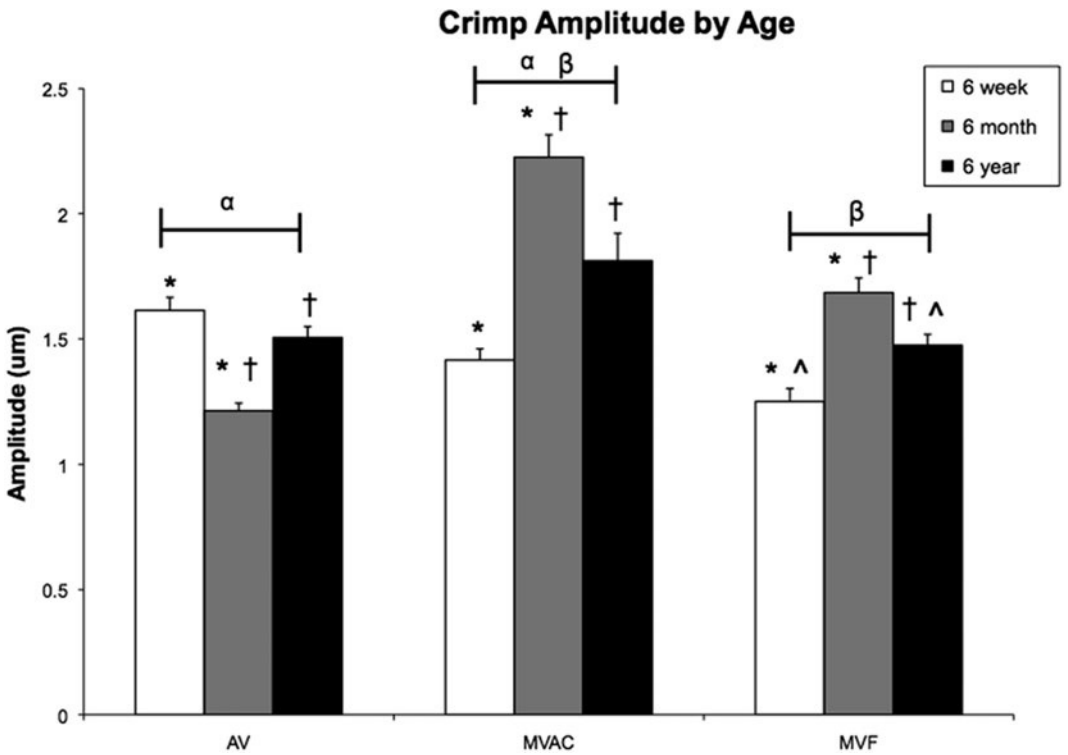

Fig. 3.6 Crimp amplitude by age. α, β signify statistical difference between valve types. *, ^, † signify statistical difference between ages within each valve type

the 2 older groups ($p \leq 0.0001$), but there was no significant difference between 6 month and 6 year old valves ($p = 0.848$). The crimp amplitude was significantly different between all age groups, being lowest in the 6 week old valves, higher in the 6 year old valves, and highest in the 6 month old valves.

In comparing the overall patterns with age between different valve types, the AV showed a decrease in period and amplitude at 6 months and an increase at 6 years, whereas the 2 MV sections (MVAC and MVF) showed an increase in both period and amplitude at 6 months.

We also examined differences between the valves within age groups. At 6 weeks, the period of the AV and MVAC was larger than the MVF ($p \leq 0.025$) and the amplitude of the AV was larger than the MVF ($p = 0.017$). Within the 6 month age group, all three valve sections showed significant differences in period and amplitude with MVAC being the largest and AV being the smallest ($p \leq 0.05$). The period of the MVAC at 6 years was larger than both the AV and the MVF ($p \leq 0.025$) with no significant differences in amplitude.

3.3.2 Study 2: Effect of Type of Heart Valves

The second part of the study consisted of comparing radial and circumferential sections of all four valves in the 6 month age group (Figs. 3.7 and 3.8). The most noteworthy finding was that the period and amplitude of the MVAC (which was by definition a circumferential orientation) was significantly larger than all other valves regardless of region ($p < 0.025$). The period and amplitude for the AV radial, AV circumferential, and PV radial sections were not statistically different from each other ($p > 0.517$) and smaller than all other valve regions ($p < 0.004$). With the exception of PV and MVAC, there was no difference in period or amplitude between radial and circumferentially oriented sections ($p > 0.092$). For the PV, the period and amplitude in the circumferentially oriented sections was larger than in the radially oriented sections. Similarly, the crimp and amplitude in the MVAC (circumferential) was larger than for the MV-anterior radial section ($p < 0.005$). Overall, these data reflect the well known alignment of collagen in the circumferential direction of heart valves.

3.4 Discussion

The crimped nature of fibrillar collagen is fundamentally important to the extensibility of soft biological tissues and is responsible for the initial low slope "toe region" of the biological stress–strain curve. The degree of crimping is also known to vary amongst different types of biological tissues (i.e., tendons, heart valves, etc.) and between species. We have previously reported differences in heart valve extensibility depending on age and which type of heart valve was being examined [9], which motivated this study. Our major findings were first, that there is a pattern of lower crimp period and amplitude in the 6 month old porcine AVs, compared to the younger (6 week) and older (6 year) samples. This result was actually a finding that resulted from a pilot analysis of crimp period in the AV, and motivated the inclusion of the mitral valve anterior leaflets in the study. In contrast to the AV, the MVAC (although not the MVF) had the highest crimp period and amplitude at 6 months. The age-based differences in heart valve crimp most likely translate into differences in physiological valve function, which is due to the effect of aging on the heart and vasculature. In general, the unexpected finding that crimp amplitude generally scaled with crimp period may indicate that the collagen fibers are changing in size overall as opposed to becoming more or less wavy with age.

The second major finding was that the center of the anterior mitral leaflet had such higher level of crimp period and amplitude (in the circumferential direction) than was found in all other leaflets in the four heart valves. Given that the crimp period and amplitude were again proportionately increased in scale, there may not be a profound impact of this finding on the leaflet mechanics. It is worth noting, however, that this region is the most thick region of all valve tissue, with a robust layer of highly aligned collagen that bears the majority of the trans-valvular pressure load across the mitral valve when it is closed.

The third major finding was that there the differences in crimp period and in crimp amplitude between the circumferential and radial directions, even when statistically significant, were not large. This result may be due to the splay of collagen fiber orientation throughout all heart valve leaflets. Collagen fibers are oriented in a mesh-like network that is presumed to distribute load across the leaflet tissues and prevents leaflet prolapse and rupture when the valves are pressurized.

There were some limitations to this study that should be considered when interpreting the study results. First, the three different ages of pig heart valves were obtained from two different commercial abbatoirs: the two younger ages were from one abbatoir and the older hearts were from a different vendor. It may be that there are some breed-specific differences in crimping that explain some of the data reported here. However, these are the same ages and vendors of pigs that were used in

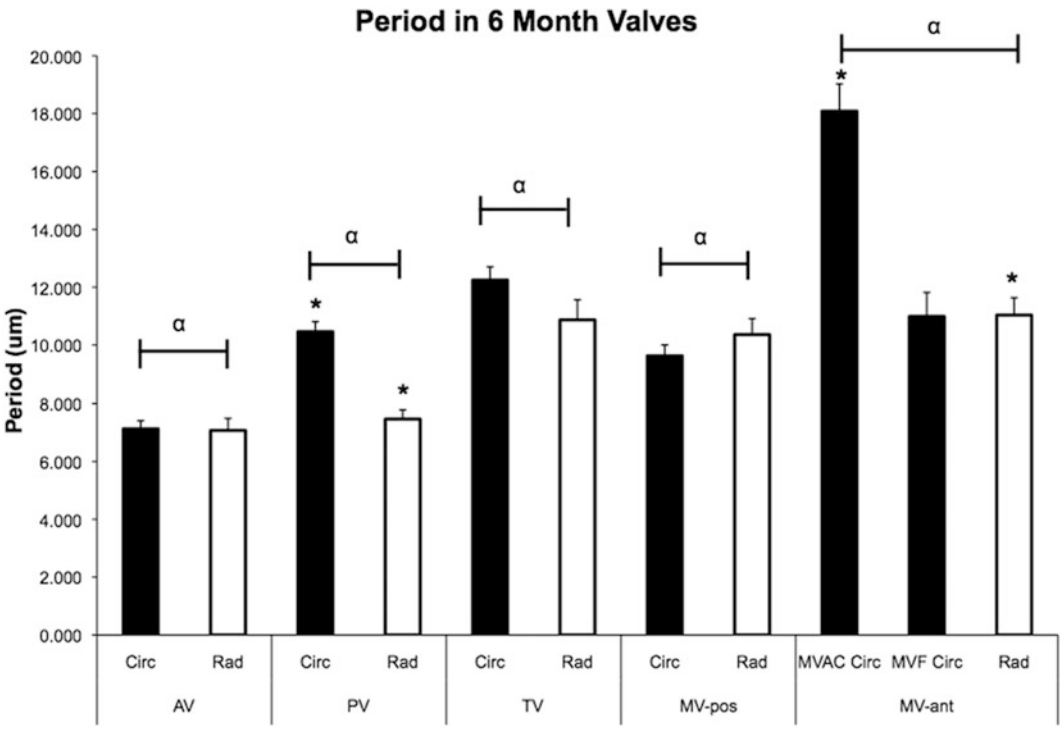

Fig. 3.7 Period in 6 month valves. α signifies statistical difference between valve types. * signifies statistical difference between sample orientation

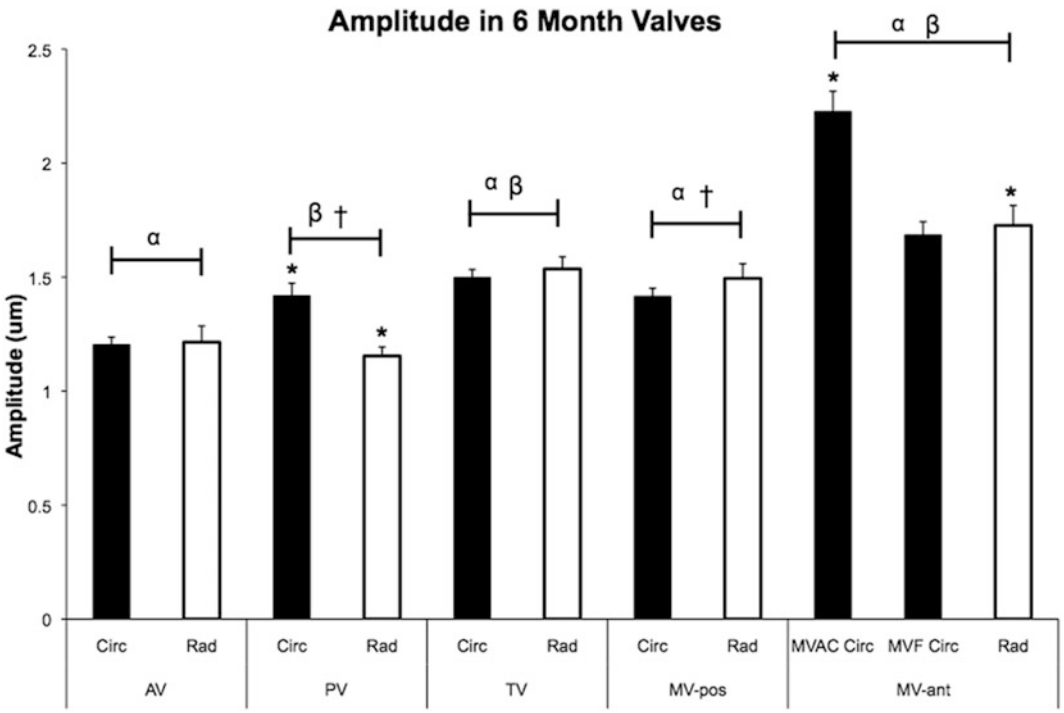

Fig. 3.8 Amplitude in 6 month valves. $\alpha, \beta, \dagger$ signify statistical difference between valve types. * signifies difference between sample orientation

our previous study of the mechanical behavior of the aortic and mitral valve tissues. Second, there are some limitations related to the method of collecting the data about the crimp measures. There was subjectivity employed in finding and capturing the images of the samples that had enough visible collagen crimp to measure. To overcome this inevitable source of human error, we tried to make the areas on each image measured as objectively as possible by measuring only collagen fibers that crossed the lines at 25 %, 50 %, and 75 % of the vertical.

In conclusion, this study demonstrated for the first time that there is a statistically significant difference in collagen crimp between different valvular ages and differing valvular types. Future work is required to improve our understanding of the relationship between collagen crimp and mechanical behavior of heart valves, and may involve integrating the degree of crimp into constitutive models of heart valve elasticity. Better understanding the biomechanics of heart valves will help to optimize the development of improved heart valve replacements, whether these are bioprosthetic valves or tissue engineered heart valves, and perhaps promote the development of new valve replacement devices that can be tailored for patients in different ages groups.

Acknowledgements The authors thank Elizabeth Stephens, M.D., Ph.D., for providing some of the porcine valve samples. This research was funded by the March of Dimes.

References

1. Balguid A, Driessen NJ, Mol A, Schmitz JP, Verheyen F, Bouten CV, Baaijens FP (2008) Stress related collagen ultrastructure in human aortic valves–implications for tissue engineering. J Biomech 41(12):2612–2617
2. Cochran RP, Kunzelman KS, Chuong CJ, Sacks MS, Eberhart RC (1991) Nondestructive analysis of mitral valve collagen fiber orientation. ASAIO J 37(3):M447–M448
3. Joyce EM, Liao J, Schoen FJ, Mayer JE Jr, Sacks MS (2009) Functional collagen fiber architecture of the pulmonary heart valve cusp. Ann Thorac Surg 87(4):1240–1249
4. Liao J, Vesely I (2003) A structural basis for the size-related mechanical properties of mitral valve chordae tendineae. J Biomech 36(8):1125–1133
5. Vidal Bde C, Mello ML (2009) Structural organization of collagen fibers in chordae tendineae as assessed by optical anisotropic properties and Fast Fourier transform. J Struct Biol 167(2):166–175
6. Flomenbaum MA, Schoen FJ (1993) Effects of fixation back pressure and antimineralization treatment on the morphology of porcine aortic bioprosthetic valves. J Thorac Cardiovasc Surg 105(1):154–164
7. Hilbert SL, Barrick MK, Ferrans VJ (1990) Porcine aortic valve bioprostheses: a morphologic comparison of the effects of fixation pressure. J Biomed Mater Res 24(6):773–787
8. Aikawa E, Whittaker P, Farber M, Mendelson K, Padera RF, Aikawa M, Schoen FJ (2009) Human semilunar cardiac valve remodeling by activated cells from fetus to adult: implications for postnatal adaptation, pathology, and tissue engineering. Circulation 113(10):1344–1352
9. Stephens EH, de Jonge N, McNeill MP, Durst CA, Grande-Allen KJ (2010) Age-related changes in material behavior of porcine mitral and aortic valves and correlation to matrix composition. Tissue Eng 16(3):867–878
10. Kunzelman KS, Cochran RP (1992) Stress/strain characteristics of porcine mitral valve tissue: parallel versus perpendicular collagen orientation. J Card Surg 7(1):71–78
11. Grande-Allen KJ, Calabro A, Gupta V, Wight TN, Hascall VC, Vesely I (2004) Glycosaminoglycans and proteoglycans in normal mitral valve leaflets and chordae: association with regions of tensile and compressive loading. Glycobiology 14(7):621–633

Chapter 4
The Cohesive Law and Toughness of Engineering and Natural Adhesives

Ahmad Khayer Dastjerdi, Elton Tan, and François Barthelat

Abstract Polymeric adhesives play a critical role in engineering applications, whether it is to bond components together or to serve as matrix for composite materials. Likewise, adhesives play a critical role in natural materials where adhesion is needed (e.g. mussel byssus) or to simply preserve the integrity of natural composite materials by holding fibers together (e.g. extra-collagenous proteins in bone). In this work we use a newly developed technique to measure the cohesive law and toughness of adhesives which is similar to a standard double cantilever beam configuration, but in which the beams are replaced by two rigid blocks. We originally developed this method for extracting the cohesive law of soft and weak biological adhesives, and we here show that it can be modified to include high strength of engineering adhesives. Using this method, the cohesive law of the adhesive is directly computed from the load-deflection curve of the experiment, without making initial assumption on its shape. The cohesive law reveals the strength and extensibility of the adhesives, which is richer in information than the toughness (which is the area under the cohesive law). We also define a non-dimensional parameter which can be used to quantitatively investigate whether the assumption of rigid substrates is valid. For values of the parameter close to unity, the RDCB rigidity assumption is valid and the method directly yields the cohesive law of the adhesive. The engineering and natural adhesives we tested showed a wide range of strength, toughness and extensibility, and revealed new pathways which can be exploited in the design and fabrication of biomimetic materials.

Keywords Adhesives • Fracture toughness • Double-cantilever beam test • Cohesive law • Interfacial adhesion

4.1 Introduction

In recent years, engineering adhesives are increasingly being used in many industries such as automotive and aerospace for bonding various structures [1, 2]. In comparison with classical joining methods such as fastening or spot welding, adhesive joints provide distinct advantages which enable them to be extensively used in a variety of technological and industrial applications. Bonded components transfer stresses more uniformly even if they are made of dissimilar materials, and a glued joint is lighter and less expensive than other traditional joining methods [1]. The main failure mode of adhesive joints is shearing, and the most common testing method to characterize their performance is shear lap test, yielding the strength of the interface [3]. Despite the fact that the strength of an adhesive interface is a key factor controlling its mechanical performance, it is now well-understood that the strength of a material can highly be affected by presence of defects and flaws which may form due to inaccurate joint assembly or inappropriate curing; these defects under certain loading condition may propagate into large crack and eventually lead to its failure. It is therefore essential to characterize and evaluate the toughness of the bond line, which directly affects strength, reliability and energy absorption of the material. Several experimental techniques have so far successfully designed and employed to measure the fracture toughness of adhesive joints under mode I fracture loading (opening mode) which include double cantilever beam (DCB) test [4, 5], blister test [6], and indentation test [7, 8]. Amongst them, the DCB test, developed by Ripling and Mostovoy [4] has gained considerable popularity owing to its relative simplicity of analysis and

A. Khayer Dastjerdi • E. Tan • F. Barthelat (✉)
Department of Mechanical Engineering, McGill University, Montreal, QC, Canada
e-mail: ahmad.khayerdastjerditoroghi@mail.mcgill.ca; elton.tan@mail.mcgill.ca; francois.barthelat@mcgill.ca

F. Barthelat et al. (eds.), *Mechanics of Biological Systems and Materials, Volume 4*,
Conference Proceedings of the Society for Experimental Mechanics Series,
DOI 10.1007/978-3-319-00777-9_4,

easiness of sample preparation. This test method has also been adopted as an ASTM standard [9]. A DCB specimen consists of two rectangular beams, of uniform thickness, bonded together by a thin layer of adhesive in such a way that one end of the beams remains free of the adhesive. The specimen is then loaded by pulling the free ends of the two beams in a direction normal to the fracture surface, so that a crack extends along the interface of the two beams. The elastic energy which is stored in the deformed portion of the beams and released upon crack extension is calculated to measure the toughness (energy required to extend a crack) of the adhesive [4, 10].

The basic DCB method can be combined by other experimental techniques for example in-situ imaging to obtain the cohesive law (traction-separation function) of adhesives [11–16]. The cohesive law of the adhesive can then serve as the basis for cohesive zone modeling (CZM), which is a powerful technique to simulate crack initiation and growth often used to model fracture and fragmentation processes in metallic, polymeric, and ceramic materials and their composites [17–19]. In order to propagate the crack by an increment of distance, the cohesive forces will produce work over the opening distance, so that the toughness (in terms of energy per unit surface) is simply obtained by measuring the area under the cohesive law. The full cohesive law provides more information (including the maximum traction exerted by adhesive on the crack walls, stiffness of the adhesive layer, and maximum separation prior to the final de-cohesion) than a simple measurement of toughness.

The experimental determination of full cohesive laws is more involving than measuring toughness and requires more experimental and/or numerical elaborations. The developed methods for cohesive law determination are generally classified into two main categories: direct and inverse techniques. In direct methods, cohesive law is essentially obtained from the results of fracture experiments [11–13, 20–22] and using the concept of J-integral approach. While these techniques are valuable, they, however, are expensive in terms of experimental procedure and often need additional experimental setup. The inverse methods represent another type of approach which consists in modeling the experiment using finite elements, and identifying the parameters of the cohesive law which produce the best match between the model and the experiments [11, 23–25]. In general, direct and indirect methods assume a shape for the cohesive law, typically a bi-linear function (triangular cohesive law), which is characterized by three independent parameters (for example strength, maximum opening and toughness). In spite of the usefulness of these techniques, a method to directly measure cohesive laws without experimental and numerical complications is needed. In this article, we present a novel and simple experimental technique to measure the cohesive law of engineering adhesives. First developed to measure the interfacial fracture toughness of soft, weak biological adhesives [26], this technique is not modified to determine the cohesive law of tough, strong engineering adhesives. The new rigid-double-cantilever-beam (RDCB) technique is similar in concept to the standard DCB test, with an important difference: the substrates are assumed to be rigid. In the RDCB configuration the strain energy eventually released upon crack propagation is therefore stored in the adhesive itself. The assumption of rigid substrates also means that the opening of the adhesive can be easily computed along the entire bond line, without the need for contact or non-contact optical extensometers. The analysis for this test is also extremely simple, and directly leads to the full cohesive law of the adhesive, without any initial assumption on its shape.

4.2 RDCB Test Setup and Sample Preparation

Test setup of the rigid-double-cantilever-beam (RDCB) experiment is relatively similar to the traditional DCB test but the substrates are considered to be sufficiently stiff with respect to the adhesive as they can be assumed rigid. Here we used two rigid steel blocks (with the geometries shown in Fig. 4.1) as substrate for adhesives to be studied. The adherent surface was mirror polished down to 0.05 μm particle size in order to ensure a smooth surface, minimizing the effect of roughness on the results. We did not study rougher surfaces in this work, while they can easily be tested using RDCB method. The adhesive was used to join the two blocks, by partially covering their interfaces. The prepared specimen was then placed on a miniature loading stage (Fig. 4.1). An opening displacement at a rate of 50 μm/s was applied on the RDCB specimen using two steel pins (Fig. 4.1). The applied load and displacement were measured during the experiment using a 100 lbs load cell and one LVDT, respectively. The compliance of the machine was independently measured by mounting a calibration sample consisting of a single steel block with the same overall dimensions and the same slot as shown in Fig. 4.1, but with no interface. All the experimental curves reported here were then corrected for machine compliance.

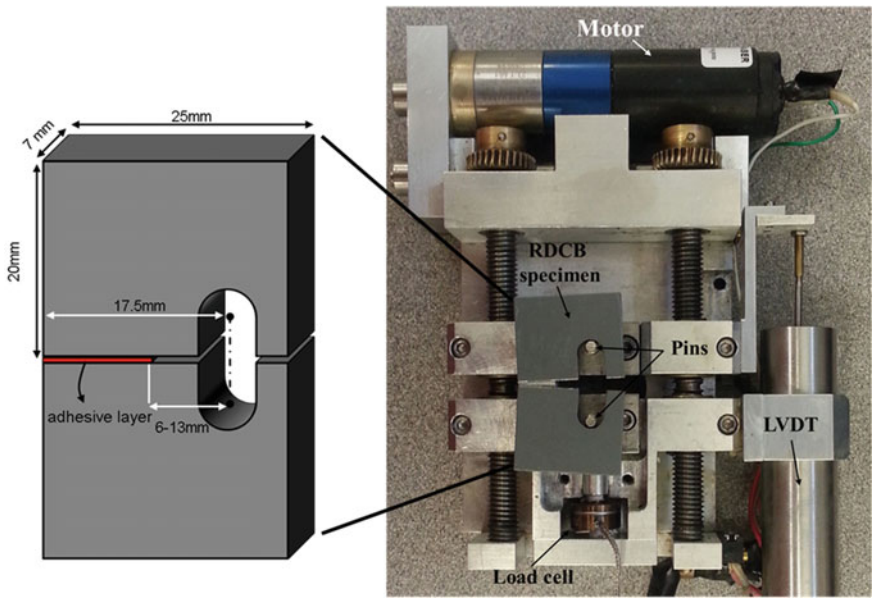

Fig. 4.1 Schematic illustration of the RDCB sample geometry (*left*); actual picture of the setup showing an opened sample mounted on the miniature loading stage (*right*)

4.3 RDCB Test Analysis

The key part in RDCB analysis is the assumption of a rigid substrate compared to the deformable adhesive. In order to meet this assumption, the deformation of the substrate during the course of the loading should be negligible compared to that of the adhesive layer. We further discuss the validity of this assumption in Sect. 3. Since the substrates are considered to be rigid, they only rotate about the hinge point O located at the end of the beams (Fig. 4.2). This assumption enables us to directly calculate the opening of the interface $u(x)$ anywhere along the bond line:

$$u(x) = \frac{x}{L}\Delta \tag{4.1}$$

Where x is the position from the hinge point, L is the distance from the line of action of the pulling force to the hinge point O, and Δ is the pins separation displacement. Writing the balance of moment (about the hinge point) exerted by the closure force of the adhesive with the moment generated by the applied external load F yields:

$$B\int_0^b xt(x)dx = LF \tag{4.2}$$

Where B is the thickness of the substrates, b is the length of the bond line, and $t(x)$ denotes the traction function which is unknown and is to be determined. Since the opening along the entire length of the substrates is known, we can now use Eq. 4.1 for a change of variable in Eq. 4.2, yielding:

$$\left(\frac{L}{\Delta}\right)^2 \int_0^\delta ut(u)du = \frac{L}{B}F \tag{4.3}$$

Where δ is the separation at the crack tip. Differentiating from Eq. 4.3 with respect to δ and using $\delta = \frac{b}{L}\Delta$ lead to the traction function of the adhesive layer, as follows:

$$t(\delta) = \left(\frac{L}{B(L-a_0)^2}\right)\left(2F + \Delta\frac{dF}{d\Delta}\right) \tag{4.4}$$

This equation simply gives the cohesive law of the interface from the traction function of the load–displacement curve and its derivative, and from the geometry of the specimen. Unlike many other methods developed to determine the cohesive

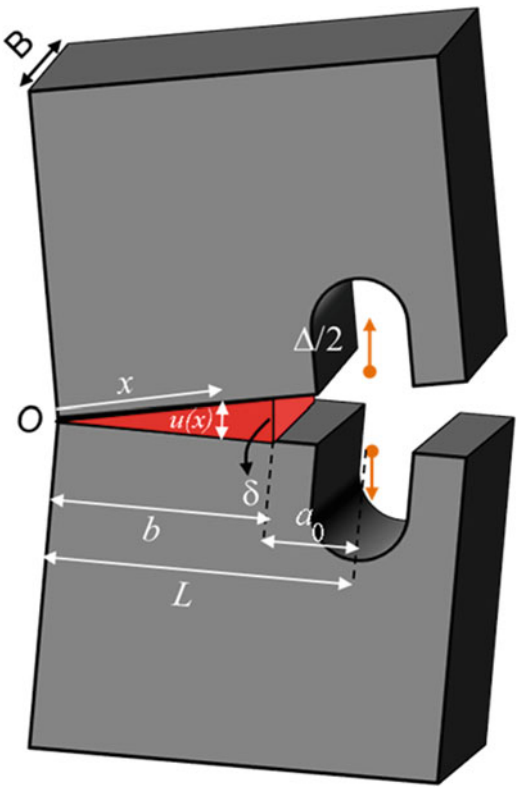

Fig. 4.2 Schematic illustration of a RDCB specimen with relevant variables used here for analysis

law of the adhesive interfaces, Eq. 4.4 does not require any initial assumption on the shape of the cohesive law which is a significant advantage. When the cohesive law is determined, the fracture toughness of the interface can simply be calculated by the area under the cohesive law which is also called cohesive energy:

$$J_{IC} = \int_0^{\infty} t(u)du \tag{4.5}$$

The toughness obtained from Eq. 4.5 is equal to the work-of-fracture, defined as the area under the F- Δ divided by the initial surface area of the adhesive (i.e. work-of-fracture measures the energy required to separate a unit surface of adhesive).

We also validated the result of the presented RDCB model by testing a 1 mm-thick double-sided polyethylene foam adhesive tape sandwiched between two steel substrates. Using Eq. 4.4, the obtained F- Δ curves yielded the cohesive law of the tape. Equation 4.5 was then used to compute the toughness of the tape which was $J_{IC} = 116 \pm 21$ J/m^2 (five samples were tested). We also measured the toughness of this adhesive (taped on the same polished steel surface) using a standard peel test configuration (ASTM D6862-04) which gave a toughness of $J_{IC} = 127 \pm 15$ J/m^2 (five specimens were tested). The values given by the RDCB and peel tests are comparable within experimental errors, which validated the RDCB test procedure and data analysis.

4.4 Rigidity Assumption Validation

We noted earlier that the RDCB model relies on the assumption of a rigid cantilever compared to the adhesive. In order to verify the validity of this assumption, the deformation of the substrate must be negligible compared to the deformation of the adhesive interface. Since the highest deformation occurs when the interface passes the yield point of the cohesive law, it is sufficient to compare the deflection of the substrates and adhesives at the end of the elastic regime.

In order to identify the critical parameters governing the deflection of the substrate and the adhesive, we consider the free body diagram of the upper substrate (Fig. 4.3). The opening force was modeled as point load, and the adhesive was modeled

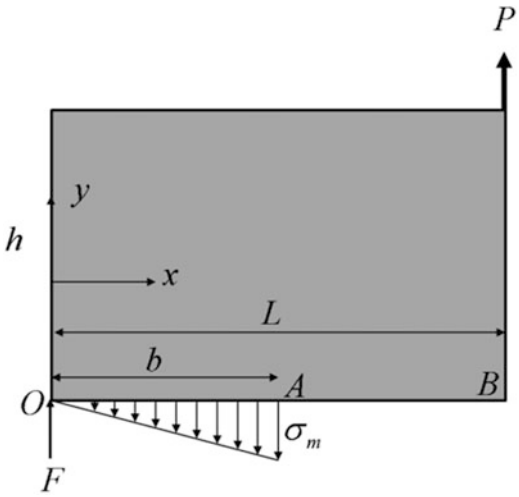

Fig. 4.3 Free body diagram of the upper substrate in RDCB configuration

as a linear distribution of tractions, consistent with a linear elastic regime. Writing the balance of the external work done by load P and moment $P(L-b)$ with the energy stored in the half thickness of the adhesive gives:

$$P\delta_{tip} + P(L-b)\frac{\delta_{tip}}{b} = 1/2\int_0^b SBu^2 dx \tag{4.6}$$

Where δ_{tip} is half the crack tip separation (at $x = b$), S is the stiffness of the half thickness of the adhesive layer which is as twice as the initial slope of the cohesive law ($S = 2S_{\text{int}}$), and u is separation at distance x from the hinge point O. Substituting $u = \frac{\delta_{tip}}{b}x$ in Eq. 4.6 yields:

$$\delta_{tip} = \frac{3PL}{Bb^2 S_{\text{int}}} \tag{4.7}$$

The maximum deflection of the substrate occurs when the traction at the crack tip reaches the cohesive strength of the interface σ_m and it can simply be obtained using Castigliano's second theorem [27], considering deformations from bending moments and from shear forces. The strain energy of the system can be written:

$$U = \int_0^b \frac{M_1^2}{2EI}dx + \int_0^b \frac{3V_1^2}{5GA}dx + \int_b^L \frac{M_2^2}{2EI}dx + \int_b^L \frac{3V_2^2}{5GA}dx \tag{4.8}$$

Where M_i and V_i are bending moment and shear load, respectively, G and E are shear modulus and Young's modulus of the substrate, respectively. A and I denote the substrate cross section area and the substrate second moment of area respectively. Balancing the forces in y direction and moment around the hinge point O gives $F = \left(\frac{3L}{2b} - 1\right)P$ and $\sigma_m = \frac{3PL}{Bb^2}$. The bending moment and shear load in OA (M_1 and V_1) and AB (M_2 and V_2) part of the substrate can be written:

$$\begin{cases} M_1 = \dfrac{B\sigma_m x^3}{6b} + \left(1 - \dfrac{3L}{2b}\right)Px \\ V_1 = -\dfrac{\sigma_m B}{2b}x^2 - \left(1 - \dfrac{3L}{2b}\right)P \\ M_2 = P(L-x) \\ V_2 = P \end{cases} \tag{4.9}$$

Substituting the shear loads and bending moments from Eq. 4.9 into Eq. 4.8, and taking derivative from Eq. 4.8 with respect to P yields the deformation of the substrate at the loading line:

$$\delta_1 = P\left(\frac{\alpha_s}{GA} + \frac{\alpha_b}{EI}\right) \tag{4.10}$$

With $\alpha_s = \frac{9}{5}L\left(\frac{L}{b} - 1\right)$ and $\alpha_b = \left(\frac{L^3}{3} + \frac{Lb^2}{10} - \frac{2L^2b}{5}\right)$. By assuming a homogeneous isotropic linear elastic property for the substrate material (with rectangular cross section), Eq. 4.10 can further be simplified as:

$$\delta_1 = \frac{P\left((1+v)\alpha_s' + \alpha_b'\right)}{E} \tag{4.11}$$

With $\alpha_s' = \frac{2\alpha_s}{Bh}$ and $\alpha_b' = \frac{12\alpha_b}{Bh^3}$. Where v and h denote the poison's ratio and thickness of the substrate, respectively. In addition to this opening, resulting from bending moments and from shear forces, the adhesive layer separation also produces opening along the loading line which must be considered in the calculations. This is taken into account by rotating the substrate around the hinge point O so that the crack tip opens up to $2\delta_{tip}$ which gives:

$$\delta_2 = \left(\frac{L}{b}\right)\delta_{tip} \tag{4.12}$$

Adding the opening from Eqs. 4.11 and 4.12 gives the total substrate tip opening:

$$\Delta' = P\left(\frac{(1+v)\alpha_s' + \alpha_b'}{E} + \frac{3L^2}{Bb^3 S_{\text{int}}}\right) \tag{4.13}$$

We now define a non-dimensional ratio $\alpha = \frac{\delta_{tip}L}{\Delta' b}$ which can be used to assess the rigidity of the substrate. This ratio must be equal, or close to unity for the substrate to be considered rigid. In this case the surface of the substrate remains uniformly straight and Eq. 4.1 can be used. Substituting half the crack tip opening from Eq. 4.7 and the substrate tip opening from Eq. 4.13 into this ratio results:

$$\alpha = \frac{\delta_{tip}L}{\Delta' b} = \left(1 + \frac{Bb^3 S_{\text{int}}\left((1+v)\alpha_s' + \alpha_b'\right)}{3L^2E}\right)^{-1} \tag{4.14}$$

This equation can now be used to verify the rigidity assumption of the substrates. It incorporates the geometry of the specimens, as well as the elastic properties of the substrate and the cohesive strength of the adhesive layer. Using this equation, we plotted the ratio α as a function of dimensionless material parameter σ_m/E (ratio of the cohesive strength of the interface to the modulus of the substrate) for the fixed dimensions specified in Fig. 4.1 (Fig. 4.4). The model confirms that the ratio is equal to one for low cohesive strength of the adhesive and/or high substrate modulus. When the ratio σ_m/E gets larger, α deviates from unity, indicating substrate deformation. α becomes smaller than 0.95 for $\sigma_m/E > 8.3 \times 10^{-4}$. As the ratio α becomes larger the traditional DCB method becomes more appropriate.

Finally Eq. 4.14 was verified using finite element method. We constructed the RDCB configuration in ABAQUS (v. 6.9, ABAQUS Inc., Providence, RI), with the geometry shown in Fig. 4.1. Using symmetry about the plane defined by the bond line, only the upper half of the system was modeled: one substrate, and half of the thickness of the bond line. The substrate was modeled as linear elastic with plane strain condition. The interface was modeled with user defined cohesive elements, with the upper nodes joined with the node from the substrate, and the lower nodes only constrained to remain on the plane of symmetry. A trapezoidal cohesive law was chosen to simulate crack propagation within the adhesive layer. The upper pin of the fixture was modeled as a rigid surface in contact with the inner surface of the fixture. The pin was displaced at a fixed rate to simulate the opening of the interface. Figure 4.4 shows a good agreement between the finite element results and the analytical result of Eq. 4.14, validating the accuracy of the presented analytical method.

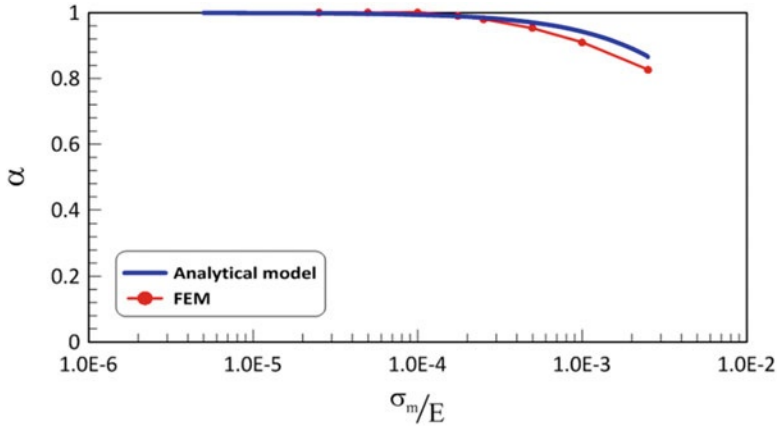

Fig. 4.4 α as a function of dimensionless parameter $\frac{\sigma_m}{E}$ showing intimate agreement between results obtained from finite element and from analytical model (Eq. 4.14)

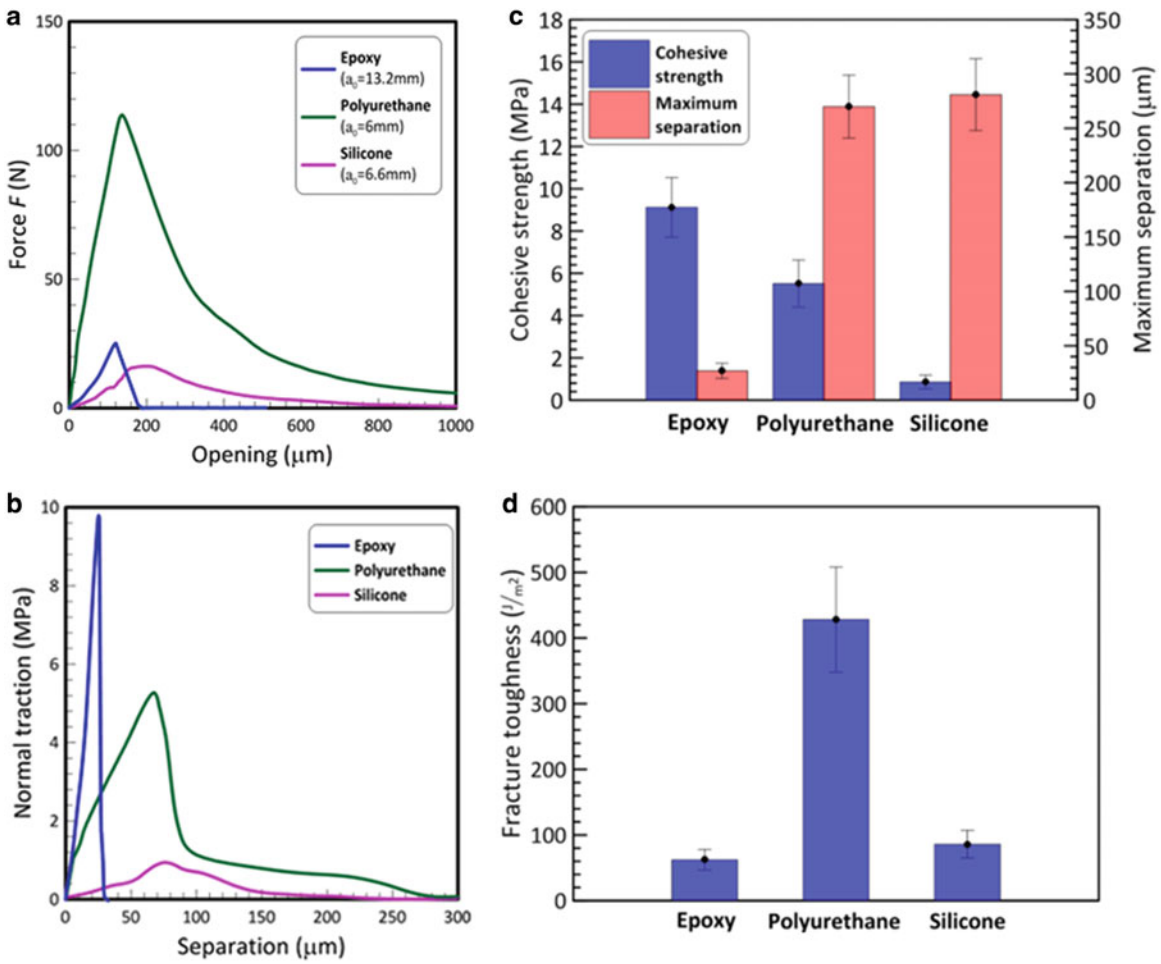

Fig. 4.5 Typical force-opening curves of the three tested types of adhesive; (**b**) typical cohesive laws obtained from RDCB model; (**c**) cohesive parameters for the three adhesive tested in this work: (**a**) cohesive strength and maximum separation, and (**d**) toughness

4.5 RDCB Test on Typical Engineering Adhesives

Using RDCB method we tested three engineering adhesives with a wide range of mechanical behavior from soft elastomer to stiff thermoset polymer: silicone (Silicone, General Electric, Huntersville, NC, USA), polyurethane (PL Premium, Lepage, Brampton, ON, Canada), and epoxy (EpoThin epoxy, Buehler, Lake Bluff, IL, USA). Typical load-opening curves resulting from RDCB tests on each of these three adhesives are shown in Fig. 4.5a. Polyurethane and epoxy showed a linear increase

at the initial part of the loading which is followed by an almost abrupt drop corresponding to the onset of crack propagation. For the case of silicone, the failure process was more progressive exhibiting a bell shape force-opening curve. Using optical microscope, posttest fracture surface of the specimens was further explored. The fracture surfaces of epoxy and silicone clearly indicated adhesive failure (the crack propagated at the adhesive-substrate interface) along one interface. Polyurethane displayed a mixed failure mode including cohesive failure, adhesive failure (the crack propagated through the adhesive) and crack deflections. From a fracture mechanics perspective, the latter failure mode is more desirable because it involves more energy dissipation, which translates into increased fracture toughness for the interface. The obtained force-opening curves were then processed through RDCB analysis explained in Sect. 2; the typical cohesive laws for the three studied adhesives are shown in Fig. 4.5b. This data was used to measure the cohesive strength of the adhesive (maximum traction) and the maximum separation (opening at which the cohesive law vanishes). Figure 4.5c presents the average values of theses cohesive law parameters. Epoxy was the strongest but also the most brittle of the three adhesives, with a cohesive strength of 8–10 MPa and maximum opening of about 25 μm. In contrast, silicone showed a low cohesive strength about 10 times lower (1 MPa) but a maximum separation about 10 times larger than epoxy

Figure 4.5d presents the toughness of the adhesives which was obtained from Eq. 4.5. Amongst all the tested adhesives, polyurethane is the toughest with average fracture toughness being approximately 430 J/m^2. This was predictable from parameters (cohesive strength and maximum separation) shown in Fig. 4.5c, because it exhibits both high strength and large extensibility. Epoxy and silicone (despite being either strong or deformable) display low fracture toughness mainly due to the shortage of extensibility (in epoxy) and strength (in silicone). In order to investigate the validity of the results we obtained for these adhesives using RDCB model, we determined the ratio α (Eq. 4.14) for each case. For all the cases, parameter α is approximately unit (maximum deviation from unit happens in the case of epoxy adhesive which is 0.3%) which confirms that all the results presented in this study are valid and can be used for further studies on the fracture behavior of the adhesives.

4.6 Conclusions

In this study, a simple yet robust experimental method called RDCB test was presented to determine the cohesive law and fracture toughness of engineering adhesive in the opening fracture case (Mode I). First developed for soft, deformable biological adhesives, RDCB method can be modified to include high strength of tough engineering adhesives using thick rigid substrates. The method is very useful and unlike many other developed techniques needing an initial assumption for the shape of the cohesive law and requiring complex experimental setup, imaging or numerical modeling, RDCB test provides the full cohesive law of the adhesive without any initial assumption on it shape. The method only needs the initial geometry of the specimen as well as the load–displacement data from experiment. In order to validate the results of the model, we defined a non-dimensional parameter called α which can be used to quantitatively investigate whether the assumption of rigid substrates is valid. For values of α close to unity, the RDCB rigidity assumption is valid and the method directly yields the cohesive law of the adhesive. Finally we successfully implemented the RDCB method on three typical engineering adhesives: epoxy, polyurethane and silicone. The results showed very different cohesive laws for these adhesives. Epoxy showed high cohesive strength but small extensibility, while silicone showed high extensibility but low strength. Polyurethane, with both high strength and extensibility, was found to be the toughest of the adhesives tested here. The RDCB method is a simple and accurate method to obtain the cohesive law of adhesives, and can serve as an experimental platform to investigate their mode of failure or to optimize their performance.

Acknowledgements This work was supported by a Discovery Grant from the Natural Sciences and Engineering Research Council of Canada. AKD was partially supported by a McGill Engineering Doctoral Award.

References

1. Adams R, Comyn J, Wake W (1997) Structural adhesive joints in engineering. Chapman and Hall, London
2. Dunn DJ (2004) Engineering and structural adhesives, vol 169. Smithers Rapra Technology, Shrewsbury
3. ASTM (1986) ASTM D 3983: Standard test method for measuring strength and shear modulus of nonrigid adhesives by the thick-adherend tensile-lap specimen. West Conshohocken, PA, pp 412–428
4. Ripling EJ, Mostovoy S, Corten HT (1971) Fracture mechanics: a tool for evaluating structural adhesives. J Adhes 3(2):107–123
5. Dastjerdi AK et al (2012) Cohesive behavior of soft biological adhesives: experiments and modeling. Acta Biomater 8(9):3349–3359

6. Dannenberg H (1961) Measurement of adhesion by a blister method. J Appl Polym Sci 5(14):125–134
7. Chicot D, Démarécaux P, Lesage J (1996) Apparent interface toughness of substrate and coating couples from indentation tests. Thin Solid Films 283(1–2):151–157
8. Lawn BR (1993) Fracture of brittle solids. Cambridge University Press, Cambridge, United Kingdom
9. ASTM (2012) ASTM D3433–99: Standard test method for fracture strength in cleavage of adhesives in bonded metal joints. West Conshohocken, PA
10. Anderson TL (1995) Fracture mechanics: fundamentals and applications. CRC Press, Boca Raton, FL
11. Andersson T (2006) On the effective constitutive properties of a thin adhesive layer loaded in peel. Int J Fract 141(1–2):227
12. de Moura M (2012) A straightforward method to obtain the cohesive laws of bonded joints under mode I loading. Int J Adhes Adhes 39:54
13. Biel A (2010) Damage and plasticity in adhesive layer: an experimental study. Int J Fract 165(1):93
14. Sørensen BF (2003) Determination of cohesive laws by the J integral approach. Eng Fract Mech 70(14):1841
15. Carlberger T, Stigh U (2010) Influence of layer thickness on cohesive properties of an epoxy-based adhesive—an experimental study. J Adhes 86(8):816–835
16. Zhu Y, Liechti KM, Ravi-Chandar K (2009) Direct extraction of rate-dependent traction-separation laws for polyurea/steel interfaces. Int J Solids Struct 46(1):31–51
17. Shet C, Chandra N (2002) Analysis of energy balance when using cohesive zone models to simulate fracture processes. J Eng Mater Technol Trans Asme 124(4):440–450
18. Bouvard JL et al (2009) A cohesive zone model for fatigue and creep–fatigue crack growth in single crystal superalloys. Int J Fatigue 31 (5):868–879
19. Aymerich F, Dore F, Priolo P (2009) Simulation of multiple delaminations in impacted cross-ply laminates using a finite element model based on cohesive interface elements. Compos Sci Technol 69(11–12):1699–1709
20. Barthelat F et al (2007) On the mechanics of mother-of-pearl: a key feature in the material hierarchical structure. J Mech Phys Solids 55 (2):306–337
21. Sørensen BF (2002) Cohesive law and notch sensitivity of adhesive joints. Acta Mater 50(5):1053
22. Andersson T (2004) The stress–elongation relation for an adhesive layer loaded in peel using equilibrium of energetic forces. Int J Solids Struct 41(2):413
23. de Moura MFSF, Morais JJL, Dourado N (2008) A new data reduction scheme for mode I wood fracture characterization using the double cantilever beam test. Eng Fract Mech 75(13):3852
24. Sun C et al (2008) Ductile–brittle transitions in the fracture of plastically-deforming, adhesively-bonded structures. Part I: experimental studies. Int J Solids Struct 45(10):3059–3073
25. Sun C et al (2008) Ductile–brittle transitions in the fracture of plastically deforming, adhesively bonded structures. Part II: numerical studies. Int J Solids Struct 45(17):4725–4738
26. Khayer Dastjerdi A et al (2012) The cohesive behavior of soft biological “glues”: experiments and modeling. Acta Biomater 8:3349
27. Timoshenko S (1940) Strength of materials Part 1: Elementary theory and problems. (2nd edn) D. Van Nostrand Company Inc., New York

Chapter 5
Comparing the Passive Biomechanics of Tension-Pressure Loading of Porcine Renal Artery and Its First Branch

Mohamed G. Gabr, Michael A. Sutton, Susan M. Lessner, Stephane Avril, and Pierre Badel

Abstract Renal arteries provide blood and nutrients to the kidneys, which are high demand organs. It is important to determine how these arteries behave under physiological loadings and their stress/strain response to increasing pressure and tension. To determine the passive mechanical behavior of both the porcine renal artery and its first branch, we performed simultaneous pressurization and axial loading on porcine artery specimens. Biomechanical experimental studies of soft-tissue are highlighted in this paper. The measurements will be used to identify parameters in the Holzapfel soft-tissue constitutive formulation describing the mechanical behavior of these arteries, a model that is widely used to describe the mechanical behavior of arteries Holzapfel GA, Gasser TC, Ogden RW (J Elast 61:1–48, 2000). Preliminary data from the experiments show that there is a difference in mechanical response behavior between the renal artery and its branch.

Keywords Renal • Porcine • Biomechanics • Soft-tissue • Constitutive model

5.1 Introduction

Tissue engineers have extensively studied what cells need to be utilized when developing scaffolds for soft-tissue replacement vessels, and they have effectively made a list of criteria that the new replacement vessel has to meet. To be able to say that one has effectively created a replacement, the replacement must be able to effectively mimic the native artery not only biologically but also mechanically. Though the mechanical responses of arteries have been generally studied by many, not all major arteries have been mapped out and described in terms of their biomechanical properties. In particular, the properties of renal arteries have not been actively studied, resulting in a paucity of experimental data. Since, such baseline data is necessary for the development of an ideal scaffold for replacement renal artery constructs, the enclosed work presents the results from recent studies focusing on quantifying the behavior of renal arteries.

5.2 Material Characterization

Since there is general agreement in the community that the anatomy and structure of porcine and human renal arteries are similar, in this study porcine renal arteries were used. Renal arteries are muscular arteries that branch from the abdominal region of the aorta and connect to the kidneys at a location called the hilus. In most cases, a person has two primary renal arteries, one to supply the left kidney and one to supply the right kidney. Each of these arteries will bifurcate into the anterior and posterior segmental arteries before entering the hilus. Oftentimes there are anomalies in the geometry; a renal artery might fork into two or three segmental arteries, and one of those may bifurcate once more before entering the hilus. There

M.G. Gabr (✉) • M.A. Sutton • S.M. Lessner
Biomedical Engineering Program, University of South Carolina, Columbia, SC 29208, USA
e-mail: gabr@email.sc.edu

S. Avril • P. Badel
Center for Health Engineering, Ecole Nationale Superieure des Mines Saint-Etienne, Saint Etienne 42023, France

F. Barthelat et al. (eds.), *Mechanics of Biological Systems and Materials, Volume 4*,
Conference Proceedings of the Society for Experimental Mechanics Series,
DOI 10.1007/978-3-319-00777-9_5,

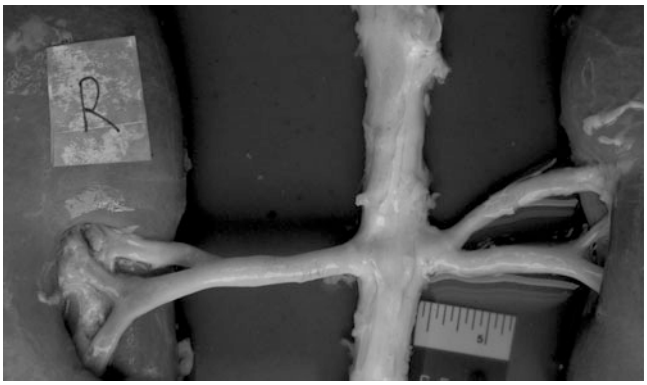

Fig. 5.1 Supernumerary porcine renal artery abnormality

Table 5.1 Collagen and elastin content in primary and first branch renal artery specimens

	% Collagen	% Elastin
Renal artery	11.95 ± 0.25 %	9.03 ± 0.14 %
First branch/segmental	11.38 ± 0.19 %	8.97 ± 0.04 %

can also be a supernumerary renal artery, which occurs when there are two renal arteries that branch off the aorta and go to the same kidney; a supernumerary renal artery is shown in Fig. 5.1. Though both of these anomalies have been observed in our dissections, our studies will focus on comparing the mechanical response of the main renal artery (without anomaly) and its first branch when subjected to mechanical stress.

Like all arteries, the renal artery can be considered to consist of three layers. The innermost layer in direct contact with circulating blood is the intima. This layer provides negligible mechanical strength as it is just one layer thick of endothelial cells (ECs). The next layer is the media, primarily composed of smooth muscle cells, collagen, and elastin, which is considered the primary load-bearing layer in an artery. The elastin is engaged during periods of low strain (5–10 %), and its elasticity helps the artery recoil quickly. It is believed that the network of collagen and elastin is responsible for the anisotropic behavior of the material, as well as the overall strength of the vessel. The outermost layer, the adventitia, is also composed of collagen and elastin but with the addition of adipose tissue (fat).

Since the literature suggests that collagen and elastin are major bearers of load, we investigated the collagen and elastin content of our specimens. Paraffin sections of arterial segments were stained with picrosirius red and Verhoeff's stain to determine area percent of collagen and elastin present, respectively, by image analysis. Results from our studies are shown in Table 5.1. As shown in Table 5.1, collagen and elastin content are nearly the same in both branch levels of the renal artery.

5.3 Material/Experimental Methods

The porcine renal artery specimens with intact kidneys are shown in Fig. 5.2. The aortic specimens with kidneys attached were acquired from a local processing facility in Lexington, SC, allowing us to estimate in situ axial and circumferential stretches. After removal from the carcass, the specimens remained in 1× PBS solution until the mechanical loading process was complete. All experiments were performed within a few hours after acquisition. Ten segments of renal arteries from five different pigs were tested. Five segments came from the right renal artery (RRA) of the pigs, one from the left renal artery (LRA) and four others came from the left segmental artery (LSA).

When detaching the porcine renal and first branch specimens from the kidneys, the in situ axial and circumferential stretches were estimated through measurement of (a) the axial contraction of the artery specimen during removal and (b) the final outer diameter of the artery specimen after removal. The change in geometry associated with a typical excision of the renal artery specimens is shown in Fig. 5.3.

In addition to the measurement of the in-situ deformations that an artery experiences, studies have shown that the excised artery specimens also have internal circumferential "residual" strains. To quantify this strain, the common practice is the remove ring specimens from the renal artery.

Each ring specimen is then sliced across the thickness so that the ring will open due to the removal of the residual circumferential strains. After slicing through the thickness, the specimen is allowed to relax for 30 min while in solution. This process is shown in Fig. 5.4.

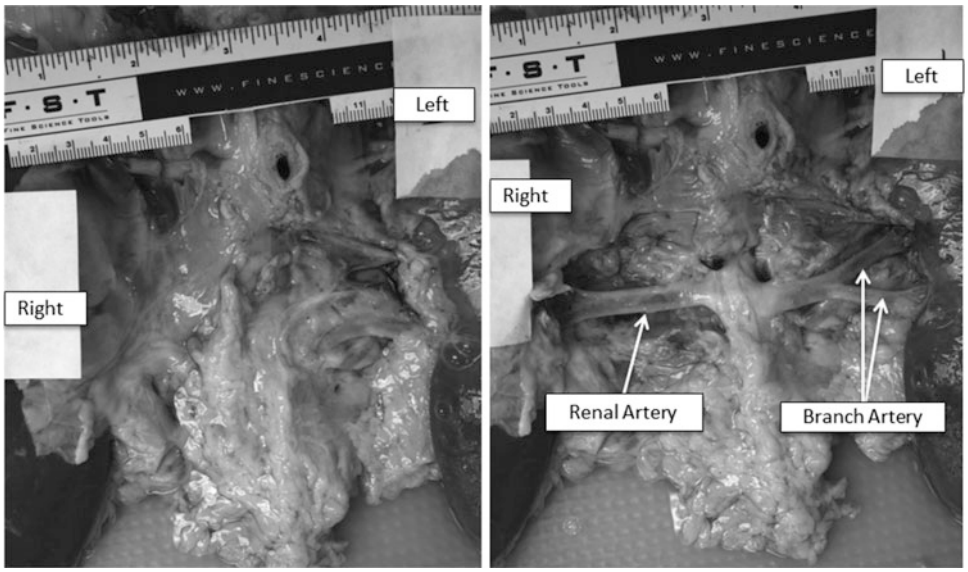

Fig. 5.2 Kidneys attached to the aorta via the renal artery. Before (*left*) and after dissection (*right*)

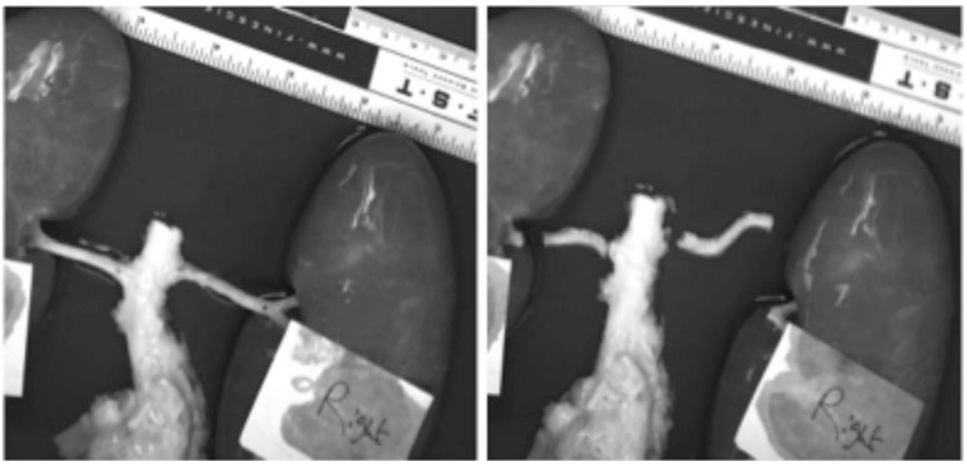

Fig. 5.3 Extraction of renal artery specimens for in-situ measurement of axial and circumferential stretches

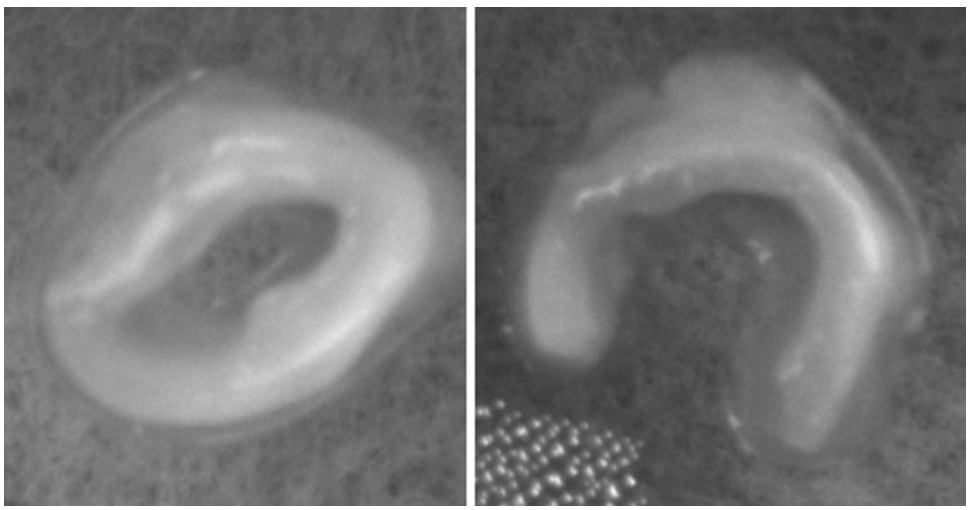

Fig. 5.4 Ring specimen from renal artery before and after slicing across thickness

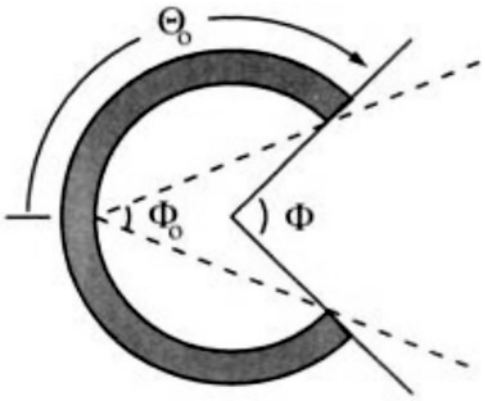

Fig. 5.5 Schematic defining opening angle

Fig. 5.6 Test bench (*left*) and close up of the components (*right*)

To quantify the residual strain, the opening angle Φ_o defined graphically in Fig. 5.5 is measured after 30 min. Along with vision-based measurements, this angle is used to estimate the final length of the opened ring specimen so that the residual circumferential strain can be determined

Once the initial measurements were obtained, the remaining artery specimens were prepared for combined pressurization and axial load experiments. All experiments were carried out on a Bose Electroforce Biodynamic 5100 Test Bench (Bose, Eden Prairie, MN) shown in Fig. 5.6. The Bose Test Bench includes (a) 22 N load cell, (b) micro-pump capable of delivering 102 ml/min, (c) catheter-mounted pressure sensor with a range of 0–300 mmHg, (d) actuator that can produce a total displacement of 13 mm, (e) environmental chamber to maintain hydration of the arterial specimens and (f) Bose software to control the entire mechanical loading process. A typical renal artery specimen mounted in the test fixture is shown in Fig. 5.7.

To perform the experiments, each arterial specimen was mounted to hollow cylindrical, barb-ended Luer stubs (McMaster-Carr) using 3–0 silk sutures. After the specimen was sutured onto the Luer stubs, the stub-artery combination was attached to the end fixtures of the Bose Test Bench and immersed in a bath of 1× phosphate-buffered saline (PBS) solution within the environmental chamber. The specimen was immediately perfused internally with the same solution at room temperature and perfusion was maintained throughout the loading process. The length of the specimen (between the 2 sutures) at zero load is the initial undeformed length. Prior to initiating the experiments, each arterial specimen is pre-conditioned mechanically by pre-stretching to an axial strain of 3.5 %. In our experiments, we have found that a preconditioning stretch of 3.5 % of the traction-free length was sufficient to obtain consistent results while minimizing damage to the specimen.

Experiments were performed in axial displacement control and pressure control. The specimens are subjected to pressure loading over the range of 20 mmHg $\leq$ P $\leq$ 140 mmHg and axial stretch ratios encompassing the range of 1.00 $\leq \lambda_z \leq$ 1.25. To determine the axial stretch ratio, the initial undeformed length was defined to be the length of the specimen between the sutured ends when the axial load is zero. During the displacement control test, the pressure was held constant (P = 20, 60, 100, 140 mmHg) and axial displacement was applied at a constant rate until the maximum stretch ratio,

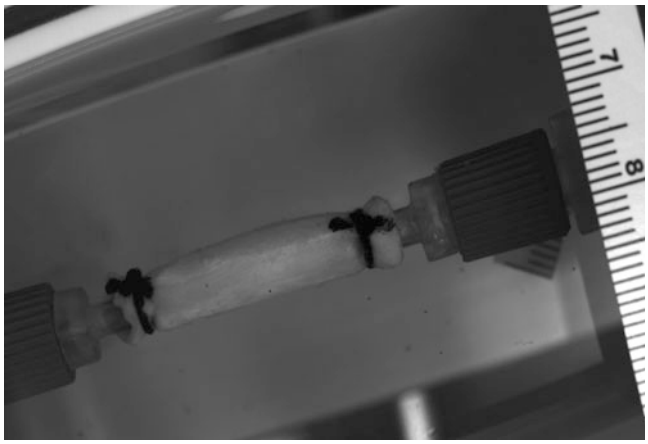

Fig. 5.7 Renal artery specimen in test fixture for combined pressure-axial load experiment

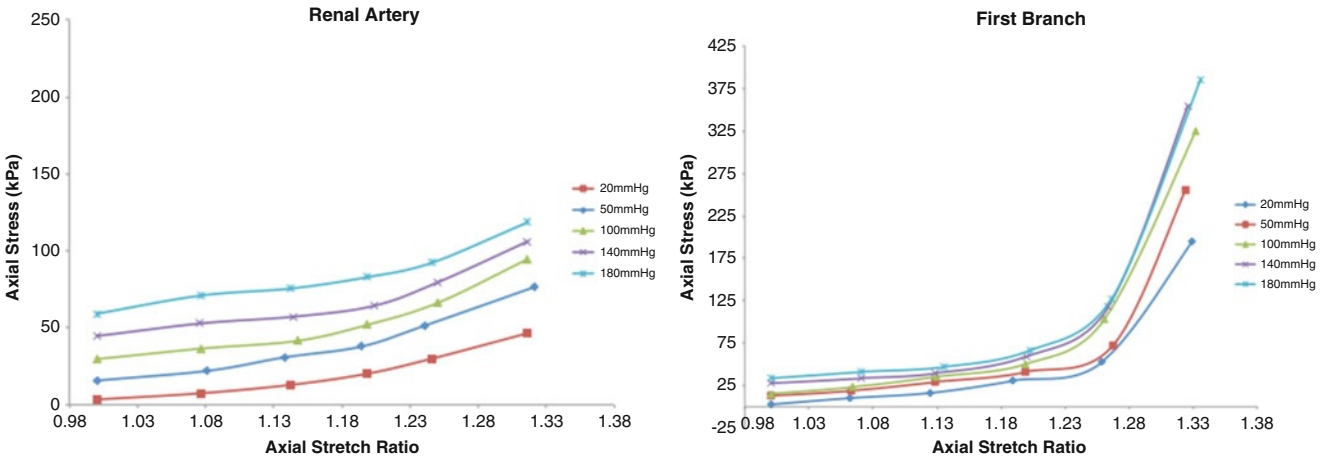

Fig. 5.8 Axial stress (kPa) versus axial stretch ratio for the renal artery (*left*) and the first branch (*right*)

$\lambda_z = 1.25$, was reached. During the pressure control test, the axial stretch ratio was held constant and the pressure was consistently increased from the initial 20 mmHg until the maximum pressure of 140 mmHg was reached.

During the mechanical loading process, the deformed outer diameter and length of the specimen were determined at each loading step by analyzing images of the specimen. In this study, all images were acquired using a Grasshopper 50S5M 5.0 megapixel CCD camera (Point Grey, Richmond, BC) with a 28 mm Nikon lens. Image acquisition was performed using Vic-Snap 2010 Software (Correlated Solutions, Columbia, SC). The images were analyzed using ImagePro Plus 5.1 image analysis software (Media Cybernetics, Rockville, MD) to determine the average deformed diameter in the central region and the deformed length.

5.4 Results

The force-displacement data was analyzed to determine stress/strain behavior of the material. Representative axial stress-axial stretch ratio curves are presented below in Fig. 5.8.

The circumferential stress-circumferential stretch ratio curves are presented below in Fig. 5.9. Figure 5.9 shows the fit of the experimental data to the adopted 4-fiber family Holzapfel constitutive model. The best-fit parameters of this model are listed in Table 5.2.

The parameters are as listed: (a) The opening angle: α (b) The stress-free orientation angle of helical fibers: β_0 (c) the stiffness property of the helical fiber: $k_{\beta 1}$ (d) the exponential stiffening coefficient of the helical fibers: $k_{\beta 2}$

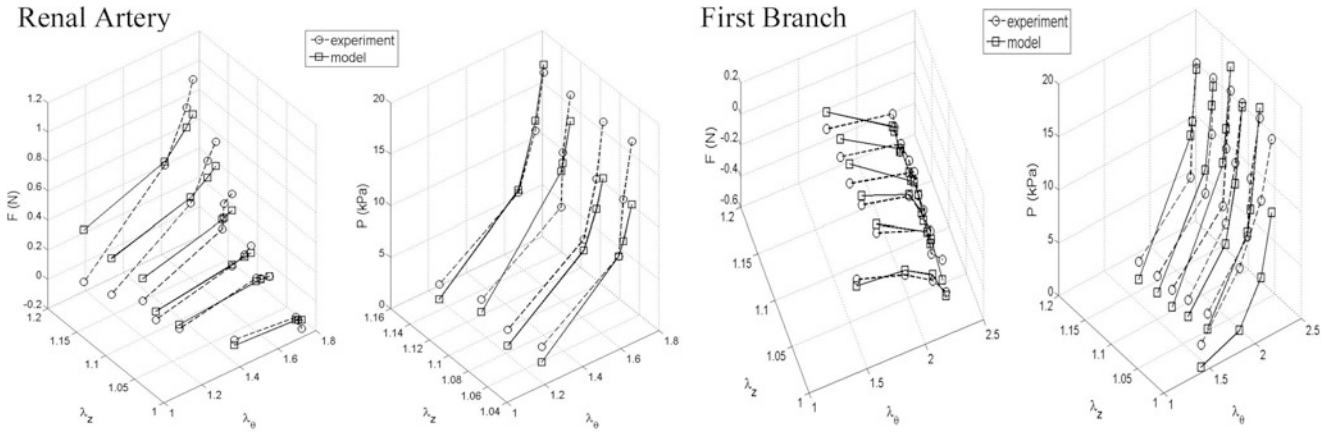

Fig. 5.9 Circumferential load (N) and pressure (kPa) versus circumferential stretch ratio for the main renal artery (*left*) and the first branch (*right*)

Table 5.2 Identified model parameters for renal artery and first branch

Specimen	α (°)	$k_{\beta 1}$ (kPa)	$k_{\beta 2}$	β_0
Main renal	105	20	2.5	50°
First branch	82	49.8	0.54	43°

5.5 Conclusions

In this paper, we have described a method for testing porcine renal artery specimens and have presented data showing the mechanical response to loading. The results show that under combined tension-pressure loading of the specimens there was a difference in mechanical behavior between the main renal artery and the first branch. The first branch had a stiffer response to axial strain than the main renal artery at axial stretch ratios greater than 1.25, although the responses were similar at smaller stretch ratios. For axial stretch ratios greater than 1.25, the axial stress of the first branch was higher than that of the renal artery by greater than a factor of 2. The histological analysis of the test samples showed that there was a negligible difference in elastin and collagen composition between the two types of vessels. Even though both types of specimens had similar collagen content, a potential reason for the difference in mechanical behavior is believed to be variations in average collagen fiber angle, which will be quantified in both vessels. Future work will also include determining the percent of smooth muscle cells that are in the specimens to see if there is a difference in composition. The data was fit to a 4-fiber family Holzapfel constitutive model and it was determined that these arterial specimens could be modeled using the parameters listed above in Table 5.2. The model parameters suggest that we should expect to see a lower average collagen fiber angle in the first branch than in the main renal artery.

Acknowledgements This projected was funded by the South Carolina Project for Tissue Biofabrication NSF EPS-0903795. We would like to thank Caughman's Meat Plant for providing the samples. A special thanks to Dr. Xiaomin Deng for his input on this research project. Lastly, we would like to thank our lab manager, John Johnson.

Reference

1. Holzapfel GA, Gasser TC, Ogden RW (2000) A new constitutive framework for arterial wall mechanics and a comparative study of material models. J Elast 61:1–48

Chapter 6
Indentation Measurements on Soft Materials Using Optical Surface Deformation Measurements

M.J. Wald, J.M. Considine, and K.T. Turner

Abstract Instrumented indentation is a common technique for measuring the elastic properties of bulk materials as well as thin films on substrates. However, in traditional indentation, it can be difficult to determine the true deformation of a specimen due to the effects of machine compliance and thermal drift. In the present work, a method is developed to track the in-plane and out-of-plane deformation of a specimen during indentation tests using fluorescent microparticles. Bead tracking and quantitative defocusing methods are used to track the in-plane and out-of-plane displacements of the beads, respectively. Here, we describe the calibration of the system and assess the effects of particle size and magnification on the accuracy and resolution of the system. In addition, results from preliminary indentation tests performed on bulk polydimethylsiloxane specimens are reported. An analysis algorithm was developed to extract the elastic properties by measuring the displacements on the surface as a function of applied indentation force. Results are compared to traditional indentation measurements in which load and displacement are only measured at the indenter.

Keywords Indentation • Soft materials • Particle tracking • Modulus • Poisson's ratio

6.1 Introduction

Instrumented indentation is a common method for characterizing the mechanical properties of bulk materials. This technique is capable of testing small volumes of material at low loads and small displacements and allows for simple sample preparation compared to traditional tension or compression tests. Oliver and Pharr [1] describe a widely accepted method based on Sneddon's solution [2] for axisymmetric indentation of an elastic halfspace for determining a specimen's effective modulus ($E_{eff} = E/(1-\nu^2)$) from the measured applied load and displacement of the indenter. However, Young's modulus, E, and Poisson's ratio, ν, which are commonly used in engineering applications, cannot be independently determined using this analysis. To find E, it is necessary to guess or estimate ν, which is difficult to measure directly on small volumes of material with established techniques.

The Oliver-Pharr method is also affected by the sensitivity of measured stiffness to errors in the measurement of the true deformation of a specimen. These errors are commonly due to machine compliance and thermal drift. Machine compliance is commonly calculated by indenting a material with known elastic properties, such as fused silica, and subtracting the theoretical compliance of the material from the experimentally measured compliance [3, 4]. While this method provides an estimate for the machine compliance, it relies on an accurate measurement of the contact area and the ability to accurately detect the initial contact between the indenter and specimen, which is challenging when testing soft materials [5, 6]. Thermal drift, or the change in position of the sample relative to the indenter due to small changes in temperature, is often minimized by either conducting indentation tests in a closed environment in which the temperature is stable or performing indentation tests quickly [7].

M.J. Wald (✉) • K.T. Turner
Department of Mechanical Engineering and Applied Mechanics, University of Pennsylvania, 220 S. 33rd St, Philadelphia, PA 19104-6315, USA

J.M. Considine
US Forest Service, Forest Products Laboratory, One Gifford Pinchot Drive, Madison, WI 53726, USA

F. Barthelat et al. (eds.), *Mechanics of Biological Systems and Materials, Volume 4*,
Conference Proceedings of the Society for Experimental Mechanics Series,
DOI 10.1007/978-3-319-00777-9_6,

In the present work, the displacement of the surface of the sample is measured independently of the indenter. Specifically, the displacement of fluorescent microparticles near the surface of the specimen during an indentation test are measured. In-plane motion is measured by tracking the particle center and out-of-plane motion is measured using the quantitative defocusing method. Measuring the displacement of the specimen surface at multiple locations in the vicinity of the indenter allows mechanics models that relate both in-plane and out-of-plane displacements to the applied load to extract elastic properties. The use of both in-plane and out-of-plane displacement permits both E and ν to be obtained. In addition, separating the displacement measurements from the indenter allows the deformation to be measured independently of machine compliance and drift.

The purpose of the present work is to assess the accuracy and precision of the in-plane and out-of-plane displacement measurements using particle tracking and quantitative defocusing, respectively. The accuracy of these techniques depend on experimental conditions including optical properties of the microscope and specimen, thus the effect of magnification and particle size on the accuracy and resolution of the technique are investigated for particles on PDMS. Preliminary cylindrical flat punch indentation tests are performed on PDMS specimens and the in-plane and out-of-plane displacements are used along with load data to identify E and ν. These results are compared with E_{eff} calculated using standard indentation analysis.

6.2 Background

6.2.1 Instrumented Indentation

Instrumented indentation is a frequently used technique for evaluating mechanical properties of soft materials, including polymers and biological tissues [8]. This method is capable of testing at low loads and displacements and sample preparation is simple compared to traditional tension or compression tests. Here, we consider flat punch indentation in which a force, P, is applied to a cylindrical flat punch with radius, a, indenting it into an elastic halfspace with Young's modulus, E, and Poisson's ratio, ν. The origin of the Cartesian coordinate system used in the present work is located on the surface of the specimen and along the centerline of the indenter. z is positive into the material, such that a compressive force deforms the specimen in the positive z-direction. For rigid cylindrical flat punch indentation, E_{eff} relates to the stiffness measured during an indentation test as follows [1, 2]:

$$E_{eff} = \frac{E}{1-\nu^2} = \frac{k}{2a}, \tag{6.1}$$

where E is the Young's modulus, ν is the Poisson's ratio, k is the stiffness, and a is the contact radius.

The in-plane and out-of-plane displacements of a point on the surface of an elastic halfspace that is being indented with a cylindrical flat punch are a function of E, ν, a, in-plane position, x and y, and applied load, P [9]. The relationships were transformed to Cartesian coordinates to simplify the application to measured displacement data. Beneath the indenter, the displacements are

$$u_x = -\frac{(1-2\nu)(1+\nu)}{2\pi E}\frac{Px}{x^2+y^2}\left(1-\sqrt{1-\frac{x^2+y^2}{a^2}}\right)$$
$$u_y = -\frac{(1-2\nu)(1+\nu)}{2\pi E}\frac{Py}{x^2+y^2}\left(1-\sqrt{1-\frac{x^2+y^2}{a^2}}\right)$$
$$u_z = \frac{1-\nu^2}{\pi E}\frac{P}{a} \tag{6.2}$$

and outside the contact area the displacements are,

$$u_x = -\frac{(1-2\nu)(1+\nu)}{2\pi E}\frac{Px}{x^2+y^2}$$
$$u_y = -\frac{(1-2\nu)(1+\nu)}{2\pi E}\frac{Py}{x^2+y^2}$$
$$u_z = \frac{1-\nu^2}{\pi E}\frac{P}{a}\arcsin\left(\frac{a}{\sqrt{x^2+y^2}}\right). \tag{6.3}$$

6.2.2 *Quantitative Defocusing Method*

Discrete micrometer-scale particles are widely used as markers to measure displacements in both fluids and soft solids, including gels and biological materials [10]. Scanning confocal microscopy is a popular tool for quantifying the position of micrometer-scale particles in three dimensional space because the spatial resolution is superior to many other techniques [11]. However, because scanning confocal microscopes scan the specimen point by point, the data acquisition rates are generally slow [12], which becomes problematic when high acquisition rates are required to quantify time-dependent material properties.

An alternative method called quantitative defocusing [13], has lower resolution than scanning confocal microscopy, but can achieve higher acquisition rates. This method uses wide-field fluorescence microscopy to image micron-scale fluorescent particles. Unlike confocal microscopy which restricts out-of-focus light, in wide-field microscopy, out-of-focus particles appear along with particles in the focal plane. Due to spherical lens aberration, a ring pattern forms around the out-of-focus particles. The radius of the ring is a function of the distance of the particle from the focal plane [13, 14]. This method is advantageous because the entire field-of-view is captured in one image, allowing for data acquisition rates faster than conventional confocal microscopy. In addition, wide-field fluorescence microscopes are often less expensive than confocal microscopes.

Non-ideal optical conditions typically limit the use of diffraction models, thus a commonly used approach is to compare the aberration rings measured during experiments to an experimentally developed calibration curve. The calibration curve is created by collecting images of a stationary particle of the same size as those used in the experiment at known z displacements from the focal plane. The ring shape is measured to correlate ring size with out-of-plane displacement [15]. While the calibration curve depends on the objective, particle size, and the optical properties of the system and cannot be used universally, this method allows displacement to be measured in situations in which the optical properties of the system are not ideal. Zhang and Menq [16] developed a method in which the in-plane location of a particle is found using a weighted centroid method. The intensity of the particle and ring aberration is found as a function of radial distance from the centroid. This intensity profile is compared to those of calibration images to determine the out-of-plane displacement. Using this analysis technique with 4.5 μm particles and a magnification of 60×, an in-plane standard deviation of 0.35 nm and an out-of-plane standard deviation of 0.9 nm was reported. Because applying quantitative defocusing to indentation tests requires viewing the particles through the specimen, which can be several millimeters thick, a similar approach in which calibration curves are created experimentally prior to testing is pursued in the present work.

6.3 Experimental Setup

PDMS is prepared by mixing a 10:1 weight ratio of Sylgard 184 base elastomer to Sylgard 184 curing agent (Dow Corning Corporation, Midland, MI). After degassing for 1 h, the PDMS is cast on a silicon wafer to ensure a smooth surface for indentation. The PDMS is cured on a hot plate at 85 ° C for 4 h. Fluorescent polystyrene microspheres (Bangs Laboratories, Inc, Fishers, IN) are used for surface motion markers. The microspheres have an excitation wavelength of 480 nm and an emission wavelength of 520 nm. 1 μL of microparticle solution is diluted in 1 mL of isopropanol. This particle mixture was placed on the surface of PDMS in 1.5 μL drops. Specimens were allowed to sit for at least 12 h to ensure the isopropanol had completely evaporated.

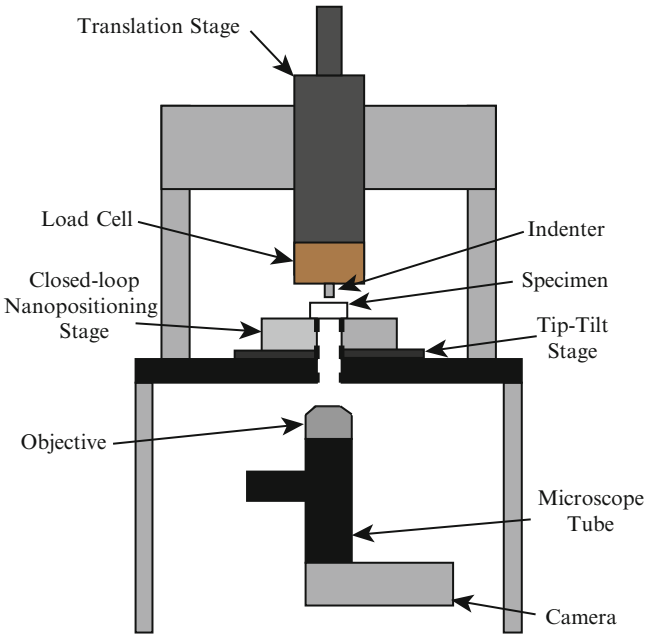

Fig. 6.1 Schematic of the indenter. A translation stage moves the load cell and indenter into and out of contact with the specimen which is mounted over an opening. The opening allows the inverted microscope to view the displacement of the microparticles during the indentation test

A cylindrical flat punch indentation experiment was developed to validate the technique proposed in this work. A wide-field fluorescence inverted microscope was built to image the particles from beneath the specimen during indentation tests. Images were collected from the microscope with a CMOS (1,024×1,280) camera (Pixelink A741, Ottawa, Ontario). The specimen is placed on a closed-loop nanopositioning stage (nPoint, Middleton, WI) which has a 100 μm in-plane and out-of-plane displacement range. To facilitate the inverted microscope, the stage has an opening in the center, giving the microscope access to the specimen. This stage is mounted on a tip-tilt stage to allow proper alignment between the sample and the indenter. A schematic of the experiment setup is shown in Fig. 6.1. The cylindrical flat punch indenter is made from a 0.5 mm diameter glass rod. Force is measured with a 10 g load cell (Cooper Instruments and Systems, Warrenton, VA).

6.4 Particle Tracking Procedure

In the present work, the *x*-coordinate was defined in the 1,280 pixel direction of the camera and the *y*-coordinate was defined along the 1,024 pixel direction. Preprocessing consists of background subtraction, image contrast adjustment, and median filtering. The background image is created by averaging five images of the specimen taken at a sufficient distance from the focal plane such that the particles are not identifiable from the background. The image contrast is adjusted to increase the brightness of the particles relative to the background noise. Lastly, a 3×3 median filter is applied to remove salt and pepper noise.

To identify peaks, the first image in an image sequence is converted to binary. Bright regions are then identified as potential particle locations. These are then filtered based on area and minimum peak height to exclude areas not associated with particles. Minimum area, maximum area, and peak height are adjustable parameters meant to allow the user to sort out particles of interest from surface contamination or noise that may not have been removed during image preprocessing.

The particles that meet these criteria are located in the grayscale image and fit with the first 30 axisymmetric Zernike polynomials. While the definition of Zernike polynomials is beyond the scope of this work, additional information can be found in [17]. Zernike polynomials were chosen because the axisymmetric mode shapes resemble the intensity distribution of both in-focus and out-of-focus fluorescent particles. A bounding box around each particle is created. The center of a bounding box created around a particle, which corresponds to the origin of the axisymmetric Zernike polynomials, is allowed to vary to minimize the error between the axisymmetric Zernike polynomial fit and the grayscale values inside the bounding box. If the error is below a threshold value set by the user, the region is

considered a valid particle. The center of the bounding boxes of valid particles are then used as initial guesses for the in-plane particle locations in all images. These regions are then fit in each image using the Zernike polynomial algorithm to determine the particle centers.

To determine the out-of-plane location of the particles, the intensity of the Zernike polynomial fits for each particle are normalized such that the peak is 1. The ring radius of the particle is determined by finding the radius of the smallest circle that will enclose the points on the Zernike polynomial in which the height is greater than or equal to 0.5. This threshold was chosen because it exceeds the noise in the fitted surface that sometimes appears along the boundaries of the bounding box.

6.5 Calibration

6.5.1 Procedure

To understand the effects of particle size and magnification on the accuracy and precision of displacement measurements, displacement calibration and noise data were collected for 1.9 and 6.3 μm diameter particles on a 3 mm thick PDMS sample using a 10× Zeiss EC Epiplan-Neofluar objective with a 9 mm working distance and 0.25 numerical aperture and a 20× Zeiss LD EC Epiplan-Neofluar objective with a 12.1 mm working distance and 0.22 numerical aperture. These objectives were chosen because the relatively long working distance is necessary to view the particles through thick specimens. For thin specimens, an objective with a shorter working distance would be advantageous because it would have a higher numerical aperture, which increases the light intensity of the particles and decrease the depth of field. In-plane displacements are calibrated by translating an undeformed specimen with the piezoelectric stage in the stage's x, y, and z directions and measuring the motion of the particle center and radius. For z-calibration the specimen is translated 100 μm in 1 μm increments. For both x-and y-directions, the specimen is moved 5 μm in 0.1 μm increments. After each step, the stage is allowed to settle for 1 s, at which point an image is captured.

6.5.2 Results

Figure 6.2 shows 1.9 and 6.3 μm particles at 10× and 20× at different distances from the focal plane. For the cases shown, as the particle moves out of focus, the observed area increases and the observed intensity decreases. Because of this effect, it is necessary to choose a particle size that will allow the particle to be seen over the desired out-of-plane displacement range. At a 20× magnification, the 1.9 μm particle is not visible at 20 or 40 μm. The 1.9 μm particle at 10× magnification begins to fade after moving more than 20 μm from the focal plane.

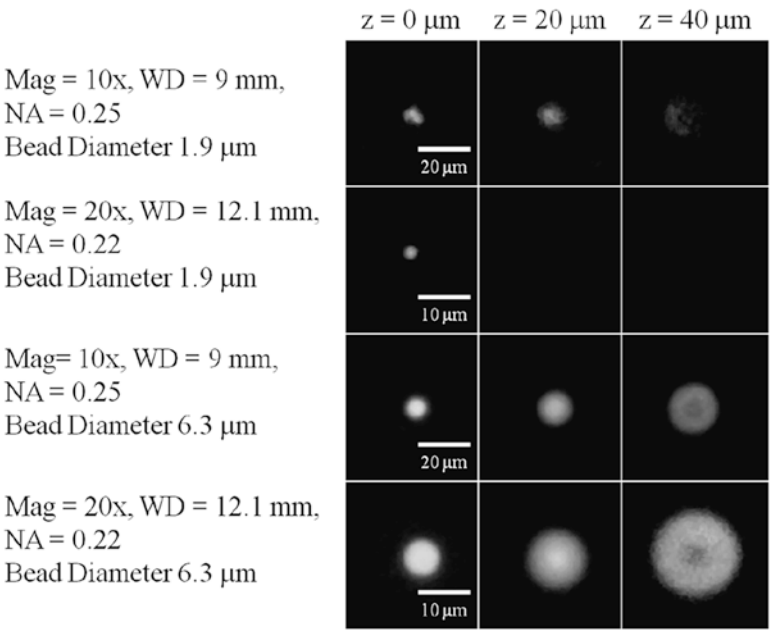

Fig. 6.2 1.9 and 6.3 μm diameter polystyrene fluorescent particles shown at 10× and 20× magnification at 0, 20, and 40 μm from the focal plane

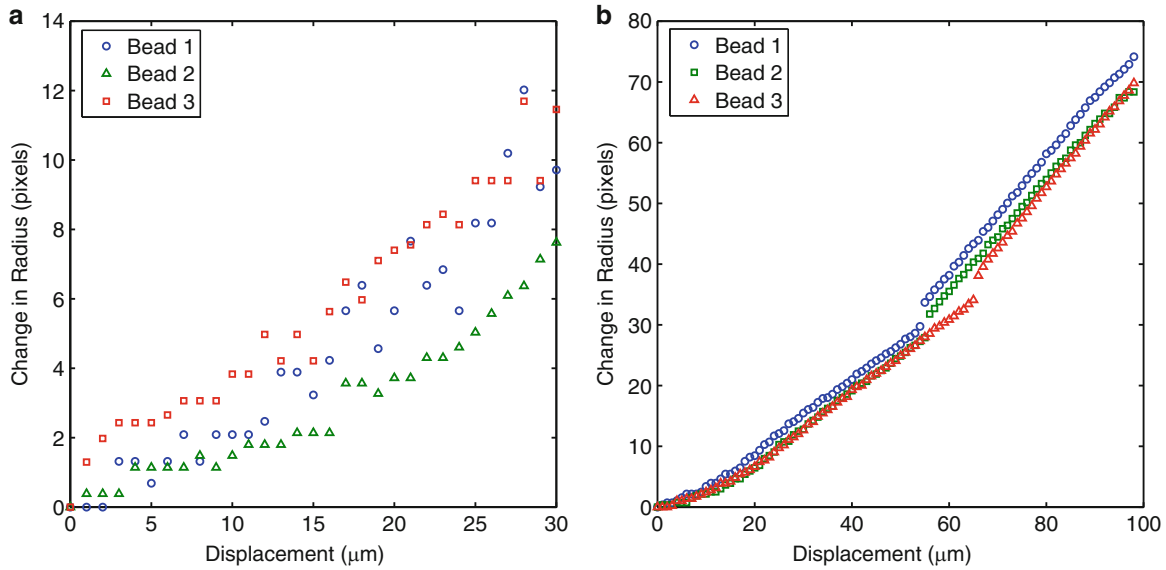

Fig. 6.3 Change in radius of the particle as a function of out-of-plane displacement for a 10× objective and (**a**) 1.9 μm diameter particles and (**b**) 6.3 μm diameter particles

It is possible to increase the out-of-plane range of this method by using an objective with a higher numerical aperture or increasing light intensity [13]. While the long working distance needed to view the particles through a specimen limits the numerical aperture that can be used, the light intensity can be increased by using larger particles. As shown in Fig. 6.2, at both magnifications, the 6.3 μm particles have a higher intensity and the edge of the bead is better defined than the 1.9 μm beads at the off-focus distances examined.

Figure 6.3 shows the relationship between the change in measured radius relative to the in-focus particle radius and distance from the focal plane for three 1.9 and 6.3 μm particles with the 10× objective. The radius of the 1.9 μm particles are shown from 0 to 30 μm away from the focal plane in Fig. 6.3a. Beyond this distance, the algorithm was unable to distinguish the particles from the background noise. In Fig. 6.3b, the algorithm was able to track the particle radius from 0 to 100 μm from the focal plane. The discontinuities in the measured change in radius that occur between stage displacements of 50 and 70 μm are currently being investigated. These results suggest that 6.3 μm particles are better suited for these experimental conditions because the increase in light intensity allows them to be identified and tracked farther from the focal plane.

The in-plane motion of 1.9 and 6.3 μm particles were calibrated with respect to the displacement of the stage for magnifications of 10× and 20×. The results of x-and y-calibrations for 6.3 μm particles at 10× and 20× magnification are shown in Fig. 6.4. As expected, the in-plane displacement of the particles are linearly related to the applied displacement from the piezoelectric stage. The slope of the pixel displacement – stage displacement relationship was found using linear least squares.

The mean and standard deviation of the slopes for all particles tracked for each case are shown in Table 6.1. The mean slopes agree reasonably well with an independent microscope calibration which used a 0.02 mm optical calibration standard. For the 10× objective, the x-calibration was 613 nm/pixel and the y-calibration was 612 nm/pixel. Using the 20× objective, the x-calibration is 303 nm/pixel and the y-calibration is 305 nm/pixel.

6.6 Uncertainty Measurement

6.6.1 Procedure

To quantify the in-plane noise in the image analysis, 50 images were collected for a stationary specimen over a period of 128 s. Using the algorithm described previously, the center of each particle is tracked in each image. The motion of the particle center can then be correlated with the displacement of stage.

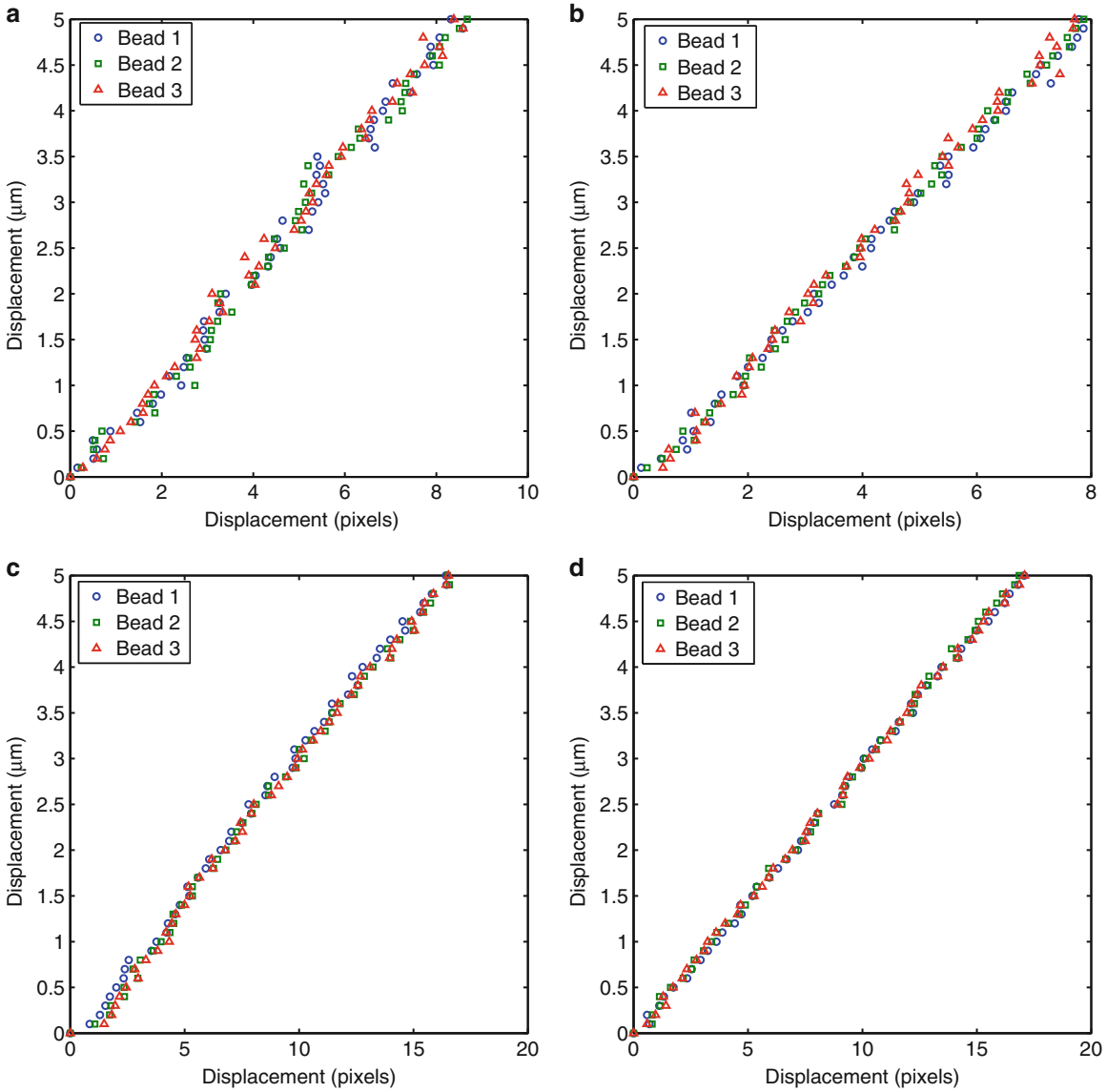

Fig. 6.4 (**a**) 10× magnification *x*-calibration, (**b**) 10× magnification *y*-calibration, (**c**) 20× magnification *x*-calibration, and (**d**) 20× magnification *y*-calibration for 6.3 µm particles

Table 6.1 Mean and standard deviation *x*-and *y*-calibration relationships for all particles at 10× and 20× magnification

	x-calibration		*y*-calibration	
	Mean (nm/pixel)	Std dev (nm/pixel)	Mean (nm/pixel)	Std dev (nm/pixel)
1.9 µm particle, Mag. 10×	576	183	548	184
1.9 µm particle, Mag. 20×	307	13	311	4
6.3 µm particle, Mag. 10×	606	4	637	26
6.3 µm particle, Mag. 20×	316	2	294	3

6.6.2 Results

A summary of the mean and standard deviation of the measured in-plane displacements for magnifications of 10× and 20× and particle sizes of 1.9 and 6.3 µm are shown in Table 6.2. The nonzero mean values may be due to drift in the sample. The standard deviations show that for both particle sizes, the 20× objective has a higher precision. This suggests that there is a trade-off between precision of the in-plane measurement and the field-of-view of the experiment.

Table 6.2 Mean and standard deviation *x*-and *y*-noise measurements for all particles at 10× and 20× magnification

	x-displacement		*y*-displacement	
	Mean (nm)	Std dev (nm)	Mean (nm)	Std dev (nm)
1.9 μm particle, Mag. 10×	125	232	− 37	201
1.9 μm particle, Mag. 20×	− 237	82	− 0.25	76
6.3 μm particle, Mag. 10×	− 242	248	− 232	294
6.3 μm particle, Mag. 20×	− 166	91	17	65

6.7 Indentation Experiments

6.7.1 Experimental Procedure

Preliminary indentation tests on a PDMS specimen with 6.3 μm beads on the surface was completed using the indentation system described previously fitted with a 20× objective. The piezoelectric stage was initially moved to 15 μm above the focal plane. The indenter was positioned such that it was within a few micrometers, but not in contact, with the specimen. The stage is then moved 40 μm toward the indenter over 10 s. The maximum stage displacement is then held for 10 s. The stage was then moved −55 μm. The additional unloading displacement is added to account for adhesion between the indenter and specimen. The measured stiffness is calculated by fitting the unloading portion of the force-displacement data from 90 % of the maximum compressive load to 10 % of the maximum compressive load with a linear relationship and calculating the slope.

6.7.2 Analysis

An optimization routine was developed to extract E and ν from displacement data for discrete particles. This model requires in-plane positions of the particles, *x*-, *y*-, and *z*-displacements at the particle locations, the measured force, and the indenter radius to be known. E and ν are found using a nonlinear least squares algorithm, which varies E and ν to minimize the error between experimental displacement data and theoretical displacements calculated from Eqs. 6.2 and 6.3. The identification of E and ν has not been optimized to reduce the effect of noise on the displacement measurements. This will be addressed in future work.

To validate the results from the optimization routine, E_{eff} is calculated using the Oliver and Pharr method [1] using stage displacement and load cell measurements. To calculate the specimen stiffness, it is necessary to account for machine compliance. Following the method proposed by Oliver and Pharr [1], the measured compliance is modeled as two springs combined in series as follows:

$$C_{measured} = C_{specimen} + C_{machine}, \tag{6.4}$$

where $C_{measured}$, $C_{specimen}$, and $C_{machine}$ are the measured compliance, specimen compliance, and machine compliance respectively. For flat punch indentation, $C_{specimen}$ is

$$C_{specimen} = \frac{1}{2E_{eff}a}. \tag{6.5}$$

$C_{machine}$ was determined by indenting a 6.35 mm thick fused silica specimen ($E = 72$ GPa, $\nu = 0.17$ [1]). Using the fused silica properties and $C_{measured}$ from 11 indentation tests in Eq. 6.4, the mean $C_{machine}$ is 880 μm/N with a standard deviation of 4.76 μm/N. The large compliance in the system is predominately due to the compliance of the 10 g load cell. Because $C_{machine}$ is a property of the instrument, it can be used along with $C_{measured}$ from indentation tests in Eq. 6.4 to find $C_{specimen}$ for materials with unknown properties. The effective modulus can then be calculated from Eq. 6.5.

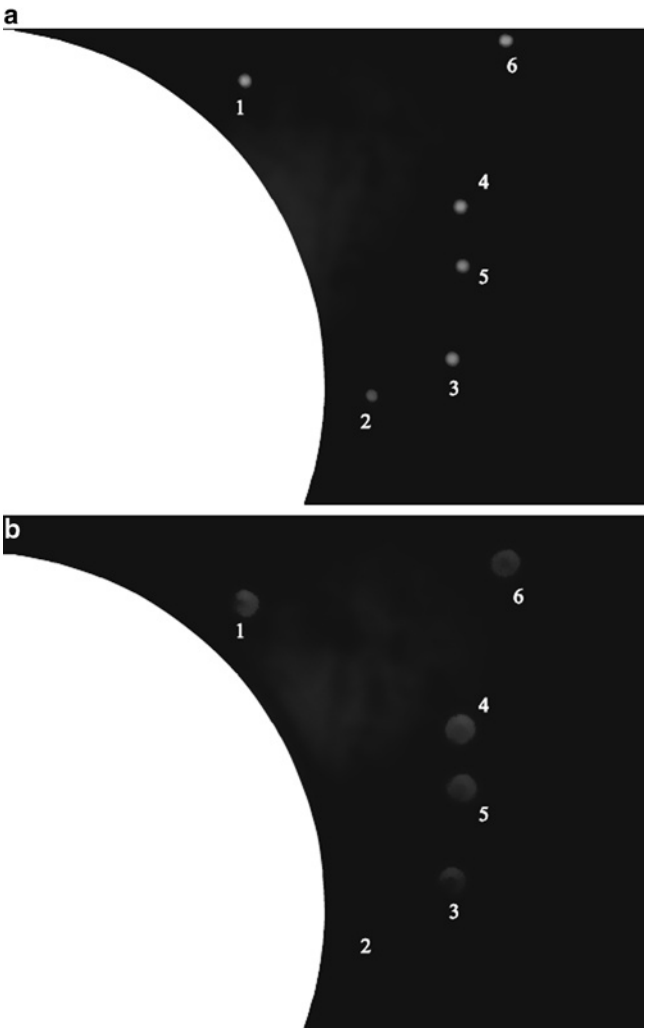

Fig. 6.5 Images of beads outside of the contact region from the experiment (**a**) 15 μm out-of-focus (**b**) 55 μm out-of-focus. The white region is the portion of the contact region visible during the experiment

6.7.3 Results

Images of the particles outside the contact area from the experiment are shown in Fig. 6.5. Figure 6.5a show the particles when they are 15 μm away from the focal plane and the indenter is not in contact with the specimen. In Fig. 6.5b, the specimen is moved 40 μm from it's initial position. As expected, the radius of all particles except particle 2 increase. It is not understood why particle 2 does not appear in Fig. 6.5b. The out-of-plane calibration was completed by fitting a sixth order polynomial to out-of-plane calibration data taken for these particles over a stage displacement range of 0–55 μm, which corresponds with the displacement range of the experiment. Because the polynomial fit does not describe the relationship between particle radius and stage displacement well for particles 1 and 6, only data from particles 3, 4, and 5 are included in this analysis. Stage displacement and measured bead displacement of particles 3, 4 and 5 are shown in Fig. 6.6a and the measured load corresponding to each image is shown in Fig. 6.6b. The surface deformation, which is needed for the analysis, is the difference between stage displacement and particle displacement at a given time.

Force measurements, indenter radius, in-plane particle location, and x-, y-, and z-particle displacements measured from images captured when the stage was at the maximum displacement were input into the analysis algorithm and E and ν were calculated for each image. ν was bounded between 0 and 0.5. E and ν were determined to be 1.98 ± 0.16 MPa and 0.5 respectively, leading to an E_{eff} of 2.64 ± 0.21 MPa. While PDMS is expected to have a Poisson's ratio near 0.5, the algorithm may be reaching the upper bound due to errors in the in-plane measurements. For comparison, E_{eff} was calculated from the compliance measured during the unloading portion of the force-displacement relationship. After correcting for machine compliance, E_{eff} is 3.23 MPa. While the particle tracking analysis and the traditional analysis do not agree, they are similar. Errors in the measured machine compliance effect the modulus calculated using the traditional analysis. There are also sources of error in the bead tracking technique. While the analytical model assumes the contact between the indenter

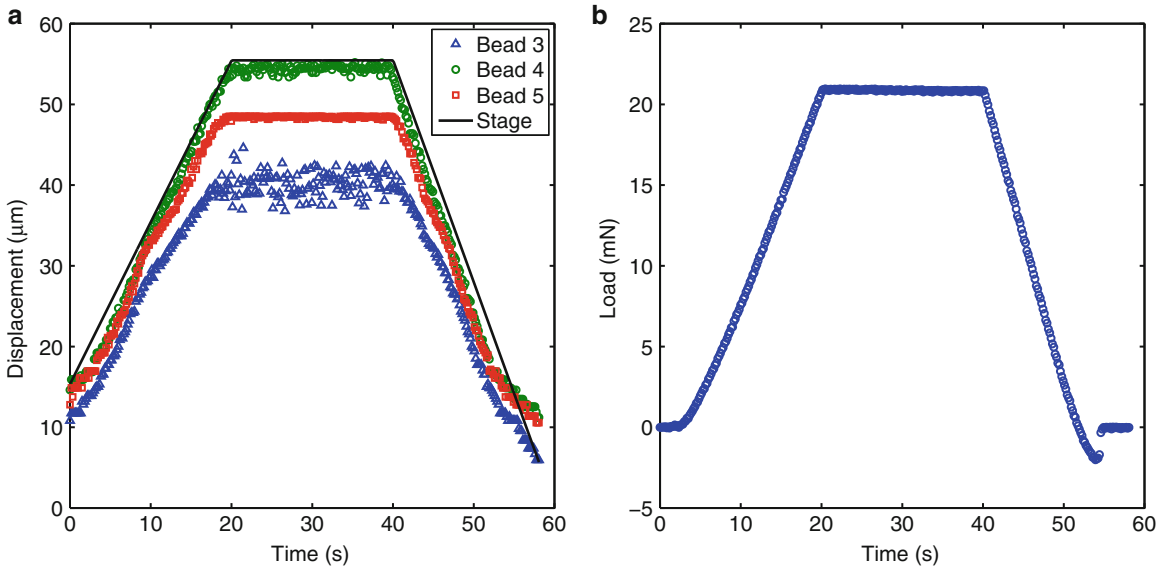

Fig. 6.6 (**a**) The measured out-of-plane displacement as a function of time for an indentation test on PDMS. Data points show the out-of-plane displacement in each image as a function of time. The *solid line* in (**a**) shows the displacement of the stage. The displacement of the surface at the particle locations is the difference between the stage displacement and measured bead location. (**b**) The measured load corresponding to each image as a function of time

and specimen is frictionless, there are friction and adhesive effects that may be influencing the in-plane displacements. Only three particles were tracked in the present work. A previous numerical study of this system suggested that at least 36 particles are required to find E and ν within ± 5 % of the true value [18]. Future work includes addressing the in-plane measurement errors and increasing the particle density to improve the accuracy and precision of E and ν calculated from the particle tracking method.

6.8 Conclusion

A technique for measuring the in-plane and out-of-plane displacements along the surface of a transparent specimen during a flat punch indentation test was designed. An algorithm was developed to track the in-plane and out-of-plane motion of discrete particles by fitting images of the particles with axisymmetric Zernike polynomials. The viability of this method was assessed by applying the algorithm to in-plane and out-of-plane calibrations and in-plane noise measurement of fluorescent particles on PDMS. For the optical system used in the present work, it was found that 6.3 μm particles provide sufficient light intensity to be tracked over 100 μm of out-of-plane displacement. The noise assessment suggests that the precision of the in-plane measurements improved at higher magnification. However, as the field-of-view decreases, less particles can be tracked, which may affect the performance of the analysis algorithm. A preliminary indentation test was completed to demonstrate the feasibility of the technique. An optimization routine was used to extract E and ν from load, particle location, particle displacement, and contact radius data. Discrepancies between E_{eff} calculated from the particle tracking method and the Oliver and Pharr method may be due to errors in machine compliance measurements, having insufficient particles within the field-of-view, and friction and adhesive effects not accounted for in the analytical model. These errors will be investigated in the future.

Acknowledgements We wish to acknowledge financial support from the US Postal Service and US Forest Service, Forest Products Laboratory.

References

1. Oliver WC, Pharr GM (1992) An improved technique for determining hardness and elastic-modulus using load and displacement sensing indentation experiments. J Mater Res 7(6):1564–1583

2. Sneddon IN (1965) The relation between load and penetration in the axisymmetric Boussinesq problem for a punch of arbitrary profile. Int J Eng Sci 3(1):47–57
3. VanLandingham MR (2003) Review of instrumented indentation. J Res Natl Inst Stand Technol 108(4):249–265
4. Fischer-Cripps A (2006) Critical review of analysis and interpretation of nanoindentation test data. Surf Coat Technol 200:4153–4165
5. Wald MJ, Considine JM, Turner KT (2013) Determining the elastic modulus of compliant thin films supported on substrates from flat punch indentation measurements. Exp Mech doi:10.1007/s11340-012-9705-2
6. Kaufman JD, Klapperich CM (2009) Surface detection errors cause overestimation of the modulus in nanoindentation on soft materials. J Mech Behav Biomed Mater 2:312–317
7. Nohava J, Randall NX, Conté N (2009) Novel ultra nanoindentation method with extremely low thermal drift: principle and experimentall results. J Mater Res 24(03):873–882
8. Oyen M (2013) Nanoindentation of biological and biomimetic materials. Exp Tech 37(1):73–87
9. Maugis D (2000) Contact, adhesion and rupture of elastic solids, 1st edn. Springer, Berlin
10. Rogers SS, Waigh TA, Zhao X, Lu JR (2007) Precise particle tracking against a complicated background: polynomial fitting with Gaussian weight. Phys Biol 4:220–227
11. Prasad V, Semwogerere D, Weeks ER (2007) Confocal microscopy of colloids. J Phys: Condens Matter 19:113102
12. Semwogerere D, Weeks ER (2005) Confocal microscopy. In: Encyclopedia of biomaterials and biomedical engineering. Taylor & Francis, New York, pp 1–10
13. Wu M, Roberts JW, Buckley M (2005) Three-dimensional fluorescent particle tracking at micron-scale using a single camera. Exp Fluid 38:461–465
14. Williams SJ, Park C, Wereley ST (2010) Advances and applications on microfluidic velocimetry techniques. Microfluid Nanofluid 8:709–726
15. Peterson SD, Chuang HS, Wereley ST (2008) Three-dimensional particle tracking using micro-particle image velocimetry hardware. Meas Sci Technol 19:115406
16. Zhang Z, Menq C-H (2008) Three-dimensional particle tracking with subnanometer resolution using off-focus images. Appl Opt 47:2361
17. Mahajan VN (1994) Zernike circle polynomials and optical aberrations of systems with circular pupils. Appl Opt 33(34):8121–8124
18. Wald MJ, Considine JM, Turner KT (2013) Improved instrumented indentation of soft materials through surface deformation measurements. In: Mechanics of biological systems, vol 5. Springer, New York, pp. 141–147

Chapter 7
Cadaveric Femoral Fractures in a Fall on the Hip Configuration

S. Javid, V. Kushvaha, G. Karami, S. McEligot, and D. Dragomir-Daescu

Abstract We fractured 100 cadaveric femora with different areal bone mineral density (aBMD) (normal, osteopenic, and osteoporotic) in a fall on the hip loading configuration using a mechanical testing system. Two single-axis and one multi-axis load cells measured the forces and moments in the femoral head, shaft, and the greater trochanter. Two high-speed video cameras recorded the events leading to fracture from the anterior and posterior directions.

Force-displacement curve of a typical experiment showed a linear elastic region followed by post-yielding associated with sinking of the superior neck region into greater trochanter (73 of the tested femora). Fatal crack initiated in tension on the inferior region of the neck or medial shaft. Femoral strength (peak trochanteric force) exhibited strong correlation with aBMD. One-way analysis of variance showed significantly lower values for means of fracture forces and moments of osteoporotic femora compared to those of osteopenic and normal femora. Fracture forces showed very weak correlation with the femoral geometric parameters measured from CT scans. Using post-fracture CT scans and with the help of an orthopedist, the femoral fractures were classified into subcapital, transcervical, intertrochanteric and pertrochanteric. One-way analysis of variance indicated that femora with intertrocanteric fracture had significantly lower neck aBMD than femora with pertrochanteric and transcervical fractures.

Keywords Cadaveric femur • Bone mineral density • Osteoporosis • Fall-on-the-hip • Fracture testing

7.1 Introduction

Characterized by micro-structural degradation and reduced bone mass, osteoporosis is a major public health issue in the elderly population because it leads to increased risk of bone fracture [1]. Osteoporotic fractures cost about $20 and $ 30 billion/year in the United States and Europe, respectively [2]. Hip fracture, the most serious fracture in osteoporotic patients [3], is usually the result of a sideways fall [4]. The current tool for diagnosis of osteoporosis, aBMD, does not take into account the three dimensional (3D) of bone geometry, does not differentiate between trabecular and cortical bone, and has a moderate correlation with bone strength [5]. Therefore, many orthopedists think that the assessment of bone fracture risk should not be based solely on aBMD measurements [6]. In-vitro experimental strength testing of proximal femora helps understand biomechanical features involved in femoral fracture during a sideways fall on the hip [7].

S. Javid
Division of Engineering, Mayo Clinic, Rochester, MN, USA

Department of Mechanical Engineering, North Dakota State University, Fargo, ND, USA

V. Kushvaha
Division of Engineering, Mayo Clinic, Rochester, MN, USA

Department of Mechanical Engineering, Auburn University, Auburn, AL, USA

G. Karami
Department of Mechanical Engineering, North Dakota State University, Fargo, ND, USA

S. McEligot • D. Dragomir-Daescu (✉)
Division of Engineering, Mayo Clinic, Rochester, MN, USA
e-mail: DragomirDaescu.Dan@mayo.edu

F. Barthelat et al. (eds.), *Mechanics of Biological Systems and Materials, Volume 4*,
Conference Proceedings of the Society for Experimental Mechanics Series,
DOI 10.1007/978-3-319-00777-9_7,

Eckstein et al. [8] studied the correlation between femoral strength (fracture load) and aBMD. They used the difference between the strength of the left and right femora to evaluate the accuracy of their femoral fracture experiments. Courtney et al. [7] investigated the effect of aging on bone strength. Their study showed that aging increases the femoral risk fracture dramatically. Pinilla et al. [9] examined the effect of impact loading direction in a sideways fall on femoral fracture load. Courtney et al. [10] performed fracture tests on a number of cadaveric femora to investigate the influence of loading rate on femoral fracture load in a fall on the hip configuration. Roberts et al. [11] conducted a set of in-vitro femoral fracture tests to develop a new biomechanical tool to assess femoral fracture risk.

Along with mechanical properties, geometric parameters may be used to assess femoral fracture risk [12]. In this respect, Bergot et al. [13] and El-Kaissi et al. [14] conducted retrospective studies to determine the femoral geometric parameters that contribute most to the fracture risk.

During a sideways fall on the hip, in addition to the impact force, torsional and bending moments are developed in the femoral neck and shaft. Although these mechanical quantities may play a role in femoral fractures, they have not been studied yet in a sideways fall configuration. We performed mechanical fracture tests on cadaveric femora in a fall on the hip configuration to better understand the biomechanics involved in bone fracture. We measured the forces and moments in the femoral head, shaft, and the greater trochanter using two single-axis and one multi-axis load cells. Two high-speed video cameras recorded the whole experiment from the posterior and anterior directions. Post-fracture reconstructed CT images where used to classify the fracture types.

7.2 Methods

Using an in-house designed fixture in conjunction with a standard mechanical testing system (MTS, Minneapolis, MN), 100 unpaired human cadaveric proximal femora were mechanically tested to failure in a fall on the hip loading configuration. The range of DXA aBMD (mean ± std: 0.779 ± 0.211, range: [0.347−1.424]) was representative of clinical aBMD in the elderly. The test dataset contained 48 left and 52 right femora. Based on neck aBMD, 27 femora had normal bone mineral density, 36 were osteopenic and 37 were osteoporotic. Table 7.1 shows the characteristics of the tested femoral specimens. Figure 7.1 presents a photograph of the experimental setup used in this study. The greater trochanter was placed in an aluminum cup filled with poly-methyl-methacrylate (PMMA) to increase the contact area and mimic the real sideways fall configuration. The femoral head was fitted into an aluminum cup connected to the upper fixture of the MTS. The upper fixture was attached to the MTS test machine through linear bearings, permitting frictionless displacement in the horizontal plane (xy-plane). The distal femur end was free to rotate about the x-axis to mimic knee rotation.

During testing the hydraulic ram of the MTS machine moved at a constant velocity of 100 mm/s. Two single-axis load cells (Transducer Techniques, Temecula, CA) measured the vertical forces on the femoral head and greater trochanter. A multi-axis load cell (JR3, Woodland, CA), connected to a fixture clamped at the distal end of the femur specimen, measured three force components and three moment components in the femoral shaft. Two high-speed video cameras (Photron Inc., San Diego, CA) recorded the fracture experiments from posterior and anterior directions. We used the high-speed video recordings to synchronize the events leading to fracture with the graph of forces and moments versus machine head displacement in the vertical direction.

Femoral neck axis length (L, mm), mean neck diameter (D, mm), and neck/shaft angle (α, °) were measured as the main geometric parameters of proximal femora from the CT scans captured before fracture tests (Fig. 7.2). After fracture, femora were scanned in a clinical Siemens Definition CT scanner (Siemens, Malvern, PA). Paper tape was used to hold the fractured parts together, such that it would not significantly distort the CT image.

One-way analysis of variance (ANOVA) was used to compare the means of forces on femoral head and trochanter and forces and moments in femoral shaft for normal, osteopenic and osteoporotic femora. We used regression analysis to correlate femoral strength with aBMD. Regression analysis was also used to examine the correlation between fracture

Table 7.1 Characteristics of 100 tested femora

	Females	Males	All
Age (yrs; mean ± std, range)	72 ± 14, [37–99]	67 ± 16, [34–91]	70 ± 15, [34–99]
Gender (n)	67	33	100

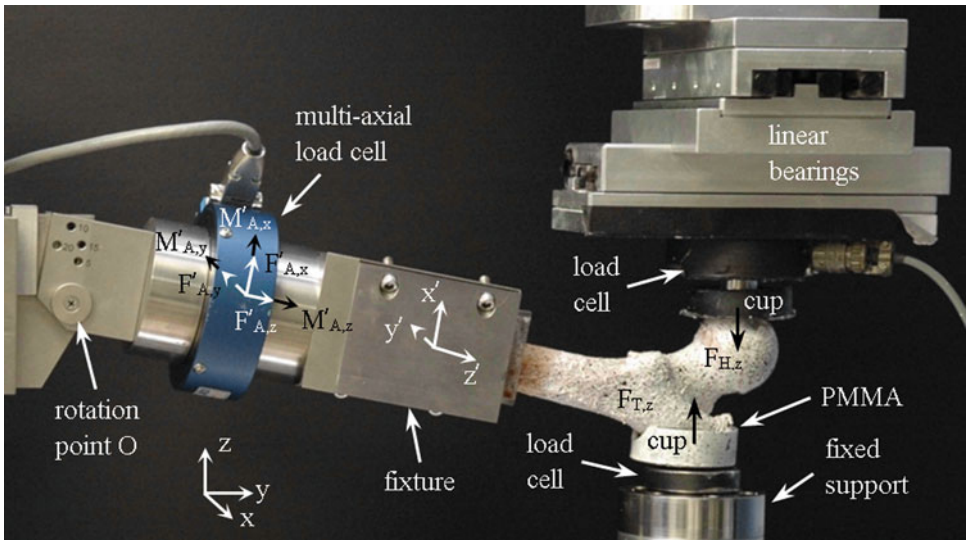

Fig. 7.1 Photograph of the experimental setup. The distal end of the femur was embedded with dental cement in an acrylic container and clamped in a fixture. The fixture was initially placed at an angle of 10° with the y-axis, and could rotate about the x-axis in the global coordinate system xyz

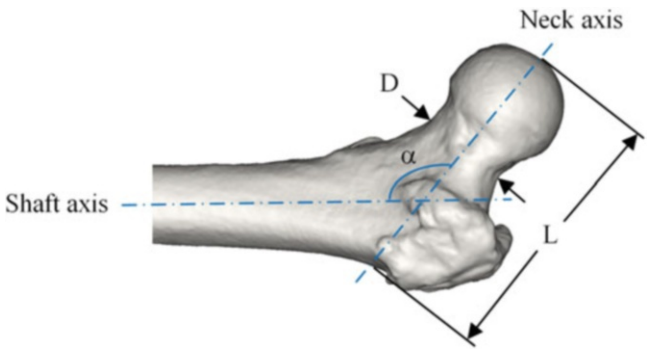

Fig. 7.2 Geometric parameters of the proximal femur, femoral neck axis length (*L*, mm), femoral neck diameter (*D*, mm), and neck/shaft angle (α, °), measured from CT scans

forces and geometric parameters. Finally, using post-fracture CT scans, we classified the femoral fractures into subcapital, transcervical, intertrochanteric and pertrochanteric based on Müller AO Classification of Fractures-Long Bones [15]. We used ANOVA to compare the fracture types of femora with different aBMD. The significant value was set to $p = 0.05$.

7.3 Results

Figure 7.3 shows graphs of trochanter force and torsional moment in the shaft as functions of the MTS ram displacement obtained with our experimental procedure for a femur with normal aBMD. The graphs have been synchronized with the high-speed video recordings. The trochanteric load showed an initial linear elastic region followed by tissue damage observed by the sinking of the superior part of the neck into the trochanteric region (Fig. 7.3b, c). Fatal crack occurred in tension at the junction between the inferior region of the neck and the medial shaft (Fig. 7.3d, e).

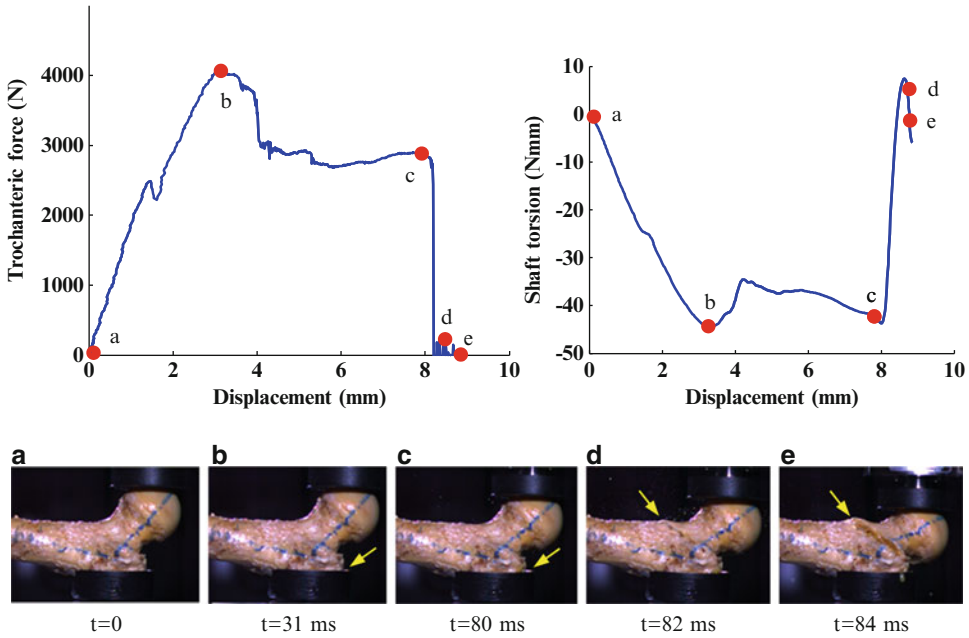

Fig. 7.3 Selection of force and moment data synchronized with high-speed video in a normal femur

Table 7.2 Forces and moments (Mean ± SD) for different bone conditions

Description	Normal	Osteopenic	Osteoporotic	All
Trochanter load (N)	6474 ± 1585	3869 ± 981	2175 ± 647*	3945 ± 2021
Head load (N)	−6158 ± 1494	−3674 ± 921	−2079 ± 616*	−3775 ± 1916
Knee load (N)	357 ± 114	210 ± 73	120 ± 40*	216 ± 121
Axial shaft load (N)	369 ± 306	208 ± 189	74 ± 151*	200 ± 244
Shaft torsion (Nm)	56 ± 21	35 ± 15	17 ± 7*	33 ± 22
Shaft bending (Nm)	−28 ± 10	−17 ± 7	−11 ± 4*	−18 ± 10
Neck bending (Nm)	−178 ± 60	−100 ± 34	−53 ± 16*	−104 ± 64

*Statistically significant

Regression analysis showed a strong correlation between femoral strength and aBMD with $R^2 = 0.82$ ($p < 0.0001$). Table 7.2 represents the mean and standard deviation for different forces and moments at the femoral head, trochanter and shaft at the time of peak trochanteric force for different bone conditions. ANOVA analyses showed statistically significant lower values for all fracture forces and moments of osteoporotic femora compared to those of normal and osteopenic femora ($p < 0.05$). Regression analysis showed very weak correlation between L and α and femoral strength with $R^2 = 0.12$ ($p = 0.0004$) and $R^2 = 0.16$ ($p < 0.0001$), respectively. No correlation was found between D and femoral strength ($R^2 = 0$).

Using the CT scans after fracture and high-speed video recordings, we classified the fractures into subcapital ($n = 13$), transcervical ($n = 44$), intertrochanteric ($n = 25$) and pertrochanteric ($n = 18$). ANOVA indicated that femora with intertrochanteric fractures had significantely lower neck aBMD than femora with pertrochanteric ($p = 0.023$) and those with transcervical fractures ($p = 0.0072$).

7.4 Conclusion

A fall on the hip event results in complex forces and moments on the head, trochanter and shaft regions of the femur. We measured various femoral forces and moments at different time points in fracture tests in a fall on the hip configuration. We used a large sample size consisting 100 femora with a good representation of all aBMD values. Applying a moderately

fast loading rate of 100 mm/s allowed for realistic simulation of femoral fractures. Force-displacement curves showed an initial elastic region followed by post-yielding, typically accompanied by sinking of the superior neck region into the greater trochanter for 73 of the 100 femora.

Osteoporotic femora withstood significantly lower forces and moments. Three-dimensional models developed from CT scans before fracture were used to measure femoral geometric parameters and investigate their effects on fracture load. CT scans after fracture were used to classify fracture types. The results of our extensive femur strength testing will be used to improve estimation of fracture risk in osteoporotic patients and to provide insights for developing new CT-based diagnostics.

Our study showed that a combination of load, moments, high speed video, and fracture CT scans can describe fracture events in more detail. Sinking, damage, crack initiation and propagation as well as final separation can be described from video recordings. This study has some limitations. First, we studied only one sideways fall position. Second, our experimental setup did not account for skin, tissue or muscle protection. Finally, fracture tests were performed at only one speed. The combination of all measurements and methods allowed for a correct characterization of fractures on a fall on the hip configuration.

Acknowledgment This study was supported by funding from the Grainger Foundation: Grainger Innovation Fund and NIH grant AR027065Z-30S1. The authors would like to thank the Musculoskeletal Transplant Foundation for providing the specimens, and the Opus CT Imaging Resources of Mayo Clinic (NIH construction grant RR018898) for CT imaging of the femora.

References

1. Lochmuller EM et al (2003) Can novel clinical densitometric techniques replace or improve DXA in predicting bone strength in osteoporosis at the hip and other skeletal sites? J Bone Miner Res 18(5):906–912
2. Cummings SR, Melton LJ (2002) Epidemiology and outcomes of osteoporotic fractures. Lancet 359(9319):1761–1767
3. Yang L et al (2009) Use of DXA-based structural engineering models of the proximal femur to discriminate hip fractur. J Bone Miner Res 24(1):33–42
4. Sambrook P, Cooper C (2006) Osteoporosi. Lancet 367(9527):2010–2018
5. Dragomir-Daescu D et al (2011) Robust QCT/FEA models of proximal femur stiffness and fracture load during a sideways fall on the hip. Ann Biomed Eng 39(2):742–755
6. McCreadie BR, Goldstein SA (2000) Biomechanics of fracture: is bone mineral density sufficient to assess risk? J Bone Miner Res 15 (12):2305–2308
7. Courtney AC et al (1995) Age-related reductions in the strength of the femur tested in a fall-loading configuration. J Bone Joint Surg Am 77 (3):387–395
8. Eckstein F et al (2004) Reproducibility and side differences of mechanical tests for determining the structural strength of the proximal femur. J Bone Miner Res 19(3):379–385
9. Pinilla TP et al (1996) Impact direction from a fall influences the failure load of the proximal femur as much as age-related bone loss. Calcif Tissue Int 58(4):231–235
10. Courtney AC et al (1994) Effects of loading rate on strength of the proximal femur. Calcif Tissue Int 55(5):402–402
11. Roberts BJ et al (2010) Comparison of hip fracture risk prediction by femoral aBMD to experimentally measured factor of risk. Bone 46 (3):742–746
12. Koivumaki JE et al (2010) Does femoral strain distribution coincide with the occurrence of cervical versus trochanteric hip fractures? An experimental finite element study. Med Biol Eng Comput 48(7):711–717
13. Bergot C et al (2002) Hip fracture risk and proximal femur geometry from DXA scans. Osteoporos Int 13(7):542–550
14. El-Kaissi S et al (2005) Femoral neck geometry and hip fracture risk: the Geelong osteoporosis study. Osteoporos Int 16(10):1299–1303
15. Yang KH et al (1996) The relationship between loading conditions and fracture patterns of the proximal femur. J Biomech Eng Trans Asme 118(4):575–578

Chapter 8
Correlation of Multi-scale Modeling and Experimental Results for the Elastic Modulus of Trabecular Bone

Elham Hamed, Ekaterina Novitskaya, Jun Li, Alexander Setters, Woowon Lee, Joanna McKittrick, and Iwona Jasiuk

Abstract Trabecular bone is a porous nanocomposite material with a hierarchical structure. In this study, a multi-scale modeling approach, addressing scales spanning from the nanometer (collagen-mineral) to mesoscale (trabecular bone) levels, was developed to determine the elastic moduli of trabecular bone. Then, the predicted modeling results were compared with experimental data obtained by compression testing of bovine femur trabecular bone samples loaded in two different directions; parallel to the femur neck axis and perpendicular to that. Optical microscopy, scanning electron microscopy and micro-computed tomography techniques were employed to characterize the structure and composition of the samples at different length scales and provide the inputs needed for the modeling. To obtain more insights on the structure of bone, especially on the interaction of its main constituents (collagen and mineral phases), trabecular bone samples were deproteinized or demineralized and, afterwards, tested mechanically in compression. The experimental observations were used, in turn, to fine-tune the multi-scale model of bone as an interpenetrating composite material. Good agreement was found between the theoretical and experimental results for elastic moduli of untreated, deproteinized, and demineralized trabecular bones.

Keywords Trabecular bone • Elastic moduli • Multi-scale modeling • Compression test • Demineralization • Deproteinization

8.1 Introduction

Bone is a hierarchically structured biological material composed of organic and inorganic phases as well as water. The organic phase (32–44 vol.%) contains type-I collagen and small amounts of non-collagenous proteins (NCPs). Hydroxyapatite minerals, with average dimensions of $50 \times 25 \times 3$ nm^3, form the inorganic phase (33–43 vol.%). Water comprises about 15–25 vol.% of bone tissue [1]. There are two main bone types: cortical and trabecular. The cortical bone is a dense tissue (porosity < 10 vol.%) which forms a hard shell around the more porous trabecular bone (with porosity of ~70–90 vol.%). Compared to cortical bone, trabecular bone is less dense, lighter, softer, and less stiff; however, it plays an important role in absorbing any shock or sudden pressure that bone may experience. The remarkable mechanical properties of

E. Hamed (✉)
Civil and Environmental Engineering Department, Technological Institute, Northwestern University, 2145 Sheridan Road, Evanston, IL 60208, USA
e-mail: elham.hamed@northwestern.edu

E. Novitskaya
Department of Mechanical and Aerospace Engineering, University of California, 9500 Gilman Dr., La Jolla, San Diego, CA 92093, USA

J. Li
California Institute of Technology, 1200 E California Blvd, MC 301-46, Pasadena, CA 91125, USA

A. Setters • W. Lee • I. Jasiuk
Department of Mechanical Science and Engineering, University of Illinois at Urbana-Champaign, 1206 W. Green St., Urbana, IL 61801, USA

J. McKittrick
Materials Science and Engineering Program, University of California, 9500 Gilman Dr., La Jolla, San Diego, CA 92093, USA

F. Barthelat et al. (eds.), *Mechanics of Biological Systems and Materials, Volume 4*,
Conference Proceedings of the Society for Experimental Mechanics Series,
DOI 10.1007/978-3-319-00777-9_8,

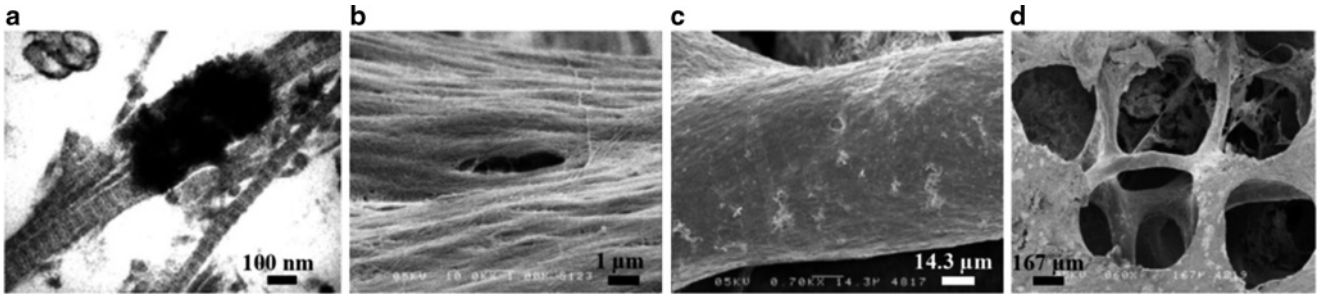

Fig. 8.1 Electron microscopy images of trabecular bone at (**a**) nanoscale (×10,000), using TEM, showing mineralized collagen fibrils, (**b**) sub-microscale (×1,000) showing single lamella, (**c**) microscale (×700) showing a trabecular strut, and (**d**) mesoscale (×20) showing a porous cellular structure of trabecular bone, using SEM [2]

trabecular bone are partly due to its hierarchical structure shown in Fig. 8.1. We distinguish four levels of hierarchy in trabecular bone, spanning from nanoscale to mesoscale. Nanoscale (1–100 nm) represents a mineralized collagen fibril consisting of helical collagen molecules and platelet-shaped hydroxyapatite crystals. Sub-microscale (1–10 μm) represents a single lamella built by preferentially oriented mineralized fibrils in an extrafibrillar matrix. At microscale, single lamellae form plywood structures where the fibrils in each lamella are oriented at a different angle with respect to the adjacent one. In trabecular bone, such lamellar structures form trabeculae in the shape of rods and/or plates, depending on the anatomical location. At mesoscale, trabecular bone consists of a porous network of trabeculae. The pores, typically on the order of 1 mm, are filled with bone marrow, fat, and bone cells.

Complex hierarchical structure of trabecular bone has made its modeling a challenging task. Still, the elastic properties of trabecular bone were predicted using various analytical and computational approaches [3–7]. However, most of the previous studies focused only on the behavior of bone at one single structural scale, which makes it difficult to build the missing links between the hierarchy of microstructures in trabecular bone and its overall mechanical properties. Moreover, recent studies [8, 9] showed that both main constituents of bone (collagen and hydroxyapatite) form continuous phases which intertwine each other. Subsequently, Hamed et al. [10] developed a multi-scale model of cortical bone as an interpenetrating composite material and verified the theoretically predicted results for elastic moduli of bone with experimentally measured values.

In this study, the elastic moduli of the untreated (UT), demineralized (DM), and deproteinized (DP) trabecular bone were investigated. A bottom-up modeling approach, involving four different hierarchical levels, was proposed, and theoretical results for elastic moduli of trabecular bone at the mesoscale were compared with experimental data. Volume fraction, shape, and distribution of porosity at different scales, which are important inputs for the model, were estimated from experiments; optical microscopy and micro-computed tomography (μCT). Experimentally-based theoretical models of these three types of bone can provide additional insights into the structure of bone at different scales.

8.2 Materials and Methods

8.2.1 Sample Preparation

Trabecular bovine femurs, from an approximately 18 month old animal, were obtained from a local butcher. The bone was thoroughly cleaned using a water pick. About 50 samples ($6 \times 6 \times 8$ mm^3) were prepared for structural characterization and mechanical testing. The samples were first roughly cut by a handsaw and, then, precisely with a diamond blade to make the prospective loading surfaces as parallel as possible. Trabecular bone samples were cut in two directions, as shown in Fig. 8.2; a direction oriented along the femur neck axis (A-direction) and a direction normal to that (B-direction). Samples were stored in zip lock bags filled with Hank's balanced saline solution in refrigerator until chemical procedure and mechanical testing. Ten trabecular samples were either demineralized (DM) by aging in HCl solution for a week or deproteinized (DP) by aging in NaOCl solution for two weeks, following the procedures given in [8, 11].

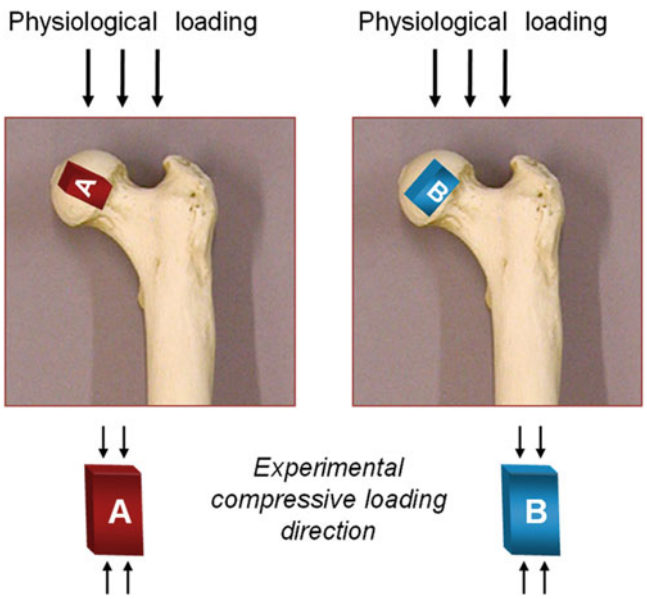

Fig. 8.2 Schematic diagram of physiological and compressive loadings on a femur head, and the sample orientation for two directions: **A** and **B**. Samples are not shown to scale. Femur bone image was taken from avocadoexplosion. wordpress.com

8.2.2 Structural Characterization

Fracture surfaces of the specimens from all three groups were analyzed by a scanning electron microscope (SEM) equipped with EDS (FEI-XL30, FEI Company, Hillsboro, OR). In order to avoid shrinkage, DM bone samples were subjected to critical point drying procedure using the fully automatic critical point drier (Tousimis Autosamdri-815, Rockville, MD) before SEM imaging. Samples from all groups were mounted on aluminum sample holders, air dried, and sputter-coated with chromium (Emitech K575X, Quorum Technologies Ltd., West Sussex, UK) before imaging.

In addition, in order to obtain more insight on bone's internal structure in 3D and characterize its porosity, all three bone groups were imaged using μCT technique at a nominal resolution of 5–10 μm. The μCT imaging was conducted in air using Xradia MicroXCT-200 (for UT and DP samples) and Xradia MicroXCT-400 (for DM samples) instruments (Xradia Inc., Pleasanton, CA). The reconstructed μCT images were, then, analyzed using Amira (Visage Imaging, Inc., Berlin, Germany) to estimate the porosity volume fraction in UT, DM, and DP samples.

8.2.3 Compression Testing

Compression testing of untreated bone samples was done on a universal testing machine equipped with 30 kN load cell (Instron 3367 Dual Column Testing Systems, Norwood, MA). For demineralized and deproteinized bone samples, a universal testing machine equipped with 500 N load cell (Instron 3342 Single Column System, Norwood, MA) was used. A strain rate of 10^{-3} 1/s was used for testing of all three bone groups. The displacement was measured by an external deflectometer (SATEC model I3540, Epsilon Technology Corp., Jackson, WY).

8.3 Modeling Methods

A multi-scale modeling approach was developed to predict the effective elastic moduli of UT, DM, and DP trabecular bones as porous composite materials with hierarchical structure. The modeling procedure started at the collagen-hydroxyapatite level (nanoscale) and moved up to the trabecular bone level (mesoscale). The results obtained for the elastic stiffness tensor of bone at a lower scale served as inputs to a higher scale. The amount of porosity employed at different steps of modeling was taken from the μCT data.

Table 8.1 Elastic properties and volume fractions of bone constituents employed in the multi-scale modeling procedure

Material	Young's modulus (GPa)	Poisson's ratio	Volume fraction (%)
Collagen	1.5	0.28	41
Hydroxyapatite	114	0.23	42
Non-collagenous proteins	1	0.45	4
	Bulk modulus (GPa)	Poisson's ratio	Volume fraction (%)
Water	2.3	0.49	13

Two well-known micromechanical homogenization methods were used throughout the modeling: self-consistent (SC) method to model a composite material with interpenetrating phases and Mori-Tanaka (MT) scheme to model a composite with matrix-inclusion geometry. The general formulas for these methods are

$$\begin{aligned}\mathbf{C}^{SC}_{composite} = \{\Phi_1\mathbf{C}_1 : [\mathbf{I} + \mathbf{S}_1 : \mathbf{C}^{-1}_{composite} : (\mathbf{C}_1 - \mathbf{C}_{composite})]^{-1} + \Phi_2\mathbf{C}_2 : [\mathbf{I} + \mathbf{S}_2 : \mathbf{C}^{-1}_{composite} : (\mathbf{C}_2 - \mathbf{C}_{composite})]^{-1}\} : \\ \{\Phi_1[\mathbf{I} + \mathbf{S}_1 : \mathbf{C}^{-1}_{composite} : (\mathbf{C}_1 - \mathbf{C}_{composite})]^{-1} + \Phi_2[\mathbf{I} + \mathbf{S}_2 : \mathbf{C}^{-1}_{composite} : (\mathbf{C}_2 - \mathbf{C}_{composite})\}^{-1},\end{aligned} \tag{8.1}$$

$$\mathbf{C}^{MT}_{composite} = \mathbf{C}_1 + \Phi_2\{(\mathbf{C}_2 - \mathbf{C}_1) : [\mathbf{I} + \mathbf{S}_2 : \mathbf{C}_1^{-1} : (\mathbf{C}_2 - \mathbf{C}_1)]^{-1}\} : \{\Phi_1\mathbf{I} + \Phi_2[\mathbf{I} + \mathbf{S}_2 : \mathbf{C}_1^{-1} : (\mathbf{C}_2 - \mathbf{C}_1)]^{-1}\}^{-1}, \tag{8.2}$$

where $\mathbf{C}_r$ and Φ_r represent, respectively, the elastic stiffness tensor and volume fraction of phase r; $\mathbf{S}_r$ is the Eshelby tensor depending on the shape of inclusion r and elastic properties of the matrix, and $\mathbf{I}$ is the identity tensor. In the self-consistent formulation, phases 1 and 2 are two types of interpenetrating inclusions, with no matrix. In the Mori-Tanaka method, phase 1 refers to a continuous matrix, while phase 2 represents the reinforcing inclusions.

The elastic moduli and volume fractions of bone constituents (collagen, hydroxyapatite, water, and NCPs) as well as the volume fraction of porosities at different scales were the main inputs to the multi-scale model. Table 8.1 lists the properties of bone constituents used in the modeling. For simplicity, all components were assumed to be linear elastic and isotropic.

8.3.1 Nanoscale

Collagen and hydroxyapatite interpenetrate each other to form a mineralized collagen fibril. Such structure motivated the use of self-consistent method to predict the effective elastic properties of the fibril. Collagen molecules were assumed to be cylindrical inclusions with an aspect ratio of 200:1:1 (following their ~ 300 nm length and ~ 1.5 nm diameter), while hydroxyapatite crystals were represented as ellipsoids with an aspect ratio of 50:25:3. The long axis of crystals is oriented along molecular axis of collagen molecules.

8.3.2 Sub-microscale

Hydroxyapatite crystals exist both inside the fibril, in the empty spaces between collagen molecules, and on the outer surfaces of fibrils. Extrafibrillar hydroxyapatite crystals are dispersed and randomly oriented and, therefore, can be represented as a porous polycrystalline foam made of crystals and some pores in between them, filled with water and NCPs. The effective elastic properties of that hydroxyapatite foam were determined using the self-consistent scheme.

Next, the fibrils coated with extrafibrillar hydroxyapatite foam were modeled. Again, the self-consistent method was used to account for the interpenetrating geometry of fibrils and the foam. It was assumed that 75 % of total hydroxyapatite crystals were interfibrillar and the remaining 25 % were extrafibrillar [12].

Finally, a single lamella was modeled using the Mori-Tanaka method with the coated mineralized fibrils as a matrix and the lacunar cavities as inclusions. Lacunae were assumed to be ellipsoidal in shape with an aspect ratio of 5:2:1 (following their approximate dimensions of $25 \times 10 \times 5\ \mu m^3$).

8.3.3 Microscale

Several single lamellae are oriented in different orientations to form the lamellar structures of trabecular bone: trabecular packets and interstitial bone. However, the exact arrangement of fibrils from one lamella to the neighboring one is still not well understood. Here, for simplicity, it was assumed that the lamellae, having the properties obtained at the previous scale, are oriented randomly which gives rise to an isotropic elastic response. In real bone, however, the trabeculae may have anisotropic and inhomogeneous elastic properties. The homogenization scheme of Sun and Li [13], originally developed for laminated composite materials, was employed to determine the elastic moduli of a single trabecula. More details on the modeling procedure can be found in reference [2].

8.3.4 Mesoscale

At mesoscale, the porous trabecular bone was modeled as an idealized open-cell foam built up by arrays of cubic cells. To that end, the analytical model proposed by Gibson [5] for cellular solids was applied to trabecular bone to predict its Young's modulus as a function of relative density as

$$\frac{E_{bone}}{E_{trabecula}} = c\left(\frac{\rho_{bone}}{\rho_{trabecula}}\right)^{n}, \tag{8.3}$$

where E_{bone} and ρ_{bone} are, respectively, the Young's modulus and density of trabecular bone, while $E_{trabecula}$ and $\rho_{trabecula}$ are the corresponding tissue values. c is the coefficient of proportionality and n is the power which depends on the structural geometry of bone. The relative density, $\rho_{bone}/\rho_{trabecula}$, which is equal to bone volume fraction, was determined from μCT data analysis. Also, the Young's modulus of a single trabecula was taken from the results obtained at the previous scale.

8.3.5 Modeling of Treated Trabecular Bone

Treated (DM and DP) bone samples were modeled following the same multi-scale modeling procedure developed for untreated bone (Sects. 3.1, 3.2, 3.3 and 3.4). The only difference is that during the treatment procedure, one of the constituents is removed: collagen in the DP samples and hydroxyapatite in the DM samples. The removed phase was replaced with voids in all the modeling steps.

8.4 Results and Discussion

SEM images of UT, DM, and DP trabecular bone samples, illustrated in Fig. 8.3, show that DM and DP bones are contiguous, self-standing structures. They, also, confirm that the shape and volume of bone samples as well as their microstructural features (such as lacunae) are preserved during demineralization and deproteinization processes.

Representative μCT images of trabecular bone are shown in Fig. 8.4; a complex network of trabecular rods and plates can be observed. Based on the analysis of μCT data, the porosities of all three bone groups were estimated and listed in Table 8.2.

Finally, Fig. 8.5 shows the elastic moduli of UT, DM, and DP trabecular bone, in both directions A and B, predicted using the multi-scale modeling procedure and compares those with the experimental data obtained by compression testing. The error bars represent standard deviation for experimental data and the range (due to a range in porosities) for the modeling results. Despite all the simplifying assumptions and selections made throughout the modeling, good agreement was found between the theoretical and experimental results. Somewhat large uncertainty was observed for the elastic modulus of UT bone which can be explained by the large range of porosity values (or, alternatively, density values) measured for the samples. Another reason for the discrepancy between modeling and experimental results is that, at the mesoscale, trabecular bone was modeled using Gibson model [5] which assumes the cellular solid to be an isotropic array of periodic cubic cells. In reality, however, trabecular bone consists of rod-plate structural cells (Fig. 8.4) with different dimensions. Analysis of μCT data for the two anatomical directions showed that the degree of anisotropy, which is defined

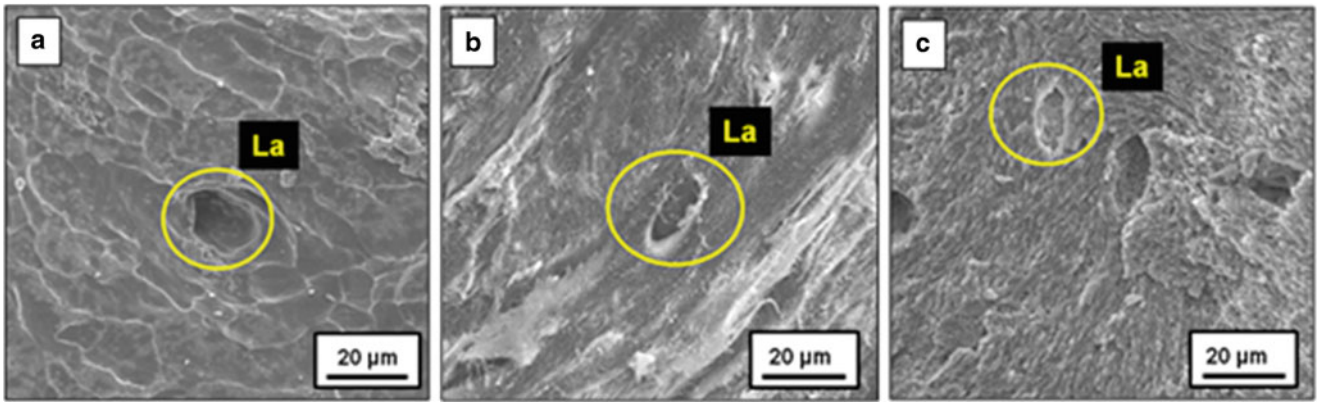

Fig. 8.3 Scanning electron microscopy images of the fracture surfaces of (**a**) untreated, (**b**) demineralized, and (**c**) deproteinized bovine trabecular bone. La = lacuna spaces

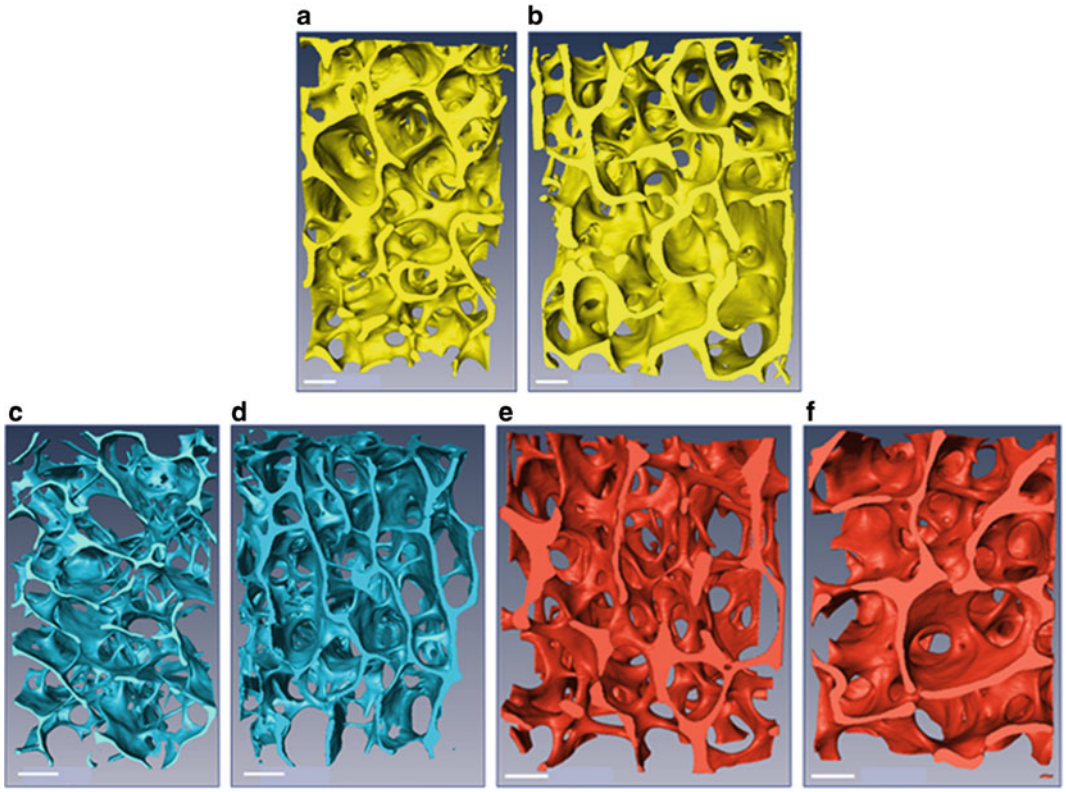

Fig. 8.4 μCT images of trabecular bone for untreated (**a**) A-direction, (**b**) B-direction, demineralized (**c**) A-direction, (**d**) B-direction, and deproteinized (**e**) A-direction, (**f**) B-direction. Scale bars = 700 μm

Table 8.2 Porosity of trabecular bone samples estimated by analysis of μCT images

Bone type (direction)	UT (A)	UT (B)	DM (A)	DM (B)	DP (A)	DP (B)
μCT imaging resolution (μm)	10.8	10.8	5.8	5.5	5.8	5.4
Porosity (%)	83.9 ± 3.3	83.2 ± 4.6	91.6 ± 1.4	90.6 ± 1.6	89.1 ± 1.1	86.9 ± 2.2

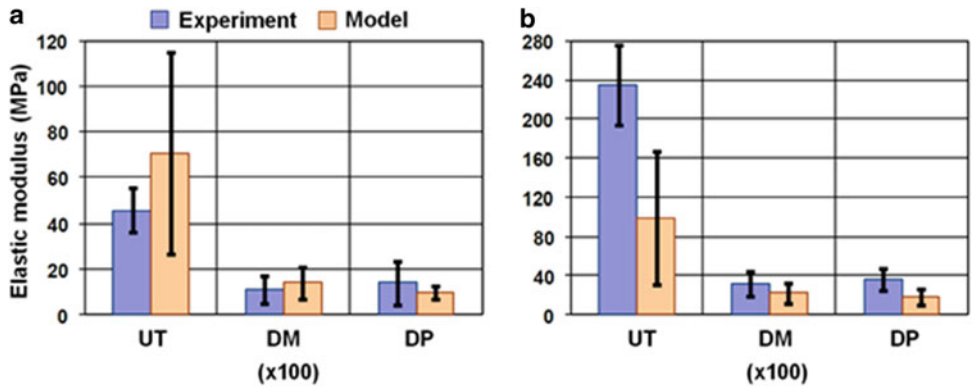

Fig. 8.5 Comparison of the experimental and modeling results for elastic moduli of untreated (UT), demineralized (DM, magnified by 100× for clarity), and deproteinized (DP) trabecular bones in (**a**) A-direction and (**b**) B-direction. The *capped lines* show the standard deviation for experimental data and the range for modeling results

as the ratio between the longest and shortest mean intercept length vectors, was 1.94 for A-direction, while 1.56 for B-direction. This data confirms that trabecular bone is an anisotropic material, which should be taken into account by using more advanced models in future.

8.5 Conclusions

A multi-scale model of trabecular bone was developed which could accurately predict the experimentally measured elastic moduli of bovine femoral bone. The model, which represents bone as an interpenetrating composite of proteins and hydroxyapatite crystals, is applicable to the modeling of untreated bone as well as demineralized and deproteinized bones. The volume fractions of porosities at different scales obtained from μCT scans were used as inputs to the model. Given the simplifying assumptions used in the analysis, the theoretical results for elastic moduli of UT, DM, and DP trabecular bones in two loading directions A and B showed very good agreement with corresponding experimental values.

Acknowledgements This work was supported by NSF Ceramics Program Grant 1006931 (JM) and the CMMI Program Grant 09–27909 (IJ).

References

1. Olszta MJ, Cheng XG, Jee SS, Kumar R, Kim YY, Kaufman MJ, Douglas EP, Gower LB (2007) Bone structure and formation: a new perspective. Mat Sci Eng R 58:77–116
2. Hamed E, Jasiuk I, Yoo A, Lee Y, Liszka T (2012) Multi-scale modelling of elastic moduli of trabecular bone. J R Soc Interface 9(72):1654–1673
3. Currey JD (1969) Relationship between stiffness and mineral content of bone. J Biomech 2:477–480
4. Fritsch A, Hellmich C (2007) 'Universal' microstructural patterns in cortical and trabecular, extracellular and extravascular bone materials: micromechanics-based prediction of anisotropic elasticity. J Theor Biol 244:597–620
5. Gibson LJ (1985) The mechanical behavior of cancellous bone. J Biomech 18:317–328
6. Turner CH, Cowin SC, Rho JY, Ashman RB, Rice JC (1990) The fabric dependence of the orthotropic elastic constants of cancellous bone. J Biomech 23:549–561
7. Muller R, Ruegsegger P (1995) Three-dimensional finite element modelling of non-invasively assessed trabecular bone structures. Med Eng Phys 17:126–133
8. Chen P-Y, Toroian D, Price PA, McKittrick J (2011) Minerals form a continuum phase in mature cancellous bone. Calcif Tissue Int 88:351–361
9. Novitskaya E, Chen PY, Lee S, Castro-Ceseña A, Hirata G, Lubarda VA, McKittrick J (2011) Anisotropy in the compressive mechanical properties of bovine cortical bone and the mineral and protein constituents. Acta Biomater 7:3170–3177
10. Hamed E, Novitskaya E, Li J, Chen P-Y, Jasiuk I, Mckittrick J (2012) Elastic moduli of untreated, demineralized and deproteinized cortical bone: validation of a theoretical model of bone as an interpenetrating composite material. Acta Biomater 8:1080–1092
11. Toroian D, Lim JE, Price PA (2007) The size exclusion characteristics of type I collagen – implications for the role of noncollagenous bone constituents in mineralization. J Biol Chem 282:22437–22447
12. Hamed E, Lee Y, Jasiuk I (2010) Multiscale modeling of elastic properties of cortical bone. Acta Mech 213:131–154
13. Sun CT, Li S (1988) Three-dimensional effective elastic constants for thick laminates. J Compos Mater 22:629–639

Chapter 9
Analysis of Stress Distribution Caused by Orthodontic Correctional Devices

A.N. Okioga, R.J. Greene, D.G. Patrick, and R.A. Tomlinson

Abstract This investigation has been carried out to support the empirical studies conducted by dentists in orthodontic correction using brackets. Both numerical and experimental methods have been implemented in order to give a clear indication of the intrinsic stress distribution throughout a tooth and its surrounding periodontum when a load is applied to the tooth in its initial translation stage. For optimal accuracy, the tooth and surrounding periodontum in both cases are assigned different values proportional to those present in actuality. From the numerical model developed using Ansys Workbench 12, the possible stress patterns are determined. These are validated by the use of 3-dimensional photoelasticity. Tooth models manufactured from polymethyl-methacrylate are stress-frozen with a known loading configuration and sectioned in order to determine the internal stress pattern. These results are then compared with the finite element model. The choice of material was due to its ability to be manufactured without residual stresses, and its birefringent properties. This investigation will be effective in the improvement of orthodontic correctional procedures, especially with the emergence of more aesthetic bracket designs.

Keywords Orthodontics • Stress distribution • Finite element analysis • Photoelasticity • Stress freezing

Nomenclature

f_σ	Stress optic coefficient
i_n	Light intensity
N	Fringe order
t	Through thickness of specimen (mm)
α	Relative retardation
θ	Isoclinic angle
σ	Principal stress (MPa)
1,2	Local coordinate systems

A.N. Okioga (✉) • R.A. Tomlinson
Department of Mechanical Engineering, University of Sheffield, S1 3JD, Sheffield, UK
e-mail: mep10ano@sheffield.ac.uk

R.J. Greene
Strain Solutions Ltd, Chesterfield S41 8NG, Chesterfield, UK

D.G. Patrick
School of Clinical Dentistry, University of Sheffield, S10 2TA, Sheffield, UK

F. Barthelat et al. (eds.), *Mechanics of Biological Systems and Materials, Volume 4*,
Conference Proceedings of the Society for Experimental Mechanics Series,
DOI 10.1007/978-3-319-00777-9_9,

9.1 Introduction

In the study of orthodontic correction via brackets, there has been limited analysis of the intrinsic stresses and strains required for an effective movement of the teeth that needed realignment. It is therefore proposed that by determining the optimal load magnitude resulting in a stable and ideal distribution of stresses throughout the tooth sections, the implementation of this current analysis can be used to confirm the established tooth loading conditions and ensure accurate and efficient alignment.

The application of interest is that of a generic adult canine tooth, and it delves into the periodontum in order to establish the stress distribution and eventually, possible resorption patterns the tooth undergoes during the initial stages of alignment. The periodontum is comprised of the tissues that surround the teeth and bones that support the root, as shown in Fig. 9.1. In the determination of the stress distribution throughout the tooth and periodontum, the load exerted on the tooth will be varied in magnitude. A conventional loading angle (perpendicular to the crown surface) will be used for this investigation, as this is the most common loading angle, empirically determined to be the ideal scenario.

The two methods used in this study are Finite Element Analysis and Experimental Mechanics. Both numerical and experimental models are implemented in order to carry out a thorough and comparative analysis, and to validate both methods in this field of study. In finite element analysis, the intricacy of the model is investigated, as the tooth and surrounding periodontum have complexities that allow for a specific output in the stress distribution. However, in the experimental method, the most important element of study is the effect of loading a tooth, and therefore, the model is simplified to reflect this, without compromising the resulting stress configuration.

9.2 Materials and Methods

9.2.1 Numerical Analysis: FE Modelling

The cross-section of a canine tooth, 27.5 mm in length, was modelled in Ansys 12. The geometry was initially extracted from a generic sketch of a canine tooth viewed from the mesial aspect, in addition to typical values of teeth dimensions from dental morphology studies [1–4]. In order to create the key points in the finite element modelling package, the image of the

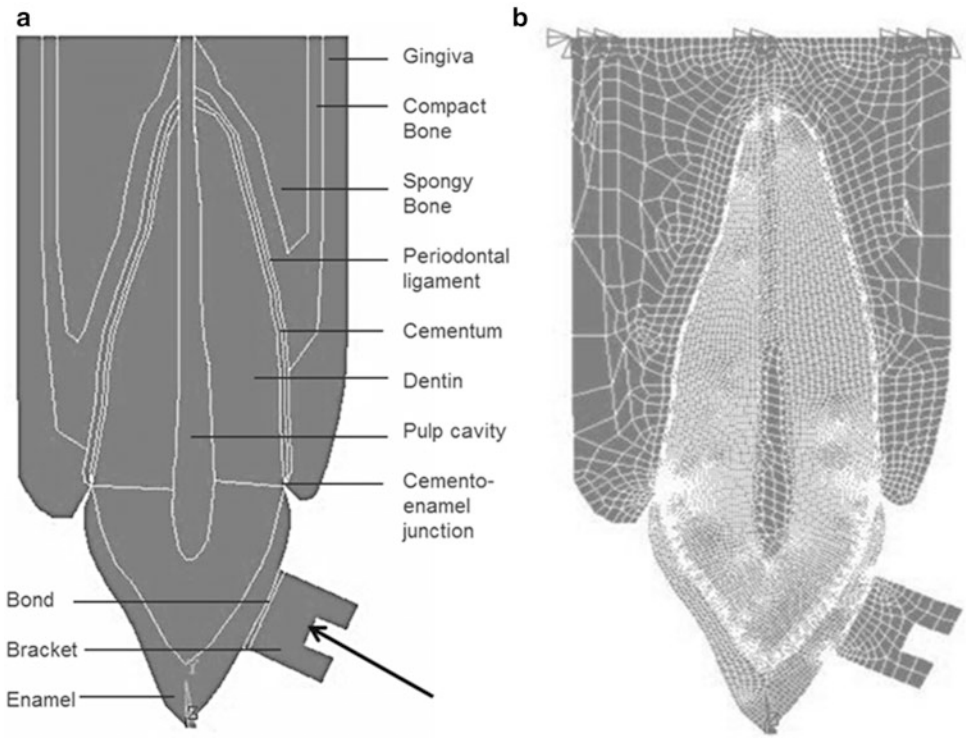

Fig. 9.1 Defined areas of (**a**) an adult canine tooth and its surrounding periodontum; with (**b**) a refined mesh for the FE model generated

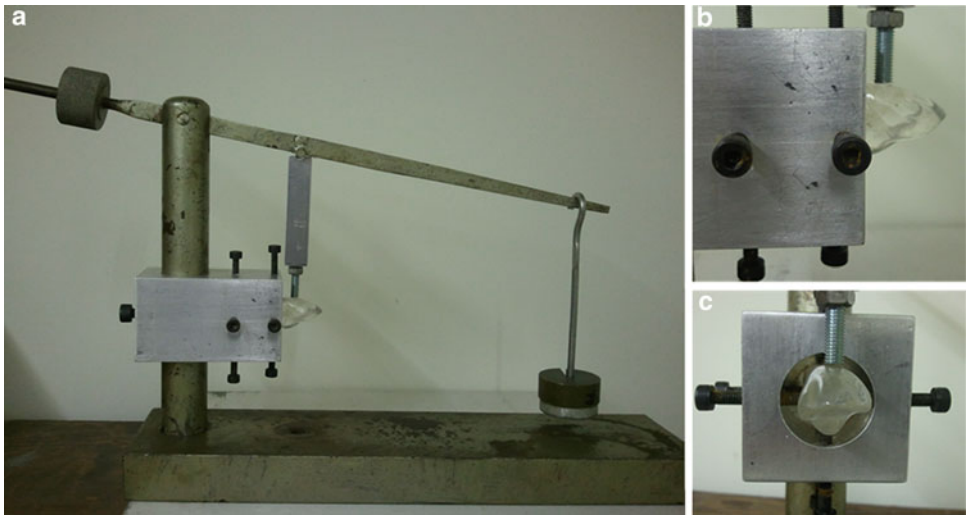

Fig. 9.2 (**a**) Loading configuration for the tooth models, with (**b**) the side profile and (**c**) front profile of the model under loading. Deadweights were used in the loading of the specimen

Table 9.1 Material properties of an adult canine tooth and surrounding periodontum [5–11]

Section	Elastic modulus (MPa)	Poisson's ratio
Enamel	48×10^3	0.23
Dentin	18×10^3	0.31
Pulp cavity, gingiva	0.002×10^3	0.45
Spongy bone	1.3×10^3	0.30
Compact bone	13×10^3	0.30
Periodontal ligament	0.00017×10^3	0.45
Cementum	9.9×10^3	0.17
Stainless steel bracket	200×10^3	0.30
Acrylic adhesive	2.8×10^3	0.37

tooth was scanned and scaled accordingly, which allowed for the determination of the particular locations of every section of the tooth. Once the key points were established, they were entered into Ansys and the relevant material properties assigned to every section. Following this, meshes were defined and refined for the denser sections of the periodontum, to reflect the actual porosity within the tooth (Fig. 9.2). The model was meshed using PLANE183 elements, which allow for good distribution within 2D components with 8 node elements (Table 9.1).

Due to the limited literature investigating the mechanical properties of the gingival cavity, it was assumed that it shares similar properties to the pulp cavity, with respect to its elastic modulus and Poisson's ratio.

The modelling assumption is that of plane strain, which has been suggested to be best for the human mandibular model [5, 12] and because the analysis is carried out on the central cross-section of the tooth. Boundary conditions are the point where the bone is connected to the jaw, which simulates the realistic structure of the periodontum, due to the rigidity of the mandibular connection. Von Mises stresses are analysed due to their efficacy in finite element analysis. This is because they allow for the combination of principal stresses into an equivalent stress that will ensure there is a comparable value to the yield stress, hence a better chance of determining the failure of the system. The loading test was to obtain the changes experienced within the model when subjected to increasing loads, between 0.3 and 1.5 N at a conventional angle perpendicular to the crown surface.

9.3 Experimental Analysis: Photoelasticity

Experimental stress analysis is extremely useful as a comparative method for finite element analysis as it provides an effective visualisation of the mechanical behaviour of the tooth under loading in an accurate manner, provided there is an appropriate configuration and material selection. Using a circular polarisope for analysis, it is possible to determine the

Table 9.2 Orientations for the polariscope output elements in the implementation of the six-step phase-stepping technique developed by Patterson, Ji and Wang and the equations yielding the isoclinic angle Eq. 9.2 and retardation Eq. 9.3 [16]

Intensity	Output $\frac{\lambda}{4}$ plate orientation	Analyser orientation
i_1	0	$\pi/4$
i_2	0	$-\pi/4$
i_3	0	0
i_4	$\pi/4$	$\pi/4$
i_5	$\pi/2$	$\pi/2$
i_6	$3\pi/4$	$3\pi/4$

stresses experienced within a birefringent specimen using the isochromatic fringes obtained and the stress optic law, given in Eq. 9.1 [13]. It states that the isochromatic fringe order, N, at each point in the model is proportional to the difference in principal stresses, $\sigma_1 - \sigma_2$ at the point of interest.

$$\sigma_1 - \sigma_2 = \frac{Nf_\sigma}{t} \tag{9.1}$$

In this study, the material selected was polymethyl-methacrylate, as it is a well-understood material in the dental industry, with particular applications in the manufacture of dentures due to its high impact and fatigue strength [14]. The tooth models were obtained from the Dental Technology Laboratory in the University of Sheffield, where the raw material is easily accessible and a two part moulding process for manufacturing dental components is well established. Production of the tooth models in-house allowed for models with favourable material properties such as high modulus, ideal glass transition temperature and flexural strength to be manufactured, as the optimal composition of liquid to polymer was utilised. Despite having quite low birefringent sensitivity in comparison to epoxies or gelatin, PMMA was still an ideal choice because modern digital photoelastic methods using grey-scale intensity maps enable accuracy in the analysis of fringe orders below 0.5 fringe [15]. Therefore the photoelastic testing method implemented was six-step phase stepping method developed by Patterson, Ji and Wang [16], as shown in Table 9.2. The phase-stepping algorithm will yield simultaneous Eqs. 9.2 and 9.3 that provide the formulae used to determine the isoclinic angle (θ) and relative retardation (α) from the different light intensities (i_n). When coupled with Eqs. 9.4 and 9.1 respectively, the fringe order, hence stresses experienced in the model may be determined.

$$\theta = \frac{1}{2} tan^{-1}\left(\frac{i_5 - i_3}{i_4 - i_6}\right) \tag{9.2}$$

$$\alpha = \frac{1}{2} tan^{-1}\left(\frac{i_4 - i_6}{(i_1 - i_2)cos2\theta}\right) \tag{9.3}$$

$$\alpha = 2\pi N \tag{9.4}$$

Five canine tooth models twice the size of a regular adult tooth were manufactured and stress-frozen whilst loaded in a configuration simulating bracket loading, with restrictions at eight specific points surrounding the tooth – two at each surface, as shown in Fig. 9.2. The stress freezing cycle was a heating stage at 20°C/h from room temperature (approximately 25°C) to 115°C, followed by a hold stage at 115°C for one hour, and finally a cooling stage at 5°C/h from 115°C to 25°C – a total of 24 h per cycle. The stress freezing temperature, 115°C, was selected as advised by Burguete and Patterson [17] – two degrees above the critical temperature. The critical temperature is defined as the lowest temperature to the right of the transition for which the modulus is less than a single standard deviation above the mean for all moduli at higher temperatures. The glass transition temperature was obtained using a dual cantilever experiment at a frequency of 0.1 Hz as it is closest to the static loading configuration experienced in the stress-freezing cycle. The glass transition temperature was found to be approximately 113°C, which was also seen as the temperature at which the test samples' load-carrying capabilities changed drastically.

There were four incremental loads used in the determination of the stress distribution experimentally – 10, 20, 30 and 40 N. Also, for a thorough analysis, an unloaded tooth was subjected to the same thermal cycle as the others in order for a clear comparison due to similar conditions. Once the teeth models had undergone the stress-freezing cycle, 1 mm thick sections were obtained from the central loading point. These sections were then observed under the polariscope, and 6-step phase-stepping used to determine the stress distribution across each tooth.

9.4 Results

Figure 9.3 shows the resulting information given for the Von Mises stress distribution with an increase in load magnitude. This shows that the greatest compressive stresses were experienced in the interfacial regions, namely the cemento-enamel junction and the interface between the dentin and pulp cavity. The reason for this is because stress is generated from the reaction force produced counteracting the force from the arch-wire, with the root tip constraining tooth rotation. However, upon data analysis, it was evident that both the enamel and compact bone are also subject to similar stress concentrations. The increase in loading results in stress distribution of increasing magnitude, as expected, with the cementum experiencing the greatest stress variation – high edge stresses which trough in the central area. This is pertinent in future planned investigations of bone resorption characteristics and growth in considering orthodontic correction. This stress is then distributed to the cementum, which, despite having the least change in an increase in load, undergoes the highest fluctuation within its distribution across the root.

Similarly to the numerical analysis, the experimental method displayed an increase in the stress concentration with an increase in load as shown in Fig. 9.4. However, due to the specific requirements for obtaining the sample to analyse, it is pertinent for the centrally loaded area to be the section of interest. This is especially evident in the sample subjected to a force of 40 N, but displays very little information, as the sample was sectioned off-centre. Therefore the validity of this particular result is questionable. The stress concentration at the enamel surface and constriction point – at which screws were simulating the periodontal bone (Fig. 9.2) – is similar to that in the numerical model, and, despite the lack of variation in the material properties throughout the tooth, shows a relatable stress distribution to that represented in the finite element model. Also, there is minimal stress concentrated at the tip of the tooth, and in the central section – pulp cavity – which is ideal for this method of orthodontic correction, as it allows for the nerves to resist damage, hence allowing tooth movement without the destruction of the tooth itself.

This initial investigation also displays an unwrapping anomaly, as the isoclinics seem to be affecting the resulting fringe information, displaying similarities in patterns on the phase-stepped images. This is especially evident in the unloaded specimen (Fig. 9.4a), which display coinciding patterns in both isoclinic and fringe order, despite being subjected to no loading. Further investigation will be performed in order to determine a method to alleviate this interference.

Further investigation to determine the effect of the surrounding periodontum in relation to the tooth is underway, with the selection of a material with a similar ratio of material properties to PMMA as the tooth has to the surrounding periodontum at elevated temperatures, especially at stress freezing temperatures. In addition to this, a model comprising of the build of materials similar in moduli to the specific sections of the tooth and surrounding periodontum could allow for a more thorough investigation of the stress distribution throughout the tooth and the interaction the bracket has with the tooth during the process of orthodontic correction.

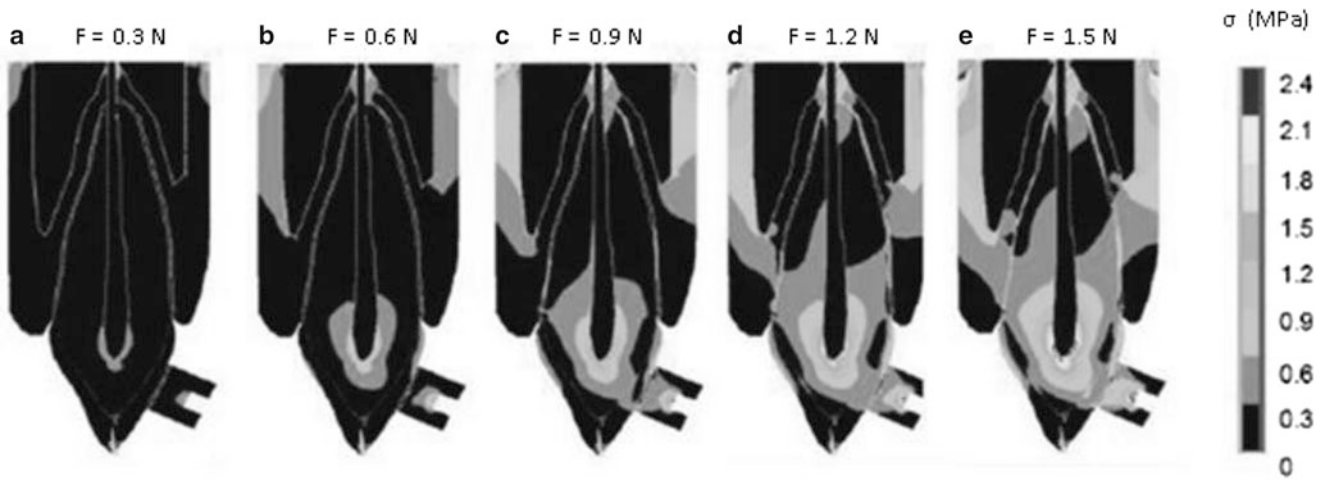

Fig. 9.3 FE results of stress distribution (MPa) across the tooth and surrounding periodontum when subjected to a force acting perpendicular to the crown surface. Incremental loads of (**a**) 0.3 N, (**b**) 0.6 N, (**c**) 0.9 N, (**d**) 1.2 N and (**e**) 1.5 N are applied yielding an increase in stress concentrations at interfacial regions

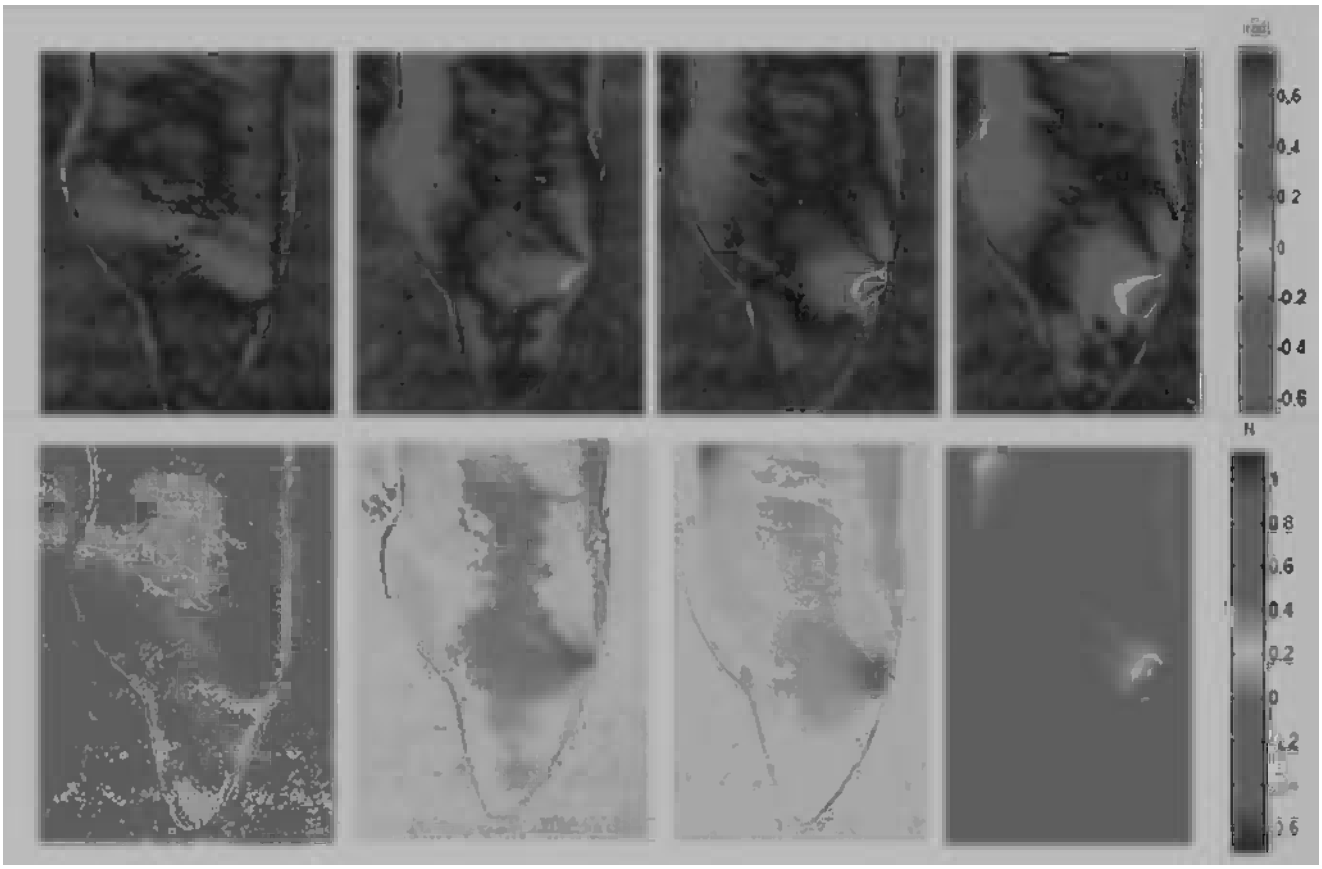

Fig. 9.4 Resulting information from six phase-stepped images taken of the central sections of the stress-frozen tooth models, with thickness 1 mm, showing the isoclinic angle in rad (*top*) and fringe order (*bottom*) of the experimental tooth models subjected to loads of approximately (**a**) 0 N, (**b**) 10 N, (**c**) 20 N, (**d**) 30 N and (**e**) 40 N

9.5 Conclusion

This study has shown that the stress distribution throughout a tooth undergoing orthodontic correction using brackets has the greatest impact on the loading surface. However, when the material properties are put into greater consideration, the interfacial surfaces are key in the investigation of the stress distribution. Both finite element analysis and experimental mechanics are viable test methods for this analysis, and further studies can be performed to enable future design constraints that cater to an optimal stress distribution configuration.

References

1. Othman SA, Harradine NWT (2006) Tooth-size discrepancy and bolton's ratios: a literature review. J Orthod 33:45–51
2. Osbourne RH, Horowitz SL, De George FV (1958) Genetic variation in tooth dimensions: a twin study of the permanent anterior teeth. Am J Human Genetics 10(3):350–356
3. Wheeler RC (1974) Dental anatomy, physiology and occlusion. W.B. Saunders Company, Philadelphie. pp 6, 172–194, 313
4. Van Beek GC (1983) Dental Morphology: an illustrated guide. Butterworth-Heinemann, Wright-PSG
5. Geng JP, Xu W, Tan KBC, Liu GR (2004) Finite element analysis of an osseiointegrated stepped screw dental implant. J Oral Implantol XXX (4):223–233
6. Toms SR, Eberhardt AW (2003) A nonlinear finite element analysis of the periodontal ligament under orthodontic tooth loading. Am J Orthod Dentofacial Orthop 123:657–665
7. Malek S et al (2001) Physical properties of root cementum: part I. A new method for 3-dimensional evaluation. Am J Orthod Dentofacial Orthop 120(2):198–208

8. Chan E, Daremdeliler MA (2005) Physical properties of root cementum: part 5. Volumetric analysis of root resorption craters after application of light and heavy orthodontic forces. Am J Orthod Dentofacial Orthop 127(2):186–195
9. Angker L, Swain MV, Kilpatrick N (2003) Micro-mechanical characterisation of the properties of primary tooth dentine. J Dent 31:261–267
10. Kinney JH, Marshall SJ, Marshall GW (2003) The mechanical properties of human dentin: a critical review and re-evaluation of the dental literature. Crit Rev Oral Biol Med 14(1):13–29
11. Hasegawa A, Shinya A, Nakasone Y, Lassila LVJ, Vallittu PK, Shinya A (2010) Development of 3D CAD/FEM analysis system for natural teeth and jaw bone constructed from X-ray CT images. Int J Biomater 2010: Article ID 659802 (Hindawi Publishing Corporation)
12. Cowin SC (1989) Bone mechanics. CRC Press, Boca Raton, pp 53–55
13. Doyle JF, Phillips JW (1989) Manual on experimental stress analysis, 5th edn. Society for Experimental Mechanics, Bridgeport (Chapter 6)
14. Combe EC (1986) Notes on dental materials, 5th edn. Churchill Livingstone, Edinburgh, p 266
15. Ajovalasit A, Barone S, Petrucci G (1998) A review of automated methods for the collection and analysis of photoelastic data. J Strain Anal 33(2):75–91
16. Patterson EA, Ji W, Wang ZF (1997) On image analysis for birefringence measurements in photoelasticity. Opt Laser Eng 28:17–36
17. Burguete RL, Patterson EA (1996) Photomechanical properties of some birefringent polymers around their glass transition temperatures. Exp Mech 36(4):399–403

Chapter 10
Hierarchical Bionanomaterials Under the Hammer: High-Rate Response of Silks

D.R. Drodge, B. Mortimer, C.R. Siviour, and C. Holland

Abstract Silks are of significant interest to scientists and the public due to their high specific strength and unsurpassed toughness. The study of their properties and formulation of physically-based models is ongoing in the biomaterials community. Interesting models and simulation data are appearing in the literature but there is a paucity of experimental data at high strain-rate or high frequency. To remedy this, high strain-rate characterisation has been undertaken alongside conventional low-rate tests, under a range of conditions. The methods reported here represent large-strain, high-rate, i.e. transverse impact; and small-strain, high-rate, i.e. vibration. Both have relevance to the use of silk in nature by organisms (protection, predation and communication) and the application/imitation of silk by materials scientists. Here we report the methodology and results to date in our investigations on silkworm and orb weaver silks.

Keywords Silk • Ballistics • Wave propagation • High-speed photography • Biomaterials

10.1 Extended Abstract

Silks are protein fibres produced by a range of arthropods, principally spiders and worms. Their properties have evolved to allow them to perform a range of biological functions, ranging from protective cocoons to structural web strands [1]. The requirement for prey capture in particular has led to superior toughness being a key property of the Major Ampullate (MA) silks of orb-weaving spiders, of which the *Nephila* family is most commonly studied. The strength of silks is often stated as superlative, but this owes more to their thin diameter than material properties [2]. Toughness is of greater interest, as energy dissipation is the key selection-driving outcome if prey is to be captured without destroying the web. *Nephila* fibres boast toughness of 214 MJ m^{-3} based on the work done to fracture [2], surpassing other silks and all other known materials [3].

Silks have been characterised extensively at low strain rates using tensile testing apparatus [4], and high strain-rate testing is a relatively new instrument in the field. Recent efforts have seen basic Kolsky bar tests used to return stress–strain data [5], and more sophisticated Brillouin scatter technique used to obtain high-frequency elastic properties [6]. Experimental investigations to date reveal some information about the physics behind the real-life energy dissipation processes in silks, as deployed in webs [7]. By invoking high-rate loading conditions we can observe the degree to which material properties and air drag contribute to the response of a single thread, from which more robust interpretations of web performance may be made in the future.

Ballistic impact, first reported by Smith and colleagues [8–10], is illustrated in Fig. 10.1. The specimen is a long thread, held under tension T_0 by a suspended weight. As a projectile strikes it at velocity V, a transverse wave propagates, giving rise to the deflection seen in Fig. 10.2.

Two aspects of this image are of interest: the position of the transverse wavefront, and the curvature of the deflected region. In theory, the deflected portion should remain straight, but for fine silken fibres, the diameter is sufficiently low for air

D.R. Drodge (✉) • C.R. Siviour
Department of Engineering Science, University of Oxford, Parks Road, Oxford, OX1 3PJ, UK
e-mail: daniel.drodge@eng.ox.ac.uk

B. Mortimer • C. Holland
Department of Zoology, University of Oxford, South Parks Road, Oxford, OX1 3SP, UK

F. Barthelat et al. (eds.), *Mechanics of Biological Systems and Materials, Volume 4*,
Conference Proceedings of the Society for Experimental Mechanics Series,
DOI 10.1007/978-3-319-00777-9_10,

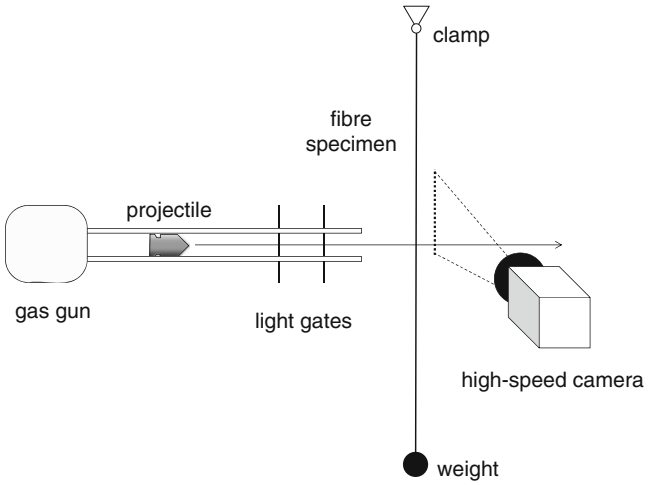

Fig. 10.1 Apparatus used for transverse impact of a fibre. Weight and projectile velocity may be varied

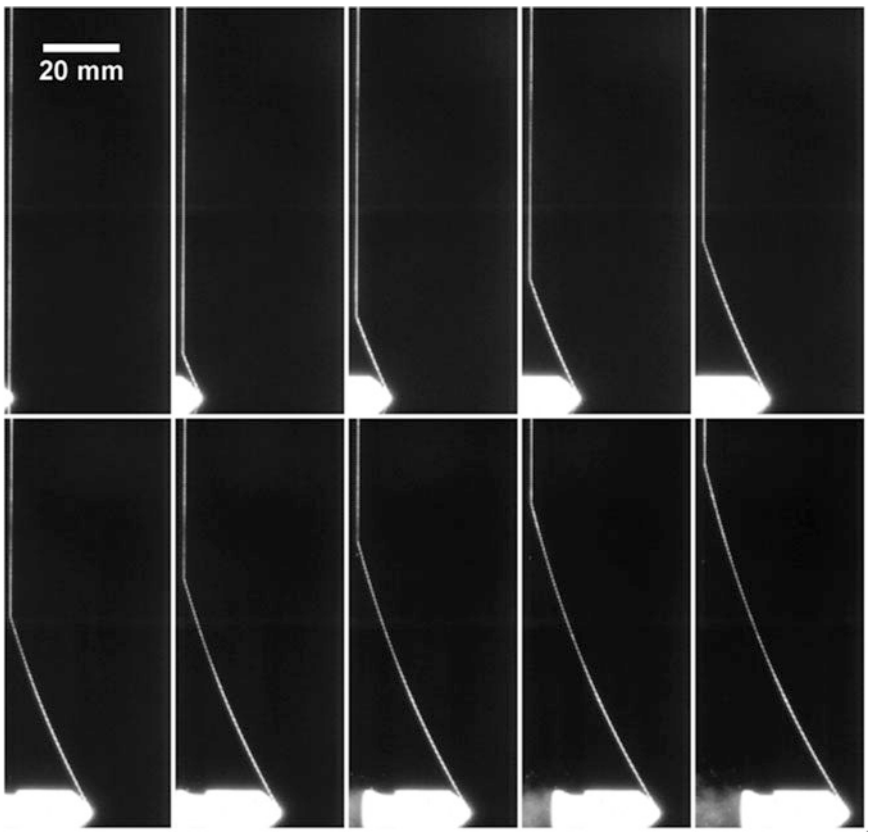

Fig. 10.2 Image sequence for transverse impact on a nylon fibre. Curvature of the thread is seen

drag to induce an effect analogous to the sagging of a cable [11]. As with this phenomenon, the curvature can be shown to be a function of the distributed transverse load on the fibre, and the axial tension. We can use this model to calculate air drag from the curvature of the thread [12].

Our analysis of the transverse wave velocity measured using this technique, and its dependence on applied tension and material constitutive response, is described in a recent paper [13].

A recent development in this project is the use of automated image processing to obtain objective estimates of transverse wavefront position and curve shape. This is illustrated in Fig. 10.3. To achieve this, background is removed prior to thresholding, and any feature wider than the silk thread is screened out, to remove the projectile and any debris. The remaining pixels, within a region of interest partly defined by the thread location in preceding frames, are used to fit a straight

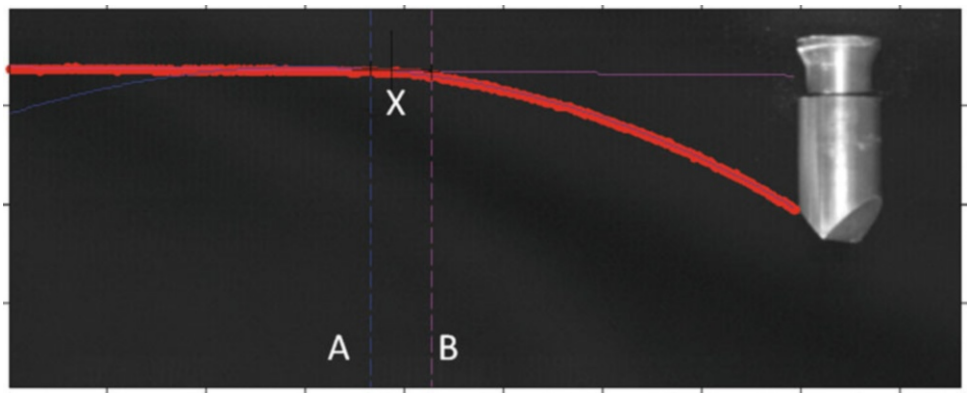

Fig. 10.3 Processed still image of impacted *Nephila* silk, showing thread pixels highlighted (*thick line*) and curve-fits to the straight and curved regions. This thread was held under 0.3 mN tension (a stress of 6.2 MPa) and struck at 110 m s^{-1}

line to the undeflected silk (to the left of marker B in the figure) and a cubic to the deflected silk (the right of marker A). The demarcation of these regions is defined as the region in which either fit fails to adequately fit the data. The midpoint is used to estimate the location for the transverse wavefront (X).

The functional forms of the thread shape, interpreted across sequential frames, provide reliable quantitative measures of curvature, allowing estimation of air drag. For example, the curved region of silk shown in frame in Fig. 10.3 has a radius of curvature ranging from 130 mm at point X to 170 mm by the projectile – this is trivially computed from the cubic fit parameters. An estimate of drag coefficient, using the inclination of the thread to calculate the cross-stream component of velocity (again, easily computed from the fit parameters), gives values of C_D ranging from 1.17 to 1.20, consistent to within 1 %. The Reynold's number of this scenario is Re ~ 100, for which a drag coefficient of around 1.2–1.4 is expected from the literature [14].

As the project progresses we anticipate being able to compare material and aerodynamic energy dissipation mechanisms in silks, and link these to the biological performance of webs.

Acknowledgements This research is supported by The Leverhulme Trust (F/08705/D), the US Air Force Office of Scientific Research (F49620-03-1-0111), the European Research Council (SP2-GA-2008-233409) and Magdalen College. Prof. David Porter and Prof. Fritz Vollrath are thanked for insightful comments and suggestions. The authors are grateful to Richard Duffin and the workshop at the Department of Engineering Science for their invaluable contributions to the design and execution of experiments.

References

1. Craig CL (Jan. 1997) Evolution of arthropod silks. Annu Rev Entomol 42(1):231–267
2. Porter D, Guan J, Vollrath F (Mar. 2013) Spider silk: super material or thin fibre? Adv Mater 25(9):1275–1279
3. Porter D, Vollrath F (Jan. 2009) Silk as a biomimetic ideal for structural polymers. Adv Mater 21(4):487–492
4. Vollrath F, Porter D, Holland C (2011) There are many more lessons still to be learned from spider silks. Soft Matter 7(20):9595
5. Hudspeth M, Nie X, Chen W, Lewis R (Aug. 2012) Effect of loading rate on mechanical properties and fracture morphology of spider silk. Biomacromolecules 13(8):2240–2246
6. Koski KJ, Akhenblit P, McKiernan K, Yarger JL (Jan. 2013) Non-invasive determination of the complete elastic moduli of spider silks. Nat Mater 12(3):262–267
7. Lin LH, Edmonds DT, Vollrath F (Jan. 1995) Structural engineering of an orb-spider's web. Nature 373(6510):146–148
8. Smith JC, McCrackin FL, Schiefer HF (Aug. 1955) Stress–strain relationships in yarns subjected to rapid impact loading: part III. Effect of wave propagation. Text Res J 25:701–708
9. Smith JC, McCrackin FL, Schiefer HF, Stone WK, Towne KM (Nov. 1956) Stress–strain relationships in yarns subjected to rapid impact loading: part IV: transverse Impact tests. Text Res J 26:821–828
10. Smith JC, McCrackin FL, Schiefer HF (Apr. 1958) Stress–strain relationships in yarns subjected to rapid impact loading: part V: wave propagation in long textile yarns impacted transversely. Text Res J 28(4):288–302
11. Smith JC, Fenstermaker CA, Shouse PJ (1964) Experimental determination of air drag on a textile yarn struck transversely by a high-velocity projectile. J Res Nat Bur Stand C 68C(3):177–193
12. Drodge DR, Mortimer B, Siviour CR, Holland C (Aug. 2012) Dynamic behaviour of silks: nature's precision nanocomposites. EPJ Web Conf 26:03007
13. Drodge DR, Mortimer B, Holland C, Siviour CR (2012) Ballistic impact to access the high-rate behaviour of individual silk fibres. J Mech Phys Solids 60(10):1710–1721
14. Sheard GJ, Hourigan K, Thompson MC (2005) Computations of the drag coefficients for low-reynolds-number flow past rings. J Fluid Mech 526:257–275

Chapter 11
A Novel Dental Restorative Composite Fabricated with Nanostructured Poly(KAMPS)/Aragonite Filler

Chad S. Korach, Matvey Sirotkin, and Ranjith Krishna Pai

Abstract A nanostructured dental restorative composite has been fabricated with a new poly(KAMPS)/aragonite filler to investigate the use of bioinspired materials in dental applications. The composite is fabricated with a common dental light activated resin and a poly(KAMPS)/aragonite filler created by biomimetic pathways and formed entirely from dilute aqueous solutions. The aragonite nanorod filler has a nanostructure with rod widths of 120 nm and polymer-filled spacings of 10–20 nm. Nanoindentation is used to characterize the mechanical properties of the novel composite. The new bioinspired composite has application as a dental restorative material.

Keywords Nanostructure • Biocomposite • Nanoindentation • Dental restoration • Bioinspired

11.1 Introduction

Advances in dental restorative techniques have allowed dental professionals to repair carious and chipped teeth in a very efficient and effective manner. The strength, hardness, wear resistance, and aesthetic properties of tooth-colored restoratives are constantly being improved. An extremely large variety of commercially available products allow dentists to tailor their material choices to each of the six classes of restorations on a by-patient basis [1, 2]. The recent rise of nanotechnology has led to many studies of nanocomposites for dental restorative applications [3, 4].

Typically, clinical dental restoratives consist of an organic epoxy resin matrix, an inorganic filler, a silane-based coupling agent, and a photoinitiator. The filler particles are dispersed in the resin matrix and are bonded to the matrix by the coupling agent [1, 2]. The photoinitiator is activated by a special light source; once activated, it initiates radical polymerization of the epoxy resin and causes the overall restorative material to harden [1]. Nanomaterials have the potential to improve all of these components [3, 4]. Here, we focus on improving the inorganic filler component with a novel bioinspired nanomaterial.

Generally, reducing filler particle size leads to an improvement in wear properties, polishability, and superficial stain resistance [1, 5]. The improvement in wear properties and polishability is due to the smaller voids left by worn filler particles [1]. Stain resistance improves due to the decreased surface roughness resulting from the increased polishability, which decreases the number of attachment nucleation sites available to typical staining culprits (i.e. coffee) [1].

Recent developments in dental nanomaterials have led to additional exciting improvements [3, 4]. For example, a calcium fluoride based nanocomposite added to restoratives as a component separate from the four listed previously aids in stress-bearing and releases fluoride ions to enrich neighboring enamel and dentin. Mitra et al. [6] report increased polish retention, glossiness, and wear resistance from nanofillers compared to hybrid macro/microfill composites. An amorphous calcium phosphate nanofiller is reported that inhibits bacterial growth, neutralizes acid, and matches the load-bearing properties of

C.S. Korach (✉) • M. Sirotkin
Department of Mechanical Engineering, Stony Brook University, Stony Brook, NY 11794, USA
e-mail: chad.korach@stonybrook.edu

R.K. Pai
International Iberian Nanotechnology Laboratory, 4715-310 Braga, Portugal

F. Barthelat et al. (eds.), *Mechanics of Biological Systems and Materials, Volume 4*,
Conference Proceedings of the Society for Experimental Mechanics Series,
DOI 10.1007/978-3-319-00777-9_11,

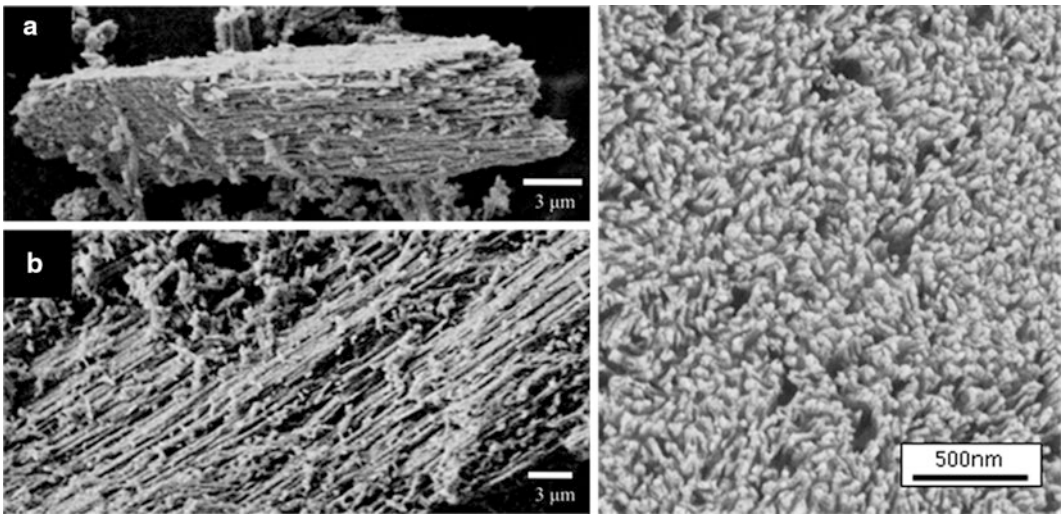

Fig. 11.1 Scanning electron micrograph of the nanofiller (*left*) showing the crystallite nanostructure; Enamel microstructure showing the hydroxyapatite crystal orientation (*right*)

typical commercial dental composites [7]. Tian et al. [8] created an aligned electrospun nylon nanofiber that can improve the mechanical properties of dental composites at a certain optimum load. Reductions in polymerization shrinkage strain have also been reported by using methacrylate and epoxy functionalized nanocomposites [3, 4].

In this paper, we report on the fabrication and mechanical property characterization of a new dental nanocomposite made with bioinspired nanofiller. The nanofiller has been previously reported [9] to have high hardness and stiffness and minimal creep, making the material an excellent candidate for a nanocomposite. Furthermore, the material has a unique nanostructure that has nanofibers of $CaCO_3$ bonded with poly(KAMPS) interlayers. The structure of the nanofiller has similarity to the hydroxyapatite (HAp) crystals found in enamel, which have orientation in the parallel direction to enamel rods (see Fig. 11.1). Similar to HAp crystals in enamel, the nanofiller has demonstrated anisotropic properties, which if harnessed using a nanoscale bottom-up approach may be able to replicate the unique mechanical properties of the enamel microstructure.

11.2 Materials and Methods

11.2.1 Nanofiller, Resin, and Preparation

The bioinspired nanofiller is synthesized via double decomposition reactions and forms a tightly packed nanostructure of aragonite nanorods with polyelectrolyte at the interfaces. Details of the synthesis can be found in [9]. The nanofiller is ground to a powder and mixed with a commercial epoxy dental resin. A light-cured hardening initator (camphorquinone) is added to the nanofilled resin. All materials are hand-mixed in the laboratory. Light curing was achieved using a 480 nm wavelength QTH light source with an intensity of 600 mW/cm^2 for 3 min to photoactivate the hardening agent. Once the nanocomposite was hardened, the sample was broken in preparation for nanoindentation.

11.2.2 Nanoindentation

All mechanical property measurements were performed by nanoindentation with a Berkovich diamond using a NanoTest nanomechanical system (Micro Materials, UK). A fused silica substrate was used to calibrate the diamond area function and machine parameters. The composite material was embedded in an epoxy resin (Buehler Epoxicure) and allowed to cure for 24 h. After curing, the molded sample was polished using a 4-step process. The indentation loading and unloading rates were

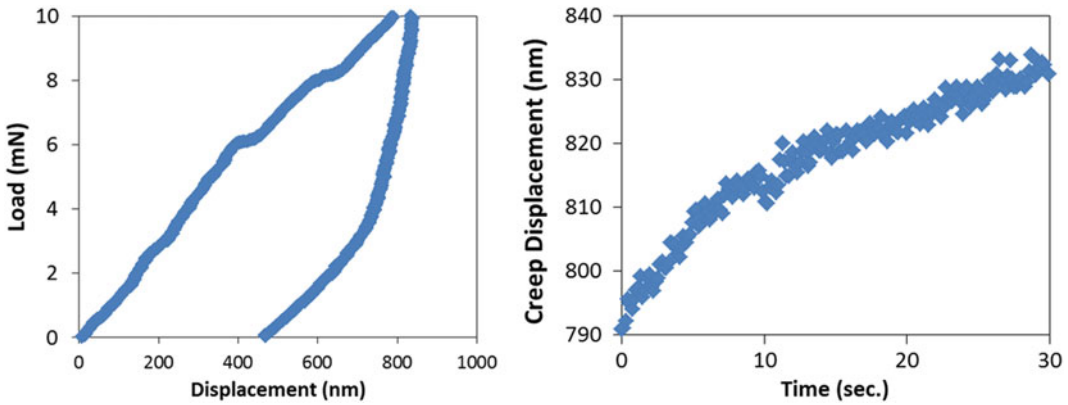

Fig. 11.2 Load versus displacement (*left*) during nanoindentation of the light-cured nanocomposite. Hardness is computed from the maximum load and plastic indentation depth; and elastic modulus from the unloading portion of the curve following the Oliver and Pharr method. Displacement data versus time (*right*) during a hold at maximum load displays material creep

0.1 mN/s, with a maximum load of 10 mN. A 30 s. hold at the maximum load is used to measure material creep effects. The slope of the initial unloading curve represents the elastic response of the material and was analyzed by the Oliver and Pharr method [10] to determine hardness and elastic modulus.

11.3 Results and Discussion

The dental nanocomposite formed from the bioinspired nanofiller and the light-cured resin and initiator combines the tough inorganic with the epoxy matrix to create a unique material for dental applications such as restorations. Nanoindentation was used to assess, at the microstructural level, material properties of the nanocomposite at multiple locations on the surface. A typical load–displacement curve from the embedded composite is shown in Fig. 11.2 (left) where maximum depths were 500–600 nm. The Oliver and Pharr method was used to analyze the load–displacement data, calculating the reduced elastic modulus (E) and hardness (H). The hardness of the nanocomposite was found to be 2.3 GPa; and the reduced elastic modulus was 23.7 GPa. The hardness values are found to be larger than those of other silica-filled nanocomposite materials which ranged from 0.25 to 0.5 GPa measured with a Knoop indenter [11]. The reduced modulus is also larger than that of epoxy resins, which are on the order of 3–5 GPa. It is hypothesized the results of the modulus and hardness have a large difference between that of silica-filled nanocomposites due to the stiff nanofiller distributed in the epoxy matrix. The indentation results provide hardness values similar to measurements on individual domains of nanofiller (cf. $H = 2.8$ GPa) [9]. This may be due to the indenter contacting the nanofiller and localized plastic deformation generated directly from this hard, stiff material. The elastic modulus of the nanofiller ($E \sim 43$ GPa) is not returned with the results of the nanoindentation. This may be due to the elastic compliance of the nanofiller within the epoxy matrix, where the indenter pushes the stiff nanofillller against the compliant matrix. The resulting elastic modulus is a composite of the nanofiller and the epoxy. A further indicator of this composite response is observed in the measurement of the creep of the nanocomposite, which was performed at a load of 10 mN. As is observed in Fig. 11.2 (right), the indentation creep was ~40 nm total over 30 s., and is similar to creep values measured for epoxy resins. The individual nanofiller domains measured previously did not exhibit creep behavior at the maximum load hold [9].

11.4 Conclusions

The novel bioinspired nanocomposite presented here is fabricated from an aragonite nanofiller and dental restorative resin. The nanocomposites were characterized by nanoindentation to assess the hardness, elastic modulus, and creep response. A composite response was found from the nanoindentation measurements that indicates plastic deformation forming in the nanofiller and an elastic response of the nanofiller inclusion within the epoxy matrix. The creep of the indentations was

similar to previously measured epoxies. This unique material created from nanostructured nanofillers thus provides a high localized hardness and a compliant bulk response that may be used as a dental restoration. Future work will look at the biocompatibility and scratch hardness of the material, which will be necessary for the long-term durability of the material in dental applications.

Acknowledgements RKP acknowledges financial support from the International Iberian Nanotechnology Laboratory (INL) in Braga, Portugal.

References

1. Albers HF (2002) Tooth-colored restoratives: principles and techniques, 9th edn. BC Decker, London
2. Powers JM, Sakaguchi RL (2006) Craig's restorative dental materials, 12th edn. Mosby-Elsevier, St. Louis
3. Chen MH (2010) Update on dental nanocomposites. J Dent Res 89(6):549–560
4. Moszner N, Klapdohr S (2004) Nanotechnology for dental composites. Int J Nanotechnol 1(1–2):130–156
5. Palaniappan S, Bharadwaj D, Mattar DL, Peumans M, Van Meerbeek B, Lambrechts P (2009) Three-year randomized clinical trial to evaluate the clinical performance and wear of a nanocomposite versus a hybrid composite. Dent Mater 25(11):1302–1314
6. Mitra Sumita B, Dong W, Holmes Brian M (2003) An application of nanotechnology in advanced dental materials. Adv Dent Mater 134:1382–1390
7. Moreau Jennifer L, Limin S, Chow Lawrence C, Xu Hockin HK (2011) Mechanical and acid neutralizing properties and bacteria inhibition of amorphous calcium phosphate dental nanocomposite. J Biomed Res Mater Part B Appl Biomater 98B(1):80–88
8. Tian M, Gao Y, Liu Y, Liao Y, Xu R, Hedin NE, Fong H (2007) Bis-GMA/TEGDMA dental composites reinforced with electrospun nylon 6 nanocomposite nanofibers containing highly aligned fibrillar silicate single crystals. Polymer 48(9):2720–2728
9. Pai RK, Zhang L, Nykpanchuk D, Cotlet M, Korach CS (2011) Biomimetic pathways for nanostructured poly(KAMPS)/aragonite composites that mimic seashell nacre. Adv Eng Mater 13(10):B415
10. Oliver WC, Pharr GM (1992) An improved technique for determining hardness and elastic modulus using load and displacement sensing indentation experiments. J Mater Res 7:1564
11. Correr AG et al (2006) Effect of exposure time vs. Irradiance on knoop hardness of dental composites. Mater Res 9(3):275–280

Chapter 12
The Effect of Dilution in Natural and Bio-inspired Staggered Composites

Seyed Mohammad Mirkhalaf Valashani and François Barthelat

Abstract The staggered structure is prominent in high-performance biological materials such as nacre, spider silk or bone. It consists of stiff and strong elongated inclusions aligned with the direction of loading. This structure leads to useful combinations of stiffness, strength and toughness, and it is therefore increasingly mimicked in bio-inspired composites. The modulus and strength of natural and bio-inspired composites are typically predicted using the shear lag model, where inclusions carry tensile stress and interfaces carry shear stresses. In this work, we have used a simple doctor blade technique to make thin film of nacre-like materials, which we tested in tension. Strength and modulus increase up to 10–15 % volume concentration of mineral reinforcement after which they degrade. Finite element analyses of staggered microstructure over a wide range of arrangement and concentrations revealed new trends which can explain the experimental results. For example the stiffness of the material can degrade in higher mineral concentrations if the tablets lack interface in the matrix. The results show that materials with combination of stiffness, strength and energy absorption can be achieved when there is an overlap between the tablets the distance between them is small in the transverse direction. This is identical with the microstructure of nacre where mineral tablets are divided by a very thin organic layer. The results suggest new approaches to simultaneously optimize modulus, strength and toughness in this class of composites.

Keywords Bio-inspired materials • Staggered composites • Biomaterials

12.1 Introduction

The staggered structure, prevalent in high-performance materials such as bone, nacre or teeth, now serves as a model for novel biomimetic composites. Nacre has come to serve as a "model material" for this structure [1], and a wide variety of fabrication approach have been explored to duplicate the structure of nacre in synthetic materials: layer by layer assembly [2, 3], freeze casting of inorganic layers followed by a polymer or a metal filling stage [4, 5], sequential Langmuir-Blodgett film/polymer deposition [6], centrifugation [7], vacuum filtration [8], sedimentation [9], ink-jet printing [10] and sputtering [11]. The most successful of these materials display interesting combinations of toughness, stiffness and strength [5, 6]. At a fixed volume concentration, the morphology and arrangement of the tablets is strongly dependant on the fabrication process, and has a significant impact on the overall performance of the composite. For examples, Bonderer et al. have reported composites fabricated from sequentially deposited self-assembled layers of the micros-sized alumina tablets and chitosan. This means that in each layer of tablets, the distance between them is small while this distance is quite high in the transverse direction [12]. They observe that the performance of the material peaks at 15 % volume concentration of tablets and decreases for higher concentration. Walther et. al. have reported composites which are fabricated from sedimentation of the nano-sized coated tablets [9], which results in composites with almost equal distance in plane and transverse directions. Meanwhile, most of the models developed for staggered natural and biomimetic materials focus on cases where the volume of tablets is very high, as in naturel nacre (95 %) [13]. How the mineral should be incorporated in the polymer matrix at lower volume concentration in order to optimize the mechanical properties is not clear. In this work a new

S.M.M. Valashani • F. Barthelat (✉)
Department of Mechanical Engineering, McGill University, Montreal, QC, Canada
e-mail: seyed.mirkhalafvalashani@mail.mcgill.ca; francois.barthelat@mcgill.ca

F. Barthelat et al. (eds.), *Mechanics of Biological Systems and Materials, Volume 4*,
Conference Proceedings of the Society for Experimental Mechanics Series,
DOI 10.1007/978-3-319-00777-9_12,

method to easily and rapidly produce nacre-like composites is presented, and the resulting materials are tested in tension. The effect of tablet arrangement on stiffness, strength and energy absorption is then explored using finite element modeling, with the ultimate goal of optimizing staggered composites over any volume concentration.

12.2 Fabrication of Alumina Chitosan Composites

Staggered composites made of chitosan matrix reinforced by alumina tablets were fabricated and tested to provide experimental references for this work. 0.1 molar solution of chitosan (Sigma Aldrich, MO, USA) from shrimp shells was prepared by adding 2.88 g of dry chitosan into 200 mLit of 2 wt% solution of acetic acid (Sigma Aldrich, MO, USA) in water. Alumina tablets (Antaria Limited, WA, Australia) with average diameter of 10.5 μm and average thickness of 0.45 μm (aspect ratio $\rho \approx 25$) were coated with APTS (3-aminopropyltriethoxysilane) and mixed into the 20 mLit of the chitosan solution following [6]. The slurry was then sonicated for 10 min to disperse the particles. This resulted in a milky suspension of tablets in the chitosan solution. This suspension was then dried with an air flow. 4 ml of milli-Q water was then added to the dried mixture and the resulting gel was stirred for several hours to prepare a uniform paste, which was then left in room temperature for one day for degasing. The thick slurry was then doctor-bladed with a spatula on a polished Teflon plate. The shear and compression forces applied onto the mixture in this process aligned the tablets in the polymer matrix resulting in a nacre-like morphology. The resulting film was dried at room temperature and was gently released from the substrate with a fresh razor blade. The process yielded a 75 mm × 20 mm × 20–30 μm films of alumina/chitosan composite (Fig. 12.1).

Figure 12.2 shows secondary electron mode SEM images of the fracture surface of the doctor-bladed alumina/chitosan composite with 10 and 20 vol% mineral concentrations, coated with a 20 nm layer of platinum. Very good dispersion of the inclusions and a high degree of alignment, resembling the structure of natural nacre is observed in the SEM pictures. The mineral concentration of the composites was measured by thermo gravimetric analysis (TGA). The TGA measurements were done with a Q500, TA instruments (DE, US) with heating rate of 20°C/min. The mass of each sample was 3–6 mgr. The carrier gas was nitrogen with flow rate of 60 mLit/min up to 550°C and then changed to air with the same flow rate. We found almost 5 wt% weight loss in temperatures below 100°C which corresponds to the evaporation of acetic acid and water. The presence of water might be necessary to maintain the deformability of the chitosan. Acetic acid also plays an important role

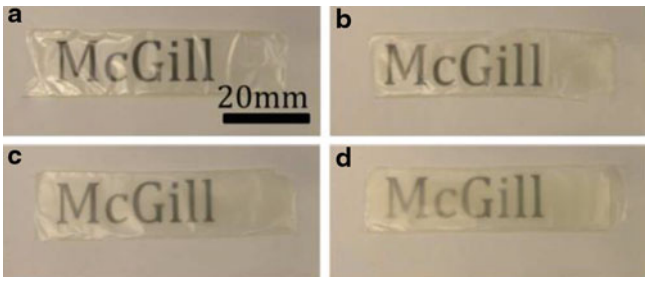

Fig. 12.1 Optical images of the composite with (**a**) 5 vol%, (**b**) 10 vol%, (**c**)15 vol%, and (**d**) 20 vol% mineral concentrations

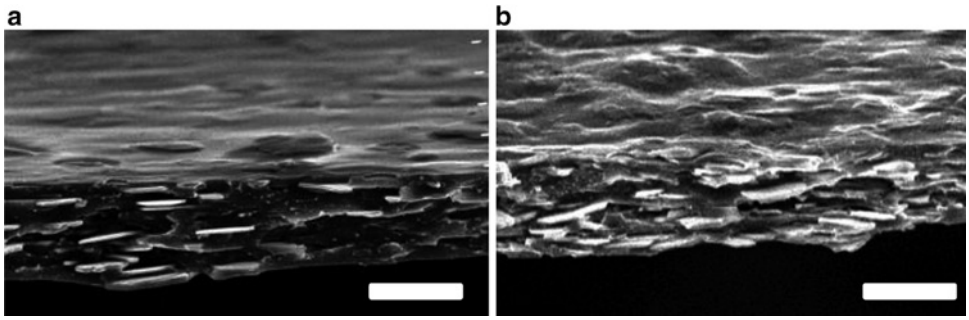

Fig. 12.2 Fracture surface images of the composite with (**a**)10 vol% alumina tablets, (**b**) 20 vol% alumina tablets (scale bar = 10 μm)

as it might favor the hydrogen bonding between the amine groups at the surfaces of coated alumina tablets and the chitosan matrix [6]. The chitosan chains were mostly thermally decomposed at 300–350 °C. The remaining carbon was then oxidized by changing the carrier gas to oxygen at 550 °C. The final remainder was alumina tablets. The results confirmed the expected mineral concentration in the composites.

12.3 Tensile Tests

Tensile dog-bone samples were cut from the composite films, and tested in tension at a strain rate of 0.5 millistrain/s using a miniature loading stage (Ernest F. Fullam, Latham, NY) and in-situ imaging of the strain gage with a digital camera. The strains were measured by digital image correlation using the commercial software VIC-2D (Correlated Solutions, SC, USA). Figure 12.3a shows the resulting tensile stress-strain curves with different concentrations of alumina tablets. For each mineral concentration, four samples were prepared and tested and the standard deviation of the stiffness and strength was found to be less than 15 %. The results show that the incorporation of 5 %, 10 % and 15 % of APTS-coated alumina micro-tablets improves the stiffness and the strength of the chitosan (Fig. 12.3b), but at the expense of ductility and energy absorption (area under the stress-strain curve). The strain however remained uniform within the gage and localization only appeared at large strains, which could be explained by the strain hardening of the chitosan matrix. All properties however degrade for tablets concentrations greater than 15 %, an observation which is consistent with Bonderer et al. [6]. This degradation could be due to imperfect arrangements of the tablets such as misalignment, clustering, or a loss of overlap between the tablets at higher mineral concentrations. The simulations presented below offer answers to some of these questions.

12.4 Simulations

In order to investigate the effect of mineral concentration, shape of the tablets, and their arrangement, 2D representative volume element (RVE) based models of the staggered microstructure were constructed using ANSYS (version 9, PA, US). The RVE was developed based on the assumption of symmetric periodic boundary conditions (Eq. 12.1, Fig. 12.4):

$$\begin{cases} u_x(0,y) = 0 \\ u_y(x,0) = 0 \\ u_x(L,y) = u_x(L,1) \\ u_y(x,1) = u_y(L,1) \end{cases} \tag{12.1}$$

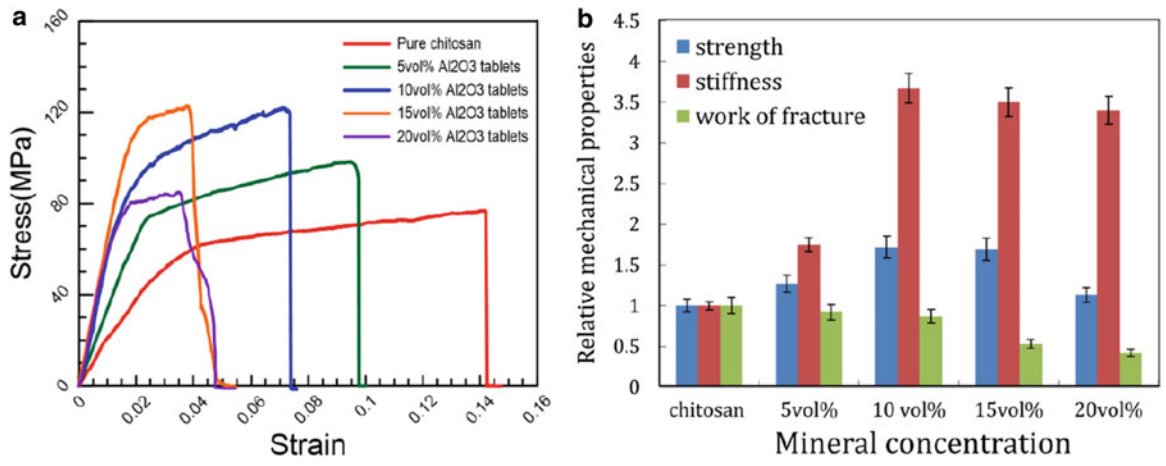

Fig. 12.3 (**a**) Tensile behavior of the composite with different mineral concentrations, (**b**) Strength, stiffness and energy absorption of the composite relative to pure chitosan

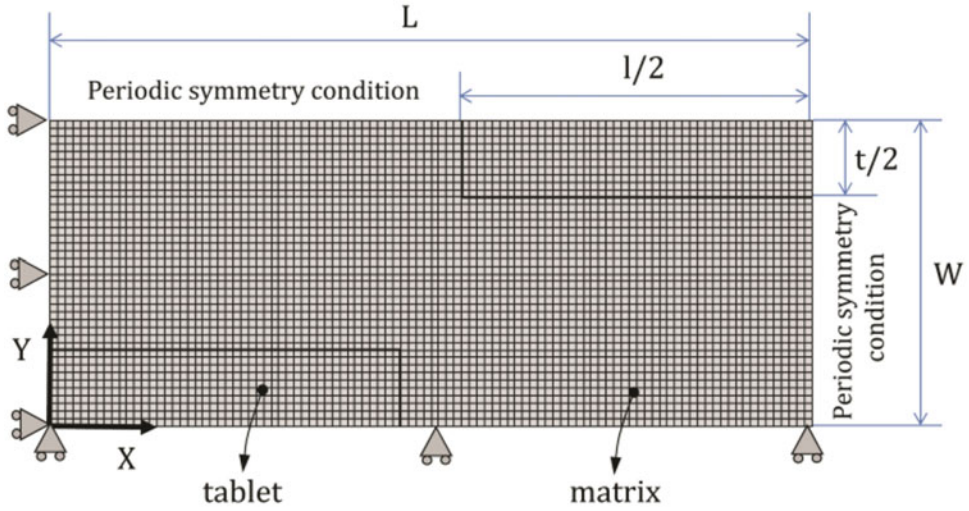

Fig. 12.4 Meshed RVE and with periodic-symmetric boundary conditions

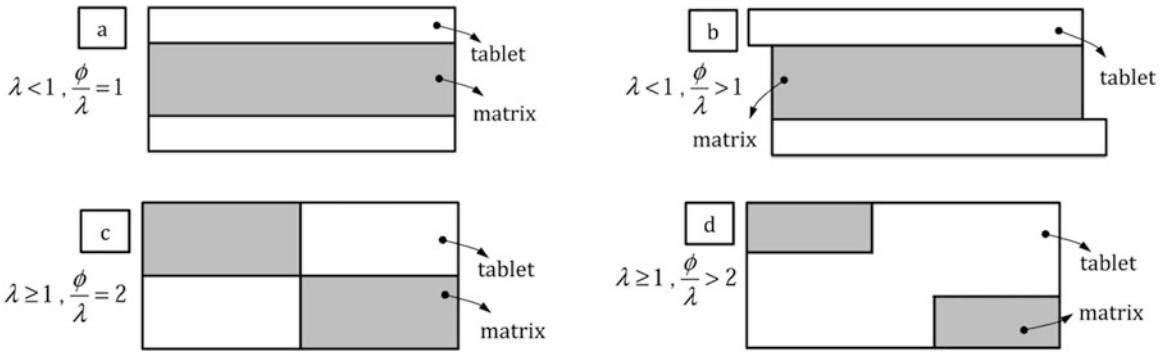

Fig. 12.5 Forbidden geometries (**a**) when $\lambda < 1$, $\frac{\phi}{\lambda} = 1$, (**b**) when $\lambda<1$, $\frac{\phi}{\lambda}>1$, (**c**) when $\lambda \geq 1$, $\frac{\phi}{\lambda} = 2$, and (**d**) when $\lambda \geq 1$, $\frac{\phi}{\lambda}>2$

As shown in Fig. 12.4, proper displacement boundary conditions were applied on the edges of the RVE to implement the symmetric and periodic conditions. Nine-node plane strain quadratic elements were used to mesh the model. The geometrical parameters for the RVE are length of the tablets l, the length of the RVE L, the thickness of the tablets t, and the width of the RVE, W (Fig. 12.4) . These four parameter were reduced to three independent dimensionless parameters: mineral concentration $\phi = \frac{1}{2}\frac{tl}{LW}$, tablet aspect ratio $\rho = \frac{t}{l}$, and ratio of the thickness of the tablets to the width of the RVE, $\lambda = \frac{t}{W}$. In the actual model the height of the RVE (W) was kept to unity since no size effect was considered.

Based on the geometry of the RVE and physics of the problem, bounds were defined for parameters ρ, ϕ, and λ. Since $\phi = \frac{1}{2}\frac{tl}{LW} = \frac{1}{2}\frac{\lambda l}{L} \rightarrow \frac{\phi}{\lambda} = \frac{1}{2}\frac{l}{L}$ and $\frac{l}{L} < 2$, only the models with $\frac{\phi}{\lambda} < 1$ are geometrically feasible. Also for $\lambda \geq 1$ (when thickness of the tablets is greater or equal to the thickness of RVE), length of the tablets must be smaller than length of the RVE to prevent mineral patches to connect to each other (Eq. 12.2). This implies:

$$\text{For}\,\lambda \geq 1, l, \text{ and we have} \begin{cases} L = 0.5\rho\dfrac{\lambda^2}{\phi} \rightarrow \dfrac{\phi}{\lambda} < 2 \\ l = \rho t = \rho\lambda \end{cases} \tag{12.2}$$

Figure 12.5 shows the RVEs which are geometrically forbidden. Figure 12.5a, b show the forbidden geometries for $\lambda<1$, and Fig. 12.5c, d show the forbidden geometries for $\lambda \geq 1$.

Equation 12.3 summarizes the physical and geometrical bonds imposed on the RVE.

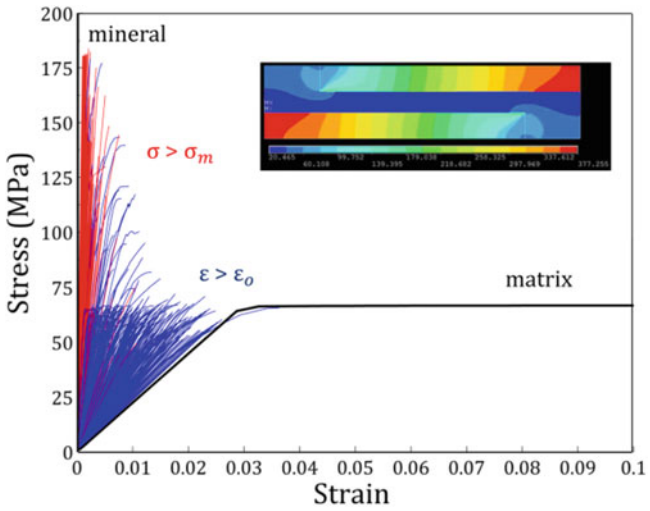

Fig. 12.6 The stress strain curves of all the staggered models

$$\begin{cases} 0 \le \phi \le 1 \\ \dfrac{\phi}{\lambda} < 1 \quad \text{if} \quad \lambda < 1 \\ 0 < \lambda < 2 \\ \dfrac{\phi}{\lambda} < 2 \quad \text{if} \quad \lambda \ge 1 \\ 0 < \rho < \infty \end{cases} \tag{12.3}$$

In the parametric exploration the following values were explored: ρ was varied from 5 to 40 by intervals of 5 (8 values). ϕ was varied from 0.1 to 0.8 by intervals of 0.1 (8 values) and λ has varied from 0.2 to 1.5 by intervals of 0.1 (14 values). This resulted in total of 896 combinations of ρ, ϕ, and λ. However, after the forbidden geometries were removed by applying the geometrical constraint (Eq. 12.3), a total of 345 models was left. The models were automatically generated and run using MATLAB (R2012a, MA, US) in combination with the ANSYS solver. The two phases (polymer/tablets) were assumed to be perfectly bonded. Following Bonderer et al. [6], an alumina-chitosan composite was modeled. The alumina tablets were modeled as linear elastic material (modulus $E_m = 330GPa$, Poisson's ratio $\upsilon = 0.2$ and tensile strength $\sigma_m = 400MPa$), and their brittle fracture was governed by a fracture criterion based on maximum tensile stress. The chitosan matrix was modeled as elastic perfectly plastic material (modulus $E_o = 1880MPa$, Poisson's ratio $\upsilon = 0.4$ and yield strength $\sigma_y = 65MPa$). A Drucker-Prager criterion with a friction angle of 20° was used to predict the yield behavior of the material. This failure criterion properly captures the effect of hydrostatic stress on yield strength, due in this case to the cavitation of the polymer under tensile stresses [14]. The failure of matrix (chitosan) was assumed to be governed by maximum tensile strain and was set at 0.5 ($\varepsilon_o = 0.5$) (We observed that the maximum local tensile strain after which the chitosan samples broke was almost 0.5). The simulation tensile stress/strain curves of the composites were cut when one of these failure criterions was satisfied whichever comes first. The mesh sensitivity analysis has also been performed and we found that the results do not change for the number of elements more than 40 in the width of the RVE. Thus the width of RVE ($W = 1$) was meshed with 40 elements and the initial length ($L_0 = 40$) was meshed with 1,600 elements. Figure 12.6 shows the stress strain curves of all the staggered models and the distribution of the maximum principal stress of one of the models ($\phi = 0.6, \lambda = 0.7, \rho = 10$) right before failure. The red curves are the ones with mineral failure and the blue ones are the ones with matrix failure. The red curves belong mostly to the composites with mineral concentrations more than 50 vol% and made of tablets with aspect ratios higher than 25. For the rest of the models, matrix failure was dominant mode of failure. Figure 12.6 also shows that the mechanical behavior of staggered composites can be manipulated and tailored to satisfy different application requirements.

Figure 12.7 shows the relative stiffness ($\frac{E}{E_o}$), relative strength ($\frac{\sigma}{\sigma_o}$) and relative energy absorption ($\frac{U}{U_o}$) as a function of mineral content ϕ, and λ, all for a fixed aspect ratio of $\rho = 25$ (the same as the average aspect ratio of the tablets in the experiments). The results suggest a transition line above which the strength of the polymer is not improved by incorporating further mineral. The level of improvement in the stiffness is also negligible compared to the materials below the line. Below this line, the strain localization is postponed and both the strength and the stiffness of the composite improve (Fig. 12.7a, b).

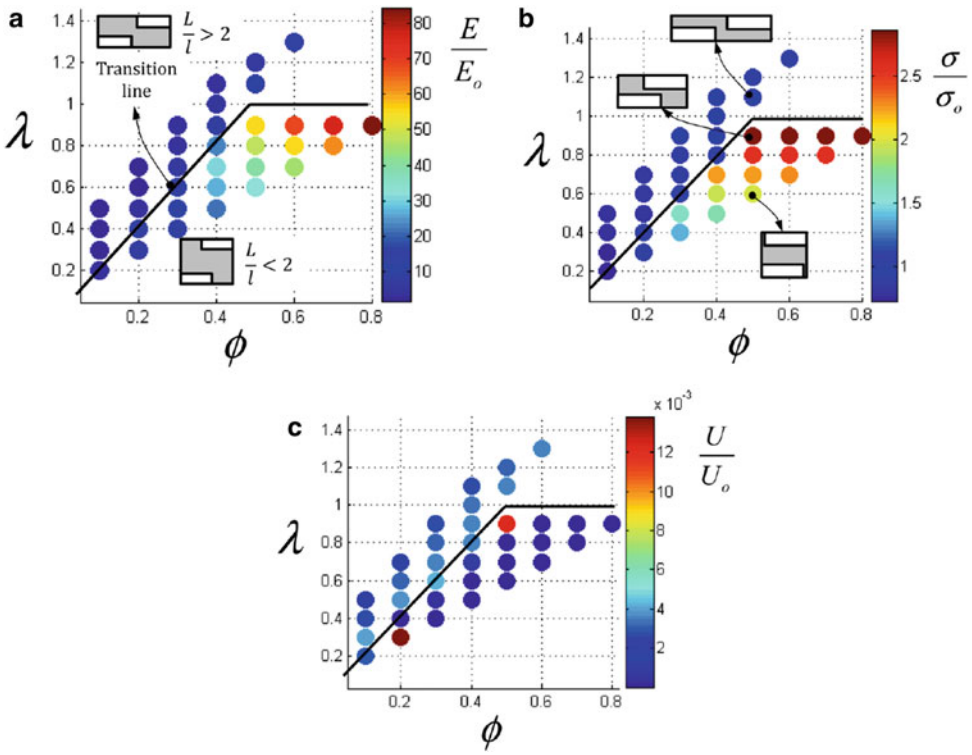

Fig. 12.7 Relative mechanical properties of the composite for $\rho = 25$; (**a**) relative stiffness, (**b**) relative strength, and (**c**) relative energy absorption

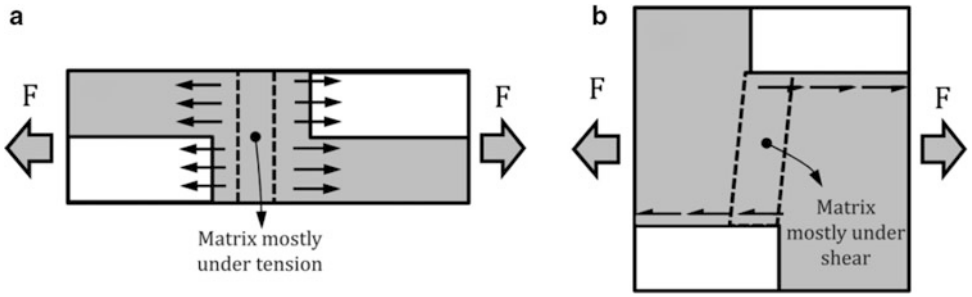

Fig. 12.8 Load transfer mechanism for materials with same mineral concentration and tablet shape but different arrangement (**a**) $\frac{L}{l} > 2$, and (**b**) $\frac{L}{l} < 2$

We found that the slope of this line for the materials with mineral concentrations below 50 vol% in the $\varphi - \lambda$ plane is 0.5. Thus, the condition for improving the strength and work fracture of the composite can be written as (Eq. 12.4):

$$\frac{\lambda}{\varphi} < 2 \rightarrow \frac{\frac{t}{W}}{\frac{1}{2}\frac{tl}{LW}} < 2 \rightarrow \frac{L}{l} < 2 \tag{12.4}$$

Figure 12.7b shows two cases where $\frac{L}{l} < 2$ and $\frac{L}{l} > 2$. The condition of $\frac{L}{l} < 2$ indicates that there should be an overlap between tablets in the polymer matrix in order to improve the strength and the stiffness of the polymer. For the materials with mineral concentrations higher than 50 vol%, the overlap is present only for $\lambda < 1$ and thus the line turns into a horizontal line at $\phi = 0.5$. Above the transition line (no overlap), the energy absorption of the material generally increases. The influence of overlap stems from the change in the load transfer mechanism from a shear-tension chain (Fig. 12.8a) where the overlap exist to a load transfer only by tensile stresses (Fig. 12.8b) where there is no overlap. This results in a significant change in the behavior of material as predicted by the model.

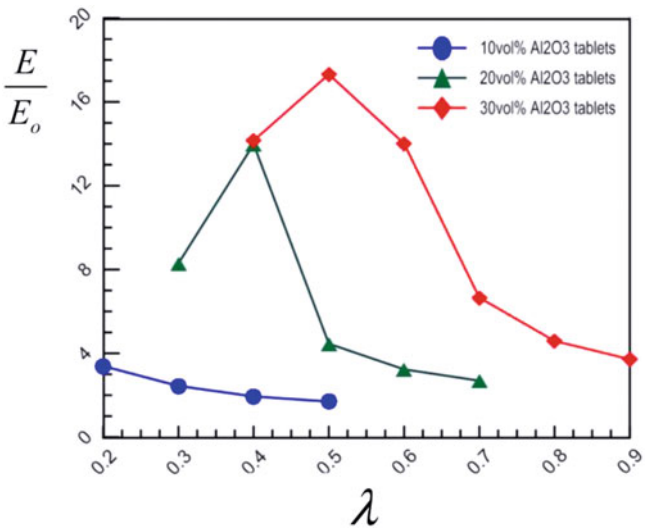

Fig. 12.9 The effect of λ on the stiffness of the material for different mineral concentrations

It is also observed that the stiffness of the composite is maximum (Fig. 12.7a) just below the transition line where the tablets overlap and concurrently have the least distance in the transverse direction. This is mainly because the shear strain imposed on a thin interface is higher compared to a thicker one at a certain average tensile strain. As a result, higher resistance to elongation is developed when the interfaces are thin. At mineral concentrations higher than 50 vol%, the least distance between the tablets in transverse direction can be achieved with λ values just below 1 which is $\lambda = 0.9$ for our simulations because of the way we discretize the problem. This small distance between tablets results in a uniform shear along the interfaces and is identical with what is observed in natural nacre [13]. Figure 12.9 shows the relative stiffness of the material as a function of λ for three different mineral concentrations (aspect ratio ρ is fixed to 25). It can be seen that for each mineral concentration, the peak value for the stiffness corresponds to λ just below the transition line. Also it can be seen the stiffness values can decrease as the mineral concentration increase if the tablets loose interface. For example the stiffness of a material with $\phi = 0.1$ and $\lambda = 0.2$ is more than the stiffness of a material with $\phi = 0.2$ and $\lambda > 0.5$. So if the processing is such that the tablets start to loose interface at higher mineral concentrations, the stiffness values start to decrease. This possibly explains why the stiffness of the doctor-bladed composites degrades for mineral concentrations higher than 10 vol%.

However, the effect of dilution on the strength is more complicated and several competing effects come into the picture. Here we discuss the possible effects of λ for the material below the transition line where the overlap exists. As the λ decreases: (i) strain non-uniformity develops in the matrix and the material start to yield at the junctions between the tablets at lower average stresses which may ultimately result in strain localization and consequently failure at lower stresses. (ii) The overlap between the tablets increases so that a larger portion of the tablets and the matrix material take part in the shear tension chain and as a result, the strength may increase if the matrix material fails before the mineral. (iii) On the other hand with increase in the overlap area, the tensile stresses increase in the tablets which lead to higher chance of tablet fracture and consequently lower strength. So the effect of dilution on the strength of the staggered composites depends on mechanical properties of ingredient particularly the ultimate tensile strength of the tablets and the deformability of the matrix material. We found that for the materials chosen for this study $\left(\frac{E_m}{E_o} = 175,\ \frac{\sigma_m}{\sigma_o} = 4,\ \text{and}\ \varepsilon_o = 0.5\right)$, the strength follows the same trends as stiffness. The highest strengths have also been achieved with models just below the transition line. Figure 12.7b shows the RVEs of three different materials with the same mineral concentration and shape of the tablets but different arrangement and their corresponding strength.

12.5 Comparison Between Simulations and Experiments

In order to compare the FEM model with the experiments, the size and arrangement of the tablets in the chitosan-alumina film were characterized with SEM images. We found an average diameter of 10.5 μm and thickness of almost 0.45 μm for the tablets ($\rho \approx 25$). The number of particles across the thickness of the film at 10 different locations was also estimated, taking

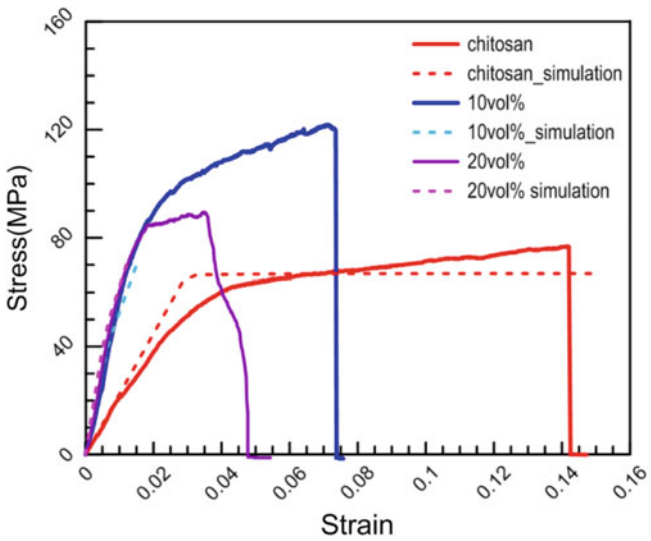

Fig. 12.10 Comparison between the simulation results and the experimental ones at mineral concentrations of 10 and 20 vol%

into account the pulled-out tablets. This number was found to be almost 4.7 tablets in a 20 μm-thick film of material with 10 vol% tablets. This number corresponds to $\lambda \approx 0.2$, the same analysis was done for the 20 vol% mineral concentration and we found $\lambda \approx 0.5$. Figure 12.10 shows the comparison between the simulation results and the experimental ones. The simulations accurately predict the stiffness of the composite. The results also suggest that the reason for slight degradation of stiffness of the composite is the loss of overlap between the tablets at mineral concentrations higher than 10 vol%. However, the model does not accurately predict the strength of the material because, in the simulations, the local strain reaches the ultimate tensile strain of the matrix material at low average strains and thus the simulations are cut before they capture the yielding and hardening in the material.

12.6 Conclusions

This study shows that very simple methods such as doctor-blading can be used to fabricate staggered composites with high level of alignment between the tablets resembling the structure of nacre. However the properties of these composites degrade for mineral concentrations more than 15 vol%. Finite element modelling was performed to explore the design space and understand the mechanism for optimizing the behavior of staggered composites with low concentration of reinforcements. The simulation results suggest that the conditions for improving the mechanical properties of the staggered composites particularly stiffness are twofold: (i) the presence of overlap between the minerals in the polymer matrix and (ii) minimum distance between the particles in transverse direction. The results also suggest that the reason for degradation of mechanical properties of the composites at higher mineral concentrations is the loss of overlap between the tablets. The comparison of the simulation results with the experimental ones show that the models can predict the stiffness of the material but underestimate its strength. The strain is localized in the models and the local strain reaches the ultimate tensile strain of the material at low average strains so that the models cannot capture the yielding behavior of the material. However, as long as the comparison between the models concerns, the models show the effect of different parameters on the performance of staggered composites.

Acknowledgments This work was supported by the Fonds de recherche du Québec – Nature et technologies and by the Natural Sciences and Engineering Research Council of Canada. SMMV was partially supported by a McGill Engineering Doctoral Award.

References

1. Barthelat F (2007) Biomimetics for next generation materials. Philos Trans R Soc Lond A 365(1861):2907–2919
2. Tang Z et al (2003) Nanostructured artificial nacre. Nat Mater 2(6):413–418
3. Podsiadlo P et al (2007) Ultrastrong and stiff layered polymer nanocomposites. Science 318(5847):80–83
4. Deville S et al (2006) Freezing as a path to build complex composites. Science 311(5760):515–518

5. Munch E et al (2008) Tough, bio-inspired hybrid materials. Science 322(5907):1516–1520
6. Bonderer LJ, Studart AR, Gauckler LJ (2008) Bioinspired design and assembly of platelet reinforced polymer films. Science 319 (5866):1069–1073
7. Almqvist N et al (1999) Methods for fabricating and characterizing a new generation of biomimetic materials. Mater Sci Eng C 7(1):37–43
8. Yao HB et al (2010) Artificial nacre-like bionanocomposite films from the self-assembly of chitosan-montmorillonite hybrid building blocks. Angew Chem Int Edit 49(52):10127–10131
9. Walther A et al (2010) Large-area, lightweight and thick biomimetic composites with superior material properties via fast, economic, and green pathways. Nano Lett 10(8):2742–2748
10. Andres CM, Kotov NA (2010) Inkjet deposition of layer-by-layer assembled films. J Am Chem Soc 132(41):14496–14502
11. He JL, Li WZ, Li HD (1997) Simulation of nacre with TiN/Pt multilayers and a study of their hardness. J Mater Res 12(11):3140–3145
12. Bonderer LJ et al (2009) Strong and ductile platelet-reinforced polymer films inspired by nature: microstructure and mechanical properties. J Mater Res 24(9):2741–2754
13. Barthelat F et al (2007) On the mechanics of mother-of-pearl: a key feature in the material hierarchical structure. J Mech Phys Solids 55(2):306–337
14. Seltzer R et al (2011) Determination of the DruckerPrager parameters of polymers exhibiting pressure-sensitive plastic behaviour by depth-sensing indentation. Int J Mech Sci 53(6):471–478

Chapter 13
New Insight into the Toughening Mechanisms of Nacre

MariAnne Sullivan and Barton C. Prorok

Abstract Many biogenic composites possess excellent mechanical properties in comparison to their abiogenic architectures (Nacre from Abalone is on the order of 3,000 times greater), which make them attractive for mechanically protective applications. The Nacre architecture has been well studied the past decade, however little work has focused on the fact that the Nacre composite is also itself a component of another composite architecture in the shells. In between thick layers of Nacre is a thin layer of an organic matrix that marks the seasonal growth patterns of the shells, analogous to tree rings. No work has focused on how these two layers interact to determine mechanical properties, which are likely as important as the tablet sliding itself. This work presents the first results in characterizing these layers.

Keywords Nacre • Mother of Pearl • Nanoindentation • Biogenic composite • Multilayer composite

13.1 Introduction

Many living organisms form biogenic minerals, or biominerals, which are composite materials containing an organic matrix and nano- or micro-scale minerals assembled in a hierarchical architecture. These biogenic composites possess excellent mechanical properties in comparison to their abiogenic architectures (some on the order of 3,000 times greater) [1–5], which make them attractive for mechanically protective applications. One biogenic material that has garnered a lot of attention is Nacre, or "Mother of Pearl," the iridescent material found on the inner surface of many Mollusk shells. Nacre is a micro-laminate composite composed of layers of organic matrix and calcium carbonate tablets (aragonite). The tablets are polygonal in shape and approximately 400–500 nm thick. They are organized in irregularly stacked columns that overlap each other, often described as stacks of coins randomly overlapping each other, see Fig. 13.1. Each tablet is covered in nano-scale asperities that help lock the tablets together. The iridescent nature of nacre has been described as various combinations of diffraction and interference [6–8].

The Nacre architecture has been well studied the past decade [1, 9–35], however little work has focused on the fact that the Nacre composite is also itself a component of another, larger-scale composite architecture in the shells. In between thick layers of Nacre is a layer of an organic matrix that marks the seasonal growth patterns of the shells, analogous to tree rings, or periods of low nutrition. Figure 13.2 illustrates this with cross-sectional shell views of a wild and farm raised samples of red abalone. The wild sample has been subjected to the seasonal environmental conditions of its natural habitat resulting in the nacreous layer containing numerous prismatic calcium carbonate layers (denoted by the numbers), whereas the farm raised sample is one large continuous block of nacre. Although the Meyers research group has recently focused on characterizing how these layers form, little to no work has focused on how these layers interact with nacre to determine mechanical properties, other than being beneficial as a crack deflection mechanism. The interplay between these layers is likely as important as the tablet sliding itself. In fact, as a qualitative observation the hammer force used to obtain these cross-sectional fracture images required six strong ball-peen hammer strikes for the wild specimen and one modest strike for the farm raised specimen. Determining this relationship would have a great impact on understanding the toughening

M. Sullivan • B.C. Prorok (✉)
Department of Mechanical Engineering, Auburn University, Auburn, AL 36849, USA
e-mail: prorok@auburn.edu

F. Barthelat et al. (eds.), *Mechanics of Biological Systems and Materials, Volume 4*,
Conference Proceedings of the Society for Experimental Mechanics Series,
DOI 10.1007/978-3-319-00777-9_13,

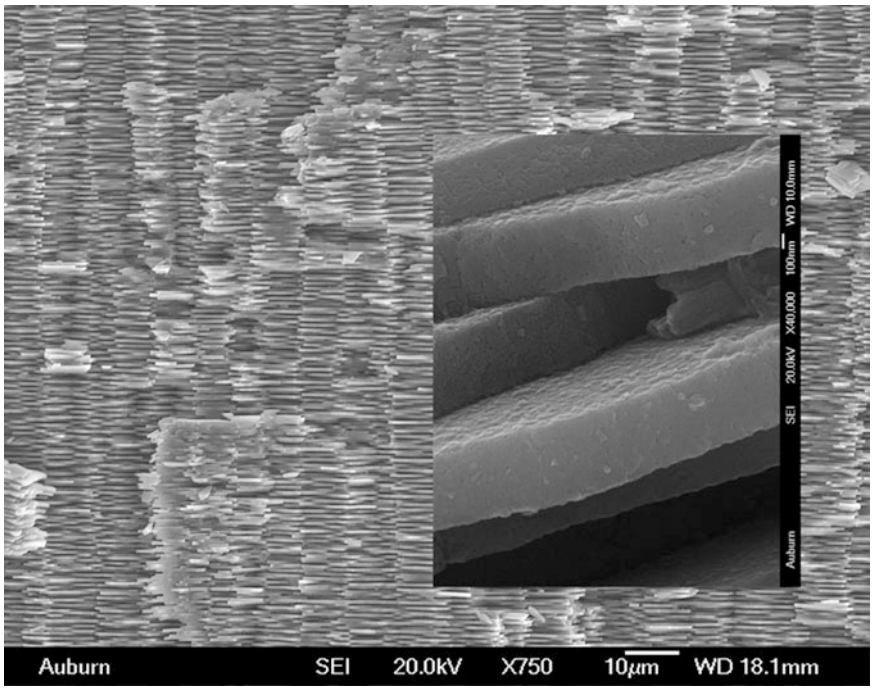

Fig. 13.1 Irregularly stacked columns of aragonite tablets of nacre of a farm raised sample

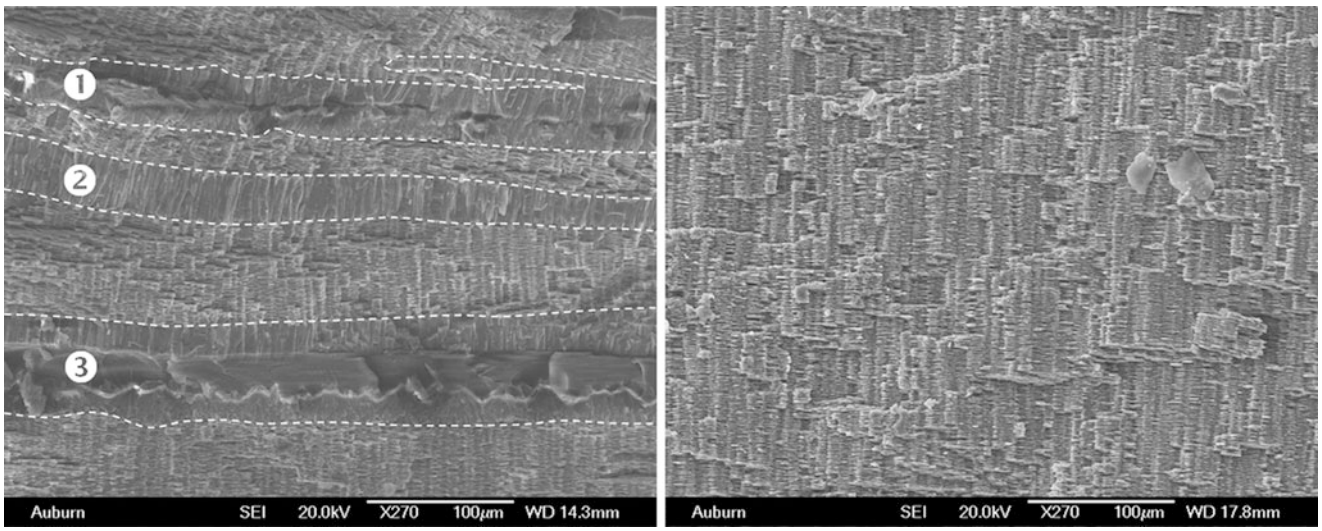

Fig. 13.2 Cross-sectional fracture images for a wild (*left*) and farm raised (*right*) red abalone. The farm raised specimen possesses interlayers that denote the seasonal growth marks of the shells or periods of low nutrition

mechanisms in mollusk shells. This information in turn can be leveraged in designing composite architectures that can improve the performance of mechanically protective coatings and armor. The aim of this proposal is to culture abalone in controlled environments such that the growth and thickness and frequency of the nacre and prismatic layers can be controlled enabling construction of predetermined composite structures. We expect to determine the optimum combination of layers that provide the best toughening properties. We also anticipate that the optimum combination may likely resemble that found in wild specimens as mollusk organisms presumably arrived at the best toughening properties via natural selection processes.

13.2 Experimental Procedure

Culturing of the abalone was performed in standard 20 gallon aquaria equipped for saltwater marine environments, see Fig. 13.3. One of the more challenging aspects of studying structure–property relationships of natural materials and tissues is that their overall structure is significantly non-uniform or irregular. This irregularity greatly complicates extracting useful material properties as structure can vary from specimen to specimen. In considering the abalone shell, extracting a representable sample of the nacre layer requires skilled sample preparation and the size of such a specimen is rather small for standard tests such as tensile testing. In this work we implanted substrates and perform nanoindentation tests to assess mechanical properties. This will enable mechanical tests to be accomplished in a stable and repeatable manner with uniformly engineered structural layers. We have leveraged techniques of others who have pioneered the implantation process [5, 17, 20, 36–39].

The purpose of the mechanical tests will be to determine the elastic modulus and Poisson's ratio of the nacre and prismatic layers as well as the composite response of the layered combinations thereof. The primary method of mechanical assessing the layered composites will be nanoindentation. There is solid rational for doing so considering the small sample size, which presents a challenge in achieving reliable and repeatable tensile or bending testing. Another aspect is that abalone shells have evolved toughening mechanisms to resist predators aiming to penetrate the shell, so a penetration based technique would be more ideal for assessing toughening mechanisms.

13.3 Results and Discussion

One of the key aspects in our work was the realization that the prismatic interlayers provide a significant amount of strength, as discussed in the introduction. These prismatic layers occur from nacre growth interuptions causes by low temperature or sustenance. Given that nutrition level and high and low temperature either slow or alter the growth process for nacre; we might expect these three conditions to result in prismatic layers with differing structure and properties as they have different physiological origins. The authors were able to initiate a growth interruption in a wild specimen using a temperature swing, illustrated in Fig. 13.4. A typical interruption starts with the formation of block-like calcite, followed by a mesolayer with high organic content, and then columnar or spherulitic aragonite before steady-state tiled nacre forms again. The literature tends to refer to these growth interruptions as prismatic layers, even though it is realized the structure varies. Their overall structure has been best detailed by the Meyers research group [37].

Fig. 13.3 Culturing Abalone in the author's lab

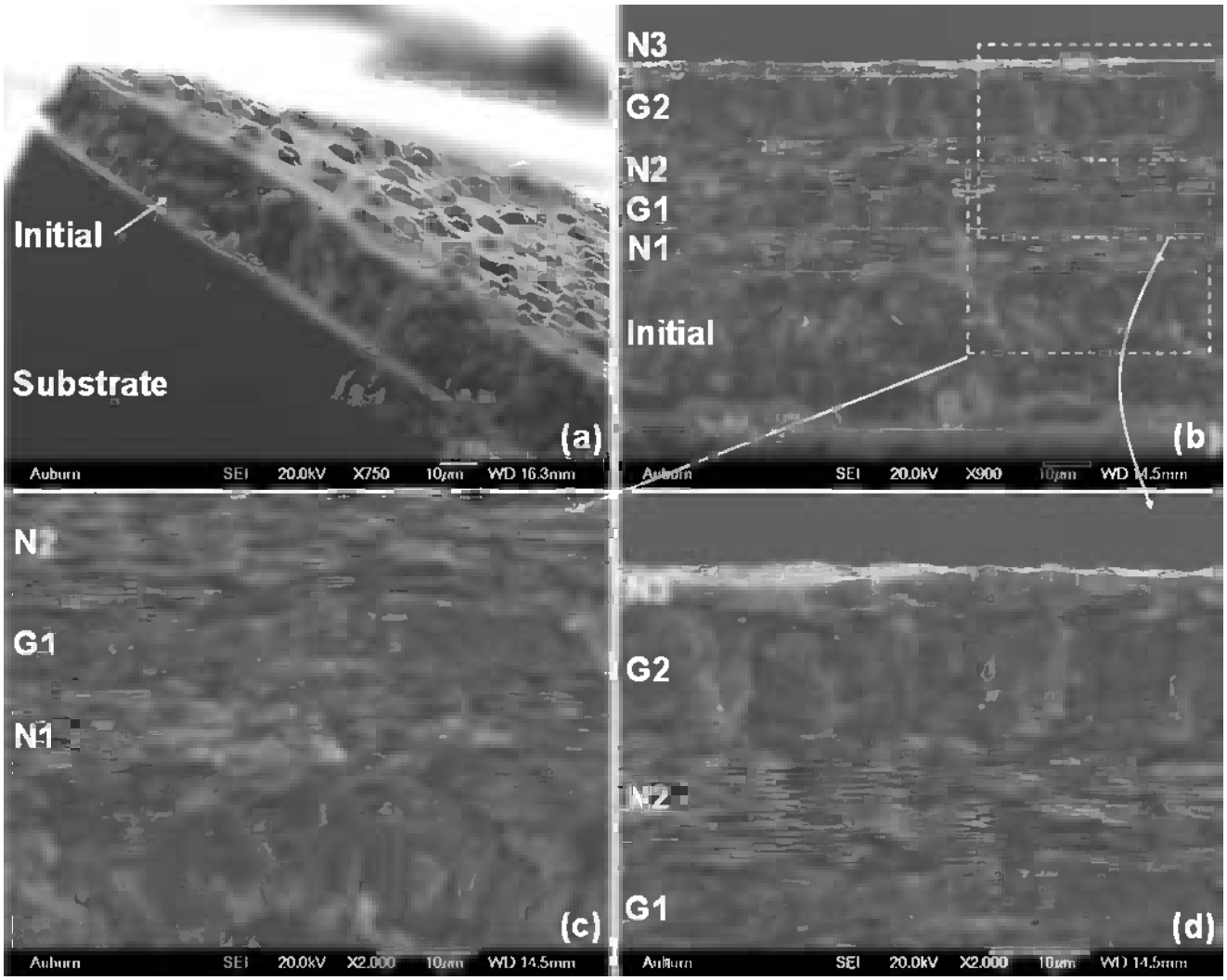

Fig. 13.4 Growth interruption layer in a wild abalone specimen from the PI's survey. Three separate prismatic-based layers are identified

Initial characterization involved indent locations directly on a tablet and at the tablet-tablet interface and assessing the modulus-depth profiles for differences. It is expected that small penetration depths will result in different values that converge to a consistent value at larger depths. These profiles will also be compared to random indent locations to determine which method is most appropriate to obtaining reliable and repeatable data. It is expected that random locations will provide the most representative data and setting up the indents in a 5 × 5 array with 200 micron spacing would best accomplish this. Given that the aim is to first assess the material properties of the different layers and then combinations of layers we will be less concerned with small penetration depths where indent location is expected to cause significant variability. Figure 13.5 illustrates this in a preliminary set of indents by the PI on farm raised nacre with a fixed 5 × 5 array. Here, the nacre layer approximately 800 microns thick and the circles represent the average value for the 25 indents. Early on there is a significant distribution of modulus values that tightens up with penetration depth. The average value though remains relatively constant even at low penetration depths. Even though the value of modulus is constant here, it is not necessarily exclusively representative of nacre. This sample was sectioned from a farm-raised abalone shell by procedures focused on keeping the nacre tablets on the surface normal to the indent axis. Thus, there is some ambiguity on how well supported the sample is as well as affects from the structural variability natural organisms possess. We are confident that our implantation and recovery technique will mitigate these issues and yield accurate elastic modulus and Poisson's ratio for nacre. Our main point in presenting this data is the reasonable consistency of results after 100–200 nm of penetration depth.

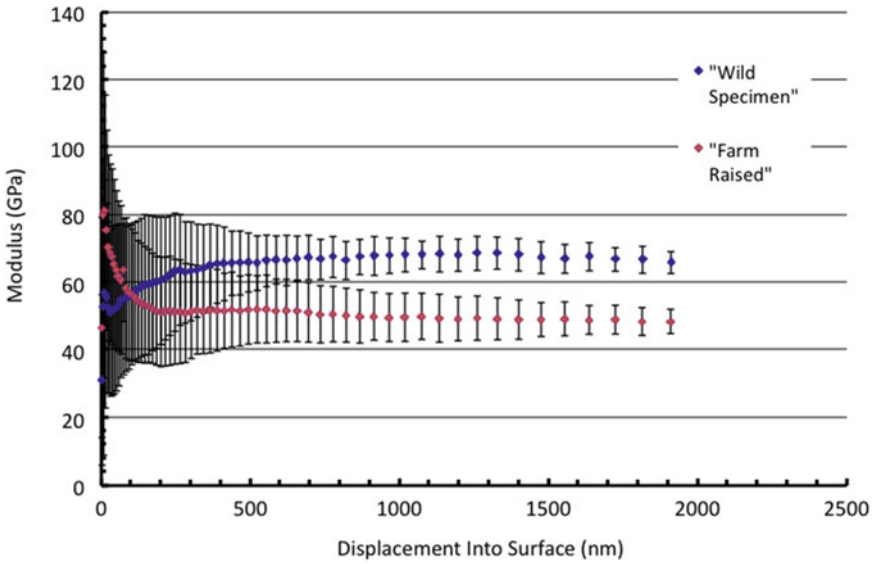

Fig. 13.5 Preliminary results of indentation testing on a farm raised specimen, elastic modulus (**a**) and hardness (**b**) The modulus appears relatively constant with indent depth while hardness varies

References

1. Belcher AM, Wu XH, Christensen RJ, Hansma PK, Stucky GD, Morse DE (1996) Control of crystal phase switching and orientation by soluble mollusc-shell proteins. Nature 381:56–58
2. Belcher AM, Margolese D, Hansma PK, Morse DE, Stucky GD (1996) Protein-inorganic assembly to form biocomposite materials. In: Abstracts of papers of the American Chemical Society, vol 212, pp 177-INOR, Aug 1996
3. Daw R (2004) Materials science – give a shell a break. Nature 427:691–691
4. Mann S, Ozin GA (1996) Synthesis of inorganic materials with complex form. Nature 382:313–318
5. Zaremba CM, Belcher AM, Fritz M, Li YL, Mann S, Hansma PK, Morse DE, Speck JS, Stucky GD (1996) Critical transitions in the biofabrication of abalone shells and flat pearls. Chem Mater 8:679–690
6. Liu Y, Shigley JE, Hurwit KN (1999) Iridescence color of a shell of the mollusk pinctada margaritifera caused by diffraction. Opt Express 4:177–182
7. Snow MR, Pring A, Self P, Losic D, Shapter J (2004) The origin of the color of pearls in iridescence from nano-composite structures of the nacre. Am Mineral 89:1353–1358
8. Wang YM, Sun CW, Lee CK, Lu CW, Tsai MT, Yang CC, Kiang YW (2004) Comparisons of the transmitted signals of time, aperture, and angle gating in biological tissues and a phantom. Opt Express 12:1157–1168
9. Barthelat F (2009) Structure and properties of mineralized tissues: the deformation and fracture of nacre from mollusc shells. Integr Comp Biol 49:E10–E10
10. Barthelat F (2010) Nacre from mollusk shells: a model for high-performance structural materials. Bioinspir Biomim 5(3):035001
11. Barthelat F, Espinosa HD (Jun 2007) An experimental investigation of deformation and fracture of nacre-mother of pearl. Exp Mech 47:311–324
12. Barthelat F, Li CM, Comi C, Espinosa HD (2006) Mechanical properties of nacre constituents and their impact on mechanical performance. J Mater Res 21:1977–1986
13. Barthelat F, Zhu DJ (2011) A novel biomimetic material duplicating the structure and mechanics of natural nacre. J Mater Res 26:1203–1215
14. Bezares J, Asaro RJ, Hawley M (2010) Macromolecular structure of the organic framework of nacre in haliotis rufescens: implications for mechanical response. J Struct Biol 170:484–500
15. Bruet BJF, Qi HJ, Boyce MC, Panas R, Tai K, Frick L, Ortiz C (2005) Nanoscale morphology and indentation of individual nacre tablets from the gastropod mollusc trochus niloticus (vol 20, pg 2400, 2005). J Mater Res 20:3157–3157
16. Dashkovskiy S, Suhr B, Tushtev K, Grathwohl G (Nov 2007) Nacre properties in the elastic range: influence of matrix incompressibility. Comp Mater Sci 41:96–106
17. Fritz M, Belcher AM, Radmacher M, Walters DA, Hansma PK, Stucky GD, Morse DE, Mann S (1994) Flat pearls from biofabrication of organized composites on inorganic substrates. Nature 371:49–51
18. Hamamoto Y, Okumura K (2009) Analytical studies on a crack in layered structures mimicking nacre. J Eng Mech-Asce 135:461–467
19. Katti KS, Mohanty B, Katti DR (2006) Nanomechanical properties of nacre. J Mater Res 21:1237–1242
20. Lin AYM, Chen PY, Meyers MA (Jan 2008) The growth of nacre in the abalone shell. Acta Biomater 4:131–138
21. Lin AYM, Meyers MA (Dec 2009) Interfacial shear strength in abalone nacre. J Mech Behav Biomed Mater 2:607–612
22. Lopez E, Milet C, Lamghari M, Mouries LP, Borzeix S, Berland S (2004) The dualism of nacre. In: Barbosa MA, Monteiro FJ, Correia R, Leon B (eds) Bioceramics, vol 16, vol 254–2, pp 733–736
23. Meyers MA, Lin AYM, Chen PY, Muyco J (2008) Mechanical strength of abalone nacre: role of the soft organic layer. J Mech Behav Biomed Mater 1:76–85
24. Mohanty B, Katti KS, Katti DR (2008) Experimental investigation of nanomechanics of the mineral-protein interface in nacre. Mech Res Commun 35:17–23

25. Nukala P, Simunovic S (2005) A continuous damage random thresholds model for simulating the fracture behavior of nacre. Biomaterials 26:6087–6098
26. Okumura K (2002) Why is nacre strong? II. Remaining mechanical weakness for cracks propagating along the sheets. Euro Phys J E 7:303–310
27. Pokroy B, Demensky V, Zolotoyabko E (2011) Inhomogeneous strain/stress profiles in the nacre layer of mollusk shells. Metall Mater Trans A Phys Metal Mater Sci 42A:554–558
28. Rabiei R, Bekah S, Barthelat F (2010) Failure mode transition in nacre and bone-like materials. Acta Biomater 6:4081–4089
29. Ren FZ, Wan XD, Ma ZH, Su JH (2009) Study on microstructure and thermodynamics of nacre in mussel shell. Mater Chem Phys 114:367–370
30. Richter BI, Kellner S, Menzel H, Behrens P, Denkena B, Ostermeier S, Hurschler C (2011) Mechanical characterization of nacre as an ideal-model for innovative new endoprosthesis materials. Arch Orthop Trauma Surg 131:191–196
31. Rousseau M, Meibom A, Geze M, Bourrat X, Angellier M, Lopez E (2009) Dynamics of sheet nacre formation in bivalves. J Struct Biol 165:190–195
32. Saruwatari K, Matsui T, Mukai H, Nagasawa H, Kogure T (2009) Nucleation and growth of aragonite crystals at the growth front of nacres in pearl oyster, pinctada fucata. Biomaterials 30:3028–3034
33. Sealy C (2008) Taking a nacre-inspired approach to composites. Mater Today 11:15–15
34. Song F, Bai YL (2001) Mineral bridges of nacre and its effects. Acta Mech Sinica 17:251–257
35. Rosen G, Langdon CJ, Evans F (2000) The nutritional value of palmaria mollis cultured under different light intensities and water exchange rates for juvenile red abalone Haliotis rufescens. Aquaculture 185:121–136
36. Lopez MI, Chen PY, McKittrick J, Meyers MA (2011) Growth of nacre in abalone: seasonal and feeding effects. Mater Sci Eng C Mater Biol Appl 31:238–245
37. Fritz M, Morse DE (1998) The formation of highly organized biogenic polymer/ceramic composite materials: the high-performance microaluminate of molluscan nacre. Curr Opin Colloid Interf Sci 3:55–62
38. Schaffer TE, IonescuZanetti C, Proksch R, Fritz M, Walters DA, Almqvist N, Zaremba CM, Belcher AM, Smith BL, Stucky GD, Morse DE, Hansma PK (1997) Does abalone nacre form by heteroepitaxial nucleation or by growth through mineral bridges? Chem Mater 9:1731–1740
39. Simkiss K, Wada K (1980) Cultured pearls – commercialized biomineralization. Endeavour 4:32–37

Chapter 14
Heterogeneity in Microscopic Residual Stress in the Aortic Wall

Takeo Matsumoto, Akihisa Fukunaga, Kengo Narita, Yohei Uno, and Kazuaki Nagayama

Abstract Aortic wall has a concentric layered structure which is a pair of relatively stiff elastic lamina (EL) and a relatively soft smooth muscle cell (SMC)-rich layer. If soft and stiff layers bear the same stress in a loaded state, tensile and compressive residual stress should appear in the soft and stiff layer, respectively, in an unloaded state. In fact, ELs are corrugated and SMCs remain stretched in an unloaded aortic wall, and ELs become straight and SMCs shrink upon isolation from the surrounding tissues. As an index of compressive residual stress, a waviness W, defined as the length along its corrugation divided by its straight length, was calculated in the sections of porcine thoracic aortas. The waviness varied widely, ranging from 1.00 to 1.35. The variation of the waviness caused wide variation of the stress borne by the ELs. For example, estimated stress was as high as 150 kPa for the ELs with $W = 1.00$, and was 0 kPa for the ELs with $W = 1.35$. The reason for the large difference in the stress in the ELs is unclear at this stage. This may be caused by local activities of the smooth muscle cells such as wall remodeling and cell division.

Keywords Artery • Elastic lamina • Lamellar unit • Remodeling • Smooth muscle cell

14.1 Introduction

It has been widely recognized that the artery wall has residual stress. For example, if you cut a ring-like segment of an aorta radially, it usually springs open to form an arc (Fig. 14.1). It has been pointed out that such opening happens because circumferential stress in the artery wall distributes uniformly in the radial direction in physiological condition, and as a result, an artery segment at no load has compressive residual stress near the inner wall and tensile near the outer as in a thick-walled cylinder [1]. The opened-up configuration is stress-free if the artery wall has homogeneous structure. Many studies have been carried out based on this assumption since 1983 when the importance of residual stress was pointed out by Vaishnav and Vossoughi for the first time [2].

However, the aortic wall shows heterogeneous morphology in a microscopic level. Aortic media has a layered structure called lamellar unit which is a pair of elastic lamina (denoted as EL in this study) composed of elastin and a smooth muscle-rich layer (denoted as SML) [3]. Elastic modulus of elastin is about 0.6 MPa [4], while that of the smooth muscle is in an order of 0.01 MPa in the relaxed state both in cellular [5, 6] and whole tissue [7] levels. Thus, the EL might be much stiffer than the SML. In fact, we examined the difference in the mechanical properties between the EL and the SML of the porcine thoracic aortas by measuring the change in thickness of the two layers during radial compression to find that the EL is about 2.5 times stiffer than SML [8].

If the ELs and SMLs have different mechanical properties, microscopic residual stress due to such difference may appear in the two layers. For example, if the ELs are stiffer than the SMLs and if the circumferential stress in the physiological state is the same for both layers as in case of aortic wall in a macroscopic level [9], compressive residual stress will appear in the stiff layer and tensile in the soft layer (Fig. 14.2a). Such residual stress is not released fully by the radial cutting, but is released in the area close to the cut surface, causing hills and valleys on the surface due to compressive and tensile stresses,

T. Matsumoto (✉) • A. Fukunaga • K. Narita • Y. Uno • K. Nagayama
Department of Mechanical Engineering, Nagoya Institute of Technology, Showa-ku, Gokiso-cho, Nagoya 466-8555, Japan
e-mail: takeo@nitech.ac.jp

F. Barthelat et al. (eds.), *Mechanics of Biological Systems and Materials, Volume 4*,
Conference Proceedings of the Society for Experimental Mechanics Series,
DOI 10.1007/978-3-319-00777-9_14,

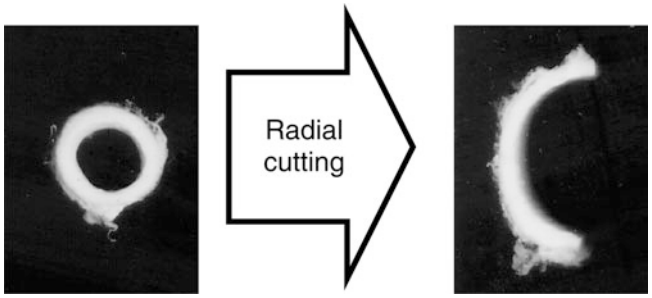

Fig. 14.1 Ring-like segments of a dog thoracic aorta before (*left*) and after (*right*) radial cutting

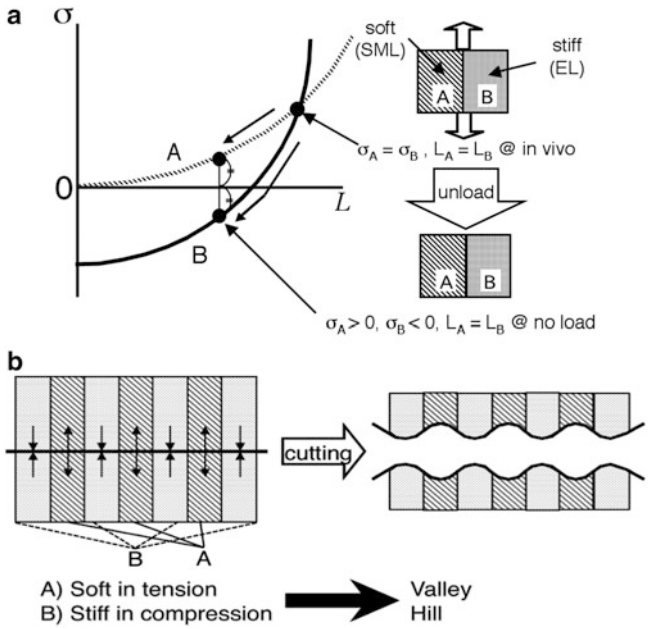

Fig. 14.2 Schematic diagram on residual stress caused by material heterogeneity (**a**) and hill and valley pattern caused by such microscopic residual stress (**b**)

respectively (Fig. 14.2b). To check this hypothesis, we recently measured the surface topography and the distribution of stiffness on the cut surface of the aortas to find that the cut surface shows hill and valley pattern [10]. We then estimated the amount of residual stress from a finite element analysis to find that the microscopic residual stress was almost comparable to that estimated in the conventional analyses (~10 kPa) [11].

Careful observation of histological sections may evidence compressive residual stress in the ELs. The ELs show concentric layers in the transversal sections of artery wall fixed under physiological condition, while they are wavy in the wall of unloaded arteries (Fig. 14.3). It is unnatural to assume that the ELs remain wavy in their stress-free state. The corrugation may indicate the buckling due to the compressive residual stress in the ELs. In fact, we found that the waviness W of the EL, i.e., the length along its corrugation divided by its straight length, decreased upon its excision from surrounding tissues (Fig. 14.4a, b) and further decreased to become almost zero after collagenase treatment to remove surrounding tissues (Fig. 14.4c).

During the course of these experiments, we noticed that there was a large variation in the waviness of the ELs. The variation of the waviness may cause wide variation of the stress borne by the ELs in a physiological condition. In this paper, we first introduce the outline of our framework to elucidate microscopic mechanical environment in the aortic walls composed of concentric layers of the SMCs and ELs and our method for estimation of stress and strain in the ELs and in the SMCs applied in the physiological states. We then report our observation of microscopic deformation of thin-sliced aortic wall specimens subjected to circumferential stretch under a microscope that was performed to check the validity of the strain estimation method. We found that deformations of the ELs and SMLs were highly heterogeneous at a microscopic level. Finally, we report our laser ablation experiment on the ELs performed to confirm the variation of stress in the ELs under the physiological condition.

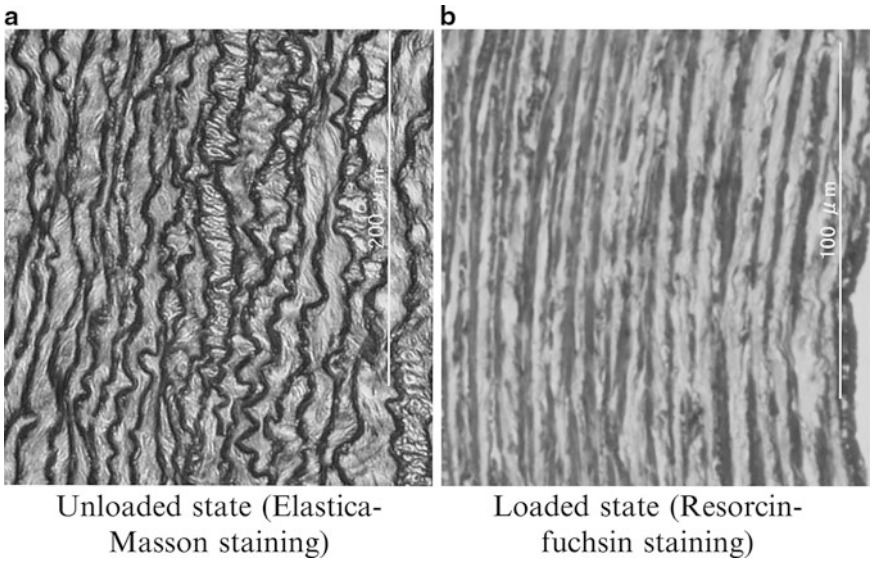

Fig. 14.3 Histological sections of rabbit thoracic aorta stained for elastic layers

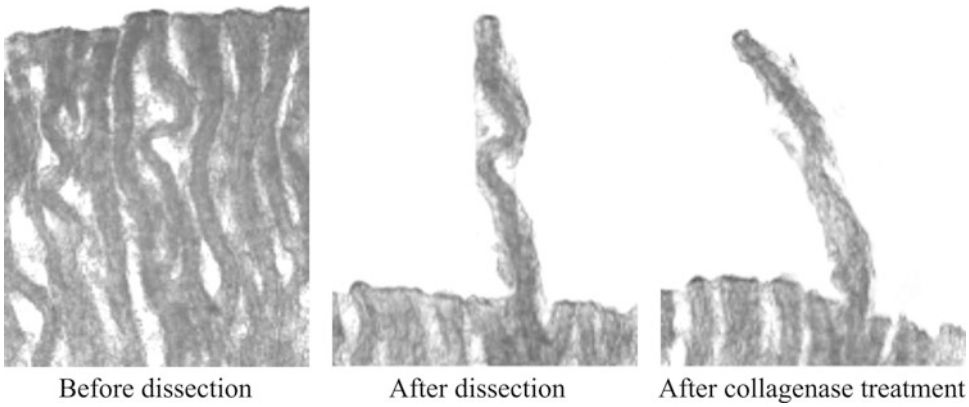

Fig. 14.4 Change in the shape of an EL of a porcine thoracic aorta following its isolation from surrounding tissues

14.2 Measurement of Microscopic Residual Strain and Tensile Properties of Aortic Wall

Porcine thoracic aortas were used as the test model. To obtain stress and strain distribution in the ELs and SMLs in a physiological state, microscopic residual strain and tensile properties were obtained for the ELs and smooth muscle cells (SMCs) separately.

ELs. Thin sections (10-μm thick) were obtained with a cryotome. An EL was identified in each section under an inverted microscope and isolated from the surrounding tissues by enzymatic digestion with a purified collagenase solution. Shape change of the EL during isolation was continuously observed to calculate the waviness W as an index of residual strain. Tensile properties of the isolated ELs were then measured with a laboratory-made micro tensile tester [6].

SMCs. The porcine thoracic aortas were sliced with a microslicer to obtain 150-μm-thick sections. Nuclei of SMCs in the wall were stained with SYTO13 to measure their length under a confocal laser scanning microscope. Then, SMCs were isolated from the sections by enzymatic digestion with collagenase and elastase. Length of the nuclei was measured again. The cells were stretched with the micro tensile tester while monitoring the shape of their nuclei to obtain cell tension-stretch ratio curve of the whole cell and the nuclei. Tension and stretch ratio when the nuclear length equals to its in situ length was used to calculate residual stress and strain in the tissue.

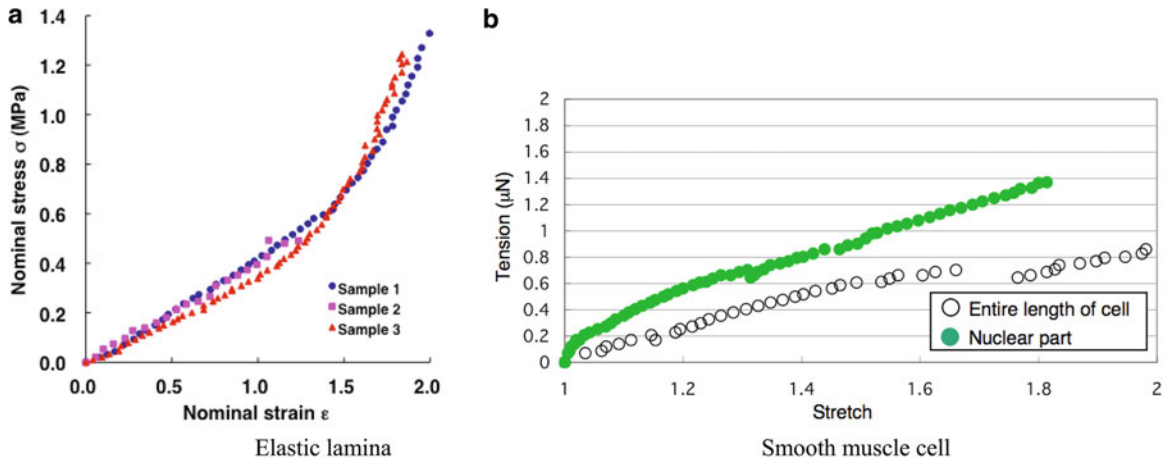

Fig. 14.5 Examples of the mechanical properties of elastic laminas (**a**) and an SMC (**b**)

The waviness of the ELs varied widely ranging from 1.00 to 1.35 with the mean value of 1.10. ELs became almost straight upon enzymatic isolation like Fig. 14.4c. Nominal stress σ_{EL}–stretch ratio λ_{EL} relation of the ELs was almost linear up to stretch ratio of 1.5 with the elastic modulus E_{EL} of 440 kPa (Fig. 14.5a). Measurement of nucleus length indicates that nuclei were stretched by 15 % in the unloaded tissue. By referring to the whole cell tension–nuclear stretch ratio and the whole cell tension–whole cell stretch ratio curves (an example is shown in Fig. 14.5b), whole cell tension when the nucleus was stretched by 15 % was found to be 0.44 mN, which corresponds to 13 kPa, and whole cell stretch ratio when whole cell tension was 0.44 mN was found to be 1.23. Thus, we found that residual stress and strain of SMCs in the tissue were 13 kPa and 23 %, respectively.

14.3 Calculation of Strain Distribution in the Aorta in Physiological States

Radial distribution of circumferential stretch ratio was calculated from pressure–diameter–longitudinal stretch ratio λ_z relationships of porcine thoracic aortas [12] as reported earlier [13] assuming homogeneity and incompressibility of the wall material. The opened-up configuration was taken as the reference state following conventional strain analysis. The opening angle that is necessary for the strain calculation was taken as 74 ± 6° (mean ± SEM, n = 11) based on our measurement. Diastolic and systolic pressures were taken as 100 and 150 mmHg, respectively, for pigs based on a previous report [14]. Since λ_z of pig thoracic aortas was unknown, circumferential stretch ratio was calculated for λ_z in a reasonable range (1.1–1.3). The macroscopic stretch ratios in the physiological states were then converted to strains of the ELs and SMCs considering residual strain of both components measured in the previous section. Microscopic stress in the ELs and SMCs in the physiological states were then obtained by referring their stress–strain relationships.

Results of macroscopic and microscopic strain analyses were summarized in Table 14.1 for typical W and λ_z. Mean circumferential stress obtained from the law of Laplace was 111 kPa in systole and 215 kPa in diastole, while local stresses were lower than the mean stress, especially in the SMCs. Theoretically, mean value of the local stresses should be equal to the mean stress. One of the reasons for this difference is that tensile test of SMCs was performed in fully relaxed cells. Maximum contraction can increase stiffness of SMCs by ~6 times [15]. Local stress applied to the SMCs might be much higher than that estimated in the present study. Another reason may be that collagen fibers whose Young's modulus is >1,000 times higher than that of the ELs were neglected in the present analysis due to technical difficulties. Although their relative amount is small, collagen fibers might bear much higher stress than the mean stress. As already mentioned in the previous section, the waviness of the ELs had a wide variation. This indicates that stress born by the ELs varies greatly due to the difference in their slack length. For example, σ_{EL} in diastole is estimated to be as high as 150 kPa for ELs remain straight in the wall (W = 1.00), and is still 0 kPa for ELs highly corrugated in the unloaded wall (W = 1.35).

Table 14.1 Summary of stress analysis ($W = 1.10$, $\lambda_z = 1.3$)

Pressure (mmHg)	Macroscopic stretch ratio λ*	Mean stress σ (kPa)	Local stress (kPa)	
			EL: σ_{EL}	SMC: σ_{SMC}
100	1.25 ~ 1.28	111	64 ~ 79	37 ~ 40
150	1.39 ~ 1.46	215	144	53 ~ 60

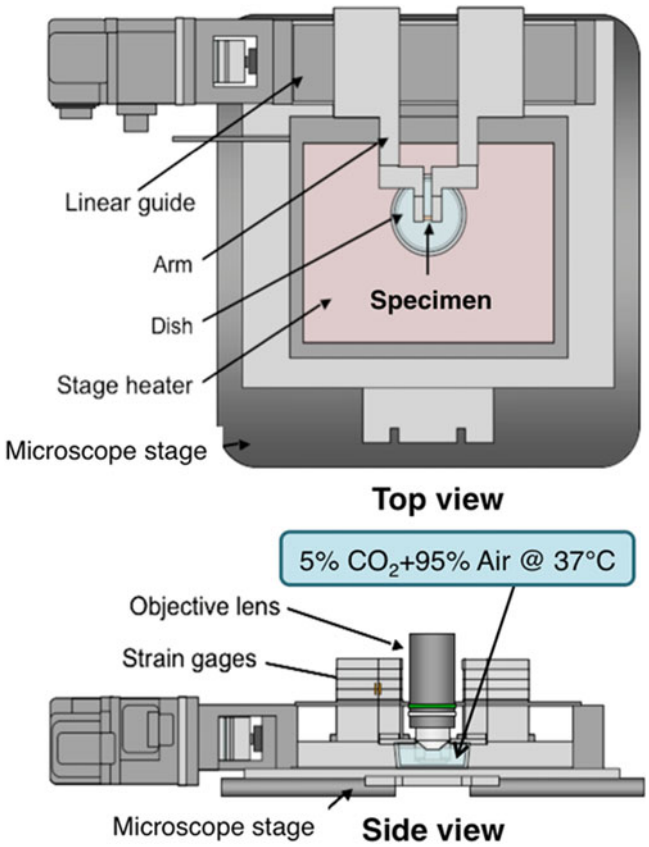

Fig. 14.6 Laboratory-made tensile tester to observe microscopic deformation of thin-sliced aortic specimens

14.4 Direct Observation of Aortic Wall Deformation at a Microscopic Level

Fifteen-μm-thick sections perpendicular to the longitudinal direction were obtained from the porcine thoracic aortas with a cryotome. They were stained with Hoechst33342 (Invitrogen) for smooth muscle cell nuclei as markers for the deformation of the SMLs. Characteristic points on the ELs were identified under a transmitted light microscope and used as markers for the deformation of the ELs. The thin slices were then stretched in the circumferential direction with a laboratory-made tensile tester (Fig. 14.6) under a microscope to observe their microscopic deformation. Local deformations of the ELs and SMLs were identified by measuring the displacement of the markers. Changes in the waviness of the ELs were also measured to evaluate the degree of straightening.

An example of changes in microscopic strain in response to circumferential stretch λ is depicted in Fig. 14.7. Microscopic strain was found to be highly heterogeneous: stretch ratio in the ELs and the SMLs was 1.1–2.3 and 1.1–2.1, respectively, at circumferential stretch ratio of 1.5. Strain difference between an EL and a SML adjacent to each other could be as high as 6 times. Shear deformation and rotation of SMCs were also observed. Basically similar results have been obtained for 200-μm-thick slices taken from fresh aorta without freezing. It was confirmed that microscopic deformation was highly heterogeneous at microscopic level. An example of change in the waviness of an EL is shown in Fig. 14.8. Change in the waviness is closer to Model 2 with no constraints from surrounding tissues, indicating that the corrugated ELs straighten first without being stretched, and they begin bearing loads after being straightened, i.e., the assumption used in the strain calculation was valid.

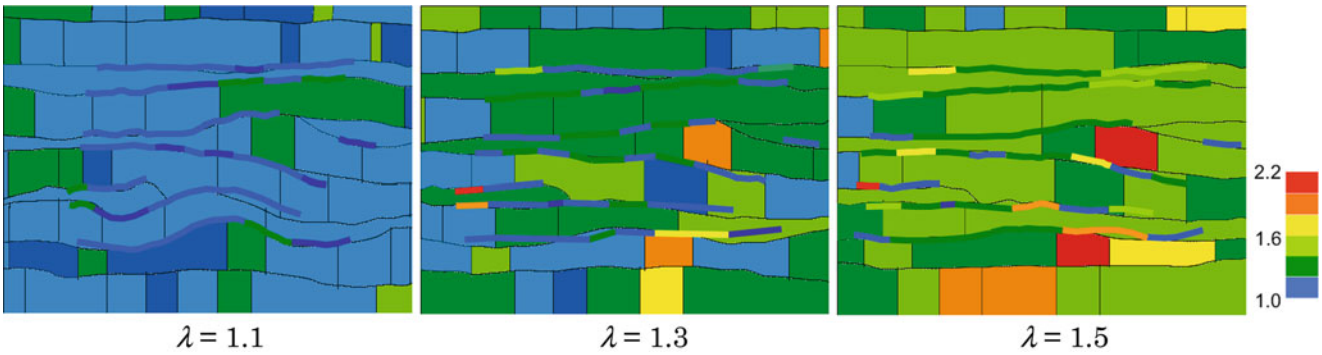

Fig. 14.7 Microscopic distribution of stretch ratios in ELs (*narrow bands*) and SMLs (*wide bands*)

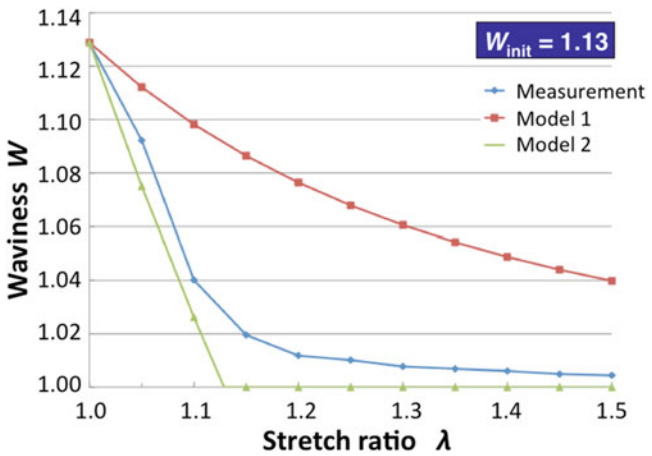

Fig. 14.8 An example of change in waviness of an EL along with model estimations. In Model 1, the EL is constrained fully from surrounding tissues just like the EL is a curve drawn on an elastic membrane being stretched. The EL has no constraints from surrounding tissues in Model 2 just like an elastic band hanging between two posts

14.5 Laser Ablation to Confirm Heterogeneity in Tension in the Elastic Laminas

To confirm the difference of the tension applied to the ELs in a physiological stretch condition predicted in the strain analysis, the thin slices were stretched in the circumferential direction by 35 % to mimic strain at systolic blood pressure, and various points on the ELs were ablated by irradiating a UV laser (Advanced Optowave; wave length, 355 nm; power, 775 mW; beam diameter, ~20 μm; pulse width, 19 ns; pulse frequency, 22.9 kHz) for 100 ms to measure the gap generated by the ablation. The length of the gap in the circumferential direction was used as an index of tension existed in that region.

As typically shown in Fig. 14.9, the gap between the ablated ends was larger in ELs with lower waviness. Cumulated data indicated that the gap had a significant negative correlation with the waviness. This result confirms that tension applied to the ELs in physiological state is heterogeneous.

14.6 Discussion

Artery walls are very interesting subject of biomechanics, because they adaptively changes their dimensions and mechanical properties in response to mechanical environment such as blood flow and blood pressure in which they are exposed. Mechanical responses of the artery walls are driven by smooth muscle cells in the media. Thus, it is very important to reveal the mechanical environment of SMCs in the artery wall in order to elucidate the mechanism of the

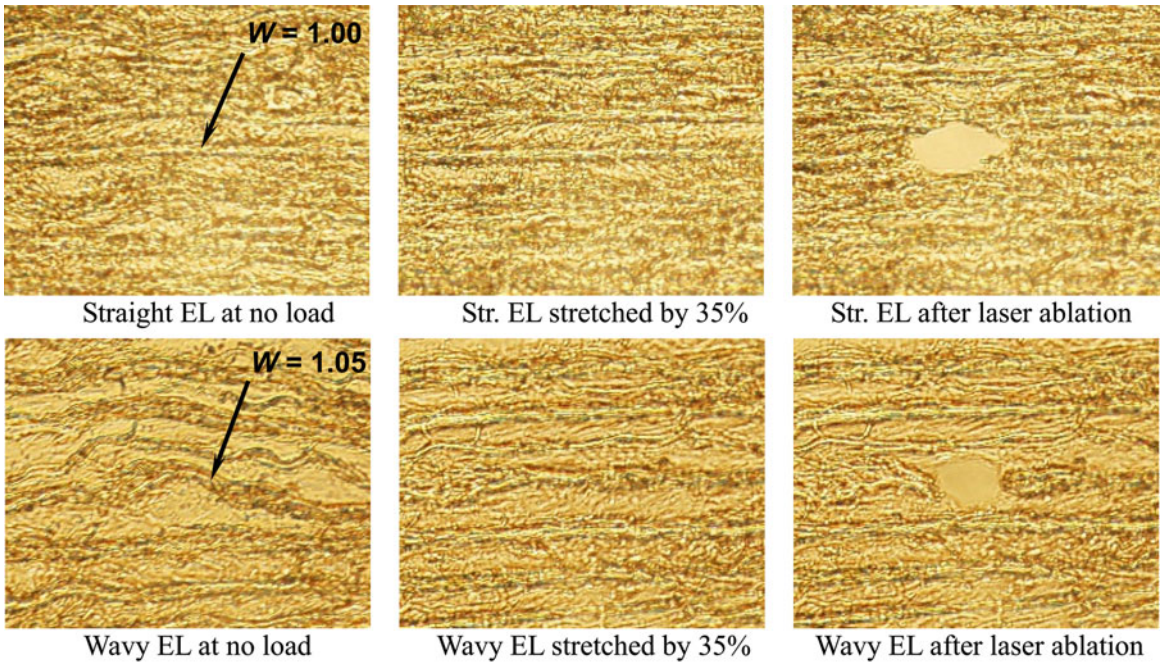

Fig. 14.9 Examples of laser ablation experiment to confirm heterogeneity in tension in ELs in physiological states

mechanical adaptation of the artery. To reveal the mechanical environment at the cellular level, we need to pay attention to microscopic structure of the artery. In case of elastic arteries, they have a concentric layered microstructure, i.e., the lamellar unit consisting of relatively stiff EL and relatively soft SML. In this study, we showed that aortic wall has microscopic residual stress caused by the difference in the stiffness of the two layers, i.e., compressive residual stress in the stiff layer and tensile stress in the soft layer. Due to such residual stresses, stresses in the two layers become equal to each other in a deformed state (Fig. 14.2a). It would be interesting if this deformed state corresponds to physiological state. However, our mechanical analysis did not support this hypothesis (Table 14.1). The mechanical analysis used in this study is simple and we need to improve it by considering smooth muscle tone and contribution of collagen fibers.

One of the most interesting findings obtained in the present study would be that the tension applied to the ELs is highly heterogeneous due to variation of their waviness. The reason for this heterogeneity remains unclear at this stage. We are speculating that this may be caused by cellular activities such as remodeling and cell division occurring regularly in the wall. However, this might also be caused by local heterogeneous alignment of smooth muscle cells. We are now planning to observe detailed structure of the aortic walls especially paying attention to the relationship between the waviness and smooth muscle alignment.

In conclusion, microscopic mechanical environment in the aortic walls is highly heterogeneous. Microscopic viewpoint is crucial to elucidate the mechanism of the mechanical adaptation and remodeling of arteries.

Acknowledgements This work was supported in part by KAKENHI (nos. 22127008 and 22240055).

References

1. Fung YC (1990) Biomechanics. Motion, flow, stress, and growth. Springer, New York, pp 382–394
2. Vaishnav RN, Vossoughi J (1983) Estimation of residual strains in aortic segments. In: Hall CW (ed) Biomedical Eegineering II, recent developments. Pergamon Press, New York, pp 330–333
3. Wolinsky H, Glagov S (1967) A lamellar unit of aortic medial structure and function in mammals. Circ Res 20:99–111
4. Fung YC (1981) Biomechanics. Springer, New York, p 202
5. Matsumoto T, Sato J, Yamamoto M, Sato M (2000) Smooth muscle cells freshly isolated from rat thoracic aortas are much stiffer than cultured bovine cells: possible effect of phenotype. JSME Int J Ser C 43:867–874
6. Nagayama K, Nagano Y, Sato M, Matsumoto T (2006) Effect of actin filament distribution on tensile properties of smooth muscle cells obtained from rat thoracic aortas. J Biomech 39:293–301

7. Whitemore RL (1968) Rheology of the circulation. Pergamon Press, Oxford
8. Matsumoto T, Goto T, Sato M (2004) Microscopic residual stress caused by the mechanical heterogeneity in the lamellar unit of the porcine thoracic aortic wall. JSME Int J Ser A 47:341–348
9. Matsumoto T, Hayashi K (1994) Mechanical and dimensional adaptation of rat aorta to hypertension. J Biomech Eng 116:278–283
10. Matsumoto T, Goto T, Furukawa T, Sato M (2004) Residual stress and strain in the lamellar unit of the porcine aorta: experiment and analysis. J Biomech 37:807–815
11. Matsumoto T, Furukawa T, Nagayama K (2006) Microscopic analysis of residual stress and strain in the aortic media considering anisotropy of smooth muscle layer. In: Holzapfel GA, Ogden RW (eds) Mechanics of biological tissue. Springer, Berlin, pp 257–268
12. Ohashi T, Abe H, Matsumoto T, Sato M (2005) Pipette aspiration method for the measurement of nonlinear and anisotropic mechanical properties of blood vessel walls under biaxial stretch. J Biomech 38:2248–2256
13. Matsumoto T, Hayashi K (1996) Analysis of stress and strain distributions in hypertensive and normotensive rat aorta considering residual strain. J Biomech Eng 118:62–73
14. Jonsson T, Ahren B, Pacini G, Sundler F, Wierup N, Steen S, Sjoberg T, Ugander M, Frostegard J, Goransson L, Lindeberg S (2006) A paleolithic diet confers higher insulin sensitivity, lower C-reactive protein and lower blood pressure than a cereal-based diet in domestic pigs. Nutr Metab 3:39
15. Matsumoto T, Nagayama K (2012) Tensile properties of vascular smooth muscle cells: bridging vascular and cellular biomechanics (review). J Biomech 45:745–755

Chapter 15
Measuring and Modeling Morphogenetic Stress in Developing Embryos

M.S. Hutson, G.W. Brodland, X. Ma, H.E. Lynch, A.K. Jayasinghe, and J. Veldhuis

Abstract The biological tissues of a developing organism are built and reshaped by intra-embryonic forces. Such morphogenetic forces can be assessed and measured similarly to residual stresses. We will discuss in vivo measurements of morphogenetic stress using two quantitative laser-microsurgery techniques. The first uses a laser to drill a sub-cellular hole in a sheet of epithelial cells. The subsequent dynamic retraction of surrounding cells allows one to infer the local mechanical stress. The second uses a laser to isolate a single cell from the rest of a cell sheet. Isolation is accomplished on a microsecond time scale by holographically shaping a single laser pulse. The subsequent retraction (or expansion) of the isolated cell allows one to separate and quantify the effects of cell-internal and cell-external stresses in the determination of cell shape. Both types of experiment are strongly supported by cell-level finite element models. We will discuss application of these techniques and models to the time-dependent biomechanics of epithelial tissues during early fruit fly embryogenesis – specifically during the processes of germband retraction and dorsal closure.

Keywords Laser ablation • Microsurgery • Morphogenesis • Dorsal closure • Finite element models

15.1 Introduction

Morphogenesis, or the development of biological form, requires the coordination of movements and shape changes in multiple cells and tissues. These movements are ultimately controlled by genetic regulatory networks, but the proximal causes are cell-generated forces. There is thus significant interest in understanding how these forces vary with space and time in living embryos – i.e., in vivo – and how these forces change when the genetic regulatory networks are mutated or manipulated. The past decade has seen strong growth in the use of laser microsurgery (also referred to as laser ablation or hole-drilling) as a means to probe these forces in vivo at cellular and subcellular scales. Although different terms are typically used to describe the results, such measurements of morphogenetic forces are variations on measurements of residual stress – ablate a cell or a small part of a cell, observe how the rest of the system relaxes, and use this information to infer the local pre-ablation stress.

The analogy to measurements of residual stress [1, 2] is however complicated by the fact that living tissues are complex physical systems that behave as active, nonlinear, viscoelastic or -plastic materials. For small deformations, the constituent

M.S. Hutson (✉)
Department of Physics & Astronomy, Vanderbilt University, Nashville, TN 37235, USA

Department of Biological Sciences, Vanderbilt University, Nashville, TN 37235, USA

Vanderbilt Institute for Integrative Biosystem Research & Education, Vanderbilt University, Nashville, TN 37235, USA
e-mail: shane.hutson@vanderbilt.edu

G.W. Brodland • J. Veldhuis
Department of Civil and Environmental Engineering, University of Waterloo, Waterloo, ON N2L 3G1, Canada

X. Ma • H.E. Lynch • A.K. Jayasinghe
Department of Physics & Astronomy, Vanderbilt University, Nashville, TN 37235, USA

F. Barthelat et al. (eds.), *Mechanics of Biological Systems and Materials, Volume 4*,
Conference Proceedings of the Society for Experimental Mechanics Series,
DOI 10.1007/978-3-319-00777-9_15,

cells act in a viscoelastic manner, but the physical properties of a particular cell type change as the cells conditionally reorganize their cytoskeleton. Thus, the mechanical properties of cells and tissues can change during a developmental event [3], can differ between in vivo conditions and in cell culture (in vitro), and even depend sensitively upon the in vitro substrate on which they grow [4]. For larger deformations, cells can individually deform plastically and can rearrange their connections to other cells, yielding large plastic deformations of tissues. All of these characteristics introduce important caveats (discussed below) for the interpretation and modeling of laser microsurgery studies in living biological tissues.

15.2 Hole-Drilling Experiments in *Drosophila* Embryos

The biological system in which laser microsurgery has been used most extensively is the common fruit fly *Drosophila melanogaster* [3, 5–15]. *Drosophila* embryos are encased in two protective shells, an outer opaque chorion and an inner transparent vitelline. The chorion is easily removed, allowing development of living *Drosophila* embryos to be followed via confocal or multiphoton microscopy using any one of a number of fluorescently labeled transgenic strains. The vitelline membrane is harder to remove without damaging the embryo, and limits direct access to embryonic tissues. Mechanical perturbations are thus best done optically.

Figure 15.1 is a schematic diagram showing the mounting of a *Drosophila* embryo for laser microsurgery experiments. This particular example represents an embryo during Bownes' stage 13 [16] that is mounted dorsal-side down. Confocal images of embryonic epithelia are normally collected *en face* as shown in Fig. 15.1a. From such images, one selects a subcellular target for ablation, and directs an automated system to steer the beam to the appropriate location and open a shutter for laser exposure [17]. Our system uses the 3rd harmonic (355 nm) of a Q-switched Nd: YAG laser (3-ns pulsewidth). When targeting a monolayer squamous epithelium like the amnioserosa, a single laser pulse at 2–3 × threshold is sufficient to ablate a 1.5-μm diameter cylinder clean through the epithelium as shown in the schematic cross-section of Fig. 15.1b. This hole corresponds to the dimensions of the laser-induced plasma, which also leaves a small hole in the embryo's vitelline membrane. Laser ablation in a fluid environment also transiently vaporizes surrounding water to generate a cavitation bubble, which expands and collapses within a few μs [6]. For near threshold pulses, these cavitation bubbles expand out to diameters <10 μm, mainly into the perivitelline fluid, and do no further damage to the targeted cells. Supra-threshold pulses can generate enormous damage.

Our group uses laser microsurgery to investigate two stages of *Drosophila* embryonic development that involve the dynamic motion of two tissues across the surface of the embryo: germband retraction and dorsal closure. At 25 °C, germband retraction begins around 7.5 h after fertilization and dorsal closure ends about 6 h later; the embryo hatches into a larva

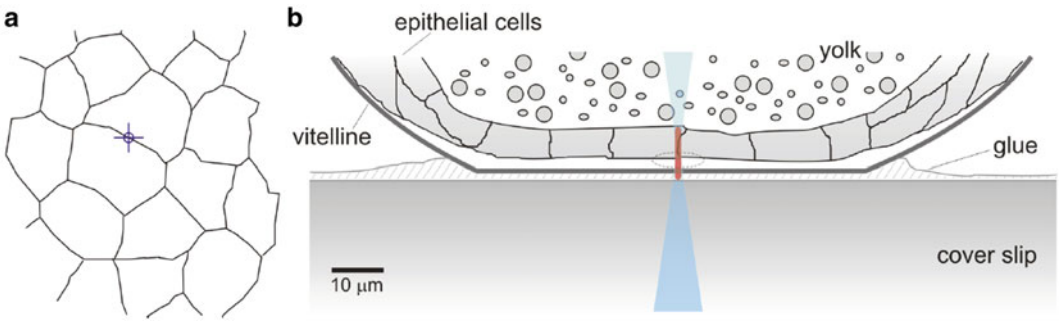

Fig. 15.1 Schematic diagram of laser hole-drilling in *Drosophila* embryos: (**a**) *en face* view of a small patch of epithelial cells (specifically amnioserosa) on the embryo surface with cross-hairs marking a cell-cell interface targeted for laser ablation; (**b**) cross-section view showing the relationship between the monolayer epithelium, over- and underlying structures and the ablating laser beam. The embryo's protective vitelline membrane is glued to a coverslip. The epithelial layer's apical surface faces a layer of perivitelline fluid. Its basal surface overlays the embryo's yolk sac. The ablating laser (*shaded blue*) propagates upwards in this schematic and is focused to a $1/e^2$ radius of ~0.75 μm just below the apical surface of the epithelial cells. A single pulse from this laser creates a cigar-shaped plasma (*shaded red*) that destroys part of the targeted cell-cell interface and leaves a small hole in the vitelline. Despite this hole, the glue layer prevents leakage of embryonic fluids. Upon recombination in the plasma, the extremely hot cylindrical region nucleates a cavitation bubble that expands out to a diameter of 6–10 μm (*dashed ellipse*) – mainly into the perivitelline fluid – and then collapses within a few μs. At 2–3 × ablation threshold, this cavitation bubble does no further damage to the epithelial cells. At higher laser pulse energies, the cavitation bubbles are much larger and can destroy large regions of the epithelium [6] (color figure in online)

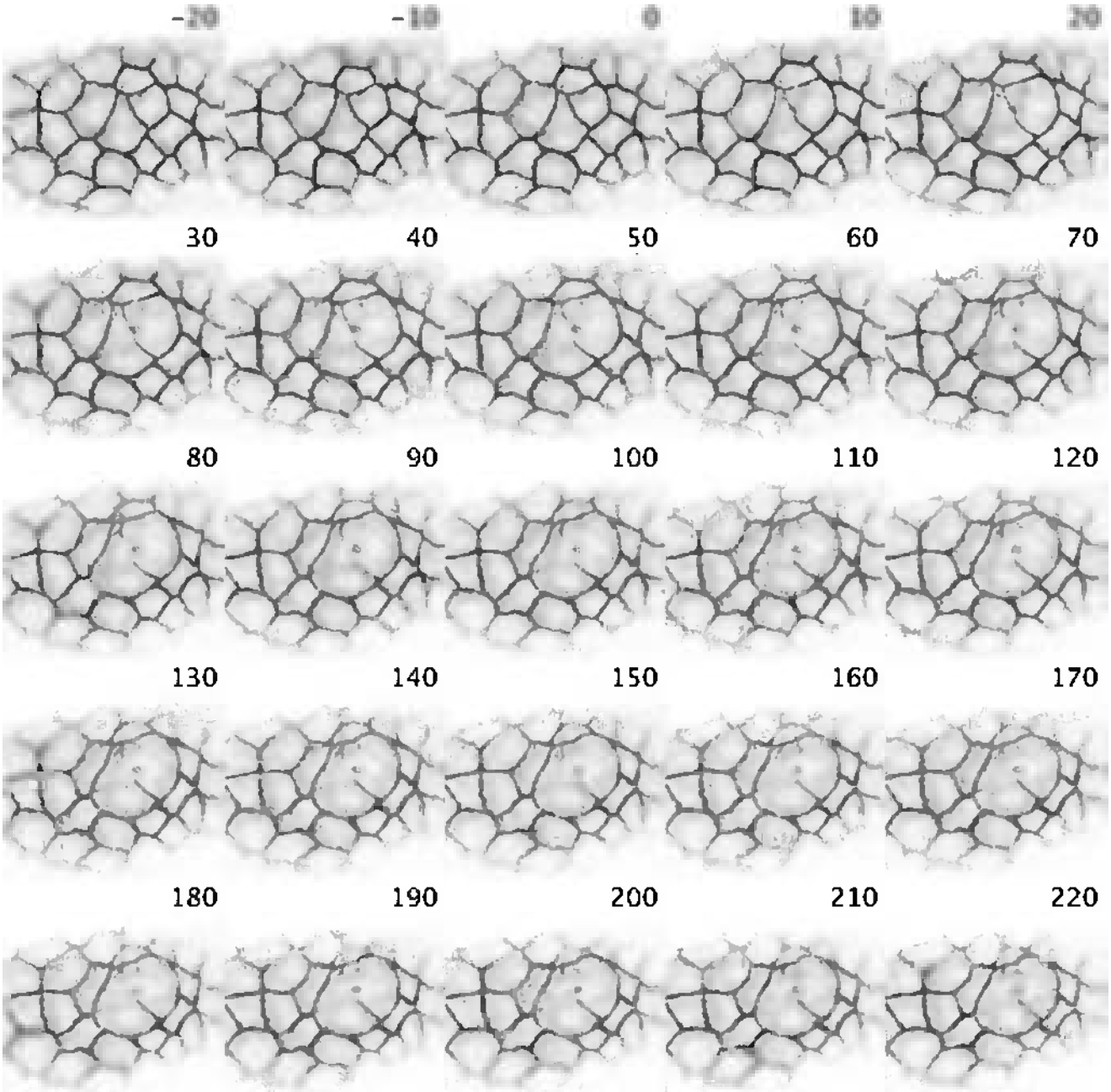

Fig. 15.2 Time-lapse confocal images of a laser hole-drilling experiment conducted on amnioserosa cells during *Drosophila* dorsal closure. The number labeling each image is the time (in seconds) before or after ablation. Ablation took place between the frames labeled $t = 0$ and 10 s, at the site marked by the stable hole in the vitelline membrane. Cell-cell interfaces were visualized using expression of GFP-E-cadherin. Note that the image gray scale has been inverted to improve print viewing. After [3]

approximately 9 h after dorsal closure ends [18]. Although much work has been done studying the relevant genetics for these stages, their mechanics are not yet fully understood. These stages also provide an accessible system to probe tissue and cell dynamics since the relevant tissues are surface epithelia.

Figure 15.2 shows an example of a laser-microsurgery experiment conducted during dorsal closure [3]. The targeted cells are those of the amnioserosa, an extra-embryonic epithelium that covers a large portion of the embryo's dorsal surface. Active contraction of these cells is a critical component of the forces that drive dorsal closure [5, 9]. The cell-cell interfaces were visualized by confocal fluorescent microscopy of a strain expressing GFP-E-cadherin. A single cell-cell interface was

ablated between the frames labeled $t = 0$ and 10 s. One can see the ablation site in subsequent frames via the stable hole left in the vitelline membrane and its surrounding hyper-fluorescent ring. The unablated sections of the targeted edge pull away from the ablation site as the surrounding cells undergo strain relaxation, demonstrating that the ablated site was under tension. The two wounded cells then reach their maximum expanded area around 60 s after ablation. After this point, the edges of these cells round up and begin to contract as wound healing commences. Within 5–10 min, the two damaged cells are extruded from the epithelium.

This example experiment highlights some of the difficulties encountered in using laser microsurgery to infer residual or morphogenetic stresses. First, the hole does not expand to a new stable equilibrium state. By the time it reaches its maximum expansion, the active process of wound healing has commenced. The surrounding cells have rearranged their cytoskeletons to accumulate both actin and myosin into a "purse-string" structure at the boundary of the wounded cells [19, 20]. Within 40–60 s after ablation, this purse-string reinforces the boundary and begins actively contracting. Inference of the pre-ablation stresses must thus rely on the initial phase of wound expansion. In practice, one tracks the displacement of one or more cellular triple junctions and fits these displacement curves with an appropriate function to extract the initial recoil velocities and strain relaxation rates. Even with this information, one cannot directly infer the pre-ablation stresses because the cells' and tissues' viscoelastic parameters are not known.

In a previous study, we conducted 179 laser hole-drilling experiments in 113 *Drosophila* embryos in both early and late dorsal closure, at sites both along and away from cell-cell interfaces [3]. From these measurements, we were able to conclude the following:

- Tensile stress is somewhat concentrated along cell-cell interfaces in early dorsal closure (1.6-fold), but is distributed uniformly in late dorsal closure;
- Amnioserosa cells have a biphasic viscoelastic response – linear at short times (<100 μs) and small displacements (1–2 μm), but power-law (exponent ~0.3–0.4) from 0.1 to 10 s after ablation; and
- This power-law exponent decreases as dorsal closure progresses, suggesting a solidification of the tissue.

Although we could not directly infer the tensile stress at either site or stage, we were able to place strong constraints that couple how the stresses, viscosity and stiffness could change. For example, the ratio of stage dependent changes in viscosity (η_{late}/η_{early}) was 0.77 ($\pm$ 0.08) times the stage-dependent change in stress along cell-cell interfaces ($\sigma_{edge,late}/\sigma_{edge,early}$). We are still investigating ways to directly measure changes in viscosity or stiffness in vivo and to thus assign absolute measures to each of the stresses.

15.3 Hole-Drilling Simulations Using Cell-Level Finite Element Models

To push further in our interpretation of laser hole-drilling experiments, we conducted simulations of post-ablation strain relaxation using cell-level finite element models [7]. These models place an active tension along each cell-cell interface, and general viscoelastic rods (a Kelvin and Maxwell element in parallel) either along the same interfaces or as a fine mesh across the entire sheet of cells. The cytoplasm of each cell is modeled as an incompressible viscous fluid and the patch of cells is subject to an applied stress that represents forces from surrounding tissues [21, 22]. Under appropriate applied stress, these finite element models can successfully reproduce the first 10 s of strain relaxation following ablation of a single cell edge, as shown in Fig. 15.3 [7]. This match occurs despite the linear nature of the model because a weak power law can be reasonably approximated over two orders of magnitude by just two exponentials.

Interestingly, the conditions under which the model matched the experiments required applied stresses that exceeded (by nearly a factor of 4) the stress generated by the active interfacial tensions. The excess applied stress was balanced by in plane, intracellular stress resultants (calculated in the model as Lagrange multipliers maintaining cytoplasmic incompressibility). This was a surprising finding and is well outside the parameter ranges used in previous finite element simulations that focused on morphogenetic processes occurring over hours [23, 24]. Interestingly, matching the experiments and models also brought us a step closer to assigning absolute mesoscopic stresses to our previous measurements. If one assumes that the viscosity of amnioserosa cells at the strain rates (1–5 s^{-1}) and length scale (1–2 μm) of our experiments matches that of sea urchin embryos under similar strain rates and length scales [25], then the mesoscopic stress in the amnioserosa increases from ~100 to ~150 Pa from early to late dorsal closure. Firmer estimates will require stage-dependent in vivo measurements of viscosity.

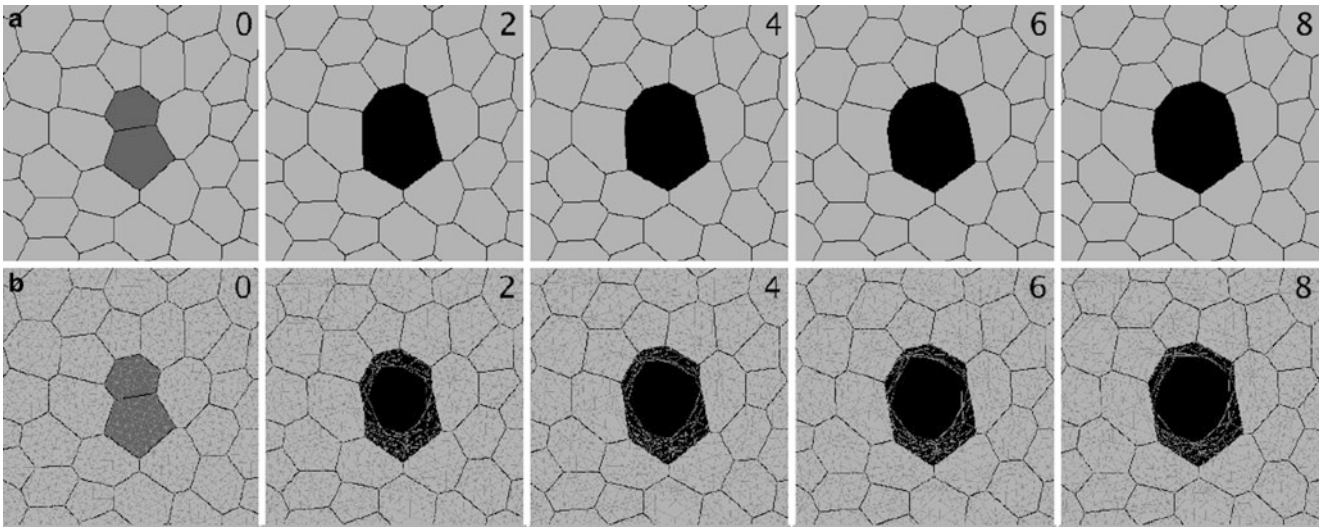

Fig. 15.3 Cell-level finite element models used to simulate strain relaxation after ablation of a single cell edge in a monolayer epithelium with viscoelastic rods along cell-cell interfaces (**a**) or with a fine mesh of viscoelastic rods across the entire cell patch (**b**). The entire modeled patch was much larger (110 cells) than the small regions shown here around each ablation site. The number labeling each panel is the corresponding experimental time in seconds. After [7].

15.4 Cell-Isolation Experiments

The information gained from hole-drilling experiments is only one side of the coin. Those experiments allow you to infer the mechanical stress that was carried by the ablated structure(s). As a complementary experiment, we'd like to measure how a single cell behaves when isolated from the surrounding epithelium. Whether its pre-ablation behavior continues unabated or not will tell us whether this behavior is cell autonomous.

To perform such experiments, we developed a new system for laser ablation based on programmable diffractive beam shaping, so-called holographic laser microsurgery [8]. This technique uses a phase-only spatial light modulator to programmably change the light's phase across the Gaussian profile of an ablating laser. This phase modification takes place in the phase plane of a microscope objective. When the ablating laser is then focused by this objective, the resulting intensity pattern is not a single Airy disk, but is a user-defined pattern of multiple spots. Given a target pattern, one can use iterative algorithms to calculate the needed phase modification [26]. With this technique, we can generate complex focused patterns (Fig. 15.4) and use patterns with up to 30 points to ablate samples (limited to avoid damaging the spatial light modulator).

We have used this technique to investigate observed dynamic oscillations in amnioserosa cells. During the early phases of dorsal closure, these cells undergo multiple cycles of contraction and expansion in apical area [10, 15, 27]. These cycles are mostly out of phase in neighboring cells and have oscillation periods around 240 s. From simple observations, it is not clear whether these oscillations are driven by autonomous cell contraction and expansion or whether cells autonomously contract, but expand due to the contractions of their neighbors.

To mechanically isolate a single amnioserosa cell, we used single holographically shaped laser pulses to ablate 5–7 pairs of closely spaced points (two per targeted cell-cell interface). An example of a cell-isolation experiment is shown in Fig. 15.5. Each pair of points generates its own local plasma and subsequent cavitation bubble. Imaging of cavitation due to similar ablation patterns in liquids suggests that these cavitation bubbles expand and touch, but they nonetheless do not strongly perturb the central isolated cell. The remarkable thing about the first image taken after ablation is how stable the isolated cell's apical surface remains. It has not been strongly perturbed by surrounding cavitation and it has not immediately collapsed – despite the fact that we know its apical surface is under tension (of order 100 Pa). In fact, when the immediate post-ablation behavior is tracked as a function of the cells' pre-ablation oscillation phase, some of the cells that were expanding just before ablation continued to expand after ablation [8, 28]. Only those cells that were contracting before ablation contracted strongly immediately afterwards. This suggests that both the contraction and expansion phases of this cycle are largely cell autonomous.

About 40 s after ablation, the isolated cell does start to collapse its apical surface. This is the same time scale on which wound healing commences after hole-drilling experiments and the same time scale on which the outer wound margin starts to round up in cell isolation experiments. This suggests that all of these behaviors are active responses of cells to changes in their mechanical environments. In fact, this eventual apical collapse can be prevented by pre-anesthetizing the fly embryos with CO_2 to eliminate active processes [28].

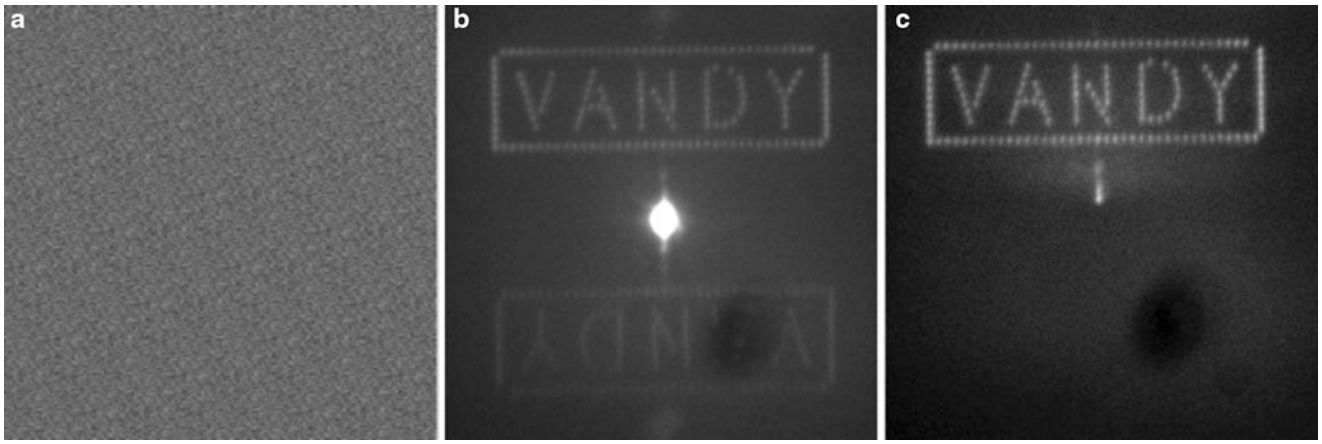

Fig. 15.4 Example of a programmed phase pattern (**a**) and focused output pattern (**b–c**). Output patterns were imaged by directing the diffracted beam onto a sheet of white paper (focused using only the microscope's tube-lens to generate a macroscopic pattern ~10-cm across). (**b**) The 1st order, 0th order and 1st negative order can be seen. (**c**) A knife-edge in an intermediate image plane is used to remove unwanted diffraction orders. The *dark area* on the *lower right* is an inhomogeneity in the paper target

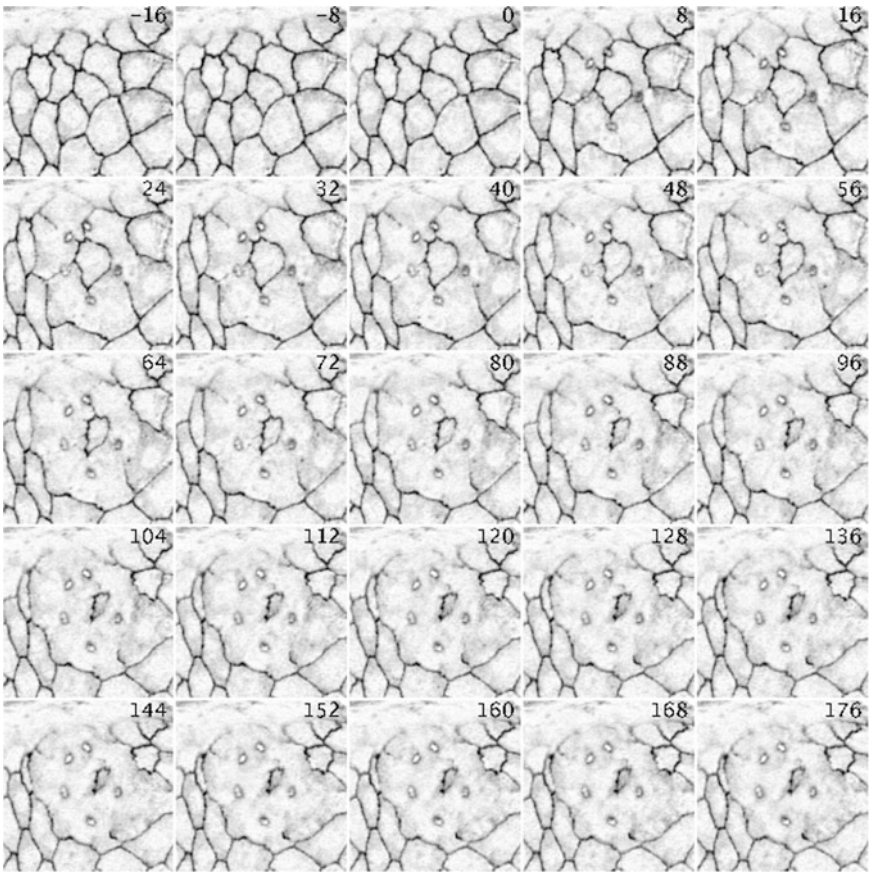

Fig. 15.5 Time-lapse confocal images of a cell-isolation experiment conducted on amnioserosa cells during *Drosophila* dorsal closure. The number labeling each image is the time (*in seconds*) before or after ablation. Ablation took place between the frames labeled $t = 0$ and 8 s, at the sites marked by stable holes in the vitelline membrane (each hole arises from two closely spaced ablation sites). Cell-cell interfaces were visualized using expression of GFP-E-cadherin. Note that the image gray scale has been inverted to improve print viewing. After [28]

15.5 Modeling Cell-Isolation Experiments

To better understand our cell-isolation experiments, we ran matching simulations using modifications of a previously published model for the oscillations [10]. This model is based on active, stretch-induced, and time-delayed contractions. The original formulation of the model does not match the experiments because it places all cell-cell interfaces under high strain in order to generate a tissue-wide tension. Our experiments and those of others have clearly shown that the amnioserosa is under tension [3, 5, 29]; however, its cell-cell interfaces are not under high strain. If the model is modified in two ways, it can match the experiments as shown in Fig. 15.6 [28]. First, the interfaces are placed under much smaller strain. This ensures that

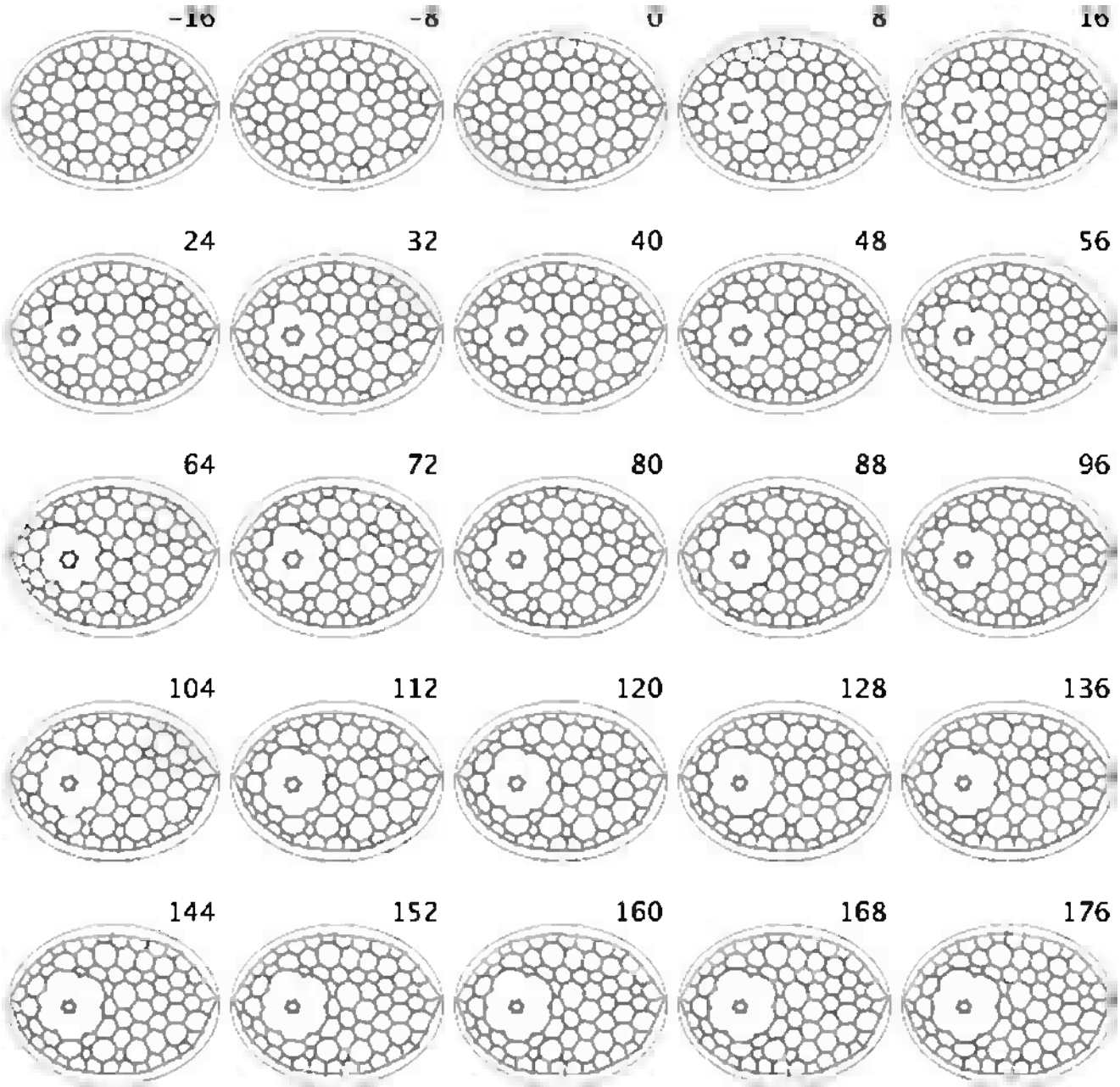

Fig. 15.6 Simulation of a cell-isolation experiment using a modification of the Solon et al. [10] model. The two modifications were placing all cell-cell interfaces under much lower strain (while maintaining tissue-wide tension) and modeling the long-term collapse of the isolated cell as an active response to a change in the cell's mechanical environment. The numbers labeling each panel represent the corresponding experimental time in seconds. Simulated ablation took place just after the frame labeled as time 0

both the contraction and expansion phases of the oscillation cycles are largely cell autonomous. Second, the long-term collapse of the isolated cell has to be modeled as an active contraction instead of the relaxation of highly stretched cell edges. These two modifications are well supported by the data and bring the models and experiments into concordance.

15.6 Conclusions

Laser microsurgery experiments, whether the drilling of a single hole or the ablation of a complex pattern that isolates a single cell, are important techniques for assessing morphogenetic stresses in living, developing embryos. They provide quantitative information as to how the forces generated by cells and the viscoelastic properties of cells change during the coordinated processes of morphogenesis. Even more information can be extracted from these experiments when complemented by appropriate model simulations. The limitations of these techniques lie in the mechanical complexity of biological tissues – active, nonlinear, viscoelastic or -plastic materials – and in our current inability to measure the relevant viscoelastic properties of tissues in vivo. These are challenges that still need to be addressed.

Acknowledgements This work supported by the National Science Foundation (IOB-0545679), the Human Frontier Science Program (RGP0021/2007C), the National Institutes of Health (1R01GM099107), the Natural Sciences and Engineering Research Council of Canada (NSERC).

Refernces

1. Schajer GS (1988) Measurement of non-uniform residual stresses using the hole-drilling method. J Eng Mater Technol Trans ASME 110:338–343
2. ASTM (2008) Standard test method for determining residual stresses by the hole-drilling strain-gage method. ASTM Standard E837-08
3. Ma X, Lynch HE, Scully PC, Hutson MS (2009) Probing embryonic tissue mechanics with laser hole-drilling. Phys Biol 6:036004
4. Yeung T, Georges PC, Flanagan LA, Marq B, Ortiz M, Funaki M, Zahir N, Ming W, Weaver V, Janmey PA (2005) Effects of substrate stiffness on cell morphology, cytoskeletal structure and adhesion. Cell Motil Cytoskeleton 60:24–34
5. Hutson MS, Tokutake Y, Chang MS, Bloor JW, Venakides S, Kiehart DP, Edwards GS (2003) Forces for morphogenesis investigated with laser microsurgery and quantitative modeling. Science 300:145–149
6. Hutson MS, Ma X (2007) Plasma and cavitation dynamics during pulsed laser microsurgery in vivo. Phys Rev Lett 99:158104
7. Hutson MS, Veldhuis J, Ma X, Lynch HE, Cranston PG, Brodland GW (2009) Combining laser microsurgery and finite element modeling to assess cell-level epithelial mechanics. Biophys J 97:3075–3085
8. Jayasinghe AK, Rohner J, Hutson MS (2011) Holographic UV laser microsurgery. Biomed Opt Expr 2:2590–2599
9. Kiehart DP, Galbraith CG, Edwards KA, Rickoll WL, Montague RA (2000) Multiple forces contribute to cell sheet morphogenesis for dorsal closure in *Drosophila*. J Cell Biol 149:471–490
10. Solon J, Kaya-Çopur A, Colombelli J, Brunner D (2009) Pulsed forces timed by a ratchet-like mechanism drive directed tissue movement during dorsal closure. Cell 137:1331–1342
11. Rauzi M, Verant P, Lecuit T, Lenne PF (2008) Nature and anisotropy of cortical forces orienting *Drosophila* tissue morphogenesis. Nat Cell Biol 10:1401–1410
12. Fernandez-Gonzalez R, Simoes Sde M, Roper JC, Eaton S, Zallen JA (2009) Myosin II dynamics are regulated by tension in intercalating cells. Dev Cell 17:736–743
13. Fernandez-Gonzalez R, Zallen JA (2011) Oscillatory behaviors and hierarchical assembly of contractile structures in intercalating cells. Phys Biol 8:045005
14. Lecuit T, Lenne PF (2007) Cell surface mechanics and the control of cell shape, tissue patterns and morphogenesis. Nat Rev Mol Cell Biol 8:633–644
15. Azevedo D, Antunes M, Prag S, Ma X, Hacker U, Brodland GW, Hutson MS, Solon J, Jacinto A (2011) DRhoGEF2 regulates cellular tension and cell pulsations in the amnioserosa during *Drosophila* dorsal closure. PLoS One 6:e23964
16. Bownes M (1975) A photographic study of development in the living embryo of *Drosophila melanogaster*. J Embryol Exp Morphol 33:789–801
17. Kiehart DP, Tokutake Y, Chang M-S, Hutson MS, Wiemann JM, Peralta XG, Toyama Y, Wells AR, Rodriguez A, Edwards GS (2006) Ultraviolet laser microbeam for dissection of *Drosophila* embryos. In: Celis JE (ed) Cell biology: a laboratory handbook, vol 3. Academic, New York, pp 87–103
18. Campos-Ortega JA, Hartenstein V (1985) The embryonic development of *Drosophila* melanogaster. Springer, Berlin
19. Bement WM, Forscher P, Mooseker MS (1993) A novel cytoskeletal structure involved in purse string wound closure and cell polarity maintenance. J Cell Biol 121:565–578
20. Kiehart DP (1999) Wound healing: the power of the purse string. Curr Biol 9:R602–R605
21. Chen HH, Brodland GW (2000) Cell-level finite element studies of viscous cells in planar aggregates. J Biomech Eng 122:394–401
22. Brodland GW, Viens D, Veldhuis JH (2007) A new cell-based FE model for the mechanics of embryonic epithelia. Comput Methods Biomech Biomed Engin 10:121–128

23. Brodland GW, Clausi DA (1995) Cytoskeletal mechanics of neurulation: Insights obtained from computer simulations. Biochem Cell Biol Biochimie Et Biol Cell 73:545–553
24. Chen X, Brodland GW (2008) Multi-scale finite element modeling allows the mechanics of amphibian neurulation to be elucidated. Phys Biol 5:15
25. Hiramoto O (1969) Mechanical properties of the protoplasm of the sea urchin egg. Exp Cell Res 56:201–208
26. Gerchberg RW, Saxton WO (1972) Practical algorithm for determination of phase from image and diffraction plane pictures. Optik 35:237–246
27. Blanchard GB, Murugesu S, Adams RJ, Martinez-Arias A, Gorfinkiel N (2010) Cytoskeletal dynamics and supracellular organisation of cell shape fluctuations during dorsal closure. Development 137:2743–2752
28. Jayasinghe AK, Crews SM, Mashburn DN, Hutson MS (2013) Apical oscillations in amnioserosa cells couple to basolateral dynamics and are cell autonomous. Biophys J. http://dx.doi.org/10.1016/j.bpj.2013.05.027
29. Peralta XG, Toyama Y, Tokutake Y, Hutson MS, Venakides S, Kiehart DP, Edwards GS (2007) Upregulation of forces and morphogenic asymmetries in dorsal closure during *Drosophila* development. Biophys J 92:2583–2596

Chapter 16
Residual Stress and Structural Anisotropy of Cortical Bone

Shigeru Tadano and Satoshi Yamada

Abstract The concept of residual stress and strain does not have long history for biological tissues. In the case of cortical bone, during remodeling process the old tissue is replaced by the new tissue with construction of osteons. Since the new tissue is generated under in vivo loadings as a non-deformed state, an indeterminate structure may be generated as a result of difference between the deformations of the old and new phases. Further, the mechanical properties (e.g. elastic modulus) are also different in these phases. Because of such non-uniform structures in cortical bone, residual stress/strain will remain in the replaced region even without external loading being applied. Tadano and co-workers initiated efforts to estimate residual stress/strain in cortical bone. In a very few applications with bone, the authors have successfully applied X-ray diffraction to quantify residual stresses at the bone surface. In this work, site-specific residual strain characteristics in relation with the mineral crystal orientation were studied and the $\sin^2\psi$ method was applied to measure residual stresses in bovine and rabbit extremities. The relationship between residual stress and osteon population density on the respective sites has also been obtained. Thus the knowledge about residual stress/strain in cortical bone, related with mineral crystal distribution and osteon population density, might play an important role in the biomechanical aspects of bone healing and remodeling.

Keywords Biomechanics • Cortical bone • Residual stress • Structural anisotropy • X-ray diffraction

16.1 Introduction

The residual stress/strain is defined as the stress/strain that remains in bone tissue or bone structure without any external loading. The presence of residual stresses in cortical bone has been noted by authors[1]. Cortical bone has a hierarchal and composite structure formed by hydroxyapatite (HAp) like mineral particles and collagen matrix [2]. The HAp in bone tissue has a hexagonal crystalline structure, and X-ray diffraction can be used to measure the interplanar spacings of HAp crystals [3, 4]. It has been shown that the distance between the lattice planes of the HAp crystals change proportionally to the deformation of the bone tissue [4]. The HAp crystal strain can be calculated by the deformation of the interplanar spacing compared with a reference state [3, 5]. Based on this, the residual stress/strain in bone tissue can be measured using the X-ray diffraction techniques [6, 7]. A $\sin^2\psi$ method of X-ray diffraction as the measurement method for the residual stress in bone tissue was proposed [7]. Further, the measurement method for the residual stress in the deeper region of bone tissue using synchrotron white X-rays has been proposed [8].

In general, residual stress is generated in a material by the indeterminate structure. It is well known that bone is usually replaced by new bone tissue with constructing osteon structures. Since the new tissue develops under in vivo loadings as the non-deformed state, an indeterminate structure may be generated by the difference of the deformation between the old and new phases. Further, the mechanical properties (e.g. elastic modulus) are also different in these phases [9, 10]. Due to the nonuniform structures in bone tissue, residual stress may remain around the replaced region without any external forces. The aim of this work is to introduce measurement method of the residual stress/strain in bovine and rabbit extremities and to investigate the relation with the mineral crystal distribution and the osteon population density.

S. Tadano (✉) • S. Yamada
Division of Human Mechanical Systems and Design, Faculty of Engineering, Hokkaido University,
N13 W8, Kita-ku, Sapporo, Hokkaido 060-8628, Japan
e-mail: tadano@eng.hokudai.ac.jp

F. Barthelat et al. (eds.), *Mechanics of Biological Systems and Materials, Volume 4*,
Conference Proceedings of the Society for Experimental Mechanics Series,
DOI 10.1007/978-3-319-00777-9_16,

16.2 Materials and Methods

To investigate the site-specific residual strain around the foramen of bovine extremities related with the mineral crystal distribution, fresh femurs and metacarpals were obtained from 24 months old bovine. The femoral diaphysis contains an observable elliptical foramen distally along the medial-posterior aspect with major axis aligned along the bone axis (Fig. 16.1a). The metacarpal has foramen towards the distal end both at the mid-dorsal and mid-palmer aspects. Rectangular cortical strips, approximately 20 × 15 mm with longer side along the longitudinal axis of the samples, were harvested with foramen almost at the center. Two femoral foramen specimens from different limbs and two metacarpal specimens from palmer and dorsal aspects were used for residual strain measurement. Thickness of the prepared specimens was uniform ranging from 0.5 to 0.8 mm among the specimens. The specimens were irradiated with Mo-Kα ($\lambda = 0.071$ nm) X-rays, tube voltage 40 kV, and tube current 40 mA generated from an X-ray generator (RINT2200: Rigaku, Japan) (Fig. 16.1b). X-ray beam was exposed to the specimen using collimator of 0.5 mm diameter for 10 min. The X-ray diffraction pattern of each specimen was detected by an X-ray Imaging Plate (IP) (BAS-SR 127 × 127 mm^2: FUJIFILM, Japan). The degree of c-axis orientation of the crystals, DO, was calculated using the X-ray diffraction pattern of the (002) planes [6]. The degree of orientation was calculated for the positions next to the edge of the foramen and away from the foramen at 2 mm distance apart along the medial and lateral sides, respectively. All these positions lie on the same medio-lateral line nearly at the center of the elliptical hole. The diffraction profile of the (211) planes was considered for strain analysis. Since the non-strained state was not known, the pseudo hydrostatic strain ε_{ph} was calculated using the ring diameters of different profile azimuths. Residual strains for both the longitudinal (sample axis) and transverse directions were calculated [6].

Next, to measure the residual stress distribution at the surface of the cortical bone and to investigate the relationship with the osteon population density, the study used bones of the extremities of adult rabbits (Japanese White Rabbits, female, average age 16.5 weeks, average weight 3.0 kg) (Fig. 16.2a). In this study, three femur, three tibia/fibula, three humerus, and three radius/ulna specimens were used. The specimens were 60 mm long in the bone axial direction and cut using a slow speed diamond wheel saw (Model 650: South Bay Technology, USA). The bone marrow and the soft tissue around the surfaces were removed and the specimens were kept in saline until just before the X-ray measurements. The measurements

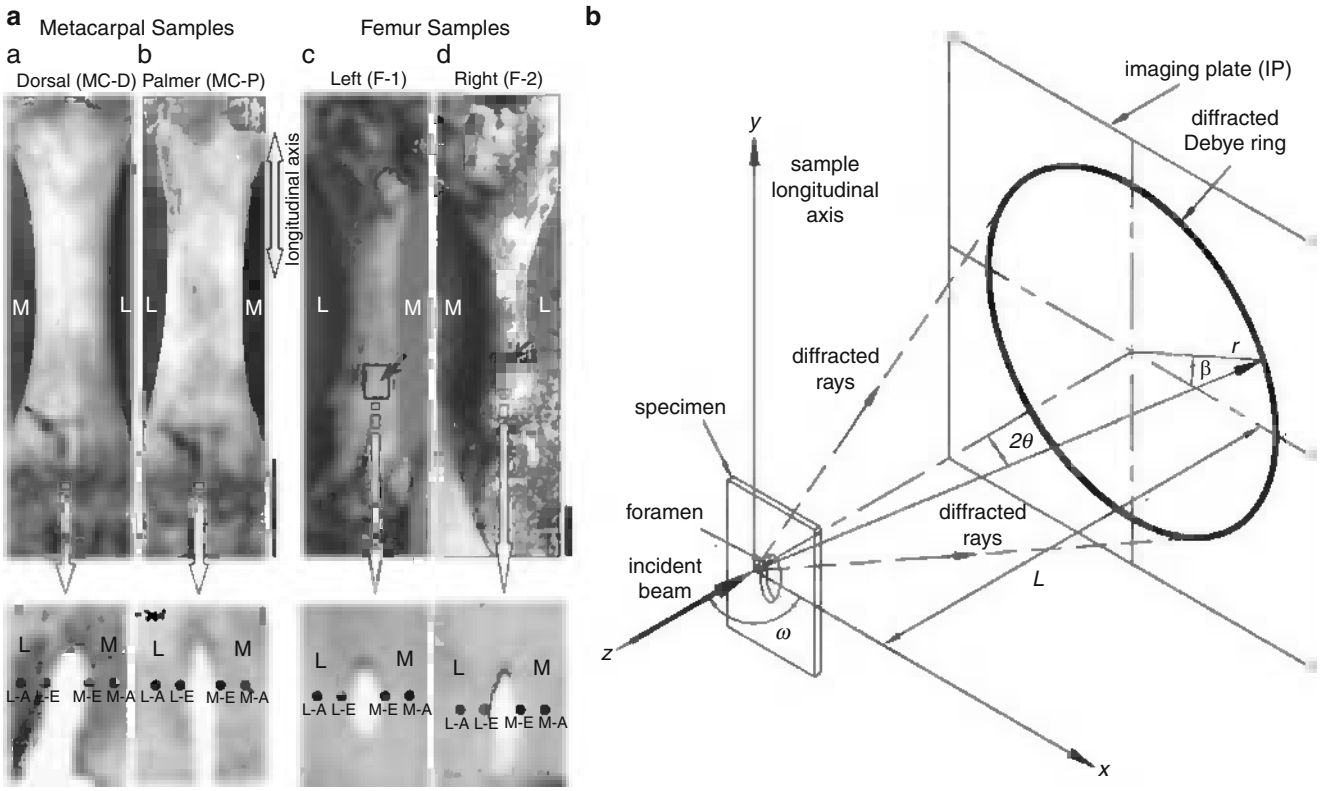

Fig. 16.1 (**a**) Metacarpal and femoral samples (*top*). Locations of foramina are shown by *arrows*. The scale bars are 50 mm. Cortical specimens (approx. 20 × 15 mm) were harvested from the samples with foramen almost at the *center* (*bottom*). The measured points are shown in the specimens with the notations to define the locations. (**b**) Schematic of diffraction phenomena in X-ray diffraction imaging-plate system [6]

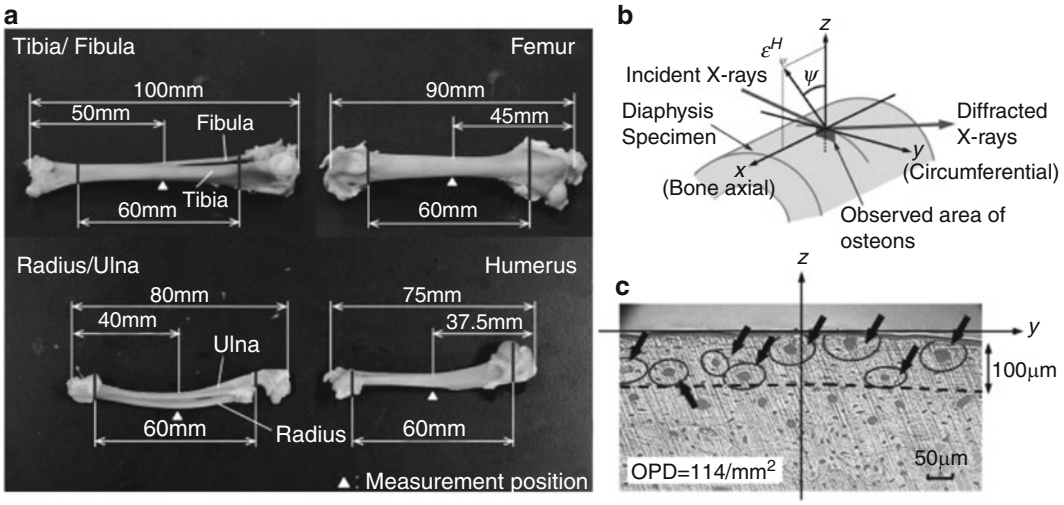

Fig. 16.2 (**a**) Specimens of the diaphysis of rabbit extremities. (**b**) Coordinate system on the specimen surface. (**c**) Measurement protocol of the osteon population density (*OPD*) in the microscopic image [11]

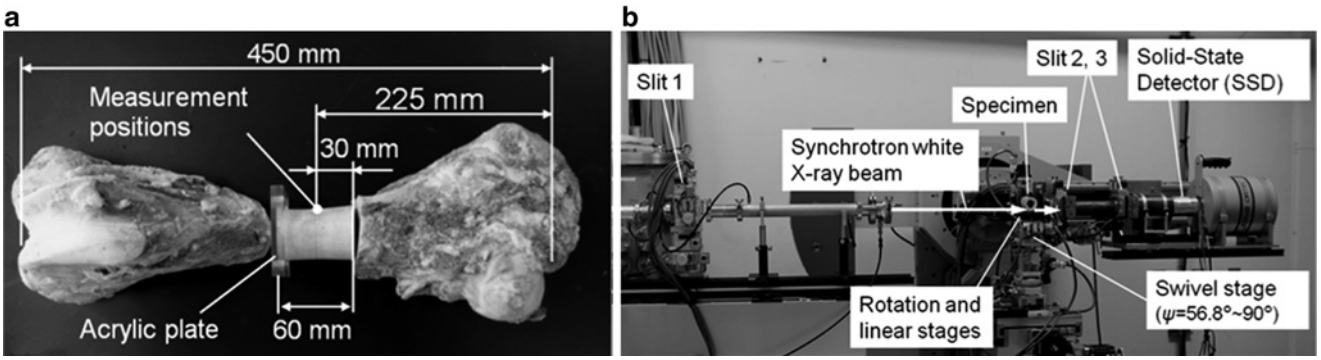

Fig. 16.3 (**a**) Diaphysis specimen taken from a bovine femur. (**b**) Measurement setup for X-ray diffraction [8]

were conducted at the anterior and posterior positions at the center of the specimens. The anterior and posterior positions in the tibia/fibula correspond to the anterior and posterior positions of the tibia, respectively. Further, in the radius/ulna, the anterior and posterior positions correspond to the anterior position of the radius and the posterior position of the ulna, respectively. The residual stresses were calculated from five measurements at each position using the $\sin^2\psi$ method of X-ray diffraction [7, 11]. The specimens were irradiated with the characteristic Mo-Kα X-rays, tube voltage 40 kV and tube current 40 mA, to obtain the diffraction profiles as shown in Fig. 16.2b. The diffraction profiles were measured between $2\theta = 13.0°$ and 17.0°, which includes the diffraction angles of the (211), (112), and (300) planes of HAp crystals, at the following ψ conditions: 0°, 10°, 20°, 30° and 40°. The specimens were air dried after the X-ray measurements and then saturated in epoxy resin for 24 h to be able to easily grind the cross sections. The 5 mm long sections of these specimens were cut out by the diamond wheel saw, with one end at the X-ray measurement position. The cross sections were ground by emery papers, and then buffed by a buffing machine (Model 900: South Bay Technology, USA). The surface regions of the diaphysis side in the section as shown in Fig. 16.2c were observed by a microscope (VH5000: KEYENCE, Japan). The observed area was down to 100 μm depths from the outer cortical surface and 700 μm wide centered on the z-axis in the section. In the study, the number of osteons in the region was counted and the osteon population density (OPD) was calculated. The osteons that were quantified were secondary osteons (Haversian systems) and primary osteons.

To measure the distribution of residual stress from the outer surface to the inner region of cortical bone, the mid-diaphysis part of a femur obtained from a 26-month-old bovine was used (Fig. 16.3a). The diaphysis specimen was 60 mm long in the bone axial direction and cut using the slow speed diamond wheel saw, and the measurement position was the center of the femur and the diaphysis specimen respectively. The bone marrow and the soft tissue around the surfaces were removed and the specimen was air dried at room temperature. To fix the specimen on the measurement instruments for the X-ray diffraction, one end of the specimen was bonded to an acrylic plate with epoxy resin. The measurement points in the

diaphysis specimen were sited at 1 mm intervals from the outer surface to the inner region of the specimen at four parts of the diaphysis: anterior, posterior, lateral, and medial. The synchrotron white X-ray diffraction was performed at the BL28B2 beam line of SPring-8 (RIKEN/JASRI). As shown in Fig. 16.3b, the specimen was irradiated with the X-ray beam, and the beam, with intensity optimized with an aluminum absorber, was collimated with a slit. Scattered X-rays were eliminated from the diffracted X-rays by two slits. The diffracted X-rays were detected by a solid state detector and the pulse height distribution of the X-rays was analyzed by a multichannel analyzer (4,096 channels). Fluorescent X-rays of Pb-Kα1 and Sn-Kα1 were measured to calibrate the MCA. The interplanar spacing d of the (002) plane in HAp crystals was measured at the following ψ conditions: 90.0°, 71.6°, 63.4° and 56.8° and the residual stress at each position was calculated from the d-ψ relation [8].

16.3 Results and Discussion

The calculated bone axial residual strains in the metacarpals and femur samples are plotted in Fig. 16.4a and the DOs with reference to the longitudinal direction of the specimens are plotted in Fig. 16.4b. There was the existence of significant amount of residual strains in the bone samples, and the results showed that their tendencies were linked with the extent of mineral crystals. It suggests the correlation between crystallites orientation and strains to be taken into account precisely. It is expected that higher the concentration of the apatite crystals, the more it is capable to resist the longitudinal load resulting in higher residual strains. The DOs here are mostly consistent with the trend of residual strains in the specimens. The lateral side of palmer metacarpal specimen and femur-2 specimen show higher difference in the residual strains at the edge compared to the far point. These could be regarded to their loading environment and show agreement with the orientation variation of the apatite crystals.

Figure 16.5a shows the distribution of residual stress in the rabbit limb bones. Each bar indicates the average of the three specimens in each position, and errors are the corresponding standard deviations. Tensile residual stresses were observed at every measurement position. The average stresses at the hindlimb bones and the forelimb bones were 210 and 149 MPa, respectively, showing that the hindlimb bones were subject to tensile residual stress 1.4 times higher than that in the forelimb bones. Figure 16.5b shows the relationship between the residual stress and the OPD, it shows a positive correlation ($r = 0.55, p < 0.01$), and the residual stresses correlated with the OPD. The results suggest that these nonuniform structures of the tissue derived from the osteon formation and the internal organization of these entities down to the nanostructural level may explain the spatial differences in residual stress. Further, this also suggests that the residual stresses being nonuniform may be related to nonuniformities in the mechanical environments in vivo and the resulting functional adaptation of the bone tissue. The residual stress in the bone is regarded as an epiphenomenon and may be a circumstantial finding of the adapted state. Thus the knowledge about residual stress/strain distribution in the cortical bone, related with the mineral crystal

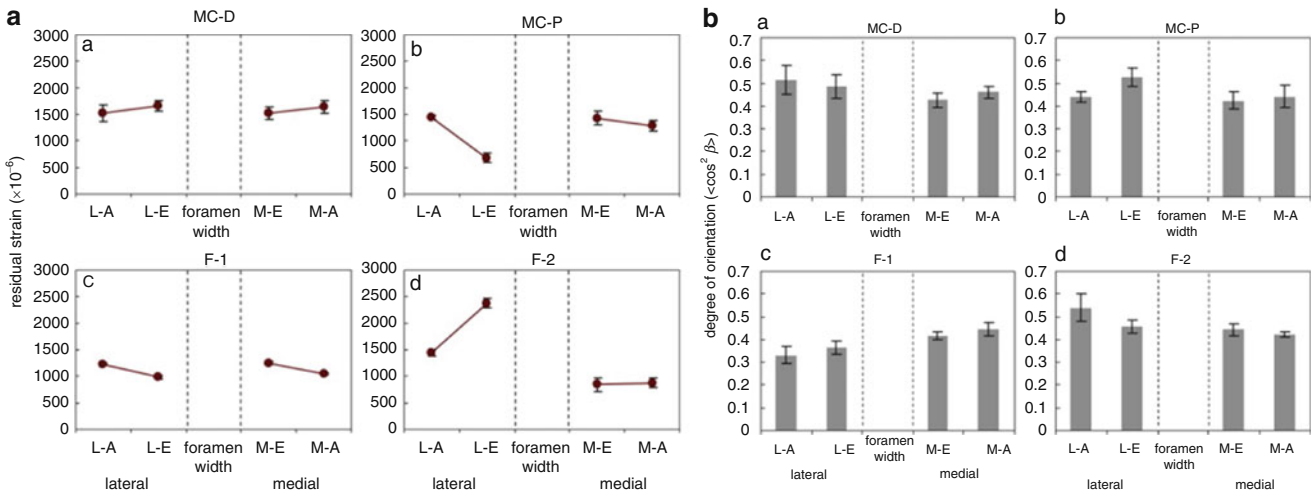

Fig. 16.4 (**a**) Lattice residual strains along the longitudinal direction near the foramen region. Locations next to the edge and away from the edge at 2 mm distance were measured along medial and lateral sides. (**b**) Degree of orientation (*DO*) with reference to the sample longitudinal direction along lateral and medial of foramen sites for dorsal metacarpal, palmer metacarpal, femur-1, and femur-2. The values are shown for the location next to the foramen edge (*L–E*, *M–E*) and away from the edge (*L–A*, *M–A*) at 2 mm distance apart [6]

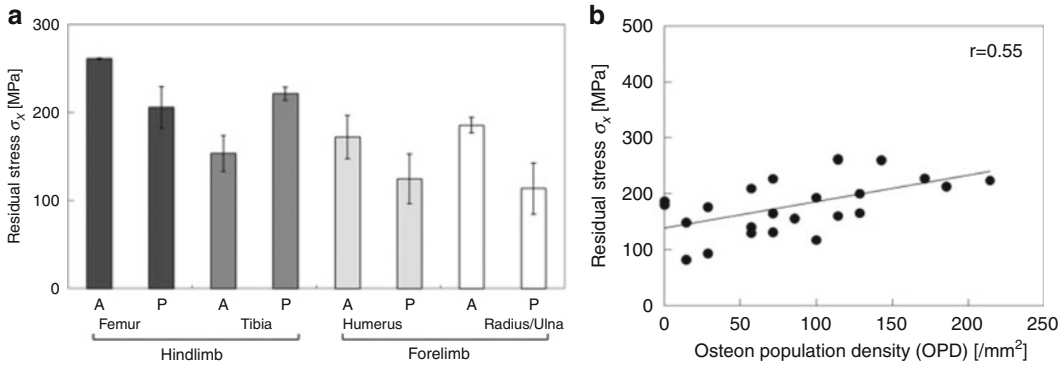

Fig. 16.5 (**a**) Distribution of the residual stresses in the rabbit limb bones. (**b**) Relationship between the residual stress and the OPD in the rabbit limb bones [11]

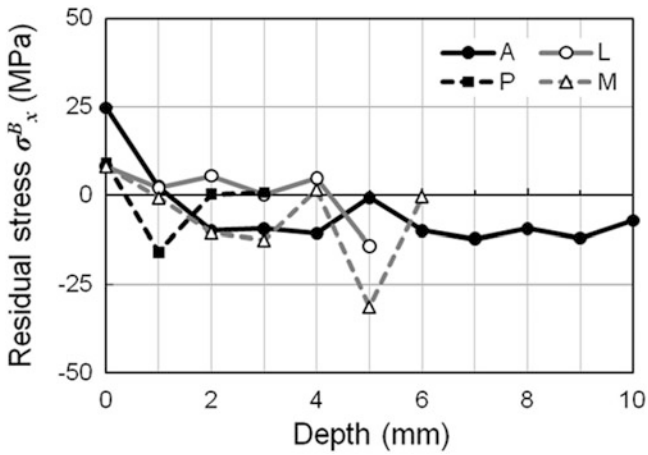

Fig. 16.6 Radial distribution of the residual stress in the bone axial direction from the outer surface to the inside of the diaphysis specimen at the four parts: anterior (*A*), posterior (*P*), lateral (*L*), and medial (*M*) [8]

distribution and osteon population density, might play an important role in the biomechanical aspects of bone healing and remodeling.

Figure 16.6 shows the radial distribution of the residual stress in the bone axial direction from the outer surface to the inner region of the bovine femoral diaphysis measured with synchrotron white X-rays. The values of residual stresses were calculated from one measurement at each position. The horizontal axis indicates the depth of the measurement positions from the outer surface of the specimen at each part. The deepest positions indicated in Fig. 16.6 do not correspond to the inner surface of the diaphysis specimen, because the intensity of the diffracted X-rays around the inner surface region was too low to calculate d. The outer surface in the bovine femoral diaphysis was subjected to tensile residual stress and the inner region of the cortical bone was subjected to compressive stress. Further, the magnitude of the tensile residual stress at the surface was larger than that of the compressive stress in the inner region. In the previous studies using characteristic Mo-Kα X-rays generated by an X-ray tube, the residual stresses in the deeper region of the diaphysis of limb bones could not be measured. To understand the generation mechanisms of residual stress in bone tissue, it is important to investigate the residual stress distribution from the surface to the deeper region of the bone tissue using this method with synchrotron white X-rays.

References

1. Tadano S, Okoshi T (2006) Residual stress in bone structure and tissue of rabbit's tibiofibula. Bio-Med Mater Eng 16:11–21
2. Tadano S, Giri B (2011) X-ray diffraction as a promising tool to characterize bone nanocomposites. Sci Technol Adv Mater 12:064708 (11pp)
3. Fujisaki K, Tadano S, Sasaki N (2006) A method on strain measurement of HAp in cortical bone from diffusive profile of X-ray diffraction. J Biomech 39:579–586

4. Fujisaki K, Tadano S (2007) Relationship between bone tissue strain and lattice strain of HAp crystals in bovine cortical bone under tensile loading. J Biomech 40:1832–1838
5. Tadano S, Giri B, Sato T, Fujisaki K, Todoh M (2008) Estimating nanoscale deformation in bone by X-ray diffraction imaging method. J Biomech 41:945–952
6. Giri B, Tadano S, Fujisaki K, Todoh M (2008) Understanding site-specific residual strain and architecture in bovine cortical bone. J Biomech 41:3107–3115
7. Yamada S, Tadano S (2010) Residual stress around the cortical surface in bovine femoral diaphysis. J Biomech Eng 132:044503
8. Yamada S, Tadano S, Todoh M, Fujisaki K (2011) Residual stress distribution in the bovine femoral diaphysis measured by synchrotron. J Biomech Sci Eng 6:114–124
9. Gibson VA, Stover SM, Gibeling JC, Hazelwood SJ, Martin RB (2006) Osteonal effects on elastic modulus and fatigue life in equine bone. J Biomech 39:217–225
10. Rho JY, Zioupos P, Currey JD, Pharr GM (1999) Variations in the individual thick lamellar properties within osteons by nanoindentation. Bone 25:295–300
11. Yamada S, Tadano S, Fujisaki K (2011) Residual stress distribution in rabbit limb bones. J Biomech 44:1285–1290

Chapter 17
Microcracking Morphology and Structure Optimization of Compact Bovine Bone Under Impact Loading

Wei Zhang, Srinivasan Arjun Tekalur, and Ziwei Zhong

Abstract Deterioration of bone is a progress of damage accumulation in the form of microcracking spanning a wide range of dimensional scales. To examine the microcracking morphology of compact bone subjected to impact loading, non-notched beam specimens of compact bovine femur were loaded with an instrumented Charpy impact system under various impact energy levels. The middle sections of the tested specimens was examined the by Frost's basic funsion technique by Frost (Med Bull 8:25–35, 1960) to investigate the microcracking morphology. The effects of size of osteon on the mechanical integrity of ostoen structure were also investigated by using of a finite element modeling (FEM), micromechanics, and constrained optimization method. The damage mechanism and energy dissipation were analyzed.

Keywords Bone • Osteon • Optimization • Microcracking • Impact

17.1 Introduction

According to their shapes, bone can be classified as long bone, flat bone, short bone, and et al. Femur and tibia are two typical long bones, which are the major support of vertebrates. The diaphysis of long bone is made of dense cortical bone, and the two ends, called epiphysis, are made of phony trabecular bone. In microstructure level (from 10 to 500 μm) [2], the primary continent of mature cortical bone (also called osteon bone) is osteon system, which grows along the loading axis and comprises center Haversian system surrounded by cylindrical lamellae formed by collagen fibrils and embedded mineral in nanostructure level (from a few hundred nanometers to 1 μm). The boundary between osteons and surrounding bone tissue, called cement line, exhibits brittle properties due to its high mineral composition. Unlike osteon bone, immature bone (laminar bone) is characterized with laminar structure. The osteon structure of bone is like a fiber-reinforced composite with hard fiber (osteon) distributed in the soft interstitial bone matrix. This unique hierarchical structure contributes bone's tough but light weight properties. The morphology and composition of osteonal cement line in human bone has been studied by Schaffler [3].

The research interest is to investigate the significant benefits the unique osteon structure and the effects of hierarchical structure such as the size, density, distribution, and properties of oseon on the overall mechanical function of bone. During their life span, bone consistently undergoes targeted and non-targeted remodeling [4] in order to assure its functional integrity. Non-targeted remodeling is bone adaption to meet metabolic needs, and targeted remodeling is triggered by microdamage induced in daily fatigue activities. Understanding the microcracking morphology and its relation to applied loading is of great clinical interest to better study targeted remodeling in bone.

The objectives of the paper are to investigate the significant benefits of unique osteon structure and its failure mechanism and microcracking morphology when subjected to impact loading. A Charpy impact testing on non-notched beam bone specimens were performed by use of an instrumented Charpy impact system. The post-failure examinations were achieved

W. Zhang (✉) • S.A. Tekalur
Department of Mechanical Engineering, Michigan State University, East Lansing, MI 48824, USA
e-mail: zhangw31@egr.msu.edu; tsarjun@egr.msu.edu

Z. Zhong
Department of Civil and Environmental Engineering, Michigan State University, East Lansing, MI 48824, USA
e-mail: Zhongziw@msu.edu

F. Barthelat et al. (eds.), *Mechanics of Biological Systems and Materials, Volume 4*,
Conference Proceedings of the Society for Experimental Mechanics Series,
DOI 10.1007/978-3-319-00777-9_17,

by a bright field microscope. The commercial software, ABAQUS, was used to model ostoen bone subjected to dynamic loading in micro-level, and the optimization tool, MatLab fmincon and Heeds will be used to optimize the size and area percentage of ostoen to obtain an optimal ostoen structure.

17.2 Material and Methods

All the specimens were machined out of fresh compact bovine femurs (60 months old) provided by a local beef abattoir. The mid-diaphysis of the bovine femur was cut into rectangular specimens. During the entire machining process, the specimens were kept wet with phosphate buffered saline (PBS) solution. After machining, the specimens were covered with gauge dipped in PBS solution and preserved in a −20 °C freezer until testing. Specimens were thawed prior to testing.

The dimensions of bone specimens are shown in Fig. 17.1. To examine the microcracking morphology and its effects on targeted remodeling of compact bone subjected to impact loading, non-notched beam specimens of compact bovine femur were loaded with an instrumented Charpy impact system under different impact energy levels. A table-on Charpy impact system with light impact mass (0.6 Kg) were designed to perform low energy (ranging from 0.1 to 2.3 J) impact tests on bone specimens. In each energy level, four specimens were tested. The preliminary tests showed that specimens most likely reach failure at around 0.6–0.7 J. After test, one piece of the broken specimen was soaked in basic funsion solution according to Frost's basic funsion technique. The other piece was preserved in freezer for further experiments. After bulk stain, a ground section (thickness, 300 μm) were cut off the end where is close to the fracturing end. The surface interested is the cross section surface which is perpendicular to ostoen direction. The thin sections then were first polished by a Leco wafering saw with a precision of 0.01 mm followed by final polishing by a Leco lapcloth polishing machine with precision of 1 μm. The other piece without bulk stain followed the same preparing procedures for ground section with bulk stain and the fine polished thin sections will be used as the substrates of cell cultures for evaluating the microcraking effects on osteoclast and osteoblast adhesion [5].

ABAQUS explicit was used to simulate osteon bone structure subjected to impact loading in micro-level. Osteon bone is of unique microstructure with hard fiber-like ostoen deposited in the soft interstitial bone matrix. This unique structure not only provides a nutrition nets connecting to the bone marrow, but also creates an orthotropic composite material with a higher Young's modulus and strength along the longitudinal direction which is the growing direction of ostoen or the loading axis compared to the transverse direction which is perpendicular to loading axis [6]. The diagram of the cross-section of osteon bone is shown in Fig. 17.2. Osteon with central hole, cement line, and interstitial bone matrix are the three major components of osteon structure. To simplify computation, the liquid inside the Harvension hole was neglect. The dimension, properties, and density of osteon are expected to have a strong correlation to the overall mechanical function of osteon bone. The mechanical properties of osteon bone were treated as a function of these three components. Young's modulus, yield strength, and stiffness of each this component were used as inputs to FEM. An optimization computation by MatLab fimincon and commercial optimization tool, Heeds, will be performed to examine the optimal ostoen dimension and properties. The diagram for the FEM modeling is shown in Fig. 17.2. The dimension of rectangular osteon piece simulated is 500 × 375 μm, and the diameter of the central canal is 30 μm. The width of the cement line is 5 μm. The average of diameter of the ostoen is about 192.7 μm.

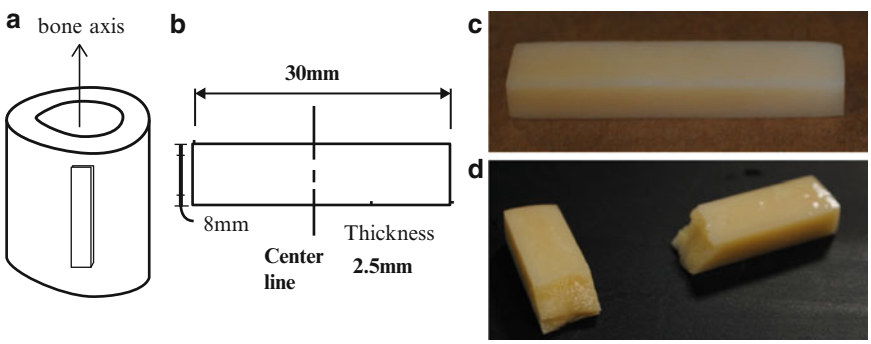

Fig. 17.1 Bone specimens: (**a**) a diagram shows the orientation of bone (osteon grows along bone axis); (**b**) dimensions of bone specimen; (**c**) a typical specimen before testing; (**d**) a typical specimen after testing

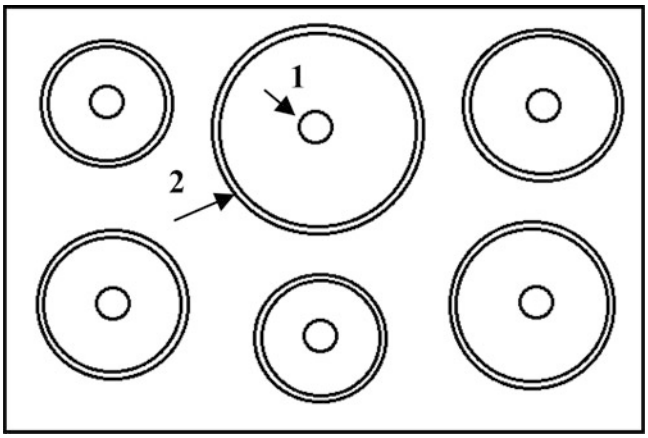

Fig. 17.2 Diagram of FEM modeling of ostoen structure: *1*, central canal; *2*, cement line. The space outside cement lines is bone matrix, and inside cement lines is osteon fiber

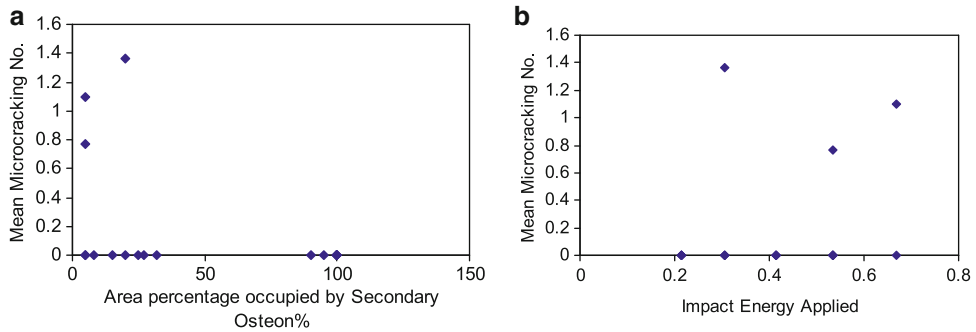

Fig. 17.3 (**a**) Correlation of mean microcracking numbers to the area percentage occupied by secondary osteon; (**b**) correlations of microcracking to the impact energy applied

17.3 Results and Discussion

17.3.1 Experimental Results

The impact energy was set up to be 0.14, 0.31, 0.41, 0.53, and 0.67 J respectively. Four specimens were tested in each energy level. It was found that there was no specimen fractured at impact energy of 0.14 J, one specimen fractured at impact energy of 0.31, 0.41, and 0.53 J respectively, and three specimens fractured at the impact energy of 0.67 J. The correlations of the microcracking numbers to the area percentage occupied by secondary osteon and the impact energy applied are shown in Fig. 17.3. The post-failure examinations showed that no microcracks were visible when the specimen was not broken. The cracks in the fractured specimens were linear and were usually larger than hundreds of micrometers in length (Fig. 17.4c). Figure 17.3a showed that no specimens fractured or no microcracks were observed when the area occupied by secondary ostoen is larger than 25 %. It seems that the threshold energy varied for each specimen. When the applied energy between 0.31 to 0.53 J, the fracture possibility of specimens is random (Fig. 17.3b) and may rely on the microstructure of bone. The testing showed that osteon bone (Fig. 17.4a) can sustain higher impact energy compared to the laminar bone (Fig. 17.4b).

17.3.2 FEM Results

In the future, an optimization procedures using commercial FEM software ABAQUS explicit and optimization software Heeds will be performed to evaluate the effects of osteon size and distributions on the overall mechanical properties of osteon bone. The role of cement line, soft interlayer on the mechanical integrity of the osteon bone will also be investigated. Figure 17.5 Shows a preliminary results of the simulation.

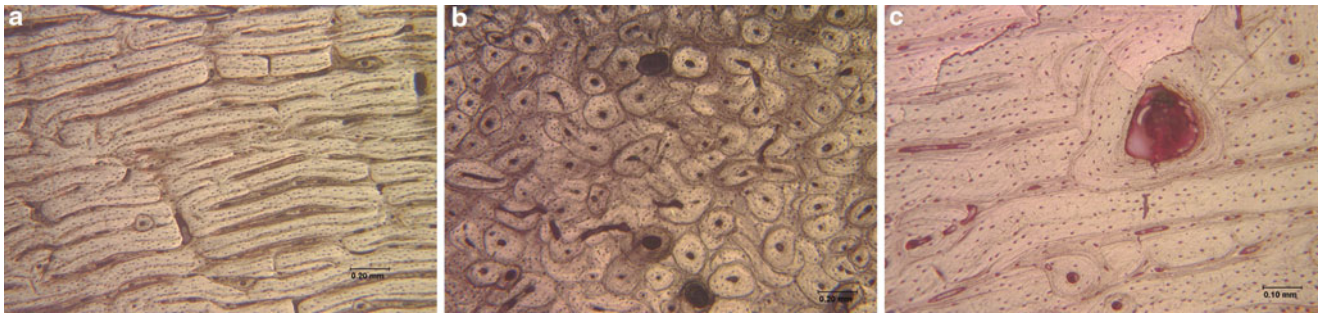

Fig. 17.4 Post-failure examinations: (**a**) a typical laminar structure; (**b**) a typical osteon structure, (**c**) a typical specimen with microcracks

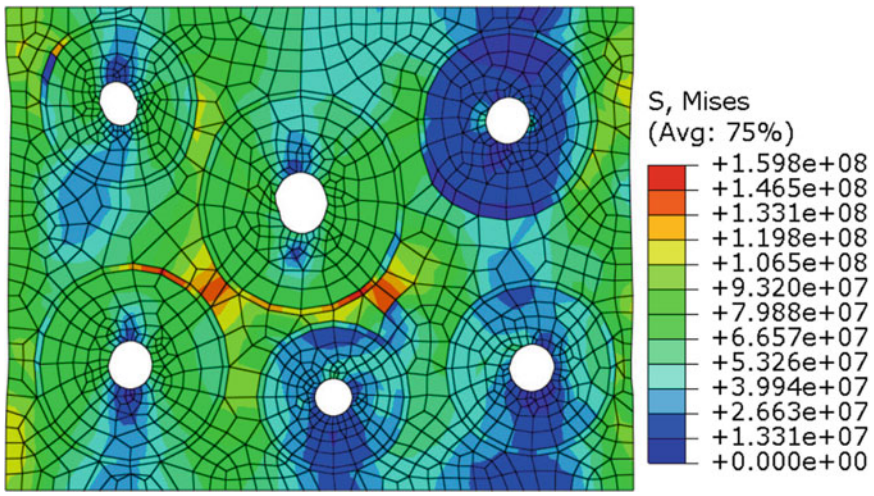

Fig. 17.5 Stress field of FEM simulation (the unit of stress is Pa)

17.4 Conclusion

The microcracking morphology of compact bone subjected to impact loading was investigated by an instrumented Charpy impact system under different impact energy levels. The experiments showed that osteon bone can sustain higher impact energy compared to the laminar bone. Optimization of ostoen bone structures will be performed in the future study.

Acknowledgements The authors wish to thank Steven Utz and Peter Howes for helping to machine the specimens.

References

1. Frost HM (1960) Presence of microscopic cracks in vivo in bone. Henry Ford Hosp Med Bull 8:25–35
2. Rho JY, Kuhn-Spearing L, Zioupos P (1998) Mechanical properties and the hierarchical structure of bone. Med Eng Phys 20:92–102
3. Schaffler MB, Burr DB, Frederickson RG (1987) Morphology of the osteonal cement line in human-bone. Anat Rec 217:223–228
4. Parfitt AM (2002) Targeted and nontargeted bone remodeling: relationship to basic multicellular unit origination and progression. Bone 30:5–7
5. Rumpler M, Wurger T, Roschger P, Zwettler E, Peterlik H, Fratzl P, Klaushofer K (2012) Microcracks and osteoclast resorption activity in vitro. Calcif Tissue Int 90:230–238
6. Huja SS, Beck FM, Thurman DT (2006) Indentaiton properties of young and old osteons. Calcif Tissue Int 78(6):392–397

Chapter 18
Biomechanical Response of Blast Loading to the Head Using 2D-3D Cineradiographic Registration

R.S. Armiger, Y. Otake, A.S. Iwaskiw, A.C. Wickwire, K.A. Ott, L.M. Voo, M. Armand, and A.C. Merkle

Abstract This paper details a method for tracking 3D kinematics of the skull and brain deformation in post-mortem human subjects (PMHS) using 2D cineradiographic images during a high-rate loading event. Brain displacement and resulting strain due to blast loading is a metric for Traumatic Brain Injury (TBI), however physically measuring brain motion experimentally is a significant challenge. A shock tube, used to simulate blast exposure, created skull and brain motion tracked using implanted radio-opaque markers and high-speed X-ray images. These images were registered to a computed tomography (CT) scan using intensity-based 2D-3D registration techniques. To register the 2D images to the 3D scan, digitally reconstructed radiographs were generated from the CT scan, and then compared to the recorded x-ray frames by maximizing similarity metrics between the images using a Covariance Matrix Adaptation Evolution Strategy. As compared to pure 2D tracking, 2D-3D registration provides out-of-plane kinematics by fully leveraging information in the x-ray projection image and prior information from the 3D CT scan. Data generated with these techniques are critical for physically understanding the mechanisms associated with blast exposure that may lead to TBI, and can be used for human computational model validation.

Keywords Image registration • Traumatic brain injury • Blast loading • High-speed x-ray • Head kinematics

18.1 Introduction

Traumatic Brain Injury (TBI) remains a significant problem for both military and civilian populations. Between 2000 and 2012, the total number of diagnosed cases of TBI for U.S. troops exceeded 253,000 [1]. Loading can vary between contact (blunt, ballistic) as well as non-contact (accelerative) scenarios; however evidence suggests that injury mechanisms are related to mechanical strain in the brain [2–4]. In non-contact TBI scenarios, tracking head motion is of importance due to the injury implications resulting from relative motion between the brain and skull. For blast loading scenarios, a two-phase response is observed governing brain injury: an initial kinetic phase due to the blast overpressure wave transmitting through the skull lasting 1–2 ms, and a kinematic phase of linear and angular rotation of the head causing relative motion of the brain and skull [5]. This effort assesses the global kinematics of the head during dynamic loading.

In addition to experimental efforts introduced here, computational modeling and surrogate development for the human head and neck are ongoing to characterize and assess brain injury response to blast [6]. These models require tissue material properties characterized at high strain rates [7–9], as well as experimental response data to validate the model. For live fire scenarios, instrumented surrogates with displacement sensors have been developed [10]; however these results must also be interpreted with respect to cadaveric testing. Previous studies measured brain displacement due to blunt impact [11] or brain pressure due to shock tube loading [12], but this is the first time high-speed cineradiographic imaging is combined with shock tube loading.

It is typical to localize 2D rigid body motion using an x-ray by localizing radiopaque markers mounted directly to the anatomy [13]. However, capturing 3D motion typically requires a separate camera system with markers mounted to the test specimen. This effort describes an alternative that uses the full cineradiographic image to track rigid body motion using

R.S. Armiger (✉) • Y. Otake • A.S. Iwaskiw • A.C. Wickwire • K.A. Ott • L.M. Voo • M. Armand • A.C. Merkle
The Johns Hopkins University Applied Physics Laboratory, 11100 Johns Hopkins Road, Laurel, MD 20723, USA
e-mail: Robert.Armiger@jhuapl.edu

F. Barthelat et al. (eds.), *Mechanics of Biological Systems and Materials, Volume 4*,
Conference Proceedings of the Society for Experimental Mechanics Series,
DOI 10.1007/978-3-319-00777-9_18,

imaging techniques that rely only on the intrinsic features of the anatomy to calculate position and orientation with a single x-ray source, and without the invasiveness of fixing markers directly to the anatomy. To achieve this, we applied our previously validated method for 2D-3D registration [14] to recover the 3D kinematics of head motion from a 2D x-ray image sequence.

This paper presents application and in-plane error analysis of a 2D-3D registration algorithm applied to an integrated high-speed x-ray and shock tube system, used to determine the 3D rigid body motion of post-mortem human subject (PMHS) head specimens under dynamic loading.

18.2 Methods

Specimens for this study were fresh-frozen, non-osteoporotic PMHS head and neck complexes, obtained from the Maryland State Anatomy Board. Computed Tomography (CT), scans were taken of each specimen at the Johns Hopkins University Medical Institutes Radiology Department before instrumentation and post-experiment at a transverse image resolution of 0.3 mm. Each neck was rigidly potted from the fifth to the seventh cervical vertebrae. Additional preparation of the specimen included implantation of radio-opaque markers within the brain, mounting of intracranial pressure sensors, and strain gauges to the skull in the frontal, parietal, temporal, and occipital locations, as well as implantation of radio-opaque markers within the brain. Results from these sensors are beyond the scope of the present paper, and will be presented in a subsequent publication.

The instrumented specimen was positioned in front of a 152 mm diameter shock tube [15] shown in Fig. 18.1. The specimen was positioned in an inverted position such that the nose was axially aligned with the center of the shock tube at a standoff distance of 152 mm. Additional tests were completed with the specimen rotated for side facing (lateral) configuration. For this study, tests were conducted with a nominal driver pressure of 1,000 kPa.

The custom-built High-Speed X-ray (HSXR) video system used for this study consisted of an x-ray generator, a 410 mm image detection unit, and a high-speed digital video camera, integrated with a shock tube system. In high-speed dynamic capture events, the high frequency x-ray generator (CPI Indico 100) provided a continuous, non-gated beam using 75–200 mA and 70–105 kVp settings. The image detection unit (Thales TH 9447 QX) included an output phosphor capable of a 3 kHz response. A high-speed video camera (Phantom v10, Vision Research) captured images from the image detection unit at 480 frames per second with a resolution of 2,400 × 1,800 pixels. Data collection between the HSXR and camera were synchronized using a trigger at the exit of the tube.

Acquired x-ray images were calibrated and corrected for distortion artifacts using a custom-built imaging phantom with a regularly spaced grid of lead markers shown in Fig. 18.2 using techniques described previously [16]. Each image frame was corrected for distortion and calibrated using a 2D interpolation.

For each frame, an intensity-based 2D-3D registration algorithm optimized the 6° of freedom (DOF) rigid body transformation parameters between a 3D CT image and the acquired 2D radiographs. The optimization was based on

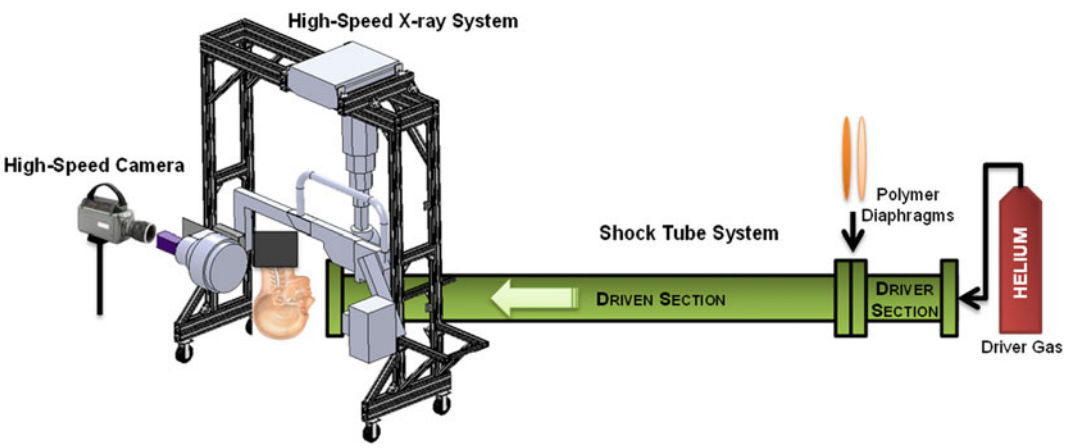

Fig. 18.1 Experimental setup showing specimen position with respect to the shock tube and orthogonally aligned to the HSXR

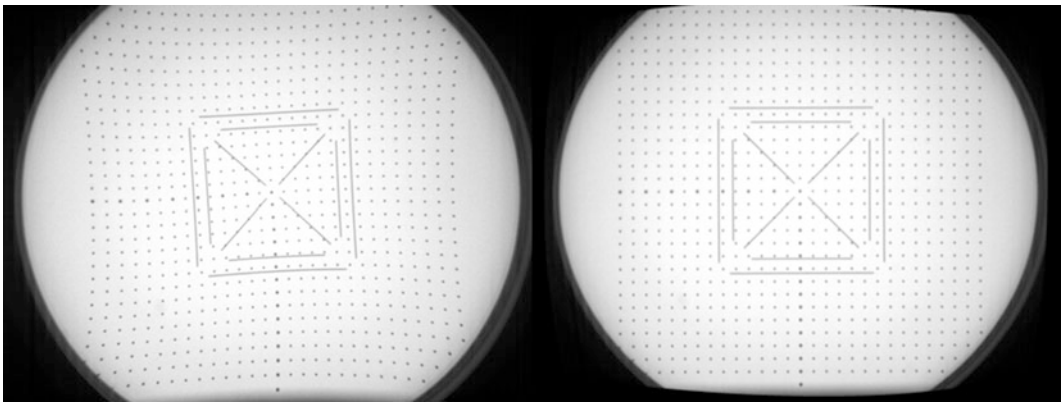

Fig. 18.2 Original (*left*), and distortion corrected (*right*) x-ray image

maximizing image similarity metrics between the real x-ray image and a digitally reconstructed radiograph (DRR) based on the CT. Thus the optimization problem (*argmax*) is formulated as:

$$\left\{\hat{t}_x,\ \hat{t}_y,\ \hat{t}_z,\ \hat{\theta}_x,\ \hat{\theta}_y,\ \hat{\theta}_z\right\} = \underset{t_x,t_y,t_z,\theta_x,\theta_y,\theta_z}{\operatorname{argmax}} S\left(p_{XRay}, p_{DRR}\left(t_x, t_y, t_z, \theta_x, \theta_y, \theta_z\right)\right)$$

where S(A,B) represents an image similarity metric between image A and B, p_{XRay} and p_{DRR} represent the x-ray image and DRR respectively. A unique DRR is generated based on the position and orientation of a virtual source and detector with respect to the CT scan, thus, six independent translation and rotation parameters (t_x, t_y, t_z, θ_x, θ_y, θ_z) are output from the algorithm.

The image similarity metric was based on gradient information (GI) [17], which was defined as

$$GI(p_1, p_2) = \sum_{i,j\in\Omega} w(i,j)\min(|\nabla p_1(i,j)|, |\nabla p_2(i,j)|)$$

$$\nabla p(i,j) \triangleq \left(\frac{d}{di}p(i,j), \frac{d}{dj}p(i,j)\right)$$

where $p_{1(i,j)}$ and $p_{2(i,j)}$ are the intensity values in each image at the (i,j) pixel position, *min*(A,B) indicates the smaller value of A and B, Ω represents the entire image domain, ∇p is a gradient vector, and the weighting function w was defined as:

$$w(i,j) = \frac{\alpha_{i,j}+1}{2},\ \alpha_{i,j} = \frac{\nabla p_1(i,j)\cdot\nabla p_2(i,j)}{|\nabla p_1(i,j)|\cdot|\nabla p_2(i,j)|}$$

where $\alpha_{i,j}$ represents the cosine between gradient vectors at location (i,j). The GI algorithm uses the *min* operator to assign higher weights only on those pixels which have greater gradients in both images, making it robust against a variety of content mismatches between two images, whereas a global similarity metric such as mutual information, or normalized cross correlation are sensitive to mismatches. In our case, mismatches include experimental equipment that appear in the x-ray image but not in the CT data, and non-rigid objects such as wires connected to sensors or movement of the mandible.

For the optimization, a derivative-free optimization approach was implemented (also known as black box optimization) since it is impractical to obtain algebraic derivative information of the GI metric with respect to the transformation parameters. Among a wealth of existing algorithms, Covariance Matrix Adaptation Evolutionary Strategy (CMA-ES) was employed due to its robustness and inherent suitability for parallelization. The CMA-ES algorithm was implemented in MATLAB® and uses an evolutionary (genetic) approach [18]. The algorithm generates a number of sample points (population size of 60 in our case) in one generation, randomly based on a normal distribution defined by a covariance matrix that changes in each generation.

Since DRR generation and GI computation were highly parallelizable, we implemented them on a Graphics Processing Unit (GPU) to leverage speed enhancement by the massively parallelized computation environment. The CMA-ES

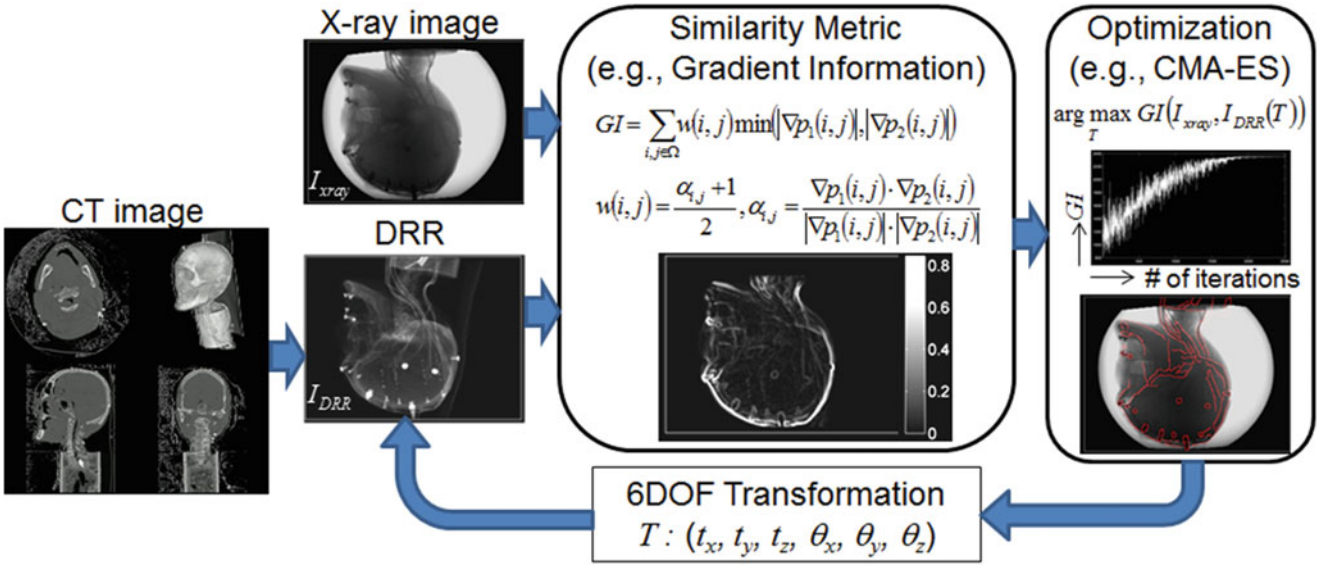

Fig. 18.3 Workflow of the intensity-based 2D-3D registration for a single frame. DRR images were created using a volumetric CT scan and an estimated 6DOF transformation. An algorithm varied the transformation parameters to maximize a similarity metric (Gradient Information) between the DRR and x-ray image

optimizer included a function call to an externally compiled shared library coded in C++ and CUDA for DRR generation and GI computation.

During preprocessing, the x-ray images were down-sampled to 600 × 300 pixels (0.714 × 0.714 mm^2) and the CT volume was down-sampled to 256 × 256 × 480 (0.966 × 0.966 × 0.602 mm^3) to fit the GPU memory size. The 2D-3D registration was applied to each image frame independently. An initial estimate for the optimization in the first time frame was provided manually and subsequent frames used the result of the previous frame as its initial estimate.

The optimization routine (Fig. 18.3) iterated until the convergence criteria was met. To avoid premature termination while minimizing unnecessary iterations, the criterion was chosen as a tolerance in the pose parameter (input) space, such that the change for each axis in one generation becomes less than 0.1 mm for translations and 1° for rotations.

18.3 Results

Results were calculated for two primary cases to highlight the effect of 2D-3D registration: the first is a frontal loading case at 1,000 kPa driver pressure, and the second is a lateral loading case at the same driver pressure. Frontal loading is expected to result in motion primarily in the sagittal plane, whereas lateral loading is expected to cause multi-axis rotation due to asymmetry of the anatomy in the loading profile. Results from the 2D-3D technique are compared to 2D based tracking using landmarks on the skull in both cases.

The average execution time for each image frame was 3.96 s using a system with 2 CPUs (Intel Xeon, 2.40 GHz) and 1 GPU (nVidia, GeForce GTX 690). The algorithm converged after an average of 3,063 function evaluations (DRR generation and GI computation). Figure 18.4 shows the convergence of the translation and rotation parameters as well as the similarity metric. In each case the deviation of translation and rotation parameters from its initial estimate (prior frame) were plotted. The transformation parameters converged in about 2,000 iterations as the similarity metric approached its maximum value (i.e. the difference between GI and GI_{max} was reduced).

The 3D kinematics of skull motion for a frontal loading case with time sequential x-ray images is shown in Fig. 18.5. The correspondence between the acquired x-ray and the DRR can be visualized directly from the lateral views, while the frontal and side views are inferred from the registration algorithm output.

The head rotation angles corresponding to the images in Fig. 18.5 are shown in Fig. 18.6. The response phase involves an initial flexion angle of 4.9°, followed by rapid extension to a maximum of 58.5°. The out-of-plane rotation for this test reached a maximum axial rotation of 14.3° (to the left) at 241 ms. Test results were compared to manual 2D angle calculation by selecting rigid landmarks from the x-ray images. Flexion angle results agreed within 4.1°.

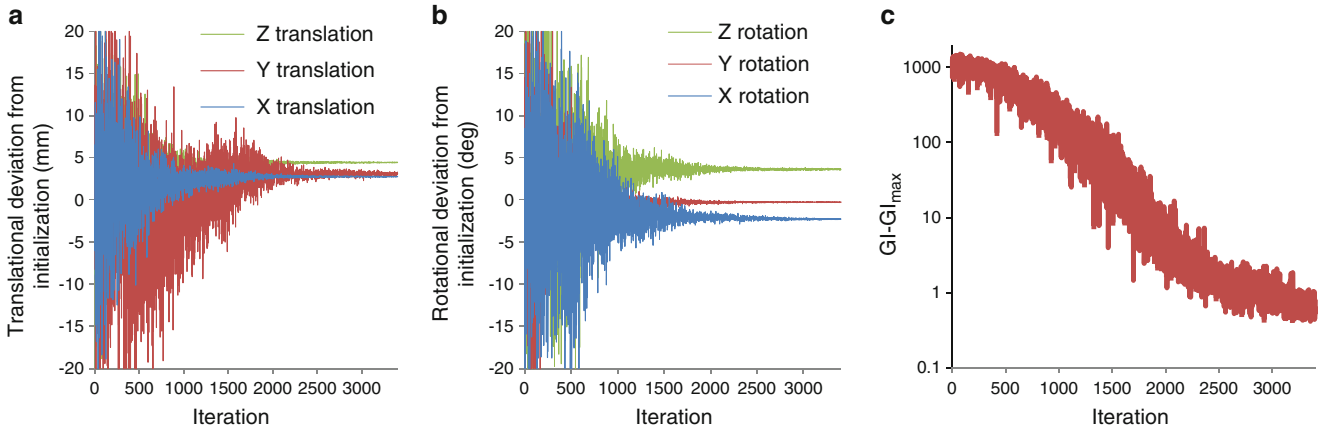

Fig. 18.4 Convergence of six transformation parameters and the similarity metric value for a single time step: (**a**) translational and (**b**) rotational deviation from its initialization as a function of number of iterations, and (**c**) similarity metric GI approaching maximum value GI_{max} (Note: the X-axis is directed forward (rostral), the Y-axis points to the left, and the Z-axis points in the superior direction (cranial))

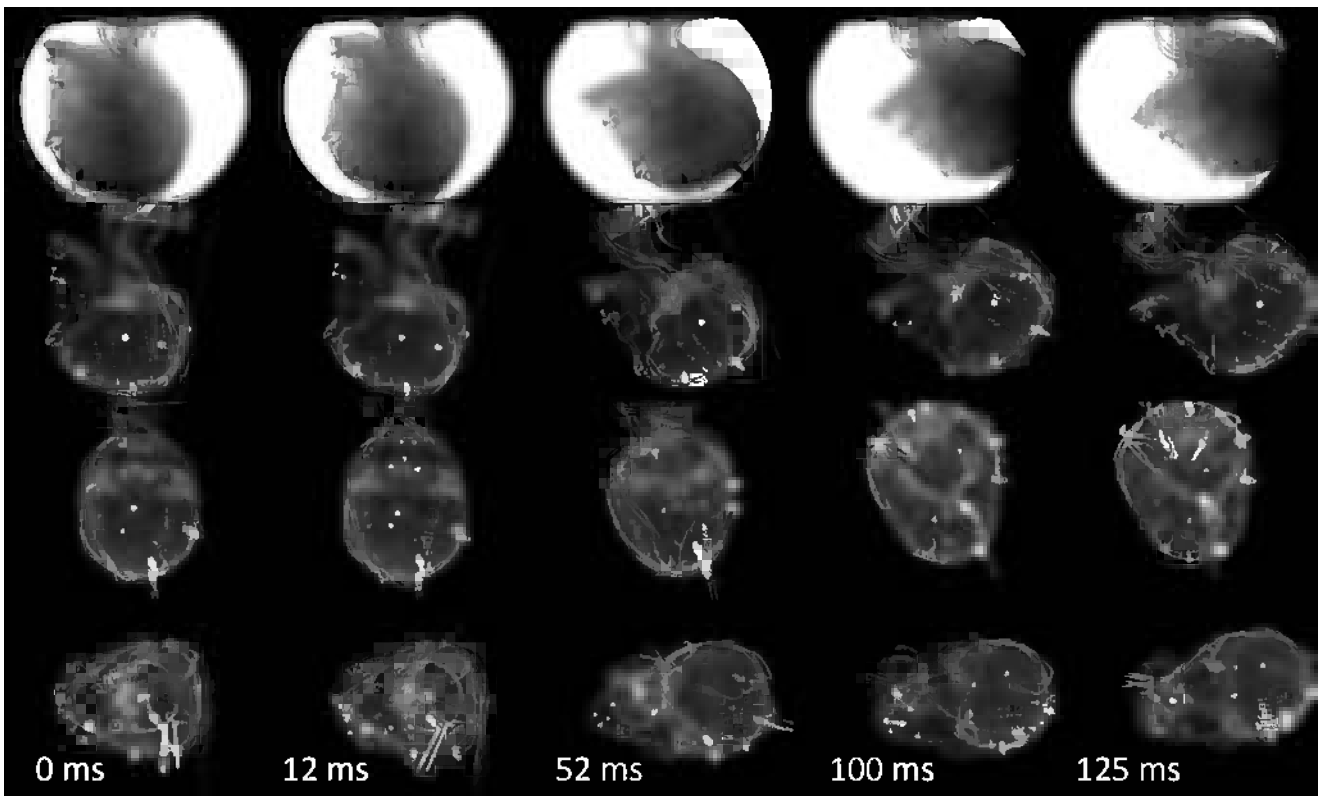

Fig. 18.5 3D kinematics of the skull motion computed by a single image 2D-3D registration (front facing test, 1,000 kPa). The *first row* shows acquired x-ray projection images, the remaining rows show DRRs of the CT scan at the estimated pose of the skull from the side (*second row*), front (*third row*), and *bottom* (*fourth row*)

In contrast to the frontal loading test, loading to the left side of the head is shown in Fig. 18.7. In this case, due to anatomical asymmetry, a more complex response is expected. The predominant initial rotation is lateral bending, which reaches a maximum of −32.3° at 50 ms. Significant out-of-plane rotations are apparent with a maximum axial rotation of 45.2°(positive angle to the left). Results are compared to the 2D only tracking method and show agreement only within the first 50 msec with a peak lateral bending of −31.9° versus −32.9 for 2D-3D and 2D respectively. Response diverges with increased out-of-plane rotations (axial rotation) from 100 to 250 ms with a maximum difference of 21.1°.

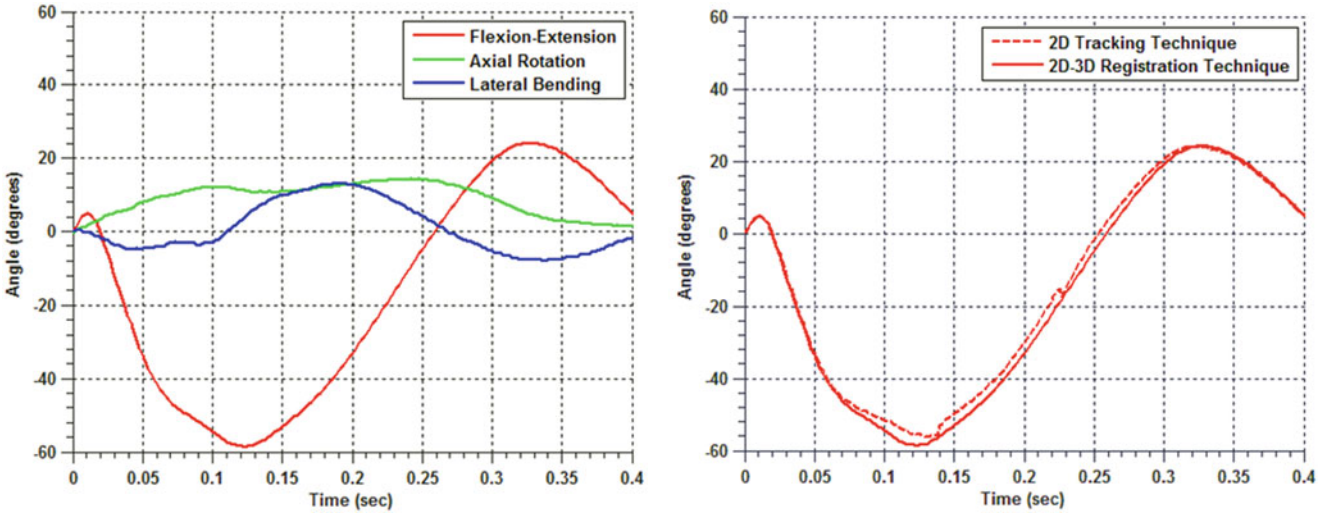

Fig. 18.6 Frontal loading head response angles using 2D-3D registration (*left*) and comparison to 2D analysis (*right*). The dominant response occurs in extension (negative angle) while out-of-plane rotations (axial rotation, lateral bending) remain relatively constant throughout

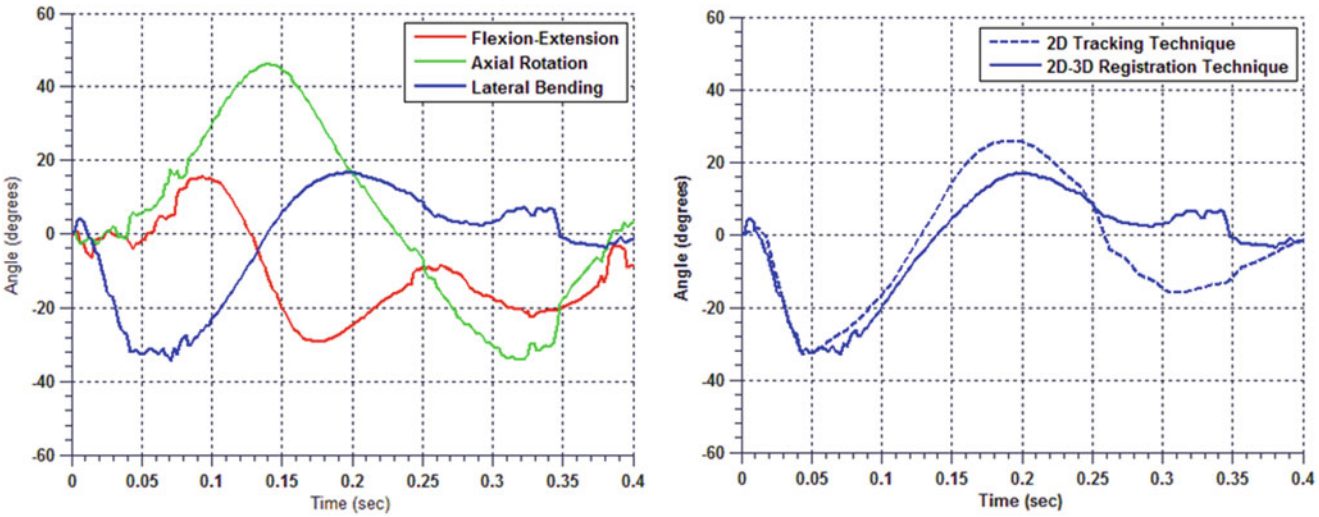

Fig. 18.7 Lateral (*left side*) loading response angles. After the maximum lateral rotation occurs, out of image plane rotations dominate the response in this complex loading scenario

18.4 Discussion

The results presented in this paper demonstrate the implementation of 2D-3D registration for use in a high-speed shock tube environment to measure 3D kinematics of the skull using a single x-ray source. Results are shown comparing a traditional 2D angle measurement method versus the 2D-3D approach. For loading scenarios occurring primarily in a single plane (i.e. sagittal) the measured 2D angle is in close agreement due to the invariance of marker positions near the sagittal plane to small out of plane rotations. Theoretically, the marker relative distances are preserved proportional to the cosine of the out-of-plane angle, which for an out-of-plane rotation of 15° would be *cos(15°)* or a factor of 0.966 (a difference of 3.4 %). However, in a multi-axis case, large out-of-plane rotations can result in position artifacts. 2D-3D registration offers a method to recover the rotations using a single x-ray source.

The algorithm showed good agreement for loading cases in which motion occurred in a single primary plan. In cases where motion occurs primarily in one plane, the algorithm is useful for understanding and bounding the error for a pure 2D analysis. Additionally the algorithm was employed for non-symmetric multi-axis loading cases and quantified out-of-plane rotations for complex loading providing additional information for head kinematics. Quantifying kinematics is important

because head and neck motion significantly contributes to the inertial loading environment that influences secondary (kinematic) phase of brain response. Having an understanding of not only the primary motion but also the out-of-plane rotations can provide insight into injury mechanisms as well as validating response for high fidelity surrogate and computational models of the human body.

This study is limited in that the comparison metric for the 2D-3D results is computed for only a single plane. While our previous work focuses on validation of the 2D-3D registration approach, additional validation would involve using an independent tracking system to validate the out-of-plane rotations for our particular setup. Also, this study implemented a single x-ray imaging device due to experimental design restrictions, although the 2D-3D registration algorithm is equally applicable to the images acquired by a biplane x-ray imager. Finally, the current 2D-3D algorithm tracks only rigid body motion and at present is unable to track deformable 3D motion such as that of the brain within the skull directly.

Possible extensions of the registration approach include simultaneous optimization of 3D kinematics in all time frames. Our current approach applies 6DOF rigid registration to each x-ray image independently, thus the information about time-sequential transition between the images was only preserved in the initial guess of subsequent frames. Rather than treating the motion as independent time steps, we could alternatively formulate the optimization problem for continuous motion as a series of Fourier coefficients for X, Y, Z rotations and translations versus time. This approach would result in a smooth continuous movement, which reflects the real phenomenon.

Further research in the application of 2D-3D registration involves tracking piecewise rigid structures (e.g., articulated bones such as individual vertebral bodies or bones of the extremities) within a single frame. Implementing this approach has the potential to measure kinematics of individual vertebrae without the need for rigidly and invasively attached markers.

18.5 Conclusions

This study shows, for the first time, application of 2D-3D registration techniques for tracking head response to shock tube loading. The HSXR images were registered to a post-test CT scan using GPU accelerated intensity-based 2D-3D registration techniques to localize the source and detector positions with respect to the skull. GI between digitally reconstructed radiographs based on the CT scan compared to the recorded x-ray frames was used as a cost function for a CMA-ES genetic algorithm. As compared to a pure 2D tracking using template matching, 2D-3D registration captures the out-of-plane motion by fully leveraging information in the projection image and prior information from 3D CT scan. Ongoing research focuses on incorporation of a priori knowledge of the brain deformation (e.g., finite element model) into the 2D-3D registration framework to elucidate 3D deformation of the brain and correlation to brain injury.

Acknowledgements This effort was funded by contract #W81XWH-09-2-0168. The U.S. Army Medical Research Acquisition Activity, 820 Chandler Street, Fort Detrick MD 21702–5014 is the awarding and administering acquisition office. The content included in this work does not necessarily reflect the position or policy of the U.S. government.

References

1. DoD worldwide numbers for TBI [Internet]. Available from: http://www.dvbic.org/dod-worldwide-numbers-tbi
2. Ravin R, Blank PS, Steinkamp A, Rappaport SM, Ravin N, Bezrukov L et al (2012) Shear forces during blast, not abrupt changes in pressure alone, generate calcium activity in human brain cells. PLoS One 7(6):e39421
3. Gennarelli TA, Thibault LE, Adams JH, Graham DI, Thompson CJ, Marcincin RP (1982) Diffuse axonal injury and traumatic coma in the primate. Ann Neurol 12(6):564–574
4. Gennarelli TA (1993) Mechanisms of brain injury. J Emerg Med 11(Suppl 1):5–11
5. Merkle AC, Wing ID, Carneal CM (2012) Effect of helmet systems on the two-phased brain response to blast loading. Personal armour systems symposium. Nuremberg
6. Roberts JC, Harrigan TP, Ward EE, Taylor TM, Annett MS, Merkle AC (2012) Human head-neck computational model for assessing blast injury. J Biomech 45(16):2899–2906
7. Ott KA, Armiger R, Wickwire A, Iwaskiw A, Merkle AC (2013) Determination of simple shear material properties of the brain at high strain rates. Dyn Behav Mater 1:139–147
8. Saraf H, Ramesh KT, Lennon AM, Merkle AC, Roberts JC (2007) Mechanical properties of soft human tissues under dynamic loading. J Biomech 40(9):1960–1967
9. Trexler MM, Lennon AM, Wickwire AC, Harrigan TP, Luong QT, Graham JL et al (2011) Verification and implementation of a modified split hopkinson pressure bar technique for characterizing biological tissue and soft biosimulant materials under dynamic shear loading. J Mech Behav Biomed Mater 4(8):1920–1928

10. Merkle AC, Wing ID, Carneal CM (2012) The mechanics of brain motion during free-field blast loading. In: ASME summer bioengineering conference, Fajardo
11. Hardy WN, Foster CD, Mason MJ, Yang KH, King AI, Tashman S (2001) Investigation of head injury mechanisms using neutral density technology and high-speed biplanar X-ray. Stapp Car Crash J 45:337–368
12. Bir C, Bolander R, Leonardi A, Ritzel D, VandeVord P, Dingell JD (2011) A biomechanical prospective of blast injury neurotrauma. RTO-MP-HFM-207 – a survey of blast injury across the full landscape of military science, Halifax
13. Sundararajan S, Prasad P, Demetropoulos CK, Tashman S, Begeman PC, Yang KH et al (2004) Effect of head-neck position on cervical facet stretch of post mortem human subjects during low speed rear end impacts. Stapp Car Crash J 48:331–372
14. Otake Y, Armand M, Armiger RS, Kutzer MD, Basafa E, Kazanzides P et al (2012) Intraoperative image-based multiview 2D/3D registration for image-guided orthopaedic surgery: incorporation of fiducial-based C-arm tracking and GPU-acceleration. IEEE Trans Med Imaging 31(4):948–962
15. Cernak I, Merkle AC, Koliatsos VE, Bilik JM, Luong QT, Mahota TM et al (2011) The pathobiology of blast injuries and blast-induced neurotrauma as identified using a new experimental model of injury in mice. Neurobiol Dis 41(2):538–551
16. Chintalapani G, Jain AK, Taylor RH (2007) Statistical characterization of C-arm distortion with application to intra-operative distortion correction. In: Proceedings of SPIE 6509, medical imaging 2007: visualization and image-guided procedures, San Diego, CA, USA
17. Pluim JP, Maintz JB, Viergever MA (2000) Image registration by maximization of combined mutual information and gradient information. IEEE Trans Med Imaging 19(8):809–814
18. Hansen N (2006) Towards a new evolutionary computation. In: Lozano JA, Larrañaga P, Inza I, Bengoetxea E (eds), Advances on Estimation of Distribution Algorithms, chapter the CMA evolution strategy: Studies in Fuzziness and Soft Computing, Vol. 192, XV, 294 p

Chapter 19
Dynamic Analysis of a Spread Cell Using Finite Element Method

Hwabok Wee and Arkady Voloshin

Abstract The dynamic analysis of a cultured cell using Finite Element Analysis is presented to understand the effect of vibration on a cell structure. The model of a spread cell on a culturing plate has been developed as a continuum model and a cellular tensegrity model. Using Finite Element modal analysis, natural frequencies and mode shapes of both models were obtained and compared with each other. Finite Element harmonic response analysis was carried out to investigate the dynamic response of a spread cell exposed to vibration in the frequency range of 1–60 Hz with 1 G acceleration. Both continuum model and tensegrity model showed that the first three natural frequencies appeared in range of 18 ~ 27 Hz and they were in the effective vibration frequency range for bone cell growth. In mode 1–3 the major oscillation was observed in horizontal direction and the resonance occurred when the base vibration frequency was closed to the calculated natural frequency. It is presumed that the optimal frequency for bone cell growth is closely related the natural frequency of cell structures and associated with the resonance of cellular structures. For better understanding resonance of cell structure future studies will consider the damping capability of cell structures.

Keywords Cell • Dynamic response • Vibration • Modal analysis • Harmonic response analysis

19.1 Introduction

The structural behavior of bone cells under mechanical loadings is important to understand how forces are transferred to bone cells and influence bone cell growth. In order to demonstrate the relationship between bone formation and the type of stimulation, mechanical stimulation to bone cells has been widely investigated using experimental and numerical studies. For experimental measurements of bone cells exposed to mechanical stimuli, compression force, stretching, fluid shear stress, and vibration have been used as mechanical stimulation in the many studies [1–5]. Among those studies, several studies utilized vibration as mechanical stimulation for cells. They have investigated the frequency range and amplitude of the vibration optimal for the growth of bone cells. The optimal vibration frequency and amplitude for cell proliferation, metabolic activity, and gene expression were observed when cultured osteoblast cell were exposed to a sinusoidal excitation in a frequency range from 20 to 60 Hz [3–5]. Rosenberg et al. [3] found that the optimal vibration for osteoblast proliferation was at 20 Hz frequency with 0.5 $\pm$ 0.1 m/s^2. Shikata et al. [4] showed that the vibration frequency at 50 Hz with 0.5 g caused 4.5 times higher ALP gene expression than that of the non-vibrating case.

Even though the effects of mechanical stimuli on cells have been investigated well, the study about the change of cellular structures according to the applied stimuli has been limited because of the difficulty of experimental measurement. Therefore, computational modeling of bone cells has been utilized to understand the response of bone cells to mechanical stimuli. In computational study for the structural analysis of cells, various modeling method, i.e. continuum model, tensegrity model, and so on, were utilized to analyze the characteristics of cellular structures. In addition, several elements,

H. Wee
Department of Orthopaedics and Rehabilitation, College of Medicine, Pennsylvania State University, Hershey, PA 17033, USA

A. Voloshin (✉)
Department of Mechanical Engineering and Mechanics, Lehigh University, 19 Memorial Drive West, Bethlehem, PA 18015, USA
e-mail: av01@lehigh.edu

F. Barthelat et al. (eds.), *Mechanics of Biological Systems and Materials, Volume 4*,
Conference Proceedings of the Society for Experimental Mechanics Series,
DOI 10.1007/978-3-319-00777-9_19,

such as structural components, mechanical properties, and input loading types have to be considered in computational modeling of cells for better understanding of the response of bone cells to mechanical stimuli. Cell elements, such as cytoplasm, nucleus, membrane and the internal cytoskeleton (microtubules and microfilaments) have been generally employed for cell models. A spreading chick embryo fibroblast cell adhered to a substrate was modeled with three dimensional geometrical images [6, 7]. It included an elliptical nucleus, a dome shape cytoplasm covered with a membrane, and an internal cytoskeleton structure composed of a tensegrity model. The tensegrity model consists of 6 struts, 24 cables, and 12 common nodes for microtubules, microfilaments, and actin filaments respectively. Nodal positions of the tensegrity model were adjusted to mimic a spreading cell shape. For focal adhesion sites, three nodes were constrained with three translation axes at the substrate surface. The nonlinear structural behavior of cells such as prestressed effects, strain hardening, variable compliance of the cell and the influence of mechanical property of cytoplasm were observed [6]. Using the same model, the response of bone cells with fluid shear stress and substrate strain loading were compared [7]. The deformation results showed that fluid flow shear stress resulted in a large vertical motion of the bone cell, the substrate strain induced deformation on the cell attachments. The additional results showed that the deforming effect of fluid flow shear stress was larger and more effective than the substrate strain loading case and that both mechanical stimuli played an independent role. A brain cell under impact loading was analyzed to examine the effect of several mechanical properties and model structures such as with or without cytoskeleton model [8]. A round brain cell in suspension was modeled as tensegrity model (prestressed cytoskeleton), continuum model (cytoplasm, nucleus, and membrane), and combined model. The viscoelastic behavior was applied to the cytoskeleton and continuum system respectively to study its influence on the dynamic response. They showed that tensegrity and continuum model with viscoelastic characteristics affected the dynamic response, such as displacement fluctuation and deflection change, and concluded that a combined model of tensegrity and continuum system would be good to analyze the prestressed cytoskeleton structure in the time domain. The cell strain distribution exposed to mechanical stimulation was investigated with the experimental method of Atomic Force Microscopy (AFM) and numerical simulation with Finite Element Method (FEM) and Computational Fluid Dynamics (CFD) [9]. Cell profiles and material property maps obtained by AFM were utilized to perform numerical simulations such as substrate stretch, fluid flow shear, intermittent hydrostatic pressure, microbead twisting, and micropipette poking. Measured small volume on the substrate was applied to the model of a cell and isotropic, linear elastic material properties were used. The effect of diverse mechanical stimuli, material property changes, Poisson ratio changes, the direction of application of stimulus, and fluid flow parameters were investigated.

In this work, Finite Element modal and harmonic base excitation analysis has been performed to provide better understanding for cellular structures exposed to vibration. Using continuum model and tensegrity model, the natural frequencies, mode shapes, and harmonic response of a spread bone cell model were obtained. The natural frequencies and mode shapes were compared according to the utilized model type (continuum model and tensegrity model). This study reveals that the natural frequency of a spread bone cell is in the optimal frequency range (1–60 Hz) for bone cell growth which was shown in previous experimental study [3, 4]. The applied harmonic excitation demonstrated the amplification of the structural amplitude around the calculated thee natural frequencies. These results are expected to serve as a reference in order to select the optimum frequency of the external vibrating loading in the future experimental research.

19.2 Method

In the bone cell culturing process, bone cells are adhering and spreading on a culturing plate after being seeded. A spread cell was modeled with continuum model and tensegrity model following previous studies [10, 11]. For continuum model, a bone cell adhered on the cell culture plate was considered as a simplified adherent ellipsoidal dome shape. The spread shapes of cells were various, but a shape was defined with one ellipsoidal shape since the natural frequency was not dependent on the shape of a spread cell [10]. The geometry information for continuum model was obtained from microscopy images [12, 13]. On the basis of available cell images the dimensions of adherent ellipsoidal dome structures were selected with the long (x) and short (z) axes equal to 100 × 40 μm with 10 μm height (y) (Fig. 19.1). The volume of cytoplasm of all shapes was 1.9e-14 m^3. The nucleus was also modeled as an ellipsoid with 8 × 5 × 5 μm (x × z × y) size, and its volume was 1.05 × e-16 m^3. The center of the nucleus was floating at 4.5 μm from the base. In the case of the continuum model, the details of microtubules, microfilament, and cell membrane were ignored, and the cells were modeled as structures composed of cytoplasm and nucleus.

The tensegrity model for a spread cell was based on a sphere with 18e-6 m diameter was modeled for a suspended single cell. A tensegrity structure was plugged into the sphere to represent the cytoskeleton of a cell (Fig. 19.2a). As shown in previous studies, six struts and twenty cables were employed to express microtubules and microfilaments

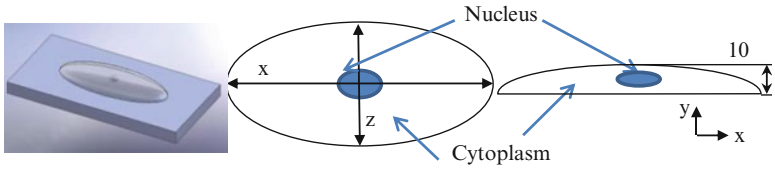

Fig. 19.1 A continuum model for a spread bone cell. A simplified ellipsoid dome shape (100 × 40 and 10 μm height) model includes cytoplasm and nucleus

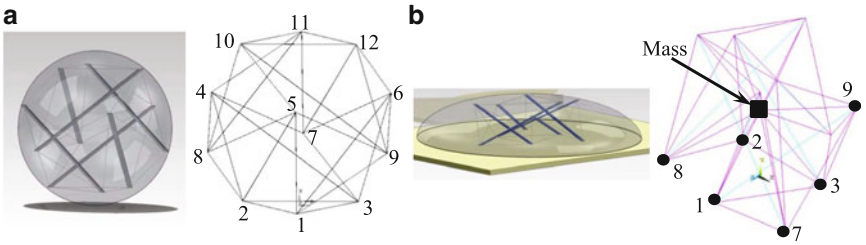

Fig. 19.2 Tensegrity models. (**a**) A tensegrity model for a suspended bone cell. (**b**) A tensegrity model for a spread bone cell. *Black dots* are the surface contacted locations of microtubules. A *red dot* is a mass for a single cell (color figure in online)

Table 19.1 Material properties of each cellular component [7]

Model components	Elastic modulus (Pa)	Poisson's ratio (ν)
Cytoplasm	100	0.37
Nucleus	400	0.37
Microtubules	1.2×10^9	0.3
Microfilaments/interfilaments	2.6×10^9	0.3

respectively [6, 11]. Additionally, nucleus was modeled on the center of tensegrity structure and connected to the end point of microtubules with interfilaments. The cross section area of microtubules and microfilament are 190 and 18 nm^2 respectively. Bottom nodes (node 1, 2, and 3) of three lower struts were anchored to surfaces similar to the phenomena which cell is adhered to surfaces after seeding. In order to mimic the cell spread shape, additional three nodes (node 7, 8, and 9) were moved vertically down with assumption which node 7, 8, and 9 were going down only in y direction when a cell spread. In Fig. 19.2b black dots represent the end of microtubules anchored on the surface, and a red dot shows a mass of a single cell (1 nanogram [14]) to compensate of small mass in tensegrity model.

Finite Element Analysis was performed with ANSYS 12.1(ANSYS Inc., Canonsburg, PA, USA). The utilized mechanical properties were assumed linear elastic (Table 19.1). The densities of cytoplasm, nucleus, microtubules, and microfilament were assumed as 125 kg/m^3 from the volume and mass of a typical cell [14, 15]. For continuum model, the ten-node (SOLID 187) high-order tetrahedral element was used to mesh cytoplasm and nucleus [16]. Tensegrity model used link 180, link10, mass 21 element types for microtubules, microfilaments, and nucleus respectively. Microfilament was assumed with no bending element and tension only assumption was employed for microfilaments.

Finite Element modal analysis and harmonic response analysis were utilized to obtain vibration characteristics of a spread bone cell. The natural frequencies and mode shapes were calculated by modal analysis, and the harmonic response analysis calculated the vibration amplitude of a spread bone cell model at a specific frequency range. The viscoelastic characteristics of a cell, which could cause damping effect, were ignored because a cell was modeled with very thin thickness and the lower frequency range was considered for harmonic analysis. The bottom of the continuum and tensegrity model was constrained in all translation directions to consider base excitation condition.

For modal analysis Block Lanczos method has been chosen to extract eigenvalues and eigenvectors from equation of motion for undamped free vibration with harmonic motion (Eq. 19.1). The first ten modes were obtained to find natural frequencies and mode shapes.

$$[M]\{\ddot{x}\} + [k]\{x\} = 0 \tag{19.1}$$

where $[M]$ and $[k]$ is a mass matrix and spring matrix respectively. $\{\ddot{x}\}$ and $\{x\}$ acceleration vector and displacement vector. Harmonic motion is $\{x\} = \{\phi\}\sin(\omega t)$ [17]. The obtained modal analysis results were used for harmonic analysis. The equation of motion response to base excited, shown in Eq. 19.2, was solved by the mode superposition method,

which express the displacement of structure using a linear combination of mode shapes [17]. Ten modes extracted from modal analysis were used for the mode superposition method.

$$[M]\{\ddot{x}\} + [c]\{\dot{x}\} + [k]\{x\} = -[M]\{\ddot{x}_g\} \tag{19.2}$$

where $\{\ddot{x}_g\}$ is the acceleration vector of the base motion. $[c]$ is a damping matrix: it was deleted with the assumption of no damping effect in the model. A large mass (1e5 kg) compared to the cell model was attached to the base of the structure and the interface between the base and the large mass was constrained as a rigid body. The large mass was excited in x, y, and z direction with 1 G acceleration to drive the base excitation of the cell structure.

19.3 Results and Discussion

The extracted eigenvalues and eigenvectors from modal analysis represented the natural frequencies and corresponding mode shapes. Table 19.2 gives the first five natural frequencies for continuum model and tensegrity model among the extracted ten natural frequencies. The first three natural frequencies were observed in the same frequency range of 18–26 in both continuum model and tensegrity model. The 4th mode of the tensegrity model jumped to high frequency over 10,000 Hz while the first five modes of the continuum model showed natural frequencies around 20 Hz. Generally the material property of structures is closely related to the natural frequencies. The higher natural frequency of the tensegrity model after 4th mode can be explained by the fact that the tensegrity model consisted of higher elastic modulus materials such as microtubules and microfilament compared to the cytoplasm and nucleus. The calculated natural frequencies of mode 1–3 for both models match with the experimental results shown in previous studies: the optimal vibration frequencies (20–60 Hz) were beneficial for bone cell growth [3, 4]. It is supposed that the vibration frequency close to the natural frequency might be able to affect the bone cell growth.

The first three mode shapes of the continuum model are shown in Fig. 19.3. The first and second modes showed one direction oscillation respectively in z and x directions. The nucleus inside cytoplasm also followed the oscillation of cytoplasm. The third mode caused two direction oscillations in z direction. Consequently, twisting oscillation about the y axis has been generated at the center part of the cytoplasm because of two opposite oscillations, and the nucleus was rotating about the y axis. Figure 19.4 shows the mode shapes of the tensegrity model. Because of lots of microtubules and microfilaments, mode shapes were expressed with arrows. The mode 1 and 2 produced z and x direction oscillation similar to the continuum model. However, the third mode showed vertical movement in y direction instead of two direction oscillation (Fig. 19.4). The observed mode 1 and 2 in both models indicate that the plane direction deformation might be a major deformation direction of a spread cell when it is vibrating around its natural frequency. Applying horizontal vibration to cell spread direction is possibly an optimal vibration type for an experimental design to promote bone cell growth.

The harmonic response of a spread bone cell exposed to base vibration was expressed with the displacement amplitude at the center of nucleus in Figs. 19.5 and 19.6. The rapid increase of the displacement amplitude was generally observed around the calculated natural frequencies regardless of model type. As described in mode shapes, the y direction amplitude increase of the continuum model was relatively less than x and z direction even though y direction base acceleration was applied (Fig. 19.5). In continuum model the horizontal amplitude increase was observed around 18–23 Hz, whereas the vertical amplitude increase was shown in the range of 29–37 Hz. The amplitude values seem to be a resonance at natural frequencies.

The harmonic response of the tensegrity model was dependent on the direction of the base excitation. In the tensegrity model the base excitation in x and z direction caused resonance at the calculated mode 1 (15 Hz) and mode 2 (17 Hz) while y direction base excitation showed a resonance in y direction at 27 Hz (mode 3) (Fig. 19.6).

In experimental studies [3, 4] the vibration was utilized with similar frequency range (20–60 Hz) to the calculated resonant frequencies, nevertheless cells were grown without structural damage. It is presumed that there might be a damping

Table 19.2 The natural frequencies of a spread bone cell according to the applied model type

Mode	Continuum model	Tensegrity model
1st mode	18.11	15.483
2nd mode	18.13	17.084
3rd mode	19.31	26.677
4th mode	20.87	10,614
5th mode	21.05	12,140

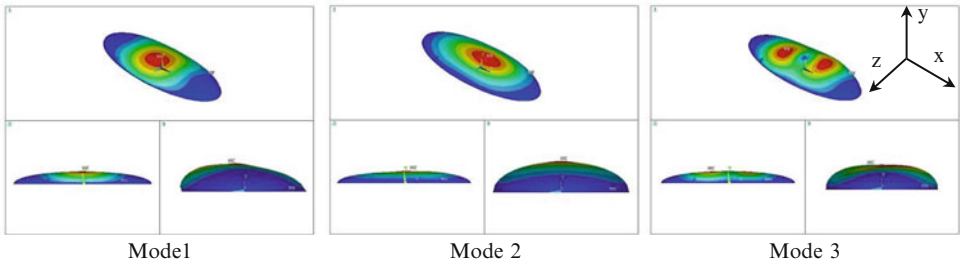

Fig. 19.3 The first three mode shapes of the continuum model for a spread cell [10]

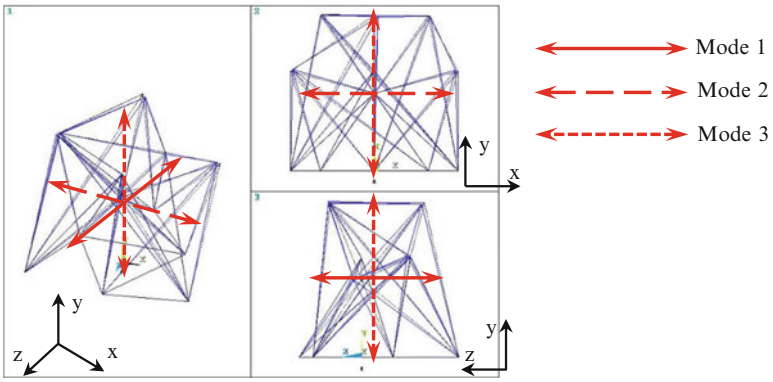

Fig. 19.4 The first three modes of the tensegrity model for a spread cell. *Solid line* represents the oscillation direction of mode 1, *dashed line* represents the oscillation direction of mode 2, and *dotted line* represents the oscillation direction of mode 3

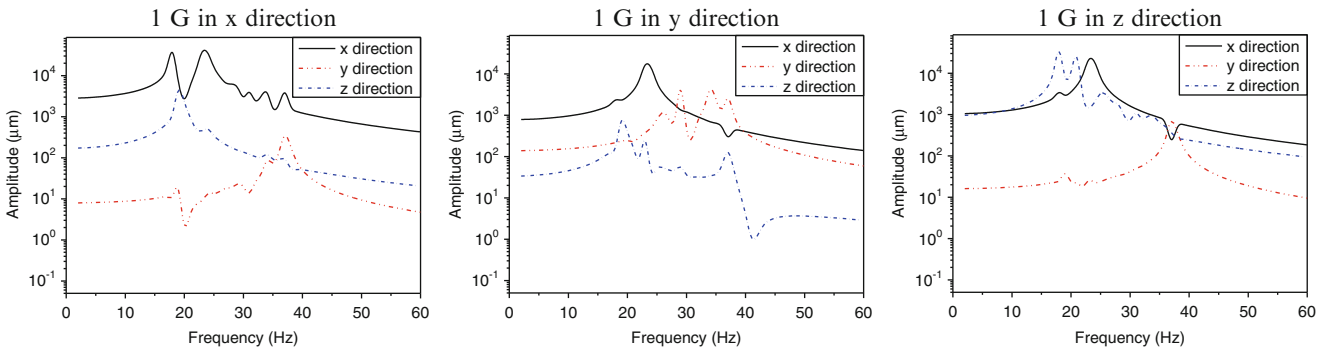

Fig. 19.5 Continuum model frequency response of x, y, and z displacement amplitude

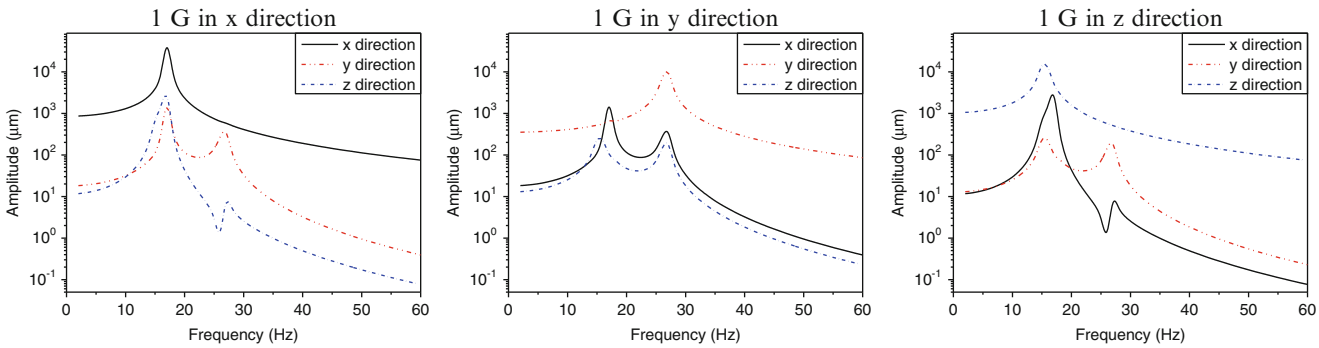

Fig. 19.6 Tensegrity model frequency response of x, y, and z displacement amplitude

ability in cell structure to relive or regulate the resonance. The use of damping capability of cell structures in modal analysis and harmonic response analysis could be expected to provide more accurate dynamic characteristics of cellular structures. Rosenberg et al. [3] reported that the optimal frequency for proliferation was around 20 Hz and the effective frequency for metabolism was around 60 Hz. The amplitude amplification in horizontal direction at the lower frequency (mode 1 and 2) might be related to cell proliferation. The observed amplitude amplification in vertical direction might have a correlation with cell metabolism since the amplitude amplification of the continuum model was observed in y direction.

19.4 Conclusion

The dynamic characteristics of a spread bone cell were analyzed using Finite Element Analysis. A spread bone cell was modeled with an ellipsoidal dome shape continuum model and a tensegrity cytoskeletal model. Using both models the natural frequencies and mode shapes were calculated and the response to harmonic base excitation was investigated. The calculated natural frequencies of mode 1, 2, and 3 (18–26 Hz) were in the range of the optimal vibration frequency range (20–60 Hz) for bone cell growth reported in previous studies. This result implies that the optimal vibration frequency for cell growth is closely associated with the natural frequency of cells. The damping characteristics of cellular structure are necessary to be considered to express the ability to absorb resonance of cell for future study. The oscillating direction of cell structures might have a relationship with two different optimal vibration frequencies for cell proliferation and metabolism.

References

1. Brown TD (2000) Techniques for mechanical stimulation of cells in vitro: a review. J Biomech 33(1):3–14
2. Hasegawa S, Sato S, Saito S, Suzuki Y, Brunette D (1985) Mechanical stretching increases the number of cultured bone cells synthesizing DNA and alters their pattern of protein synthesis. Calcif Tissue Int 37(4):431–436
3. Rosenberg N, Levy M, Francis M (2002) Experimental model for stimulation of cultured human osteoblast-like cells by high frequency vibration. Cytotechnology 39(3):125–130
4. Shikata T, Shiraishi T, Morishita S, Takeuchi R, Saito T (2008) Effects of amplitude and frequency of mechanical vibration stimulation on cultured osteoblasts. J Syst Des Dyn 2(1):382–388
5. Tanaka SM (1999) A new mechanical stimulator for cultured bone cells using piezoelectric actuator. J Biomech 32(4):427–430
6. McGarry J, Prendergast P (2004) A three-dimensional finite element model of an adherent eukaryotic cell. Eur Cell Mater 7:27–33
7. McGarry JG, Klein-Nulend J, Mullender MG, Prendergast PJ (2005) A comparison of strain and fluid shear stress in stimulating bone cell responses—a computational and experimental study. FASEB J 19(3):482–484
8. Abolfathi N, Karami G, Ziejewski M (2008) Biomechanical cell modelling under impact loading. Int J Model Simul 28(4):470–476
9. Charras GT, Horton MA (2002) Determination of cellular strains by combined atomic force microscopy and finite element modeling. Biophys J 83(2):858–879
10. Wee H, Voloshin A (2012) Modal analysis of a spreading osteoblast cell in culturing.In: Bioengineering conference (NEBEC), pp 1–2
11. Coughlin MF, Stamenovic D (1998) A tensegrity model of the cytoskeleton in spread and round cells. ASME J Biomech Eng 120:770–777
12. Single cell mechanobiology. http://www.nanofunction.org/single-cell-mechanobiology. Accessed 21 Jan 2012
13. Charras GT, Horton MA (2002) Single cell mechanotransduction and its modulation analyzed by atomic force microscope indentation. Biophys J 82(6):2970–2981
14. Chauhan AK, Varma AA (2009) Textbook of molecular biotechnology
15. Freitas RA (1999) Nanomedicine, vol I, Basic capabilities. Landes Bioscience Georgetown, Austin
16. ANSYS Element Reference, ANSYS Inc (2009)
17. ANSYS Theory Reference for the Mechanical APDL and Mechanical Applications, ANSYS Inc (2009)

Chapter 20
Imaging Targets to Identify Chromosomal Abnormalities in Cells

S. Acevedo-Acevedo, B. Napiwocki, and W.C. Crone

Abstract Ensuring genetic stability in pluripotent stem cell (PSC) cultures is essential for the development of successful cell therapies. Many laboratories have found the emergence of genetic abnormalities in PSCs when cultured in vitro for prolonged amounts of time. These cells are mostly cultured in non-physiological stiff substrates like tissue culture polystyrene which produces the suspicion that the cause of these abnormalities may be influenced by substrate mechanics. In order to verify this, it is important to be able to determine and image, using fluorescence microscopy, potential targets within the cells that are indicative of genetic abnormalities. These genetic abnormalities are most likely to occur during cell division. Microtubules, comprised of the cytoskeletal protein tubulin, organize and separate chromosomes during cell division, thus it has been our main imaging target. We have been able to detect chromosomal abnormalities in human embryonic stem cells by fluorescence microscopy.

Keywords Pluripotent stem cells • Chromosomal abnormalities • Cytoskeleton • Substrate stiffness • Immunofluorescence

20.1 Introduction

Pluripotent stem cells (PSCs) such as induced pluripotent stem cells (iPSCs) and embryonic stem cells (ESCs) are being widely researched for diverse applications such as cell therapies, disease modeling and drug screening. For these applications to be successful, it is important to conserve the genetic stability of these cells. In recent years, many laboratories have reported the emergence of chromosomal abnormalities in PSCs [1, 2, 6–9]. There are several mechanisms that lead to abnormal cell division. Figure 20.1 [3] depicts four common ways in which mitotic errors can lead to chromosomal abnormalities.

Previous work suggests evidence that substrate stiffness influences cell fate in PSCs. A recent study done by Holubcová et al. provides evidence that culture substrates on which human ESCs are grown on influence the frequency of supernumerary centrosomes [5]. In 2011, Zoldan et al. showed that human ESCs were able to differentiate into specific cell types of all three germ layers when placed in 3D scaffolds with stiffness values respective to each germ layer [11]. Although the root cause is still an open question, a common factor between the different abnormal cell lines obtained is that they were cultured in stiff substrates like plastic. This leads to the hypothesis that substrate mechanics affect cell division in PSCs and promote incorrect segregation of chromosomes. To prove this, we have imaged, using fluorescence microscopy, key proteins in human ESCs that are involved in cell division.

S. Acevedo-Acevedo • B. Napiwocki
Department of Biomedical Engineering, University of Wisconsin-Madison, Madison WI 53706, USA

W.C. Crone (✉)
Department of Biomedical Engineering, University of Wisconsin-Madison, Madison WI 53706, USA

Department of Engineering Physics, University of Wisconsin-Madison, Madison WI 53706, USA
e-mail: crone@engr.wisc.edu

F. Barthelat et al. (eds.), *Mechanics of Biological Systems and Materials, Volume 4*,
Conference Proceedings of the Society for Experimental Mechanics Series,
DOI 10.1007/978-3-319-00777-9_20,

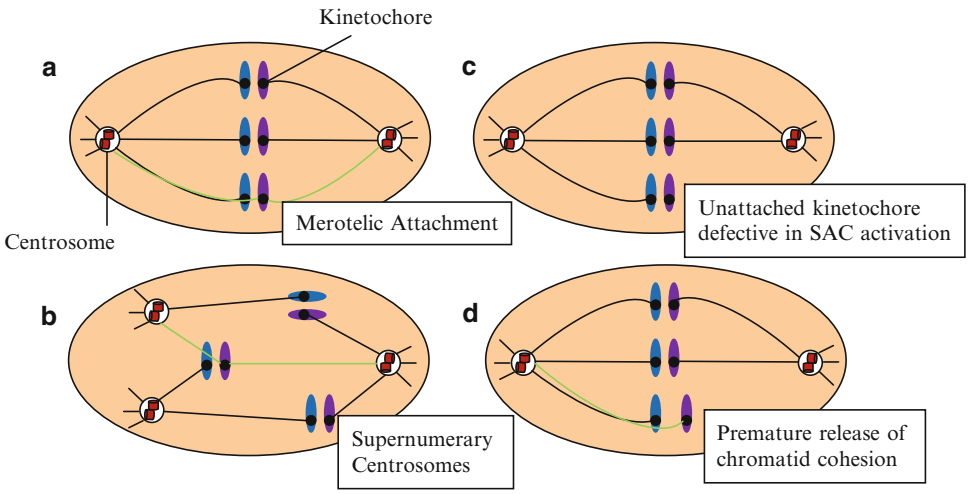

Fig. 20.1 Mechanisms that lead to abnormal cell division. Figure (Adapted from [3]) depicts four common ways in which mitotic errors can lead to aneuploidy; (**a**) Merotelic attachments (microtubules from both spindle poles attach to the kinetochore of the same chromosome causing lagging chromosomes); (**b**) supernumerary centrosomes (additional centrosomes); (**c**) Spindle Assembly Checkpoint (SAC) defects (cells may enter anaphase without proper attachment of all chromosomes); (**d**) chromosome cohesion defects (chromatids separate prematurely)

20.2 Methods

20.2.1 Human Embryonic Stem Cell Culture

H9 human ESCs (WiCell) were maintained in 6-well tissue culture polystyrene (TCPS) plates (BD Bosciences) coated with 8.3 μg/cm^2 Matrigel (BD Bosciences). Cells were passaged every 4–5 days by incubating with Versene (Life Technologies) for 5 min. Cells were removed from the surface of the TCPS plates by washing with mTeSR1 (WiCell) and transferred to a 15 mL conical tube (Corning). Cells were suspended in 6 mL mTeSR1 and 5 mM ROCK inhibitor (Tocris) was added at a ratio of 1:1000. Cell suspension was added to Matrigel-coated TCPS plates at a ratio of 1:12. Human ESCs were incubated at 37 °C, 5 % CO_2 and in mTeSR1 media which was changed daily. Matrigel coating of TCPS plates was done by resuspending 0.5 mg Matrigel in 6 mL cold DMEM/F12 (Life Technologies) and adding 1 mL/well to a 6-well TCPS plate.

20.2.2 Substrate Polymerization and Cell Seeding

Polydimethylsiloxane (PDMS) substrates were synthesized by adding SYLGARD 184 Silicone Elastomer Curing Agent (Dow Corning) to SYLGARD 184 Silicone Elastomer Base (Dow Corning) at a ratio of 1:10. Once thoroughly mixed, the polymer solution was placed into vacuum for 45 min. A transparency sheet was placed at the interface between the polymer and the glass petri dish lid. Glass coverslips and 1 mm microscope slides were used as spacers for the 0.17 mm and 1 mm thick PDMS, respectively. After applying vacuum, the PDMS mixture was poured in the center of the petri dish without covering the spacers. Another transparency sheet was placed on top of the polymer mixture followed by an inverted petri dish lid. The mold was placed on a hot plate at 80 °C for 4 h. After polymerization, samples were carefully removed from the petri dish mold and placed in an extractor for 4 h to remove toxic residues. PDMS squares were cut out using a scalpel and placed on 12-well TCPS plates where they were coated with 8.3 μg/cm^2 Matrigel for 1 h at 37 °C. Cells were seeded onto the gels using the same passaging method and cell concentration described in the previous section. Cell media was changed every day.

The procedure for polyacrylamide (PA) hydrogel synthesis follows a method previously described by Hazeltine et al. [4]. Pre-polymer stock solutions were prepared by adding 10 % acrylamide (Acros Organics) and 0.03–0.6 % N,N′-methylenebisacrylamide (Acros Organics) and stored in glass vials at 4 °C. Aliquots of pre-polymer solutions were warmed to room temperature and placed under vacuum for degassing. Hydrogels were polymerized between two glass petri dish lids which were treated with Rain-X (ITW Global Brands), and 1 mm

PDMS spacers were used to control gel thickness. For polymerization, 5 % (w/v) ammonium persulfate (Acros Organics) and 5 % (v/v) *N*,*N*,*N*′,*N*′-tetramethylethylenediamine (TEMED, Sigma) were added to the pre-polymer solution at a ratio of 1:100. The solution was poured onto the petri dish base and covered with the inverted petri dish lid. After 75 min, 50 mM HEPES (Sigma) buffer, pH 8.5, was added to petri dish molds to stop polymerization and hydrate the gels. PA hydrogels were allowed to swell in HEPES buffer for 1–2 days.

Using a 1.59 cm punch cutter (Grainger), circular PA hydrogels were cut out from the polymer slab. They were functionalized for protein adhesion by drying 60 μL/gel of 1 mM *N*-Sulfosuccinimidyl-6-(4′-azido-2′-nitrophenylamino) hexanoate (sulfo-SANPAH, Pierce) in HEPES buffer on a hot plate at 60 °C for 90 min. The gels were then exposed to UV light (365 nm, 4 mW/cm^2) for 50 min. Sulfo-SANPAH addition and UV exposure steps were repeated once. Gels were rehydrated in phosphate buffered saline (PBS, Invitrogen) and placed in 12-well TCPS plates. They were exposed to germicidal UV for 30 min and subsequently coated with 8.3 μg/cm^2 Matrigel and stored overnight at 37 °C.

Cells were seeded onto the gels using the same passaging method and cell concentration described in the previous section. Cell suspension was diluted to a density of 500,000 ESCs/mL and ROCK inhibitor was added at a ratio of 1:1000. Plates with Matrigel-coated PA were placed in a biosafety cabinet under germicidal UV for 20 min. The PBS was aspirated from the wells and using tweezers, a sterilized 12 mm circular Raschig Ring (Sigma) was placed on top of the center region of each gel. Using a micropipette, 0.5 mL cell suspension was added to the center of each raschig ring. The plates were carefully placed in the incubator at 37 °C. The next day, the raschig rings were removed and 1 mL/well of fresh mTeSR1 media was added. Cell media was changed every day.

20.2.3 Fluorescence Staining

In preparation for staining, we fixed human ESCs by adding 4 % paraformaldehyde (Electron Microscopy Sciences) in PBS to each well for 15 min. Cells were washed twice with PBS and permeabilized with 0.1 % Triton X-100 (Sigma) for 15 min. After two PBS washes, cells received different treatments based on the type of stain used. For actin staining, 2 % phalloidin tetramethylrhodamine B isothiocyanate (Sigma) in PBS was added to each well and incubated for 45 min. For α-tubulin staining, blocking solution containing 0.1 % Triton X-100, 2 % goat serum, 5 % (w/v) BSA in PBS, was added to each well for 30–90 min. Primary antibody against α-tubulin (Mouse monoclonal DM1A to Anti-α tubulin, Sigma) was added at a dilution of 1:1000 and incubated for 2 h at room temperature or overnight at 4 °C. After incubation with primary antibody, cells were washed for 5 min with PBS. During the wash, the plate was gently rocked. This step was repeated twice. Goat polyclonal secondary antibody to mouse IgG – H&L conjugated to DyLight 488 (Abcam) was added at a dilution of 1:500 and incubated for an hour. Cells were washed again with PBS for 5 min. During the wash, the plate was gently rocked. This step was repeated two more times. After actin or α-tubulin staining, cells were washed twice with PBS and two drops of 4′,6-diamidino-2-phenylindole (DAPI; Life Technologies) were added to each well and incubated for 30–60 min.

20.2.4 Sample Preparation for Imaging

PDMS or PA gels were removed from TCPS plates and placed on glass coverslips (Fisher) with the side containing the cells facing upward. No. 1 glass coverslips (Fisher) were then placed on top of the polymer substrates. Cells were imaged using a Nikon Eclipse T*i* inverted microscope system.

20.3 Results

To determine the effect of stiffness on human ES cell division, we cultured genetically normal and abnormal hESCs on substrates with different Young's modulus values between 1 kPa and 100 kPa. Our initial substrate was PDMS coated with a thin layer of Matrigel (which is a combination of extracellular matrix proteins, mainly laminin) to facilitate cell attachment. We controlled the stiffness sensed by the cells by varying the thickness from 0.17 mm (coverslip-thin) to 1 mm. We also cultured human ESCs on glass coverslips as controls.

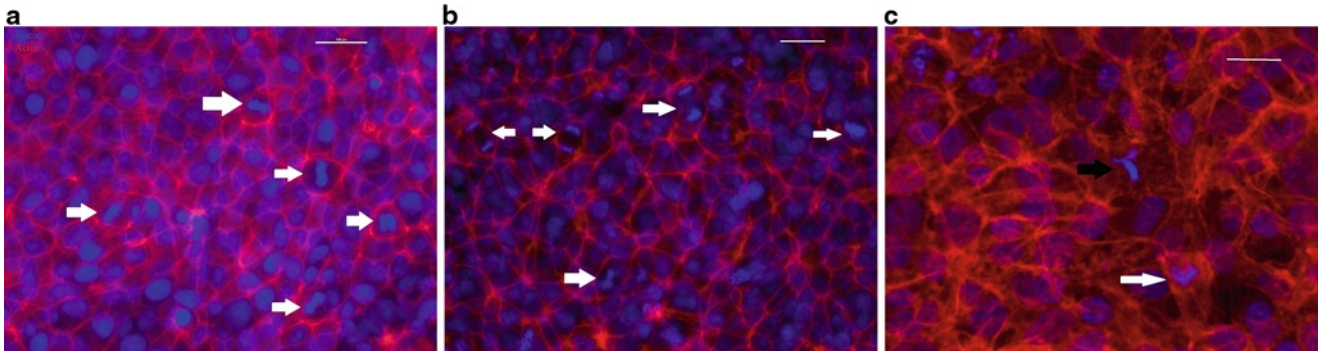

Fig. 20.2 Epifluorescent actin/nuclei co-stain of abnormal human ESCs grown on Matrigel-coated PDMS or coverslips. White arrows point to dividing cells. (**a**) Human ESCs cultured on Matrigel-coated 0.17 mm PDMS; (**b**) Human ESCs cultured on Matrigel-coated 1 mm thick PDMS; (**c**) Human ESCs cultured on Matrigel-coated glass coverslips. *Black arrow* points to a potentially abnormal cell division based on the Y-shape organization of the DNA. Scale bars = 50 μm

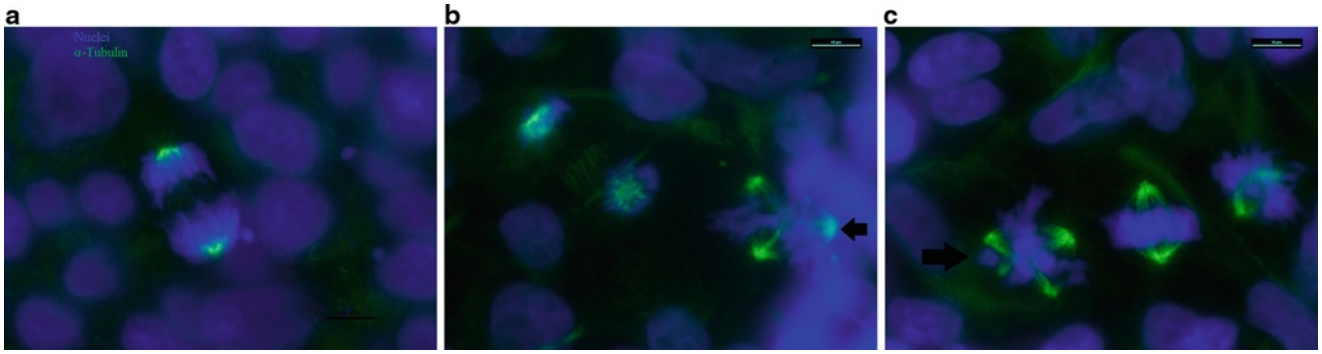

Fig. 20.3 Epifluorescent α-tubulin/nuclei co-stain of normal human ESCs grown on Matrigel-coated PA hydrogels or coverslips. Black arrows point to abnormally dividing cells. (**a**) Human ESCs cultured on Matrigel-coated 0.6 % PA. Cell undergoing normal anaphase shows a bipolar mitotic spindle (two centrosomes; *bright green dots*). (**b**) Human ESCs cultured on Matrigel-coated 0.6 % PA. The cell on the right displays abnormal metaphase showing a tripolar mitotic spindle (three centrosomes). On the *left side*, another human ESC is shown undergoing normal late anaphase/early telophase. (**c**) Human ESCs cultured on Matrigel-coated glass coverslip. Three cells shown in metaphase with the left most cell showing an abnormal metaphase with a tetrapolar mitotic spindle (four centrosomes). Scale bars = 10 μm (color figure in online)

While culturing cells in PDMS, we stained for the cytoskeletal protein actin, with the goal of determining if there were differences in actin organization between the different stiffness conditions. As can be seen in Fig. 20.2, we were not able to quantify significant differences between the conditions. We were concerned that with this system the cells were not able to sense the stiffness of the underlying substrate. For this reason, we decided to use PA hydrogels as a new substrate on which to culture human ESCs. This synthetic polymer has been used for many biomedical applications, more recently in human ESCs [4, 10]. We altered the mechanical properties of these gels by varying the bisacrylamide cross-linker concentration from 0.03 % to 0.6 %.

By staining for DNA using DAPI, we were able to identify dividing cells based on the nuclear morphology. However, we detected cells that had an unusual Y-shaped morphology (Fig. 20.2c). We hypothesized that these cells were undergoing abnormal cell division and potentially had three centrosomes which would explain their unusual shape. Nevertheless, without a tubulin stain to detect mitotic spindles it was not possible to say with certainty that these were abnormally dividing cells. To solve this problem, we visualized the mitotic spindle, made up of microtubules, utilizing a monoclonal anti-α tubulin antibody stain. By staining for α-tubulin, we were able to observe formation of the mitotic spindle and chromosome segregation during mitosis and identify supernumerary centrosomes (Figs. 20.1b and 20.3b, c).

For future studies, we plan on incorporating additional antibody stains that will allow us to visualize these abnormal events more clearly and employ high throughput methods for quantification such as flow cytometry. We will label cells with a mitosis marker to easily separate dividing cells from non-dividing ones. Furthermore, we will use a centrosome marker to quantify the number of centrosomes per dividing cells. By imaging these protein targets in human ESCs cultured on substrates of varied stiffness, we are able to identify chromosomal abnormalities. This will allows us to quantify them and determine if there is a significant influence of the different stiffness conditions on the presence of abnormalities.

20.4 Conclusions

Culturing human ESCs on PDMS substrates did not reveal differences in actin organization and did not give us information about structural abnormalities in mitotic spindle formation (e.g. additional centrosomes); however our original hypothesis cannot be disproved at this point. PA hydrogels will allow us to synthesize substrates encompassing a large range of E values which will be used in future experiments. Imaging microtubules in conjunction with DNA allowed us to visualize the mitotic spindle at the different phases of cell division. This stain also enabled us to identify supernumerary centrosomes due to the bright staining concentrated at the poles.

Acknowledgements This research was supported with funds from the National Institutes of Health Grant K18 HL105504 from the Heart, Blood and Lung Institute and the Graduate School of the University of Wisconsin-Madison. S. Acevedo-Acevedo has been supported by the Graduate Engineering Research Scholars program of the University of Wisconsin-Madison. The authors would like to thank William Bement, Max Salick, Chandler Benjamin and the Kamp/Lyons Lab Group for helpful conversations.

References

1. Catalina P, Montes R, Ligero G, Sanchez L, de la Cueva T, Bueno C, Leone P et al (2008) Human ESCs predisposition to karyotypic instability: is a matter of culture adaptation or differential vulnerability among hESC lines due to inherent properties? Mol Cancer 7(1):76
2. Draper JS, Smith K, Gokhale P, Moore HD, Maltby E, Johnson J, Meisner L et al (2004) Recurrent gain of chromosomes 17q and 12 in cultured human embryonic stem cells. Nat Biotech 22(1):53–54
3. Gordon DJ, Resio B, Pellman D (2012) Causes and consequences of aneuploidy in cancer. Nat Rev Genet 13(3):189–203
4. Hazeltine LB, Simmons CS, Salick MR et al (2012) Effects of substrate mechanics on contractility of cardiomyocytes generated from human pluripotent stem cells. Int J Cell Biol 2012(Article ID 508294):1–13
5. Holubcová Z, Matula P, Sedláčková M, Vinarský V, Doležalová D, Bárta T, Dvořák P et al (2011) Human embryonic stem cells suffer from centrosomal amplification. Stem Cells 29(1):46–56
6. Imreh MP, Gertow K, Cedervall J, Unger C, Holmberg K, Szöke K, Csöregh L et al (2006) In vitro culture conditions favoring selection of chromosomal abnormalities in human ES cells. J Cell Biochem 99(2):508–516
7. Laurent LC, Ulitsky I, Slavin I, Tran H, Schork A, Morey R et al (2011) Dynamic changes in the copy number of pluripotency and cell proliferation genes in human ESCs and iPSCs during reprogramming and time in culture. Cell Stem Cell 8(1):106–118
8. Mayshar Y, Ben-David U, Lavon N, Biancotti J-C, Yakir B, Clark AT et al (2010) Identification and classification of chromosomal aberrations in human induced pluripotent stem cells. Cell Stem Cell 7(4):521–531
9. Mitalipova MM, Rao RR, Hoyer DM, Johnson JA, Meisner LF, Jones KL, Dalton S et al (2005) Preserving the genetic integrity of human embryonic stem cells. Nat Biotech 23(1):19–20
10. Pelham RJ, Wang Y (1997) Cell locomotion and focal adhesions are regulated by substrate flexibility. Proc Natl Acad Sci 94(25):13661–13665
11. Zoldan J, Karagiannis ED, Lee CY, Anderson DG, Langer R, Levenberg S (2011) The influence of scaffold elasticity on germ layer specification of human embryonic stem cells. Biomaterials 32(36):9612–9621

Chapter 21
3D Neutrophil Tractions in Changing Microenvironments

Jennet Toyjanova, Estefany Flores-Cortez, Jonathan S. Reichner, and Christian Franck

Abstract The mechanical properties and geometry of the surrounding microenvironment play a significant role in regulating cellular behavior including cell adhesion, migration and generation of traction forces. In many 3D tissue culture scenarios, changing the local matrix geometry, or cellular confinement simultaneously alters matrix stiffness, which makes the two physical factors coupled. In this study we design an interchangeable 2D-3D sandwich gel structure system with tunable mechanical properties capable of changing matrix stiffness and cellular confinement independently. Using a double-hydrogel system and our previously developed 3D TFM technique we investigate neutrophil migration and traction forces as a function of varying matrix stiffness and confinement.

Keywords 3D Cell traction forces • Matrix dimensionality • Neutrophil • Digital volume correlation • Double-hydrogel-system

21.1 Introduction

In recent years, the importance of mechanical forces in directing cellular function has been recognized as a significant factor in biological and physiological processes. In fact, these physical forces are now viewed equally as important as biochemical stimuli in controlling cellular response. Not only do these cellular forces, or cell tractions, play an important role in cell migration, they are also significant to many other physiological and pathological processes, both at the tissue and organ level, including wound healing, inflammation, angiogenesis, and embryogenesis. A complete quantification of cell tractions during cell-material interactions can lead to a deeper understanding of the fundamental role these forces play in cell biology. Thus, understanding the function and role of a cell from a mechanical framework can have important implications towards the development of new implant materials and drug treatments.

Previous research has contributed significant descriptions of cell-tissue interactions by quantifying cell tractions in two-dimensional environments; however, most physiological processes are three-dimensional in nature [1, 2]. Several studies have shown morphological differences in cells cultured on two-dimensional substrates versus three-dimensional matrices, and that the intrinsic extracellular matrix interactions and migration behavior are different in three dimensions versus two dimensions[3–8].

Several experimental techniques and in-vitro surrogate material systems have been developed to address this issue and to capture certain microenvironmental cues that native 3D in-vivo environments provide. Fibrous gels, like collagen, fibrin, and Matrigel are composed of adhesive ligands and contain proper structural topography and are a natural choice for

J. Toyjanova (✉) • C. Franck
School of Engineering, Brown University, Providence, RI 02906, USA
e-mail: Jennet_Toyjanova@brown.edu

E. Flores-Cortez • J.S. Reichner
Department of Surgery, Rhode Island Hospital and the Warren Alpert Medical School of Brown University, 182 Hope St, Providence, RI 02912, USA

F. Barthelat et al. (eds.), *Mechanics of Biological Systems and Materials, Volume 4*,
Conference Proceedings of the Society for Experimental Mechanics Series,
DOI 10.1007/978-3-319-00777-9_21,

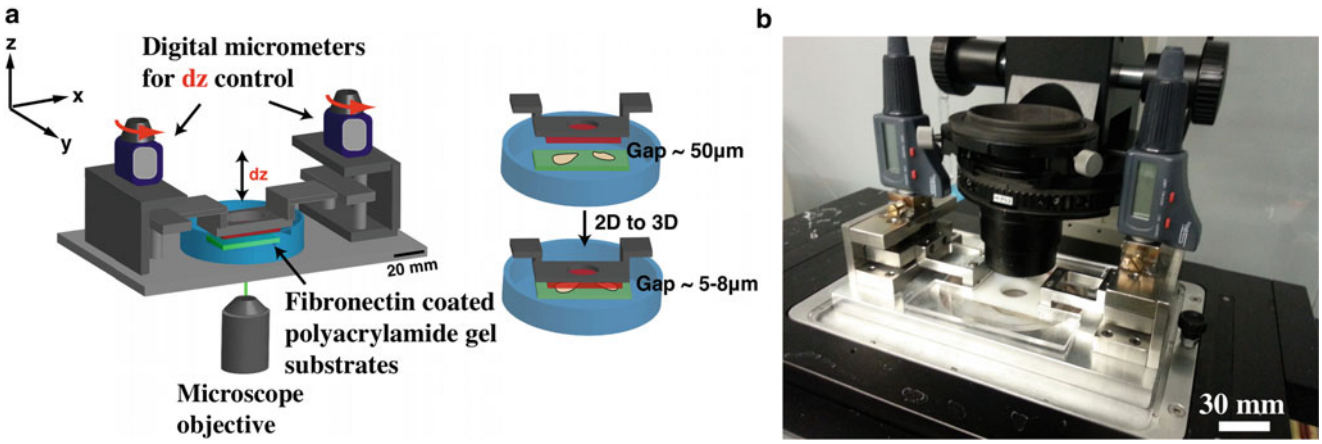

Fig. 21.1 (**a**) Schematic overview of our custom-built micro-manipulator to switch from a 2D to a confined 3D neutrophil gel-system. (**b**) Picture of the double-hydrogel system mounted on top of aconfocal microscope stage

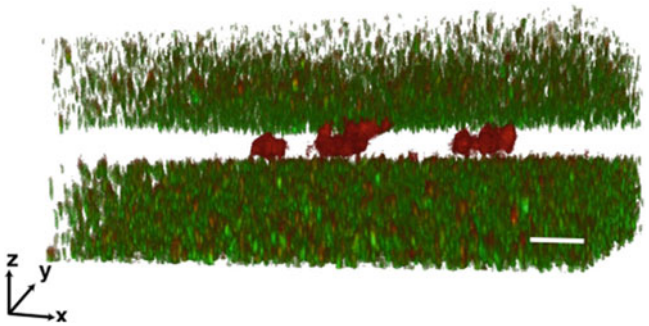

Fig. 21.2 Visualization of closed double-hydrogel system with *top* and *bottom* substrates impregnated with *green* fluorescent microspheres. Fluorescently labeled neutrophils (*red*) migrating between two substrates. Scale bar = 10 μm (color figure in online)

mimicking 3D cellular environments [2]. However, these materials are challenging to use for direct comparisons to investigate the effect of individual material cues on cells including matrix stiffness and geometry. By switching from a planar 2D system to a fibrous 3D system, not only does the dimensionality of the environment change, but also the local topography, ligand density, and nutrient transport, thus making it difficult to study the effect of a particular microenvironmental feature on cell behavior in isolation[2]. To address these challenges our objective was to create a simplified 3D system in which ligand density, mechanical properties, and local topography can be precisely controlled and varied independently of each other.

To achieve full spatial control of the geometry, topography and mechanical properties of the microenvironment we adapt a modified version of the polyacrylamide sandwich structure previously developed by Beningo et al. [3]. This particular double-hydrogel sandwich arrangement creates a vertically enclosed space, which permits cell-surface contact on both top and bottom cell surfaces simultaneously. This configuration creates a well-controlled confined geometry, which we will refer to as a 3D environment or 3D system throughout the remainder of this paper (Fig. 21.2). The reductionist experimental setup allows precise control of ligand density, mechanical properties and local topography, all of which can be varied independently of each other. Being capably of decomposing the mechanical and geometrical properties of a tissue microenvironment into the design of in-vitro experiments, may lead to a more robust and fundamental approach to identify key mechanistic pathways that are important in the pathophysiology of neutrophil function, as well as many other cell types (Fig. 21.2).

21.2 Experimental Design of an Interchangeable 2D-3D Sandwich Gel Culture System for 3D Traction Measurements

21.2.1 Fabrication and Mechanical Characterization of the Hydrogel Substrates

The hydrogel substrates are utilized in the double-hydrogel cell experiments are made from polyacrylamide using an established protocol [9]. Polyacrylamide gels are commonly used in traditional TFM applications due to their optical transparency, elastic properties and tunable Young's modulus over a wide range of physiologically relevant moduli [10, 11].

Thin substrates of polyacrylamide gel are prepared from acrylamide and methylene-bis-acrylamide stock solutions as described previously [3, 10, 12, 13]. Different concentrations of acrylamide and methylene-bis-acrylamide change the mechanical properties of the gel. The concentration of 3 % Acrylamide and 0.2 % Bis-acrylamide yields a Young's modulus of 1.5 +/− 0.1 kPa (Fig. 21.3). All substrates contain 14 % (w/v) fluorescent microspheres (0.5 μm in diameter). In order to visually differentiate between top and bottom substrates within the double-hydrogel system, each substrate is impregnated with either red or green fluorescent microspheres. Both top and bottom substrates are prepared to yield thicknesses of about 60 μm. Figure 21.2 displays a 3D laser scanning confocal image of neutrophils sandwiched between two polyacrylamide substrates that are visualized via its embedded fiduciary microspheres.

Mechanical characterization of all polyacrylamide gels is based on previously established testing protocols on a custom-built uniaxial compression device (Fig. 21.3) [12]. Briefly, the gels are cast in circular nylon molds and submersed in DI water. The custom-built compression device equipped with a centrally positioned linear actuator (Series A, Ultramotion) and a built-in linear encoder provides displacement information with a displacement resolution of 1 μm. To measure the compressive forces acting on each sample a 50-gram linear force transducer (LCFA-50 F, Omega Engineering Inc) is attached to the end of the linear actuator. To ensure uniaxial compression conditions, a ballpoint tip-platten top was placed on each gel sample, and all samples are carefully aligned along the central compression axis of the linear actuator. Nominal stress, σ, is computed by dividing the measured applied force by the circular cross-sectional area. Nominal strain, ε, is calculated by measuring height changes of each sample divided by the sample's original height. Each sample is compressed at three different strain rates (10^{-2}, 10^{-1}, 10^{0}) to capture any time-dependence in the material behavior. Young' moduli are calculated from the slope of each linear stress–strain curve as $E = \sigma/\varepsilon$ (Fig. 21.3). As shown previously, the material behavior of polyacrylamide can be appropriately described as a linearly elastic, homogenous, and isotropic solid with a Poisson's ratio of 0.45 [14].

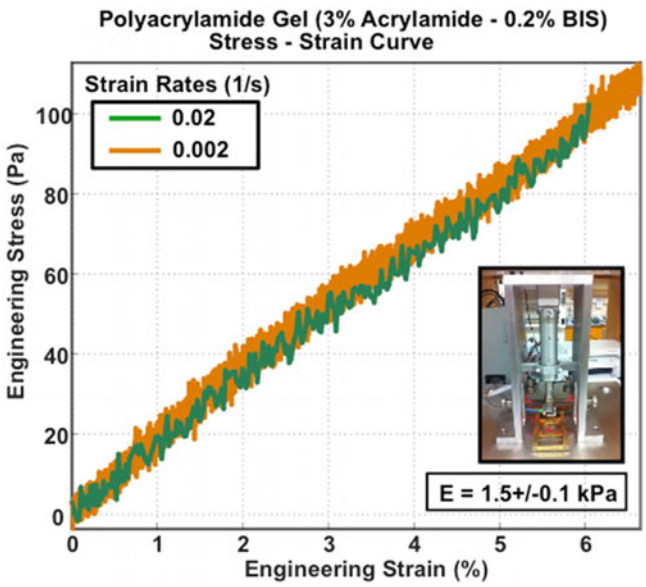

Fig. 21.3 Stress-strain curve of unconfined compression test of a cylindrical hydrated polyacrylamide samples with inserted figure of soft matter compression device

21.2.2 Double-Hydrogel System

The novelty of the system lies in its capability to dynamically alter the dimension of a cell's environment, and thus capture changes in motility and traction force signature of the same cell in both 2D and 3D dimensions. Two digital micrometers control the gap distance between a movable top and stationary bottom substrate within a precision of 1 μm (Fig. 21.1). Using this device the gap distance between the upper and lower polyacrylamide gels can be precisely controlled to achieve the desired level of cell confinement without mechanically compressing the cells. In order to change the geometry of the cell-gel system while imaging the same cell, a custom-designed micro-manipulator system is built. Figure 21.1 presents a schematic of the micromanipulator and the cell-gel system (Fig. 21.1).

Next, three dimensional image stacks are acquired using Nikon AR-1 confocal system, mounted on a TI Eclipse inverted optical microscope controlled by NI-Elements Nikon Software. Fluorescent microspheres embedded in the substrates are imaged with green Argon (488 nm) and red Helium Neon (561 nm) lasers. The cell outline is captured using standard phase microscopy. A 40× plan fluor air objective mounted on a piezo objective positioner was used for all the experiments, which allows to image at speeds up to 30 frames per second. 512 × 512 × Z voxels confocal volume stacks are recorded every 15 s with Z ranging from 128 to 256 pixels (~38–75 μm) depending whether only one or both top and bottom substrates are imaged simultaneously. To ensure physiological imaging conditions within the imaging chamber, temperature and pH are controlled and monitored through the experiments.

21.3 Measuring 3D Cell Traction Forces

Cell-generated full field displacements and traction forces are determined using our previously published 3D TFM technique [13, 15]. Briefly, three-dimensional time-lapsed volumetric images of fluorescent beads embedded in polyacrylamide substrates are recorded using laser scanning confocal microscopy. A digital volume correlation (DVC) algorithm is used to track the motion of embedded fluorescent beads in all three dimensions between each time increment [12, 13, 15]. The DVC algorithm is an extension to a well-known deformation measurement technique, known as digital image correlation (DIC). The idea behind the DVC algorithm is based on the cross-correlation of cubic subsets filled with microspheres within each image per given time [1]. In Eq. 21.1, f(**x**) and g(**x**) are intensity distribution functions of fluorescent microspheres filling the subsets, where f(**x**) refers to undeformed (initial) state, and g(**x**) refers to the time-incremented state. The displacement vector **u** is calculated by determining the spatial location of the peak of the correlation function (1). Computing cross-correlation function using Fast Fourier Transform (FFT) algorithm makes the computation more efficient (2).

$$m(u) = \int f(x)g(x+u)d\Omega_x \tag{21.1}$$

$$m(u) = \Im^{-1}\left[\Im[f\ (x)] * \Im[g(x)]\right] \tag{21.2}$$

Once full-field displacements are computed, the three-dimensional strain tensor **ε** is calculated using a displacement gradient method [12, 13]. For an isotropic, linear elastic material such as polyacrylamide, cell-generated substrate stresses can be determined from calculated strains (Eq. 21.3).

$$\sigma_{ij} = \frac{E}{1+v}\left(\varepsilon_{ij} + \frac{v}{1-2v}\,\varepsilon_{kk}\,\delta_{ij}\right) \tag{21.3}$$

In Eq. 21.3, E and ν are the Young's modulus and Poisson's ratio of the polyacrylamide gels, and the subscript indices range from i = 1,2,3 accounting for deformations in all three spatial dimensions. In-plane and out-of-plane traction forces arising from cell contact with the surface of the substrate can be calculated by using Cauchy relationship, where **n** is the normal unit vector (positive denotes pointing away from the surface of the substrate) (4).

$$T_{\mathrm{i}} = n_j\ \sigma_{ji} \tag{21.4}$$

Total force exerted by the cells on its substrate can be calculated by integrating the magnitude of surface tractions over the total cell area S (Eq. 21.5). The force vector contains three force components, which include the in-plane (shear) and out-of-plane (normal) forces.

$$F = \oint_s |T| dS \tag{21.5}$$

By combining the double-hydrogel system with our 3D TFM technique, we are able to quantitatively measure cell-generated traction forces as the confinement changes from 2D to 3D dimensions.

21.4 Results: Matrix Dimensionality Affects Neutrophil Force Generation

The double-hydrogel system and similar systems have been used in the past to demonstrate the differences of cellular migration, focal adhesion organization, and cytoskeleton structures in 2D and 3D cultures [3, 5, 7, 16]. In 2008 Lämmerman et al. conducted a series of measurements on motile leukocytes confined in fibrillar gels showing that even when functional integrins and myosin II were inhibited leukocytes were still able to migrate forward in 3D, however not on 2D, planar substrates [17]. Previous investigations into the mechanisms of neutrophil migration have focused on 2D planar systems, however neutrophils that enter injury-inflicted tissue in-vivo migrate through three-dimensional space. A neutrophils' inflammatory response to infection or injury depends on adhesive and migratory capacities through the matrix, which require generation of traction forces ranging from 40 to 800 Pa depending on the stiffness of the underlying substrate [18–20]. We used our system to study leukocyte force generation, specifically neutrophil migration and traction force generation as the neutrophil's environment changes from a 2D planar system to a 3D confined system (Fig. 21.4), while keeping all other experimental variables fixed.

Initially neutrophils are seeded on the bottom gel while maintaining a gap distance of about 50 μm, thus simulating a 2D environment. Once cells are adhered to the substrate, data was collected every 15 s for 10 min. Then the top substrate is lowered to a gap distance of 5–8 μm, which is slightly less than the typical diameter of a neutrophil (~10 μm) [21]. This represents a change in confinement since neutrophils migrating between top and bottom substrates have the opportunity to selectively bind to either top and bottom polyacrylamide gel surfaces thus representing a closer in-vivo configuration. Volumetric confocal images of neutrophils in the 3D system are taken every 15 s for 10 min. Thus, this reductionist experimental setup allows investigating the precise spatial and temporal effect geometry has as the neutrophil's surrounding is switched from 2D to 3D dimensions. Figure 21.4 presents neutrophil traction force data of the same neutrophil, first in a 2D system (left, $t = 0$) and then in a3D system (right, $t = t^*$). The time point t^* denotes the time when the top substrate is lowered within a gap distance of 5–8 μm, which is slightly less than the typical diameter of a neutrophils. Contour plots show that the same neutrophil generates higher magnitude of traction forces on both, top and bottom, substrates as the local cell environment switches from 2D to 3D. Due to the small size of neutrophils, our DVC algorithm was validated down to 1 μm resolution by applying translation to the volumetric images in x, y, z directions (Fig. 21.6).

In Fig. 21.5, we demonstrate the breakdown of the total force into its in-plane [6] and out-of-plane [7] components during the dimensional switch. Figure 21.5a illustrates strong up-regulation of the out-of-plane force component as the same neutrophil switches from two to three dimensions with little attenuation in its in-plane force component. To account cell-to-cell variability, we statistically represented the total in-plane and out-of-plane forces for both 2D and 3D systems, summarized in Fig. 21.5b, c by their median and standard error. Both in-plane and out-of-plane components increase in magnitude as the cell environment changes from 2D to 3D.

$$F_{\parallel} = \int_s \sqrt{T_x^2 + T_y^2} dS \tag{21.6}$$

$$F_{\perp} = \int_s |T_z| dS \tag{21.7}$$

These data suggests that confinement alone can significantly alter neutrophil-generated traction forces per given substrate stiffness.

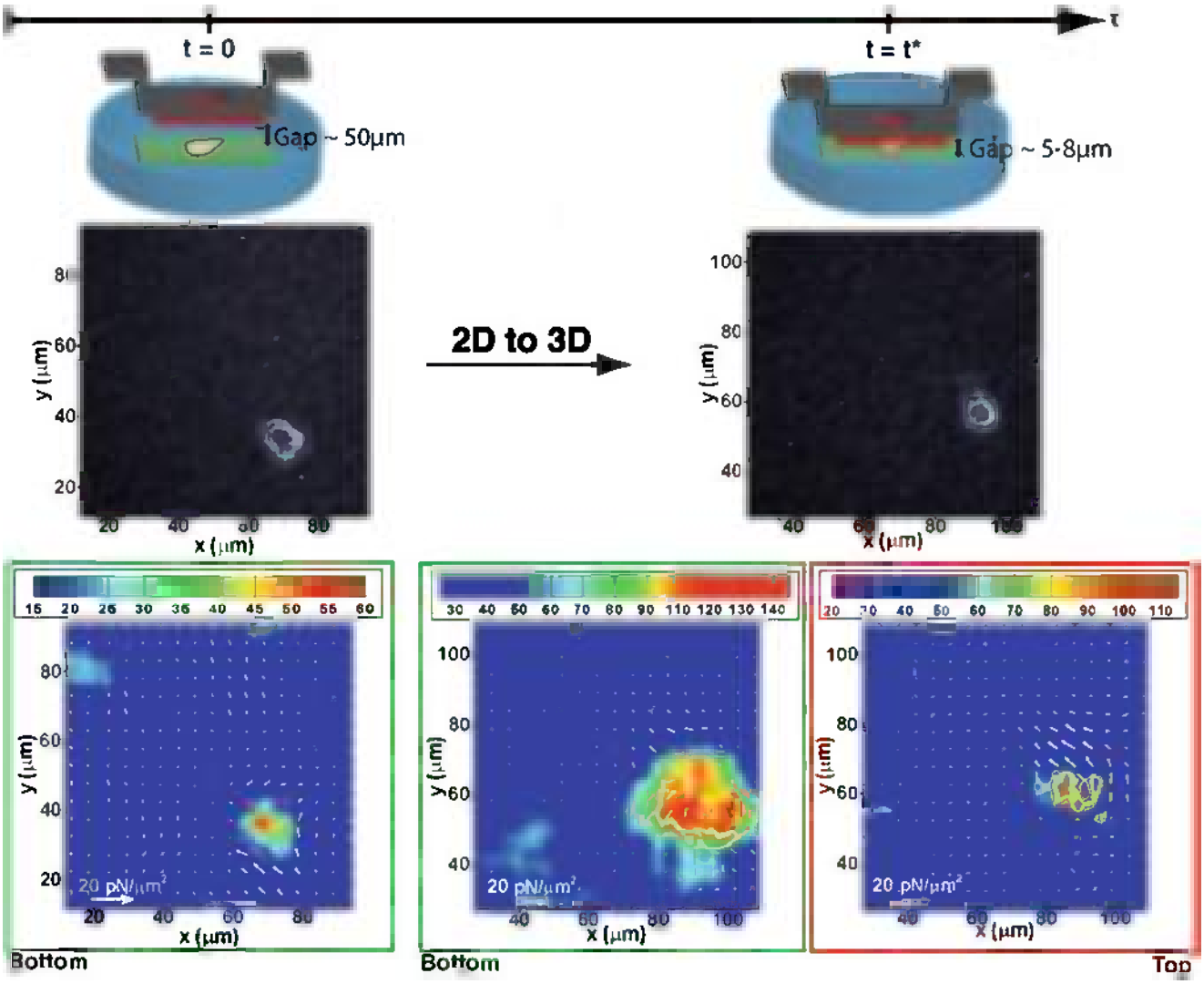

Fig. 21.4 Phase contrast images of a neutrophil and traction force profiles superimposed with the vector field of in-plane traction force components in 2D and 3D systems

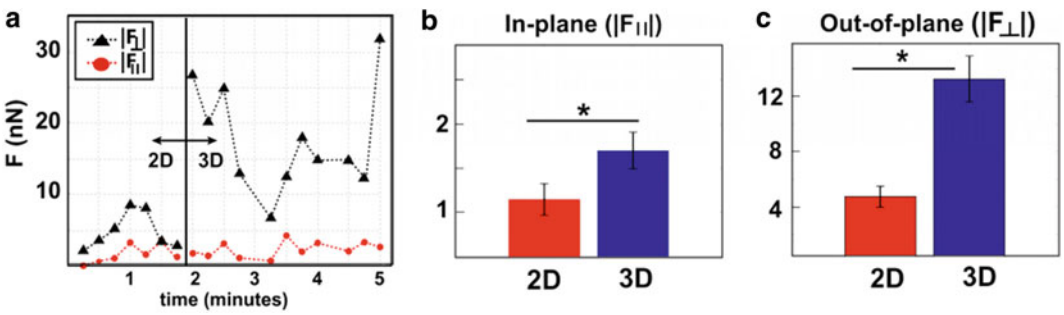

Fig. 21.5 (**a**) Dynamic out-of-plane (*black*) and in-plane (*red*) total forces for the neutrophil during dimensional switch from 2D to 3D. (**b**) Total in-plane force components in 2D (*red*) and 3D (*blue*) systems on the substrate with E = 1,500 Pa. (**c**) Out-of-plane total force components in 2D (*red*) and 3D (*blue*). $N = 20$ per each experimental setup ($P^* < 0.05$) (color figure in online)

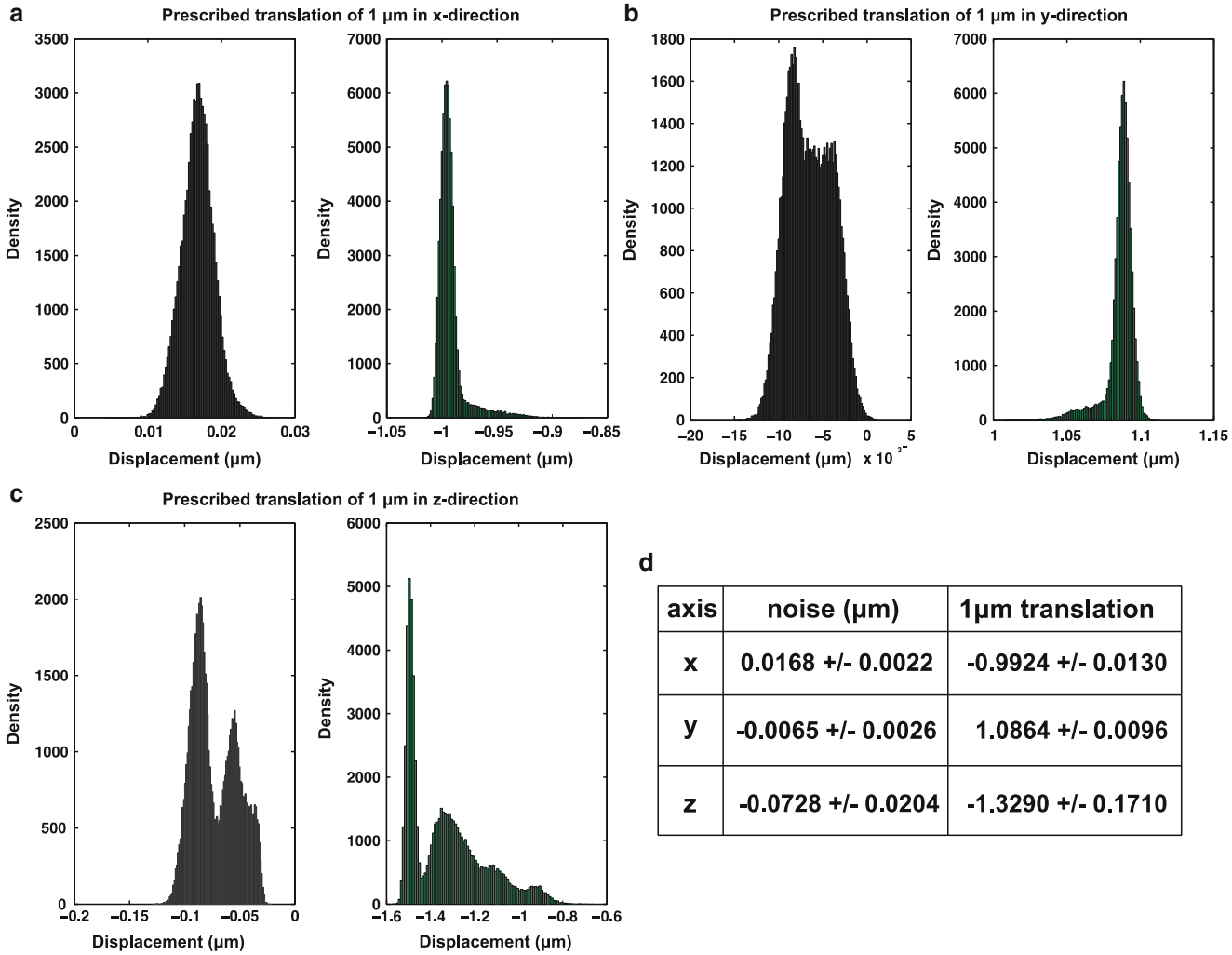

d

axis	noise (μm)	1μm translation
x	0.0168 +/- 0.0022	-0.9924 +/- 0.0130
y	-0.0065 +/- 0.0026	1.0864 +/- 0.0096
z	-0.0728 +/- 0.0204	-1.3290 +/- 0.1710

Fig. 21.6 Resolution check of DVC algorithm, by prescribing translation of 1 μm in (**a**) x-direction, (**b**) y-direction and (**c**) z-direction. (**d**) Noise in the system without and with prescribed translation

21.5 Conclusion

Cells assume 2D or 3D geometries through their ability of forming contact points between their basal and apical surfaces and the surrounding environment. By coupling the double-hydrogel system to our 3D TFM technique, we are able to create variation in the spatial distribution of cell surface contact points with the ECM and measure cellular traction forces that are generated due to those contacts. Tuning individual features of the microenvironment independently is generally challenging, but by developing a reductionist experimental setup of an otherwise complex 3D in-vivo environment, we are able to show that neutrophil generated traction forces increase as a function of geometric confinement and substrate stiffness. Double-hydrogel sandwich systems are simplified material environments compared to other fibrillar systems, however they allow isolating confinement and matrix stiffness as either individual or combined cues that affect cellular behavior. Thus, such systems as the one presented here, can aid in constructing a quantitative understanding of the effects of single environmental variables in determining cellular behavior in 3D matrices, which will lead to a better overall understanding of cell behavior in in-vivo (Fig. 21.6).

References

1. Griffith LG, Swartz MA (2006) Capturing complex 3D tissue physiology in vitro. Nat Rev Mol Cell Biol 7(3):211–224
2. Baker BM, Chen CS (2012) Deconstructing the third dimension: how 3D culture microenvironments alter cellular cues. J Cell Sci 125 (Pt 13):3015–3024
3. Beningo KA, Dembo M, Wang YL (2004) Responses of fibroblasts to anchorage of dorsal extracellular matrix. Proc Natl Acad Sci USA 101 (52):18024–18029
4. Lammermann T, Sixt M (2009) Mechanical modes of 'amoeboid' cell migration. Curr Opin Cell Biol 21(5):636–644
5. Jacobelli J et al (2010) Confinement-optimized three-dimensional T cell amoeboid motility is modulated via myosin IIA-regulated adhesions. Nat Immunol 11(10):953–961
6. Kraning-Rush CM, Carey SP, Califano JP, Smith BN, Reinhart-King CA (2011) The role of the cytoskeleton in cellular force generation in 2D and 3D environments. Phys Biol 8(1):015009
7. Pathak A, Sanjay K (2012) Independent regulation of tumor cell migration by matrix stiffness and confinement. Proc Natl Acad Sci USA 109 (26):10334–10339
8. Tong Z et al (2012) Chemotaxis of cell populations through confined spaces at single-cell resolution. PLoS One 7(1):1–10
9. Tse JR, Engler AJ (2010) Preparation of hydrogel substrates with tunable mechanical properties. Current protocols in cell biology/editorial board, Juan S. Bonifacino . . . [et al.] Chapter 10: Unit 10 16
10. Pelham RJ, Wang YL (1997) Cell locomotion and focal adhesions regulated by substrate flexbility. Proc Natl Acad Sci USA 94:13661–13665
11. Engler AJ et al (2004) Substrate compliance versus ligand density in cell on gel responses. Biophys J 86:617–628
12. Maskarinec SA, Franck C, Tirrell DA, Ravichandran G (2009) Quantifying cellular traction forces in three dimensions. Proc Natl Acad Sci USA 106(52):22108–22113
13. Franck C, Maskarinec SA, Tirrell DA, Ravichandran G (2011) Three-dimensional traction force microscopy: a new tool for quantifying cell-matrix interactions. PLoS One 6(3):e17833
14. Baselga J, Hernandez-Fuentes I, Pierola IF, Llorente MA (1987) Elastic properties of highly cross-linked polyacrylamide gels. Macromolecules 20:3060–3065
15. Franck C, Hong S, Maskarinec SA, Tirrell DA, Ravichandran G (2007) Three-dimensional full-field measurements of large deformations in soft materials using confocal microscopy and digital volume correlation. Exp Mech 47:427–438
16. Malawista SE (Chevance AB) Random locomotion and chemotaxis of human blood polymorphonuclear leukocytes (PMN) in the presence of EDTA: PMN in close quarters require neither leukocyte integrins nor external divalent cations. PNAS 94:11577–11582
17. Lammermann T et al (2008) Rapid leukocyte migration by integrin-independent flowing and squeezing. Nature 453(7191):51–55
18. Smith LA, Aranda-Espinoza H, Haun JB, Dembo M, Hammer DA (2007) Neutrophil traction stresses are concentrated in the uropod during migration. Biophys J 92(7):L58–L60
19. Oakes PW et al (2009) Neutrophil morphology and migration are affected by substrate elasticity. Blood 114(7):1387–1395
20. Jannat RA, Dembo M, Hammer DA (2011) Traction forces of neutrophils migrating on compliant substrates. Biophys J 101(3):575–584
21. Ting-Beall HP, Needham D, Hochmuth RM (1993) Volume and osmotic properties of human neutrophils. Blood 81:2774–2780

Chapter 22
Correlations Between Quantitative MR Imaging Properties and Viscoelastic Material Properties of Agarose Gel

Erica D. Chin, Jenny Ma, Christopher L. Lee, and Hernan J. Jara

Abstract This study determines and assesses correlations between quantitative magnetic resonance imaging (qMRI) parameters (proton density, diffusion, T1 and T2 relaxation) and viscoelastic material properties (storage modulus) for various low concentrations (0.5–3.0 % weight/volume) of agarose gel. MR imaging was done using a 3T (Philips Achieva) scanner. Dynamic mechanical analysis (DMA) was used to characterize the viscoelastic properties of the gels. The repeatability and accuracy of the DMA measurements have some dependence on various geometric sample and measurement parameters. An optimal set of parameters (for compression mode testing) that would produce reliable and repeatable measurements was identified for ranges of sample geometry. Higher concentrations of agarose were associated with higher storage moduli and lower relaxation times, diffusion coefficients, and proton densities. Of the qMRI parameters, T2 relaxation is the most sensitive to changes in concentration.

Keywords Agarose • qMRI • PD • T1 • T2 • Storage modulus • Magnetic resonance • DMA

22.1 Introduction

To meet the needs of emerging research topics such as tissue engineering, cellular mechanotransduction, and medical diagnostics, many metrology methods, such as quantitative magnetic resonance imaging (qMRI) and dynamic mechanical analysis (DMA), can be applied to inspect and characterize the microstructure of soft materials.

The potential for using qMRI measurements for tissue evaluation is an active research area since qMRI parameters can indicate the structural changes resulting from disease. qMRI parameters include proton density (PD), diffusion, T_1 and T_2 relaxation times. Proton density (PD) and diffusion, unlike the relaxation times, are independent of the induced magnetic field [1]. PD (also known as spin density) is a measure of mobile proton concentration in the material relative to free water and often represents areas where water content or lipid concentration is high [1, 2]. Diffusion is a measure of water's Brownian motion due to factors such as the concentration gradient, thermal agitation, and neighboring surfaces [1]. T_1 relaxation time, or spin–lattice relaxation, describes the rate at which a system of protons relaxes back into equilibrium following application of radiofrequency waves. Since the rate at which the system recovers is affected by the dipole-dipole interactions caused by the motion of neighboring molecules, the T_1 relaxation time is also an indicator of the mobility of water molecules and if they are bound to macromolecules [1, 3]. T_2 relaxation time (also known as transverse relaxation time or spin-spin relaxation) is the rate at which the transverse magnetization signal decays in the absence of magnetic field gradients and is affected by the presence of static internal fields, such as those from protons in large molecule [1, 4].

The measurement of viscoelastic properties of tissues is another method for quantifying and detecting potential structural changes in tissues due to disease. One such technique is dynamic mechanical analysis (DMA), where the phase lag (δ) and

E.D. Chin (✉) • J. Ma • C.L. Lee
Franklin W. Olin College of Engineering, 1000 Olin Way, Needham, MA 02492, USA
e-mail: erica.ding.chin@gmail.com

H.J. Jara
Department of Radiology, Boston University Medical Center, 820 Harrison Avenue, Boston, MA 02118, USA

F. Barthelat et al. (eds.), *Mechanics of Biological Systems and Materials, Volume 4*,
Conference Proceedings of the Society for Experimental Mechanics Series,
DOI 10.1007/978-3-319-00777-9_22,

strain (ε) resulting from an applied oscillatory stress (σ) is measured. The storage modulus, E′, (also known as the elastic modulus, the in-phase modulus, or the real modulus) represents the sample's elasticity as indicated in Eq. 22.1, where σ_0 and ε_0 are respectively the maximum stress and strain [5].

$$E' = \frac{\sigma_0}{\varepsilon_0} \cos \delta \tag{22.1}$$

Gels are often used as soft tissue substitutes due to their availability and ease of manufacture. In particular, agarose gels, which have the highest gelling capacity, have been shown to have mechanical properties similar to that of biological (e.g. brain) tissues at low concentrations [6]. Additionally, further characterization of agarose gels may aid the development of tissue engineering that uses agarose gels as scaffolds for soft tissues [7].

The goal of this study was to evaluate the correlations between the quantitative MRI parameters and the viscoelastic storage modulus for low concentrations of agarose gel.

22.2 Methods

22.2.1 Agarose Gel Preparation

Agarose gels with concentrations of approximately 0.5, 1.0, 1.5, 2.0, 2.5, and 3.0 % (weight/volume) were prepared by dispersing Sigma Aldrich agarose (A9539-50G, EEO = 0.09−0.13, sulfate ≤0.15 %) in distilled water with a magnetic stirring hot plate. The solution was boiled (98–100 °C) for 30 min at 250 rpm in a sealed beaker and poured into tubes or petri dishes at room temperature. Once cured, samples were sealed and stored at room temperature.

22.2.2 DMA Measurements

Harris Uni-Core punches (with diameters of 2.5–4.0 mm) were used to core the gels. Surgical blades set 1 and 2 mm apart were used to cut the cored samples into discs. The mechanical properties of the gels were measured in the compressive configuration on the PerkinElmer DMA 8000 as shown in Fig. 22.1. To prevent the discs from slipping, 220 Grid sandpaper (LECO, St. Joseph, MI) was adhered to the surface of the clamp plates. Frequency scan tests were conducted from 10 to 60 Hz.

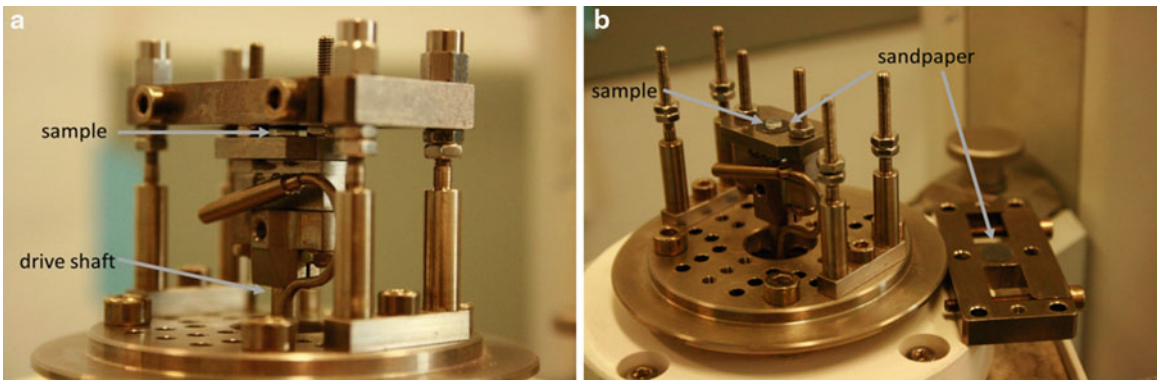

Fig. 22.1 Perkin Elmer DMA 8000 compressive fixtures. Agarose gel disc samples were sandwiched between two clamps, with one clamp acting as a moving piston. To reduce slippage, sandpaper was adhered to the surfaces of the clamps

Table 22.1 Testing parameters for MR imaging using a 3T (Philips Achieva) scanner

Geometry	–	Contrast	–
Scanning mode	MS2D	Acceleration type	TSE
Acquisition matrix (FE × PE)	108 × 96	TR (ms)	11,950.52
Percent sampling	100	Number of echoes (n)	2
Reconstructed matrix	176 × 176	ETL	16
Field of View (mm × mm)	160 × 160	TE (ms)	N/A
Percent field of view	100	TE1eff (ms)	6.4
Reconstructed voxel dimensions (mm × mm)	0.909 × 0.909	TE2eff (ms)	80
Slice thickness & gap (mm)	3 & 0	ES (ms)	6.4
Number of slices	20	TI1 (ms)	700
–	–	TI2 (ms)	5,975.26
–	–	FA	90
–	–	b-values (s mm-2)	N/A

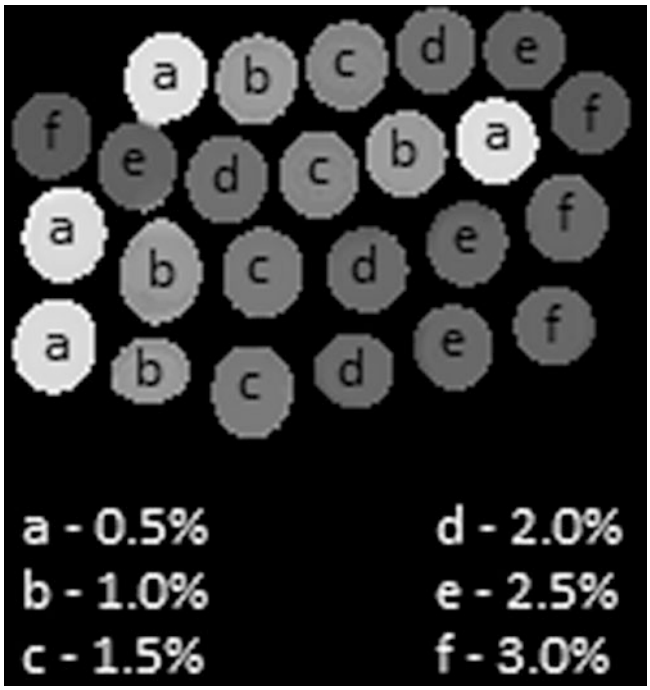

Fig. 22.2 MR image generated from the multi-spin echo test of different agarose concentrations in test tubes

22.2.3 qMRI Measurements

Imaging was performed with a 3T MR (Philips Achieva) scanner. Table 22.1 lists the parameters applied for the mixed-TSE sequence. A body coil was used for RF-transmit and the SENSE-knee coil was used to receive the signal. Directly acquired DICOM (Digital Imaging and Communication in Medicine) images files, such as Fig. 22.2, were analyzed using model-conforming T_1 and T_2 Q-MRI algorithms in MathCAD (Parametric Technology Corporation, Needham) [8, 9].

22.3 Results

22.3.1 DMA Measurements

As shown in Fig. 22.3, the storage modulus decreases slightly with higher excitation frequencies and increases with higher concentrations. Figures 22.4 and 22.5 show that storage moduli consistently increase with larger diameters and smaller thicknesses. Low concentrations of agarose yielded negative storage values for compression testing on the DMA 8000.

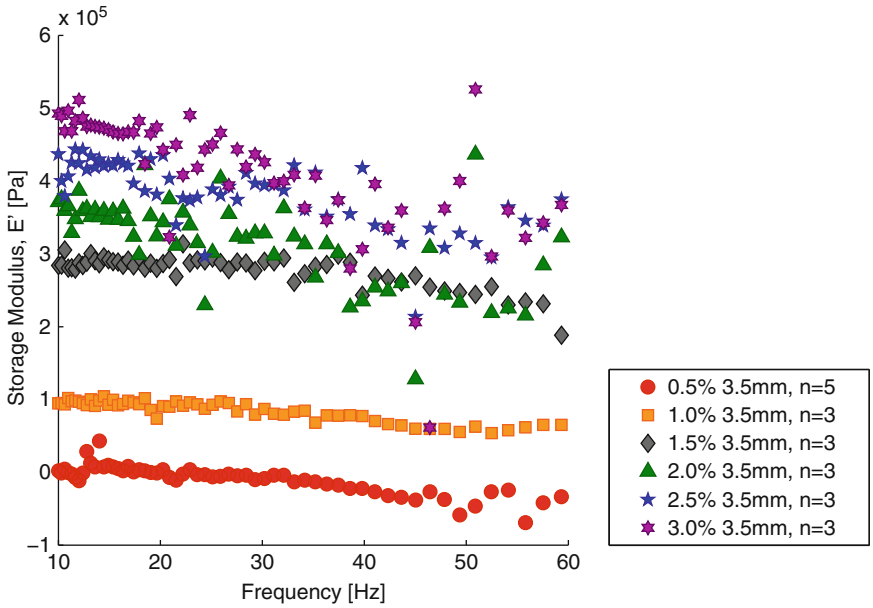

Fig. 22.3 Averaged results (n = 3 − 5) of the oscillatory stress applied in a frequency range of between 10 and 60 Hz. The storage modulus increases with higher concentrations of agarose gels for compression testing on the DMA 8000

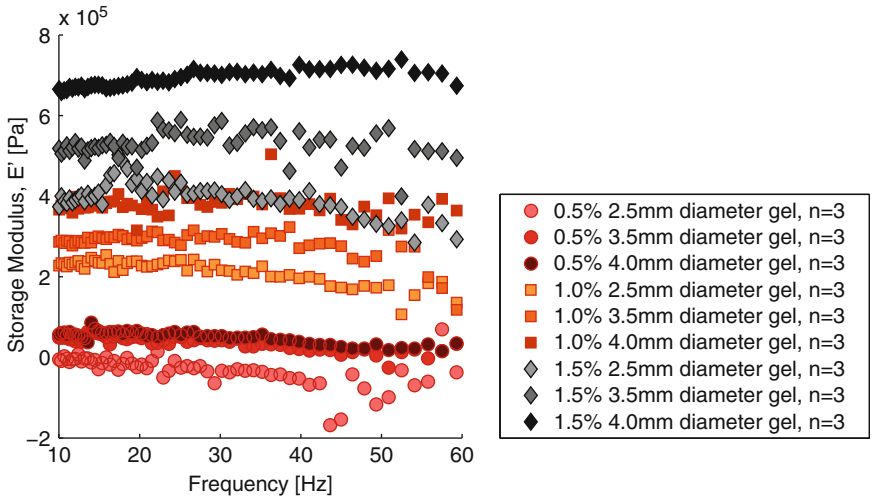

Fig. 22.4 Averaged results (three repeated tests) of the oscillatory stress applied in a frequency range of between 10 and 60 Hz for different diameters. The storage modulus increases with larger diameters of agarose gels for compression testing on the DMA 8000

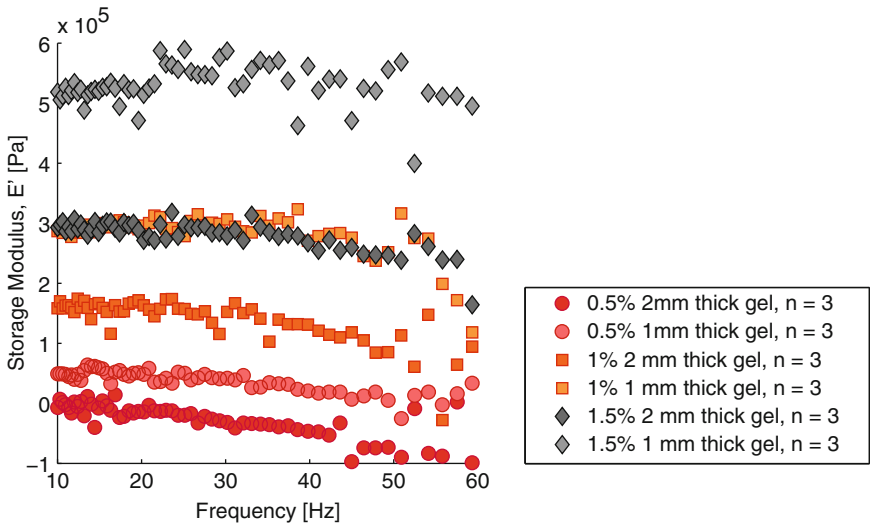

Fig. 22.5 Averaged results (three repeated tests) of the oscillatory stress applied in a frequency range of between 10 and 60 Hz for different thicknesses. The storage modulus increases with thinner samples for compression testing on the DMA 8000

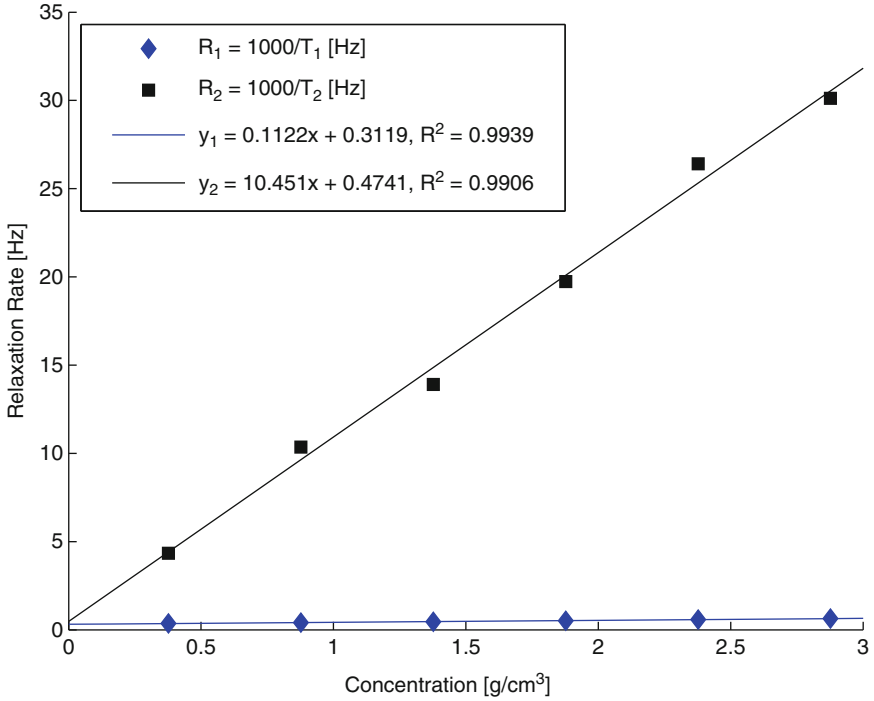

Fig. 22.6 Relaxation rates R_1 and R_2 (or $\frac{1,000}{T_1}$ and $\frac{1,000}{T_2}$ respectively) linearly increase with higher agarose concentrations

22.3.2 qMRI Measurements

As shown in Fig. 22.6, relaxation rates R_1 and R_2, where $R_1 = 1,000/T_1\ Hz$ and $R_2 = 1,000/T_2\ Hz$, linearly increase with higher agarose concentrations. In Fig. 22.7, proton densities and diffusion coefficients linearly decrease with lower agarose concentrations. The y-intercepts of the linear equations, shown in Fig. 22.6, for R_1 and R_2 correspond to the relaxation rates for water (i.e. water has T_1 and T_2 values of 3,200 and 2,100 ms respectively) [10, 11]. As indicated in Fig. 22.8, as the storage moduli measured by the DMA increases, the relaxation times, the diffusion coefficient (D), the diffusion coefficient due to the pulsed field gradient (Dpfg), and the relative proton density (rPD) decrease.

22.4 Discussion and Conclusions

Higher concentrations of agarose are correlated to higher storage moduli and lower relaxation times, diffusion coefficients, and proton densities. More cross-linking occurs with higher concentrations of agarose, increasing the gel's capacity to store energy and thus raising the storage modulus. Since more water molecules are bound, the mobility of water molecules and polarization effects should also be reduced; hence proton densities, diffusion coefficients, and T_1 and T_2 should also be reduced.

The storage modulus varies with sample geometry, frequency range, and agarose. As illustrated in the results, storage moduli measured using the DMA 8000 compressive setup is dependent upon the sample geometry, as was similarly indicated by Chen's measurements of agarose gels shear moduli using Perkin Elmer DMA 8000 shear setup [12]. Additionally, by nature of the equipment, measurements were limited to low frequencies, especially for lower concentrations of agarose gels. In addition, the mechanical properties of agarose gels are dependent upon the source of agar and the manufacturing method [13]. Furthermore, the agarose used in this study has noted impurities of at most 10 % moisture content. Hence the concentrations of agarose may actually be slightly lower than presented. There are clear and consistent correlations between qMRI parameters and DMA-measured storage moduli for low concentrations of agarose. Higher concentrations of agarose were associated with higher storage moduli and lower relaxation times, diffusion coefficients, and proton densities. Of the qMRI parameters, T2 relaxation is the most sensitive to changes in concentration.

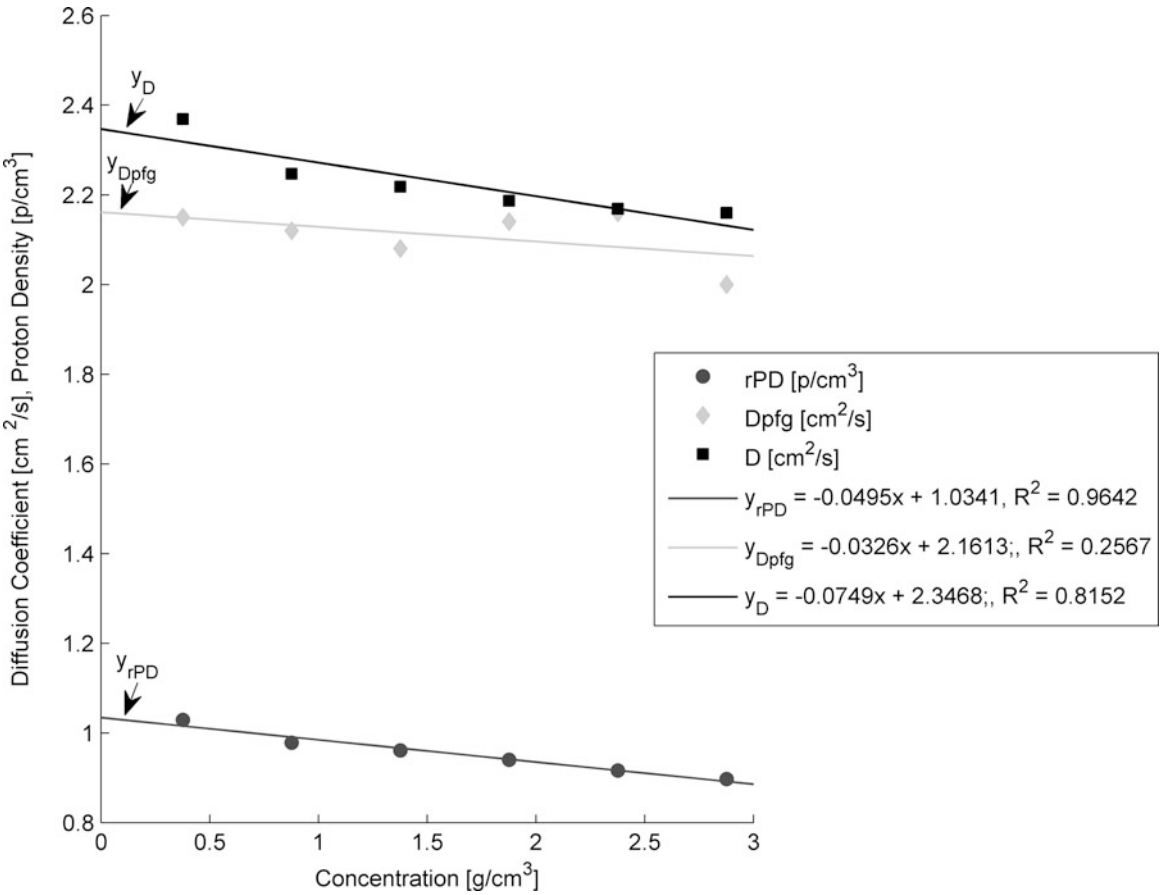

Fig. 22.7 Diffusion coefficients and proton densities linearly decrease with higher agarose concentrations

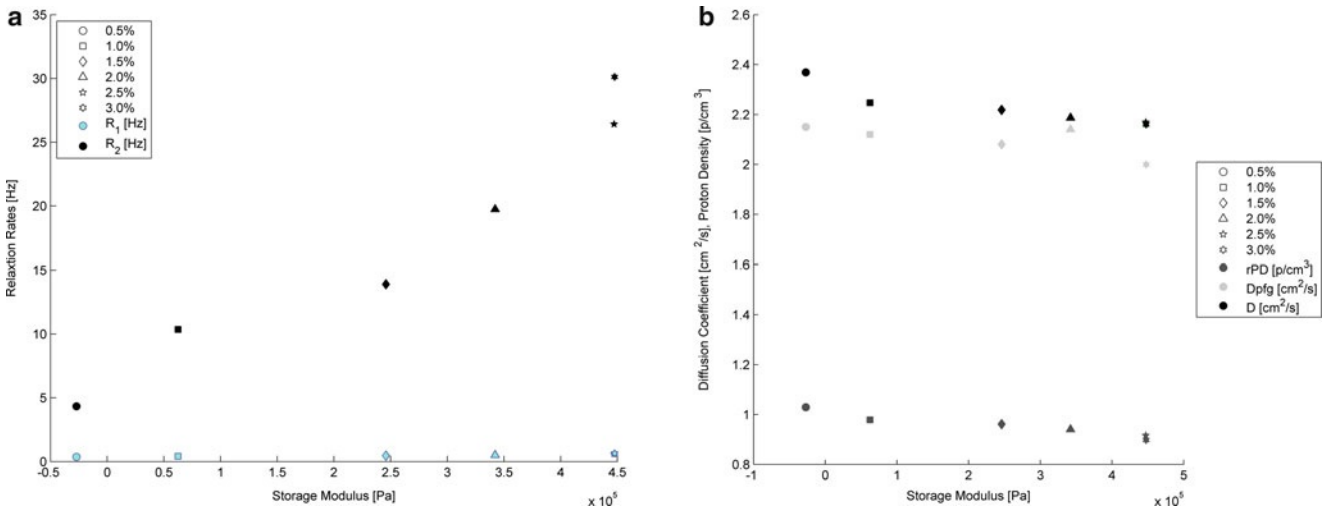

Fig. 22.8 (**a**) Relaxation rates increase with higher storage moduli. (**b**) Diffusion coefficients and proton density decrease with high storage moduli. Higher concentrations correspond to higher moduli, relaxation rates, proton density, and diffusion coefficients

Acknowledgements The authors wish to acknowledge the contributions of Matthew Neal (Olin College) and Peter Kokias (PerkinElmer, Inc.).

References

1. Shah B, Anderson SW, Scalera J, Jara H, Soto JA (2011) Quantitative MR imaging: physical principles and sequence design in abdominal imaging. Radiographics 31:867–880
2. Tofts PS (2003) PD: proton density of tissue water. In: Tofts PS (ed) Quantitative MRI of the brain. Wiley, England, pp 85–109
3. Gowland PA, Stevenson VL (2003) T_1: the longitudinal relaxation time. In: Tofts PS (ed) Quantitative MRI of the brain. Wiley, England, pp 120–141
4. Nossin-Manor R, Chung AD, Morris D, Soares-Fernandes JP, Thomas B, Cheng HM, Whyte HEA, Taylor MJ, Sled JG, Shroff MM (2011) Optimized T1- and T2-weighted volumetric brain imaging as a diagnostic tool in very preterm neonates. Pediatr Radiol 41:702–710
5. Menard KP (2008) Dynamic mechanical analysis – an introduction. CRC Press, Boca Raton
6. Pervin F, Chen WW (2010) Mechanically similar gel simulants for brain tissues. Proc SEM Ann Conf 1:9–13
7. Aheame M, Yang Y, El Haj AJ, Then KY, Liu K (2005) Characterizing the viscoelastic properties of thin hydrogel-based constructs for tissue engineering applications. J R Soc Interface 2:455–463
8. Suzuki S, Sakai O, Jara H (2006) Combined volumetric T1, T2, and secular-T2 quanitative MRI of the brain: age-related global changes (preliminary results). Magn Reson Imaging 24:877–887
9. Anderson SW, Sakai O, Soto JA, Jara H (2013) Improved T2 mapping accuracy with dual-echo turbo spin echo: effect of phase encoding profile orders. Magn Reson Med 69:137–143
10. Hindman J, Svirmickas A, Wood M (1973) Relaxation processes in water. A study of the proton spin lattice relaxation time. J Chem Phys 59:1517
11. Meiboom S, Luz Z, Gill D (1957) Proton relaxation in water. J Chem Phys 27:1411–1412
12. Chen Q, Ringleb SI, Hulshizer T, An K (2005) Identification of the testing parameters in high frequency dynamic shear measurement on agarose gels. J Biomech 38:959–963
13. Andrasko J (1975) Water in agarose gels studied by nuclear magnetic resonance relaxation in the rotating frame. Biophys J 15:1235–1243

Chapter 23
Electrostatic Actuation Based Modulation of Interaction Between Protein and DNA Aptamer

Xiao Ma and Pranav Shrotriya

Abstract The need to design nanoscale, sensitive and flexible biotic-abiotic interface keeps increasing. The essential issue is how to facilitate biological signal transmission and modulation through controllable external stimuli. This requires a thorough understanding of the binding and dissociation process between bio-molecules under the stimuli. The purpose of this study is to demonstrate the binding and dissociation behavior between the anti-coagulation protein thrombin and single-stranded DNA aptamer with application of electrical fields. Micro-contact printing was utilized to prepare compositionally patterned gold specimen with adjacent regions covered with alkanethiol and DNA aptamer molecules, then thrombin molecules were injected into the system to form the binding pair with aptamer. Different electrical field potentials were applied to the nanoscale structure by a three-electrode electrochemical cell. Due to the negatively charged nature of aptamer DNA strands, positive electrical field can trigger a large bending-down conformational transition of the aptamer, thus can break the bonds between binding pair. Through Atomic Force Microscopy, height of the pattern was measured and the difference of height under different potentials can show the binding state of the pair. We can propose a method to actuate and modulate the dissociation behavior between thrombin and aptamer through the external electrostatic stimuli.

Keywords Micro-contact printing • Atomic force microscopy • Thrombin • DNA aptamer • Actuation and modulation

23.1 Introduction

Exquisite integration of artificial components with biological systems has recently attracted increasing interest and attention upon building seamless biotic-abiotic interface. The nanoscale, structural and functional biotic-abiotic interface can lead to highly sensitive, biocompatible and flexible bio-sensors and actuators, which have enormous and broad application in biomedical, biochemical and biomechanical fields, such as modulating biological systems and bio-molecule activity, locating disease, repairing or reprogramming genetic information, control external prostheses [1], etc. Currently the tools for implementing the above objectives are far from complete, and one of the major challenges on the biotic-abiotic interface integration is to dynamically translate external stimuli into biochemical signals and efficiently transmit such signal into the biological processes.

Among various kinds of external stimuli, such as such as pH, temperature and electro-chemical surface modifications, electrostatic mechanisms have many advantages on communicating information in biotic-abiotic interface, allowing massively parallel actuation and measurement capabilities that will ultimately be essential for biomedical applications [2–4]. In addition, application of electrostatic fields is an efficient and feasible mechanism to induce conformational transition of charged or polar bio-molecules. When applying electrical fields onto a biological system, the double layer formed near the electrode leads to generation of strong electrical fields within several nanometers, thus only affects the bio-molecules that are immobilized on or close to the electrode surface, which implies relatively low external voltages can induce the conformational transition of the bio-molecules without generating harmful byproducts. Rant et al. have demonstrated that the conformation of short DNA oligomers immobilized at low grafting densities can be reversibly switched by application of electrical fields [5, 6]. Since DNA is negatively charged, positive voltages caused the DNA to

X. Ma (✉) • P. Shrotriya
Department of Mechanical Engineering, Iowa State University, Ames, IA 50011, USA
e-mail: xma@iastate.edu

F. Barthelat et al. (eds.), *Mechanics of Biological Systems and Materials, Volume 4*,
Conference Proceedings of the Society for Experimental Mechanics Series,
DOI 10.1007/978-3-319-00777-9_23,

flatten on the surface, while negative voltages caused the DNA to orient vertically. Electrostatic fields can also influence self-assembly and hybridization of DNA [3]. Positive voltages (+300 mV) applied to single-strand DNA functionalized gold electrodes showed a threefold enhancement in complementary DNA hybridization, while for negative voltage it was an order of magnitude smaller.

Electrostatic field intrigued conformational transition is not limited to bio-molecules, Lahann et al. used an analogous approach to cause alkanethiol molecules to bend from a vertical to a horizontal orientation by applying positive electrical field, so that charged functional groups were attracted to the electrode surface, exposing the hydrophobic alkane chain on the surface, which realizes the macroscopic surface change from hydrophilic to hydrophobic property [7]. Such electrical field induced transition of the charged organic molecules also supports the feasibility for electrostatic actuation mechanism.

Besides applicable external stimuli, it is also essential to select an appropriate model bio-molecular system to investigate the specific response. The anticoagulation protein thrombin and its aptamer provide such a relevant and suitable sample model. Nucleic acid aptamers are a relatively new recognized type of molecules, with similar properties of ligand specificity and affinity to antibodies but with several specific advantages as components of sensors and biomedical devices [8–10]. Aptamers are small (15–40 nt) with affinities for proteins and other large bio-molecules in the picomolar to nanomolar range, and demonstrate exquisite specificities for their receptors due to large structural changes in the binding process, which can be utilized for detection of the target [11, 12], and thus can be a selection for various bio-molecules[13–15] and bio-medical materials and drugs[16–18]. The large structural or conformational transition of aptamer associated with binding may be hindered or enhanced through application of electrical fields as demonstrated in previous paragraph.

Thrombin, a catalytic enzyme taking effect in the synthesis of fibrin from fibrinogen during the blood clotting process, has a wide range of health effects in the human system. When thrombin is beyond the normal level, thrombosis may happen due to too much fibrin generated in the bloodstream; when thrombin is lower than the normal level, hemorrhage may happen due to too little fibrin generated. Thrombin has two binding sites to control its catalytic function. The first one is the fibrinogen binding site, where the conversion of fibrinogen to fibrin occurs so as to enhance the coagulation process, the second one is heparin binding site, where heparin binds to thrombin and inhibit the coagulation process [19]. Thrombin has a well established aptamer, which shows a hairpin structure formed by eight guanine bases sequenced in GGNTGGN2-5GGNTGG, known as G-quadruplex. The aptamer can fit into thrombin heparin binding site and affects the thrombin in the similar way as heparin [20]. This aptamer has been shown in chemical assays to have high binding specificity [19–22]. The strong binding between thrombin-aptamer pair makes it both relevant for the study of binding forces and suitable for current study.

In order to verify the actuation and modulation on the modal biomolecular system via electrostatic stimuli, the binding specificity and affinity between thrombin-aptamer pair must be first proved. Micro-contact printing (μCP), a widespread methods for creating micro and nanoscale structures outlined by Kumar and Whitesides [23], is utilized for this purpose by accessing the height changes upon binding of thrombin/aptamer pair, in which the height change was measured by Atomic Force Microscopy surface scan. After the specific binding between thrombin and aptamer was verified, different electrical fields were exerted on the pair and AFM surface scan was utilized again to discover the height changes, and compare to the results of nonelectrical field situation so as to acquire the information of binding or dissociation of the pair.

23.2 Methods

To perform micro-contact printing, a flexible polymer poly(dimethyl siloxane) (PDMS) stamp was made from a mold using a SU-8 photoresist master, with 5 μm by 5 μm squares by a 10 μm spacing. The PDMS was cured at 60 °C for a minimum of 12 h. Then hexadecanethiol was exposed to the stamp as a solution in liquid, and then the liquid was either allowed to dry or dried with a gas such as nitrogen. The dried hexadecanethiol was then printed and adhered on a substrate with a known pattern (such as a grid of squares). The PDMS stamp was removed, leaving the pattern of the hexadecanethoil printed on the substrate.

After that a solution containing 3.4 μM thrombin aptamer (sequence: 5′-thiol-GCC TTA ACT GTA GTA CTG GTG AAA TTG CTG CCA TTG GTT GGT GTG GTT GG-3′) in ddH_2O was exposed to the substrate. Due to the hydrophicility of the aptamer molecules and well packed hexadecanethiol chains, aptamer molecules can only be immobilized on the bare gold surfaces, i.e. the spacing area among the hexadecanethiol patterns, leading to compositionally patterned samples.

To bind the aptamer with thrombin, a 10 μM concentration of thrombin in high $MgCl_2$ binding buffer with Tween20 included to decrease non-specific binding (20 mM Tris-HCl pH 7.4, 140 mM NaCl, 5 mM KCl, 1 mM $CaCl_2$, 5 mM $MgCl_2$, 5 % glycerol v/v and 0.05 % Tween20 v/v in ddH_2O) was deposited on the printed surface. The mixture was allowed to stand for 1 min before being rinsed several times in binding buffer with NP40 included (20 mM Tris-HCl pH 7.4, 140 mM NaCl,

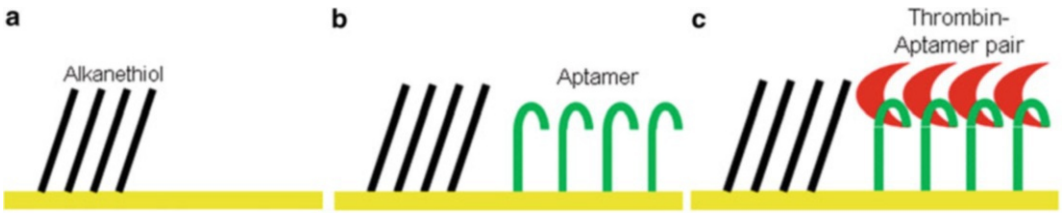

Fig. 23.1 Schematic procedure for establishing the binding pair nanostructure in a compositionally patterned sample. (**a**) Hexadecanethiol printed on gold, (**b**) Aptamer deposited on the adjacent area, (**c**) Thrombin bound with aptamer

5 mM KCl, 1 mM $CaCl_2$, 5 mM $MgCl_2$, 5 % glycerol v/v and 0.05 % NP40 v/v in ddH_2O) followed by rinsing several times with ddH_2O.

The scheme of building nanostructure of hexadecanethiol, aptamer and thrombin in a series of steps is shown in Fig. 23.1. Atomic Force Microscopy surface scan was then utilized to measure the height change of the surface with 50 runs for each situation to acquire sufficient statistical significance, and different operators involved in the data analysis of the AFM surface height image so as to eliminate or reduce the bias measurement. According to the nanostructure built as Fig. 23.1c, the different electrical fields strength of 300, 100, 0, −100 and −300 mV were applied onto the structure respectively for 1 min each via regular three electrode system. The sample serves as the working electrode, while a silver wire is used as a reference electrode and platinum wire as a counter electrode to maintain the constant potential value. After electrical fields were removed, we utilize AFM surface scan again to validate the height change of the surface.

23.3 Results and Discussion

The AFM surface scan images are shown in Fig. 23.2, Alkanethiol was first printed onto gold substrate with the assigned pattern, the height difference between alkanethiol and gold surface is 1.7 nm by section analysis. Then aptamer molecules were printed on gold surface, since the alkanethiol occupies the position of square pattern, aptamer can only reside the bare gold substrate area among the alkanethoil patterns, and the relative height difference between the alkanethoil and aptamer became 0.5 nm by section analysis, which implies the height of aptamer is 1.2 nm. Finally thrombin molecules were deposited onto the alkanethiol-aptamer surface and can specifically bind to aptamer. The binding between thrombin and aptamer increases the height to a large extent, so that now the pair shows greater height than alkanethiol, and that's why an inverse image was observed compared to the previous two cases. The relative height difference between the thrombin-aptamer pair and alkanethiol became -0.4 nm, which implies the height of thrombin is 0.9 nm. This height change is summarized in Table 23.1 to show the size scale of alkanethiol, aptamer and thrombin in the binding process.

By applying the electrical field onto the binding pair nanostructure, there might be two possible states for the sample, as shown in Fig. 23.3. The binding pair may resist the external electrical field influence and maintain the structure, as shown in Fig. 23.3a, then the height of the sample measured by AFM surface scan will keep the same level as the case shown in Fig. 23.2c; or the electrical field can break the pair, as shown in Fig. 23.3b, then the height of the sample measured by AFM surface scan will decrease and show as the case shown in Fig. 23.2a or b

The statistical results of AFM surface height measurement are shown in Fig. 23.4. In Fig. 23.4a the height difference value was 1.7, 0.5 and −0.4 nm respectively. When positive electrical fields exerted onto the binding pair, due to the negatively charged nature of the DNA aptamer, the electrostatic force can pull the aptamer down onto the gold substrate, which can break the bonds between thrombin and aptamer, thus lead to the case shown in Fig. 23.3b and height difference value changes from −0.4 to 0.5 nm, as shown in Fig. 23.4b, both for 100 and 300 mV potential applied to the system. While negative electrical fields exerted onto the system, for a smaller field strength value −100 mV, we found the height difference value to be −0.5 nm, i.e. maintain the bound state level of the pair, which means the pair can resist the electrostatic pushing force and maintain the structure. However, for a larger field strength value −300 mV, we found the height difference value change enormously from −0.5 to 1.7 nm, which implies not only the thrombin was removed from the surface, but also the aptamer were eliminated from the surface due to the much greater electrostatic pushing force. In this way, we propose a method to actuate and modulate the binding behavior between thrombin and aptamer by applying moderate electrical field strength ranging from −100 to 100 mV.

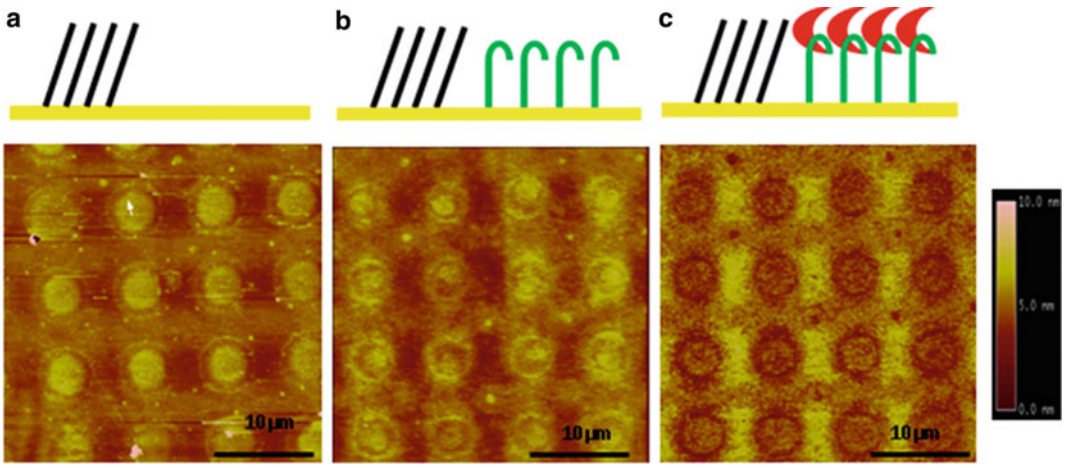

Fig. 23.2 AFM image validation of µCP pattern. (**a**) Alkanethiol, (**b**) Alkanethiol + Aptamer, (**c**) Alkanethiol + Thrombin-Aptamer pair

Table 23.1 Height change summary of µCP experiment

	Alkanethiol versus gold	Alkanethiol versus aptamer	Alkanethiol versus thrombin-aptamer pair
Height difference (nm)	1.7 ± 0.5	0.5 ± 0.3	-1.4 ± 0.3
	Alkanethiol	Aptamer	Thrombin
Height of molecules (nm)	$1.7 - 0 = 1.7$	$1.7 - 0.5 = 1.2$	$1.7 + 1.4 - 1.2 = 1.9$

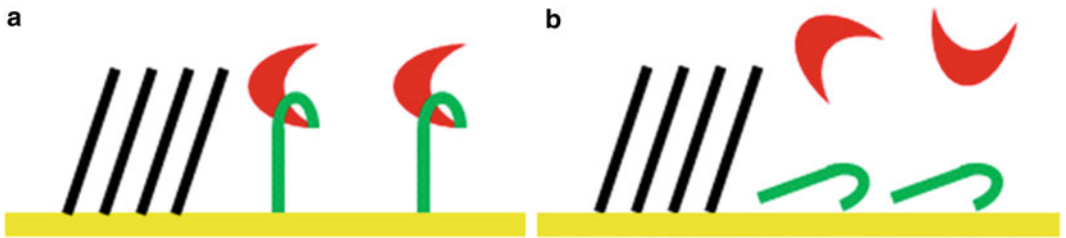

Fig. 23.3 Schematic of bound and dissociated state of the thrombin-aptamer pair in the established nanostructure. (**a**) Bound state of the thrombin-aptamer pair, (**b**) Dissociated state of the thrombin-aptamer pair

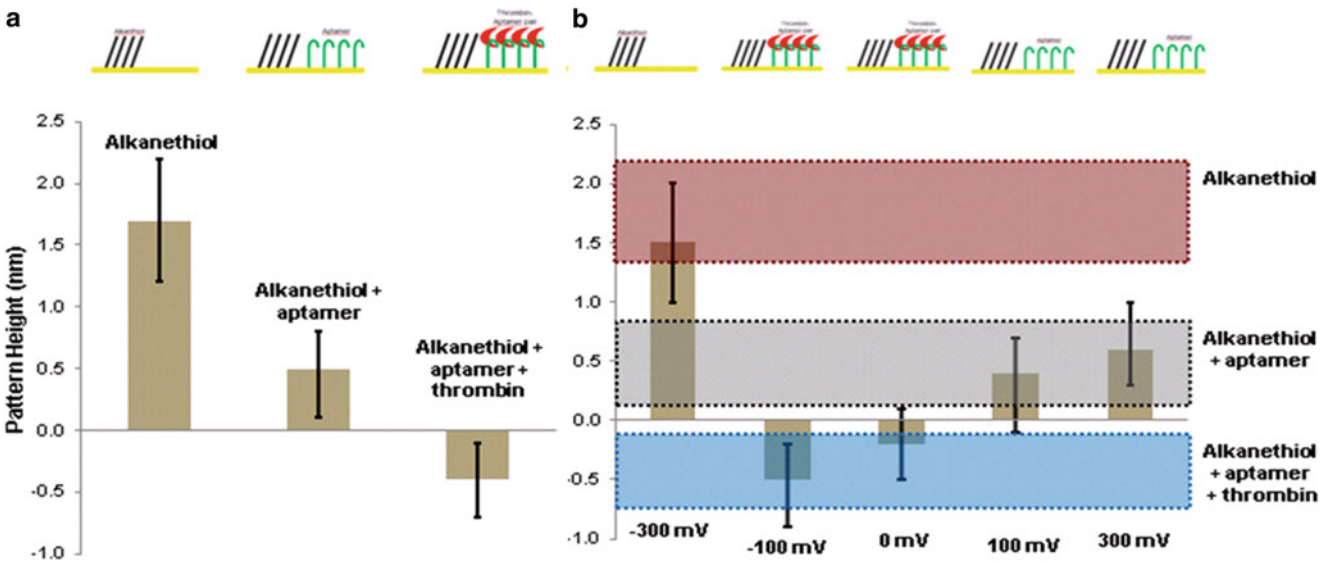

Fig. 23.4 Statistical results of AFM surface height measurement results for nonelectrical/electrical field application. (**a**) Surface height of nonelectrical field application, (**b**) Surface height of electrical field application

23.4 Conclusion

1. Through uCP technique, thrombin-aptamer binding pair can be successfully established.
2. By performing height identification experiment through AFM surface scan, specific binding between thrombin and aptamer can be verified.
3. Moderate electrical fields can be utilized to induce binding change between thrombin and aptamer pair, and thus can realize the actuation and modulation of the binding behavior between the pair:
   (a) Positive electrical fields of 100 mV can successfully break the bonds between the pair;
   (b) Neutral condition does not influence the binding between the pair;
   (c) Negative electrical fields of −100 mV can withhold the pair structure; while At −300 mV, the whole binding pair is stretched away from the gold substrate and the nanostructure was destroyed due to the too large electrostatic pushing force.

References

1. Wong IY, Almquist BD, Melosh NA (2010) Dynamic actuation using nano-bio interfaces. Mater Today 13(6):14–22
2. Wong IY, Footer MJ, Melosh NA (2008) Electronically activated actin protein polymerization and alignment. J Am Chem Soc 130(25):7908–7915
3. Wong IY, Melosh NA (2009) Directed hybridization and melting of DNA linkers using counterion-screened electric fields. Nano Lett 9(10):3521–3526
4. Wong IY, Melosh NA (2010) An electrostatic model for DNA surface hybridization. Biophys J 98(12):2954–2963
5. Rant U, Arinaga K, Fujita S, Yokoyama N, Abstreiter G, Tornow M (2004) Dynamic electrical switching of DNA layers on a metal surface. Nano Lett 4(12):2441–2445
6. Rant U, Arinaga K, Scherer S, Pringsheim E, Fujita S, Yokoyama N, Tornow M, Abstreiter G (2007) Switchable DNA interfaces for the highly sensitive detection of label-free DNA targets. Proc Natl Acad Sci USA 104(44):17364–17369
7. Lahann J, Mitragotri S, Tran TN, Kaido H, Sundaram J, Choi IS, Hoffer S, Somorjai GA, Langer R (2003) A reversibly switching surface. Science 299(5605):371–374
8. Hermann T, Patel DJ (2000) Biochemistry – adaptive recognition by nucleic acid aptamers. Science 287(5454):820–825
9. Ellington AD, Szostak JW (1990) Invitro selection of RNA molecules that bind specific ligands. Nature 346(6287):818–822
10. Tuerk C, Gold L (1990) Systematic evolution of ligands by exponential enrichment – RNA ligands to bacteriophage-T4 DNA-polymerase. Science 249(4968):505–510
11. Jenison RD, Gill SC, Pardi A, Polisky B (1994) High-resolution molecular discrimination by RNA. Science 263(5152):1425–1429
12. Yang YS, Kochoyan M, Burgstaller P, Westhof E, Famulok M (1996) Structural basis of ligand discrimination by two related RNA aptamers resolved by NMR spectroscopy. Science 272(5266):1343–1347
13. Gronewold TMA, Glass S, Quandt E, Famulok M (2005) Monitoring complex formation in the blood-coagulation cascade using aptamer-coated SAW sensors. Biosens Bioelectron 20(10):2044–2052
14. Hianik T, Ostatna V, Zajacova Z, Stoikova E, Evtugyn G (2005) Detection of aptamer-protein interactions using QCM and electrochemical indicator methods. Bioorg Med Chem Lett 15(2):291–295
15. Lavrik NV, Sepaniak MJ, Datskos PG (2004) Cantilever transducers as a platform for chemical and biological sensors. Rev Sci Instrum 75(7):2229–2253
16. Stojanovic MN, de Prada P, Landry DW (2001) Aptamer-based folding fluorescent sensor for cocaine. J Am Chem Soc 123(21):4928–4931
17. Win MN, Klein JS, Smolke CD (2006) Codeine-binding RNA aptamers and rapid determination of their binding constants using a direct coupling surface plasmon resonance assay. Nucleic Acids Res 34(19):5670–5682
18. Wang Y, Rando RR (1995) Specific binding of aminoglycoside antibiotics to RNA. Chem Biol 2(5):281–290
19. Bode W, Mayr I, Baumann U, Huber R, Stone SR, Hofsteenge J (1989) The refined 1.9 a crystal-structure of human alpha-thrombin – interaction with D-Phe-Pro-Arg chloromethylketone and significance of the Tyr-Pro-Pro-Trp insertion segment. EMBO J 8(11):3467–3475
20. Bock LC, Griffin LC, Latham JA, Vermaas EH, Toole JJ (1992) Selection of single-stranded-DNA molecules that bind and inhibit human thrombin. Nature 355(6360):564–566
21. Tasset DM, Kubik MF, Steiner W (1997) Oligonucleotide inhibitors of human thrombin that bind distinct epitopes. J Mol Biol 272(5):688–698
22. Tsiang M, Gibbs CS, Griffin LC, Dunn KE, Leung LLK (1995) Selection of a suppressor mutation that restores affinity of an oligonucleotide inhibitor for thrombin using in-vitro genetics. J Biol Chem 270(33):19370–19376
23. Kumar A, Whitesides GM (1993) Features of gold having micrometer to centimeter dimensions can be formed through a combination of stamping with an elastomeric stamp and an alkanethiol ink followed by chemical etching. Appl Phys Lett 63(14):2002–2004

Chapter 24
The Relation Between Crispness and Texture Properties of Wax Apple

S. Topaiboul, C.-C. Guo, R.-H. Gao, and N.-S. Liou

Abstract In this study, the relations between the well-like sensory properties, crispness and firmness, of wax apple (Syzygium samarangense) and the texture properties were investigated by using double-bite tests. The strains of wax apples used in this study are Black Pearl and Tubtimchan. By comparing the sensory judgment and the TPA test results, the sensory judgment of crispness could be related to the TPA parameter fracturability. The wax apple with higher fracturability is considered to be crispier. However the sensory judgment of firmness cannot be direct correlated to any single TPA parameter. The sensory feeling of firmness could be related to the difference between hardness and fracturability.

Keywords Wax apple • Texture profile analysis • TPA • Crispness • Firmness

24.1 Introduction

The wax apple, in the global market, is the most competitive fruit of Taiwan. In general, well-liked wax apples are juicy, sweet, crispy and firm. Taiwan growers have developed many well-known strains of wax apples such as Black Pearl, Black Diamond and Southern Beauties. These wax apples bear the duty to meet the highest quality control standards of their label, creating a superb level of customer trust. All these high quality strains, descendants from common ancestor, resemble a bell in shape. Beside the sweetness, the firmness of these crispy wax apples is better than that of other strains of wax apples. However, compared with the size of bullet shape wax apple (Tubtimchan) in Southeast Asian countries, the size of these bell shape wax apples is relative small. The breeding of improved strains of wax apples which have the size of bullet shape wax apple and the firmness of bell shape wax apple can optimize the production of high quality wax apples.

Texture, besides flavor and sweetness, is one of the main criteria used by human and animal to judge the taste for fruits. Fruits with well-liked texture have advantage of having their seeds dispersed and deposited with plenty fertilizer. Furthermore, from a market point of view, fruit with adequate texture would have the better chance to be accepted by consumers. Crispness and firmness are the favored gustatory sensations.

Beside subjective way such as asking people to eat food and describe the texture properties of food, objective test methods such as ultrasound or acoustic emission [1, 2], fracture tests [3], tensile tests [4] have been used for tests of texture properties of food. Test criteria such as the noise made when the fruit is chewed or the fracture properties of the fruits had been used to measure the crispiness of foods. However, the noise level is not the only function of the fruit since the acoustic properties of the chewer can have an effect on the noise. Mechanical tests have been widely used to investigate mechanical behavior of fruits. The double-bite test, a test method of texture profile analysis (TPA) [5], provides a useful way of investigating several texture parameters of fruit in one test [6].

S. Topaiboul
College of Integrated Science and Technology, Rajamangala University of Technology Lanna, 99 Moo 8 T. Papong Doi Saket, Chiang Mai 50220, Thailand

C.-C. Guo • R.-H. Gao • N.-S. Liou (✉)
Department of Mechanical Engineering, Southern Taiwan University of Science and Technology, No. 1, Nan-Tai Street, Yongkang Dist, Tainan 710, Taiwan
e-mail: nliou@mail.stust.edu.tw

F. Barthelat et al. (eds.), *Mechanics of Biological Systems and Materials, Volume 4*,
Conference Proceedings of the Society for Experimental Mechanics Series,
DOI 10.1007/978-3-319-00777-9_24,

In this study, texture profile analysis was used to investigate the crispness and firmness of wax apples. Specimens of different strains of wax apples were subjected to double-bite tests. The relations between crispiness, firmness and texture properties such as hardness, fracturability, cohesiveness, springiness measured from texture property analysis were investigated.

24.2 Material and Method

Specimen preparation. The wax apple strains used in this study are Black Pearl and Tubtimchan (Fig. 24.1). These wax apples were purchased from local market and stored in the dark at room temperature before test. All tests were completed within 2 days of purchase. Specimens were cut immediately before tests. Cubic ($1 \times 1 \times 1$ cm^3) specimens were obtained using mechanically guided razor blades. For Tubtimchan wax apple, cubic specimens were taken from the top, middle and bottom parts of slices cut perpendicular to the long axis of the wax apple. For Black Pearl wax apple, the specimens were cut only from the middle section. The section of wax apple consists of outer cortex and inner pith parts. In order to avoid the large tissue and mechanical difference exist between cortex and pith tissues, the specimens were cut from cortex part only. For each wax apple, two specimens were selected for the tests.

TPA test. In order to simulate the highly destructive process of mastication, the level of compression should be high enough to fracture the specimens. A preliminary test was performed to estimate the value of compression at rupture and decide the level of compression for TPA test of wax apple. For wax apple, the compression level when the fracture occurs is about 15 ~ 20 %, thus the level of compression of TPA test was set to 30 %. The displacement rate of compression is 1.5 mm/s, and a rest period of two seconds is between the two compression cycles of double-bite test. The tests of Black Pearl wax apples were performed by using Instron 5865 tensile test machine (Fig 24.2a) and the tests of Tubtimchan were performed by using CT3 Texture Analyzer (Brookfield, USA) (Fig 24.2b).

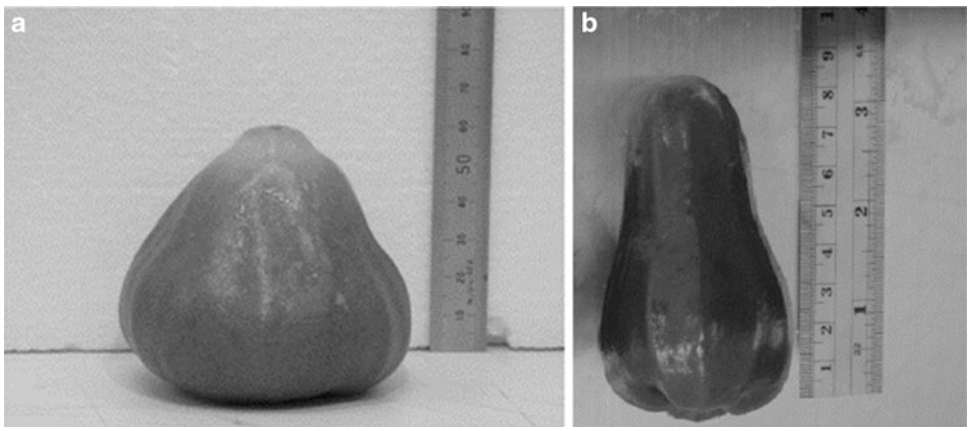

Fig. 24.1 The wax apples used for TPA tests: (**a**) Black Pearl and (b) Tubtimchan

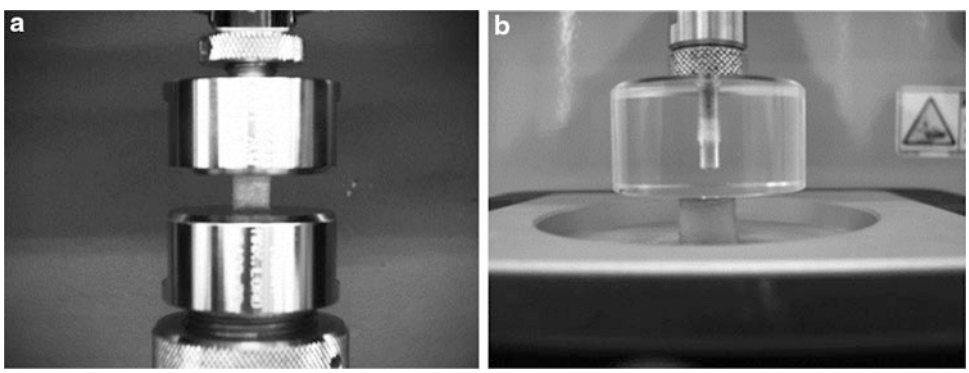

Fig. 24.2 TPA tests with (**a**) Instron 5865 and (**b**) CT3 texture analyzer

From the force-time curve of double-bite TPA test, the texture parameters such as fracturability, hardness, cohesiveness and springiness were calculated beside elastic modulus. According to practical definitions of standard TPA terms, fracturability point occurs where the force time curve has its first significant peak during the first compression cycle. The hardness value is the peak force of the first compression cycle. Cohesiveness is measured as the area of work during the second compression divided by the area of work during the first compression, and springiness is typically calculated as the ratio of the distance of the detected height of the product on the second compression divided by the original compression distance [5].

24.3 Results and Discussion

The force-time curves of double-bite tests of middle sections of Black Pearl and Tubtimchan wax apples are shown in Fig. 24.3 and the corresponding TPA parameters are listed in Table 24.1. It can be seen from the test results that Tubtimchan has the higher elastic modulus, hardness and fracturability, and the cohesiveness of Black Pearl is higher.

Four students were request to be the inspectors to perform the oral sensory tests (biting and chewing) about Black Pearl and Tubtimchan wax apples used for the TPA tests. The relative Crispness and Firmness of Black Pearl and Tubtimchan wax apples were judged and reported by the inspectors. The Black Pearl was considered to be less crispy but firm; and Tubtimchan was considered to be less firm but brittle.

By comparing the sensory judgment and the TPA test results, the sensory judgment of crispness could be related to the TPA parameter fracturability. The wax apple with higher fracturability is considered to be crispier. However the sensory judgment of firmness cannot be direct correlated to any single TPA parameter. The authors suggested that sensory feeling of firmness could be related to the difference between hardness and fracturability (i.e. Hardness value – Fracturability value). It can be seen for Black Pearl from Fig. 24.3a that the compression force keeps rising after the first fracture occurs. The continuous increasing of force during the chewing processing gives the sensory feeling of "firm". On the contrary, for Tubtimchan, it can be seen from Fig. 24.3b that the compression force keeps decreasing after the first fracture occurs. The continuous decreasing of force during the chewing processing gives the sensory feeling of "not firm".

The force-time curves of double-bite tests of top, middle and bottom sections of Tubtimchan are shown in Fig. 24.4 and the corresponding TPA parameters are listed in Table 24.2. It can be seen from Table 24.2 that the hardness, fracturability

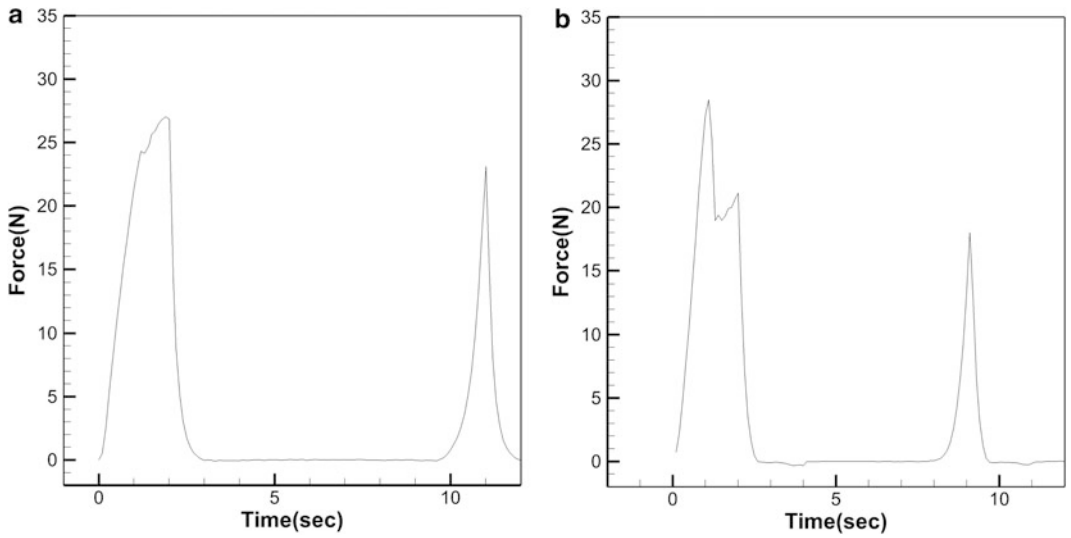

Fig. 24.3 Typical TPA test results of *middle* sections of (**a**) Black Pearl and (**b**) Tubtimchan

Table 24.1 TPA parameters of Black Pearl, Bullet and Tubtimchan wax apples (middle section)

	Hardness (N)	Fracturability (N)	Cohesiveness	Springiness	Elastic modulus (MPa)
Tubtimchan	26.2 ± 3.4	26.2 ± 3.4	0.2 ± 0.03	1.1 ± 0.3	2.0 ± 0.3
Black Pearl	20.0 ± 4.7	18.4 ± 4.9	0.3 ± 0.06	0.6 ± 0.1	1.4 ± 0.4

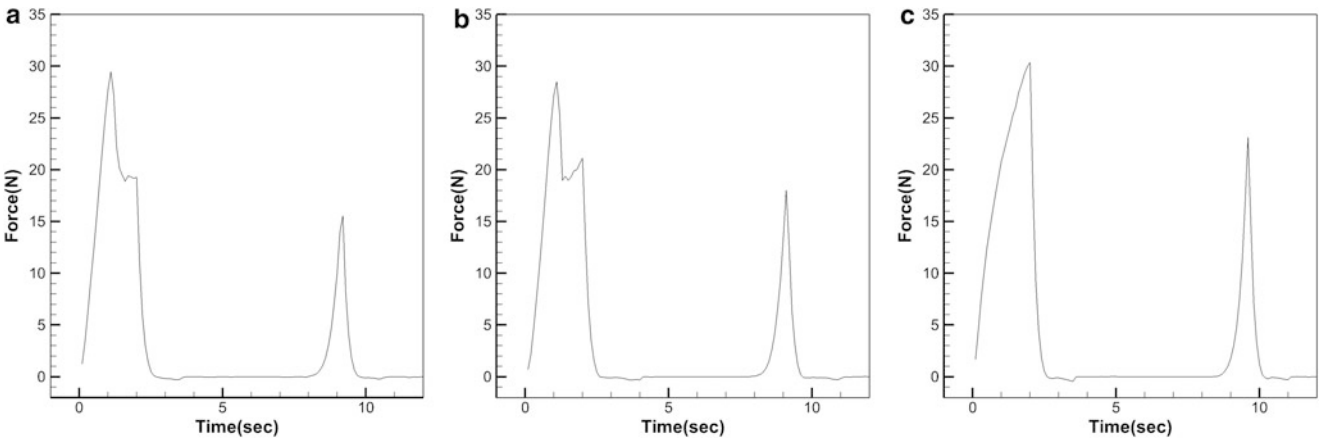

Fig. 24.4 TPA test results of Tubtimchan wax apple: (**a**) *top*, (**b**) *middle* and (**c**) *bottom* sections

Table 24.2 TPA parameters of Tubtimchan: top, middle and bottom sections

	Hardness (N)	Fracturability (N)	Cohesiveness	Springiness	Elastic modulus (MPa)
Top	23.7 ± 4.8	23.7 ± 4.8	0.2 ± 0.03	1.1 ± 0.3	1.9 ± 0.3
Middle	26.9 ± 2.1	26.2 ± 3.4	0.2 ± 0.03	1.1 ± 0.3	2.0 ± 0.3
Bottom	27.4 ± 2.9	26.8 ± 4.1	0.3 ± 0.03	0.6 ± 0.1	1.6 ± 0.3

and cohesiveness of bottom section are the highest; however the elastic modulus is the lowest. The hardness and fracturability of top section are the lowest. These results showed that the texture properties of Tubtimchan are not uniform everywhere, the top and middle sections are considered crispy but not firm, and the bottom section is both crispy and firm. If the firmness of top and middle sections of Tubtimchan can be improved by breeding, Tubtimchan has the potential to become one of the best quality and productive strains of wax apples due to its large size.

In this study, the tests were performed at 30 % compression. Higher degree of compression can be done to verify the influence of the degree of compression on the TPA test results.

24.4 Conclusion

The results of this study show that the TPA parameter fracturability could be related to the sensory feeling of crispness of wax apple, and the sensory feeling of firmness could be related to the difference between the value of hardness and fracturability. Furthermore, TPA analysis can be used to assist the breed improvement of wax apple by selecting the crispy and firm strains.

Acknowledgements Government of Taiwan R.O.C provided partial financial support to carry out this research. (NSC 101-2221-E-218 -026 -MY3)

References

1. Zdunek A, Bednarczyk J (2006) Effect of mannitol treatment on ultrasound emission during texture profile analysis of potato and apple tissue. J Texture Stud 37(3):339–359
2. Lutfi M, Herlaut C, Wahyunanto AN (2011) Designing and Creating Acoustic Ripeness Tester and Experimental Testing on Juan Canary Melon. Adv Nat Appl Sci 5(3):242–246
3. Vincent JFV (2004) Application of fracture mechanics to the texture of food. Eng Fail Anal 11(5):695–704
4. Herrero AM, de la Hoz L, Ordonez JA, Herranz B, de Avila MDR, Cambero MI (2008) Tensile properties of cooked meat sausages and their correlation with texture profile analysis (TPA) parameters and physico-chemical characteristics. Meat Sci 80(3):690–696
5. Bourne MC (1994) Food texture and viscosity. Academic, New York
6. Abbot JA, Affeldt HA, Liljedahl LA (1992) Firmness measurement of stored 'Delicious'apples by sensory methods, Magness-Taylor, and sonic transmission. J Am Soc Hortic Sci 117(4):590–595

Chapter 25
Fabrication and Mechanical Characterization of Jute Fiber/Epoxy Laminar Composites

M. Pinto, Y.K. Kim, A.F. Lewis, and V. Chalivendra

Abstract Alkali and Silane surface treatments based off of work published previously (J Appl Polym Sci 71(4):623–629, 1999; Polym Eng Sci 49(7):1253–1272, 2009; Mater Sci Eng A 508(1–2):247–252, 2009) were applied to plain weave and unidirectional jute fabric to improve epoxy compatibility and reduce moisture affinity. Efficacy of treatments was proven with the use of wicking tests. Studies performed on the hand-layup method showed unacceptable void content. Laminated jute/epoxy composites were fabricated using Vacuum Infusion to create void-free samples. This process was improved through optimization for use with jute and the addition of a pre-compaction step to increase fiber volume fraction from 25 % to a maximum of 40 %. Mechanical testing on composites fabricated with raw and treated jute fabrics showed a 300 % increase in elastic modulus for treated jute fabric over neat epoxy resin. Moisture absorption testing (ASTM D570) showed a significant improvement in moisture resistance for silane-treated fabrics.

Keywords Biocomposites • Jute composites • Vacuum infusion • Silane coupling • Water absorption

25.1 Introduction

Natural Fiber Composites (NFCs) show a great potential as sustainable structural material choices, with documented low density, good specific properties, low abrasiveness, and low environmental impact [1, 2]. NFCs provide an excellent opportunity to reduce energy consumption and pollution by providing alternatives to energy intensive synthetic materials. In fact, a study on Audi car door panels showed that replacing traditional ABS panels with hemp/epoxy composite material lowered net energy consumption by 45 % and significantly reduced CO_2 and methane emissions [3]. Because of the combined benefits of NFCs, the continued development and improvement of these materials could bring on a paradigm shift in the world of composite reinforcements. However, some major issues stand in the way of widespread commercial use of natural fibers as reinforcement. These fibers are cellulosic and therefore hydrophilic, making them very moisture sensitive and prone to dimensional instability and microbial attack [2]. The hydrophilicity of these fibers also causes poor interfacial bonding with the largely hydrophobic polymer matrices [1]. These issues must be addressed in full before NFCs can be widely adopted in structural applications.

Though there has been a great deal of work concerning jute fiber reinforced composites, there is still much room for improvement. Many published studies focused on short, chopped fiber composites with marginal strength improvements over neat resin. Still other studies using jute fabric as reinforcement made no measurement of the void content of their samples, leaving doubt in their reported properties [1]. The aim of this study is to increase the applicability of jute reinforcement in structural and automotive applications by fabricating void-free, laminated jute/epoxy composites with pre-treated plain weave jute fabric and unidirectional jute fabric and through-thickness nylon microfiber reinforcement. These materials were then characterized for mechanical and fracture properties using the appropriate ASTM standards. In addition, the effect of fabric treatment on the moisture absorption of the composites was evaluated.

M. Pinto • Y.K. Kim • A.F. Lewis • V. Chalivendra (✉)
University of Massachusetts Dartmouth, 285 Old Westport Rd., North Dartmouth, MA 02747, USA
e-mail: vchalivendra@umassd.edu

F. Barthelat et al. (eds.), *Mechanics of Biological Systems and Materials, Volume 4*,
Conference Proceedings of the Society for Experimental Mechanics Series,
DOI 10.1007/978-3-319-00777-9_25,

25.2 Fiber/Fabric Surface Treatments

The first stage of treatment used was an alkali treatment, similar to that used by various authors [4, 5]. The raw jute fabrics were stretched taught and secured on a frame as to not allow for shrinkage during treatment. The fabric and frame were then immersed in a 5 % (w/w) aqueous NaOH solution for 2 h. The fabrics were then removed, rinsed with distilled water, and immersed in a 2 % (w/w) aqueous acetic acid solution for 1 h. The fabrics were then removed, rinsed again with distilled water, and tested for neutrality with a phenolphthalein solution. Once neutrality was confirmed, the fabrics were dried at 80 °C overnight.

The procedure used for silane-coupling was modeled after that used by Seki et al. [5]. Following alkali treatment, the fabrics were soaked in a silane/methanol solution for 1 h. This solution consisted of 1 % (w/w) Dow Corning Z-6173 alkoxysilane agent mixed in methanol for 5 min using a magnetic stirrer. The fabrics were then removed, rinsed thoroughly with distilled water, and dried overnight at 100 °C.

25.3 Composite Fabrication

Two methods of composite fabrication were employed and compared: hand-layup and Vacuum Infusion (VI). For all composites, the matrix material was FiberGlast 2000/2120 epoxy resin system, mixed at a mass ratio of 27:100 hardener to resin. In the hand-layup method, the desired number of 10.5″ × 10.5″ plies were cut from the fabric roll. The epoxy resin system was then mixed at the indicated mass ratio, and de-gassed under vacuum to remove air bubbles. The cut plies were then individually impregnated with this resin system, ensuring even distribution of the matrix throughout each ply. Once all fabric layers were saturated with resin, they were carefully stacked upon one another in the desired stacking sequence, in this case (0/90). Once the wet stack was properly established, it was sandwiched between bleeder and breather cloths and sealed in a bag of Mylar film. The stack was then placed in a platen press where 120 psi of pressure was applied to consolidate the material. After curing at room temperature overnight, the material was post cured in an oven at 50 °C for 3 h and 80 °C for 3 h.

First, the desired number of 10.5″ × 10.5″ plies were cut from the fabric roll. These layers were then stacked in the desired (0/90) sequence and centered on a glass panel coated with mold release film. An additional layer of peel ply was then placed over the dry laminate stack, followed by a layer of Enkafusion distribution media. Spiral tubing wrapped in peel ply was attached to two vacuum tubes, one to be attached to the vacuum pump, and one inserted in the resin bucket. This tubing was placed on the peel-ply layer on either side of the dry laminate stack, and the entire set-up was sealed under vacuum bagging using double-sided sealant tape. The layup for this procedure is illustrated in Fig. 25.1. The vacuum pump was then started, and the pressure slowly reduced to a maximum vacuum of −30 inHg. The laminate stack was left under vacuum for at least 1 h before proceeding, to allow for fabric compaction and the boiling off of absorbed moisture. Meanwhile, the epoxy resin system was mixed at the indicated mass ratio and degassed under vacuum to remove all diffused air. Following this step, the resin was introduced into the vacuum sealed environment through the resin inlet tube. The resin was then drawn through the laminate stack by the pressure differential created by the vacuum, fully wetting the fabric plies. Once the laminate stack was fully wet-out, the vacuum was reduced to −24 inHg. Deadweight was applied to the laminate stack for additional compaction and the panel was left to cure at room temperature overnight. Following cure, the panel was disconnected from the vacuum and post-cured for 3 h at 50 °C and 3 h at 80 °C.

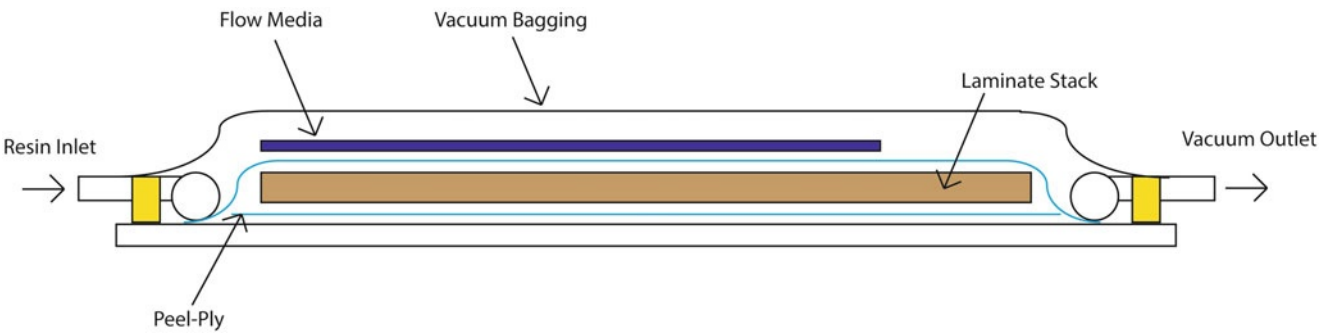

Fig. 25.1 Vacuum infusion layup diagram

A slight procedural alteration was used in the fabrication of composites with z-direction reinforcement. Through-thickness reinforcement was applied to the laminate plies using electrostatic flocking of 3 denier, 1.3 mm long nylon microfibers at a density of ~200 fibers/mm^2 prior to lay-up using the electrostatic flocking technique.

25.4 Experimental Methods

The effects of surface treatments on the epoxy and moisture affinity of jute were determined using wicking testing. For these tests, treated and untreated jute yarns were suspended vertically with one end immersed in distilled water or epoxy. The height that the fluid wicked up the yarn was used as a comparison between treatment types.

ASTM D3039 was used to determine the tensile strength and elastic modulus of the materials. Double-notch compression samples were prepared following ASTM D3846 to evaluate Interlaminar Shear Strength (ILSS). These tests were performed on composites made from untreated and treated plain weave and unidirectional jute fabrics, and their results used to compare the effects of treatment and fabric architecture on mechanical properties. At least five samples were tested for each material type.

Fracture toughness was determined using the Double-Cantilever Beam (DCB) test as outlined in ASTM D5528. To manufacture samples for this test, composite panels were fabricated following the normal procedure above while inserting a Teflon strip in the mid-plane of the laminate stack. This had the effect of creating an initial crack in the material as required by the standard. Test samples were then prepared from these panels as shown in Fig. 25.2, having a width of 20–25 mm and a length of 125 mm. These samples were loaded into an INSTRON testing machine and loaded at a crosshead speed of 0.5 mm/min while the delamination length was monitored using a digital microscope. Data reduction was performed using a robust numerical method to best capture the strain energy involved in crack growth. At least five samples were tested for each material type.

To perform moisture absorption tests, 1″ by 3″ test samples were cut from the composite panels following ASTM D570. These samples were dried in an oven at 50 °C for 24 h then weighed to determine the initial, dry mass. The samples were then immersed in distilled water and left for at least 24 h. Following this soak, the samples were removed, wiped with a clean cloth, and weighed. The percent mass gain was calculated for each sample and the samples were re-immersed. Several soaking cycles were carried out for the samples, and at least five samples were tested for each material type.

25.5 Results

Water wicking results for yarns of different treatments are included in Fig. 25.3. These results show that treatment with Dow Corning Z-6173 silane coupling agent drastically improved the yarns' resistance to water absorption. In addition, epoxy wicking test showed increased epoxy wicking for yarns with silane surface treatment. These results confirmed our choice of coupling agent and the efficacy of the treatment procedure.

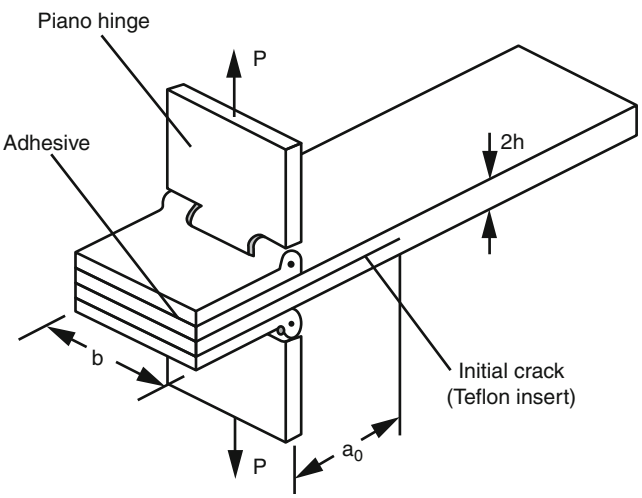

Fig. 25.2 DCB test specimen

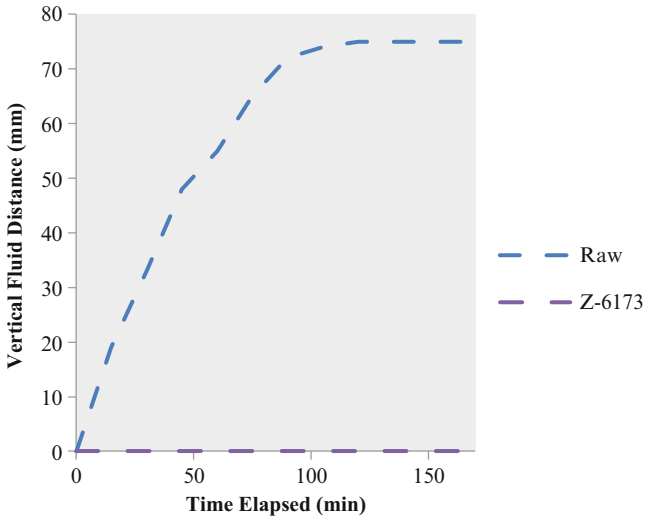

Fig. 25.3 Water wicking test results

Volume fraction analyses on composites manufactured using hand-layup revealed an unacceptably high void volume fraction of 15 %. Void content this high would drastically degrade the mechanical properties of the composite, making them unfit for service [6]. Composites manufacture using VI exhibited near-zero void content, proving that this fabrication method far superior for fabricating jute fabric reinforced composites.

Tensile testing showed a 230 % increase in Young's Modulus over neat epoxy for silane-treated plain weave fabric, and a 360 % increase for silane-treated unidirectional fabric. In addition, silane-treatment improved Young's Modulus by 36 % over untreated fabric, showing that the treatment improved stress transfer to the higher modulus fibers through an improved interface. The modulus value found in this study is 66 % higher than values published in other works [5] where hand-layup was used for fabrication rather than VI. Tensile strength experienced a slight loss as a result of treatment, implying improved stress transfer to the yarns which have a lower tensile strength than the epoxy matrix.

ILSS decreased by 26 % as a result of surface treatment. This loss was accompanied by a shift in failure mode from matrix shearing and debonding to fiber and yarn breakage. This reinforces the assertion that the fiber/matrix interface has improved as a result of surface treatment, as stress transfer to the fibers has been improved.

Water immersion testing showed that silane surface treatment reduced the water absorption of the composites by 61 %. This shows an excellent improvement in the environmental resistance of the jute composites was gained through the application of this treatment.

Fracture testing is currently underway and the results of these tests will be presented at the conference in June.

25.6 Conclusions

As a result of this study, laminated jute/epoxy composites have been successfully fabricated with near-zero void content, improved fiber/matrix interfacial strength, and greatly improved moisture resistance. The work here has shown that the current methods used in NFC fabrication, namely hand-layup, are inappropriate for these types of materials as they result in a very high void content which ruins mechanical properties. While VI is a more delicate process, it consistently provides low void content, good fiber volume fraction, and is easily scalable to larger and more complex shapes. This scalability is crucial in expanding the use of NFCs to the commercial market.

Surface treatments with Dow Corning Z-6173 silane coupling agent showed improved fiber/matrix adhesion and greatly reduced moisture absorption. This improved moisture resistance will increase the applicability of NFCs to structural applications where they may be exposed to weathering, and will greatly increase the useful life of these materials.

The effects of treatments as well as z-direction reinforcement on the fracture toughness of jute/epoxy composites will be discussed in full at the conference this June. Based on work previously performed in our laboratory on glass/epoxy composites, we expect a significant improvement in fracture toughness with the addition of through-thickness reinforcement [7].

Acknowledgements The authors acknowledge the financial support of The Massachusetts Clean Energy Center for funding this project and also thank Dr. Rice for his suggestions throughout the duration of project.

References

1. Kalia S, Kaith BS, Kaur I (2009) Pretreatments of natural fibers and their application as reinforcing material in polymer composites-a review. Polym Eng Sci 49(7):1253–1272
2. Monteiro SN, Lopes FPD, Barbosa AP, Bevitori AB, Da Silva ILA, Da Costa LL (2011) Natural lignocellulosic fibers as engineering materials—an overview. Metall Mater Trans A 42:2963–2974
3. Joshi SV, Drzal LT, Mohanty AK, Arora S (2004) Are natural fiber composites environmentally superior to glass fiber reinforced composites? Compos Part A Appl Sci Manufact 35(3):371–376
4. Gassan J, Bledzki AK (1999) Alkali treatment of jute fibers: relationship between structure and mechanical properties. J Appl Polym Sci 71 (4):623–629
5. Seki Y (2009) Innovative multifunctional siloxane treatment of jute fiber surface and its effect on the mechanical properties of jute/thermoset composites. Mater Sci Eng A 508(1–2):247–252
6. Judd NCW, Wright WW (1978) Voids and their effects on the mechanical properties of composites – an appraisal. SAMPE 14:10–14
7. Feng L (2006) Fracture toughness of through thickness flock fiber reinforced laminar composites. M.Sc. thesis, University of Massachusetts, Dartmouth

Chapter 26
A Fractional Pressure-Volume Model of Cerebrospinal Fluid Dynamics in Hydrocephalus

Justin Kauffman and Corina S. Drapaca

Abstract Hydrocephalus is a serious neurological disorder characterized by abnormalities in the cerebrospinal fluid (CSF) circulation, resulting in an excessive accumulation of CSF in the ventricles of the brain, brain compression and sometimes an increase in the intracranial pressure. It is believed that hydrocephalus may be caused by increased CSF production, or by obstruction of CSF circulation or of the venous outflow system. Therefore, the treatment is based on CSF flow diversion. Given that the response of patients who have been treated continues to be poor, there is an urgent need to design better therapy protocols for hydrocephalus. An important step in this direction is the development of predictive mathematical models that better explain the fundamental science behind this clinical condition. One of the first mathematical models of CSF pressure-volume compensation introduced by Marmarou in the 1970s provides a theoretical basis for studying hydrocephalus. However, the model fails to fully capture the complex CSF dynamics. In this paper we propose a generalization of Marmarou's model using fractional calculus. We use a modified Adomian decomposition method to solve analytically the proposed fractional order nonlinear differential equation. Our results show temporal multi-scaling behavior of the CSF dynamics.

Keywords Brain biomechanics • Hydrocephalus • Pressure-volume model • Fractional Riccati equations • Adomian decomposition method

26.1 Introduction

Hydrocephalus is a disease of the brain in which abnormalities in the cerebrospinal fluid (CSF) flow causes ventricular dilation, brain compression and sometimes an increase in the intracranial pressure. The treatment aims to reverse the dilation of the ventricles by either CSF shunt implantation or by performing an endoscopic third ventriculostomy (ETV) surgery resulting in a relief from the symptoms of hydrocephalus. However the two treatment options show no statistically significant difference in the efficacy for treating hydrocephalus; the responses of patients who have been treated with either surgery continue to be poor [1]. Therefore, there is a momentous need to improve the therapy protocols for hydrocephalus. Predictive mathematical models that help us to better understand the fundamental science behind this disorder could play an essential role in achieving this goal.

More than three decades ago Marmarou [2] formulated the first mathematical model of CSF pressure-volume compensation for studying hydrocephalus. However, with the recent discoveries in neuroscience it has become evident that Marmarou's model fails to fully capture the complex CSF dynamics controlled by CSF-brain tissue interactions. Therefore, in this paper we propose a generalization of Marmarou's model using fractional calculus. By replacing the first order temporal derivative in Marmarou's model by a fractional order time derivative we introduce in our model an inhomogeneous clock that continuously connects the global macroscopic and the local microscopic time scales. We use the modified Rach-Adomian-Meyers decomposition method proposed in [3] to solve analytically our fractional order nonlinear differential equation of Riccati type. Our results show temporal multi-scaling behavior of the CSF dynamics.

J. Kauffman (✉) • C.S. Drapaca
Department of Engineering Science and Mechanics, The Pennsylvania State University, University Park, PA 16802, USA
e-mail: jak5378@psu.edu

F. Barthelat et al. (eds.), *Mechanics of Biological Systems and Materials, Volume 4*,
Conference Proceedings of the Society for Experimental Mechanics Series,
DOI 10.1007/978-3-319-00777-9_26,

26.2 The Fractional Pressure-Volume Model of the CSF Dynamics

The conservation law of CSF hydrodynamics states that the rate of CSF formation I_f equates the sum of the rate of change of CSF volume $V(t)$ stored in the brain ventricles $\frac{dV}{dt}$ and the rate of CSF absorption defined in [2] as $\frac{(P-P_d)}{R}$, where P is the CSF pressure, P_d is the pressure of the venous system and R is the resistance of CSF to absorption. In [2], it is assumed that $\frac{dV}{dt} = \frac{1}{KP}\frac{dP}{dt}$ where $K > 0$ is a constant.

In order to account for the complex and still barely known CSF-brain dynamics that affects the CSF pressure, we propose to represent the time variation of the CSF pressure using *the fractional order Caputo derivative of order* $0<\alpha \leq 1$ which is by definition:

$$D^{\alpha}P(t) = \frac{1}{\Gamma(1-\alpha)}\int_0^t \frac{\frac{dP}{ds}}{(t-s)^{\alpha}}ds, \tag{26.1}$$

where $\Gamma(z) = \int_0^{\infty} e^{-t}t^{z-1}dt$ is the Gamma function. We notice that $D^1P = \frac{dP}{dt}$ is the classic first order derivative. Thus we assume that $\frac{dV}{dt} = \frac{1}{KP}D^{\alpha}P$, and in this case the conservation law of the CSF hydrodynamics becomes:

$$D^{\alpha}P(t) + \frac{K}{R}P^2(t) - K\left(I_f(t) + \frac{P_d}{R}\right)P(t) = 0 \tag{26.2}$$

Our model given by Eq. 26.2 is a fractional Riccati differential equation for the CSF pressure P which reduces to Marmarou's model [2] when $\alpha = 1$. Eq. 26.2 is solved for a given initial condition $P(0) = P_0 =$ constant. For simplicity we assume that $P_d = P_0$.

We solve Eq. 26.2 for the following cases [2]: (1). constant infusion of CSF: $I_f = F =$ constant, (2). bolus injection of CSF: $I_f = V\delta(t)$, and (3). volume removal of CSF: $I_f = -V\delta(t)$, where $V > 0$ is constant, and $\delta(t)$ is the Dirac distribution.

In case 1, we denote by $\beta_1 = -K\left(F + \frac{P_0}{R}\right)$, $\beta_2 = \frac{K}{R}$ and then we can immediately write down the analytic solution by using the Rach-Adomian-Meyers (RAM) modified decomposition method presented in [3] for a similar fractional Riccati differential equation. Thus the solution in this case is:

$$P(t) = \sum_{n=0}^{\infty} a_n t^{n\alpha} \tag{26.3}$$

where $a_0 = P_0$, $a_{n+1} = \frac{\Gamma(n\alpha+1)}{\Gamma(n\alpha+\alpha+1)}(-\beta_1 a_n - \beta_2 A_n)$, $n = 0,\ 1,\ 2,\ \ldots.$ with the Adomian polynomials of the non-linear term $f(P) = P^2$ given by $A_n = \sum_{k=0}^{n} a_{n-k}a_k$, $n = 0, 1, 2, \ldots..$

The radius of convergence of solution (26.3) is (see [3]): $\rho_n = \left(1/|a_n|^{1/n}\right)^{1/\alpha}$. When $\alpha = 1$ we recover the solution to the classic Riccati equation given in [2]:

$$P(t) = \frac{P_0(P_0 + RF)}{P_0 + RFe^{-K(P_0+FR)t/R}} \tag{26.4}$$

We notice that in [2] Marmarou obtained formula (26.4) by using a change of variable to reduce the Riccati equation to a first order linear differential equation which he solved using the integrating factor method. Marmarou used the same approach to solve for cases 2 and 3, as well. However, the integrating factor method provides the unique solution to an initial value problem associated to a first order linear differential equation only if the coefficients of the equation are continuous functions. This means that for cases 2 and 3 the integrating factor method cannot be used since in these cases one of the coefficients is the Dirac distribution, and therefore the solutions given by Marmarou in [2] for these two cases are invalid for times close to $t = 0$. In order to correctly solve the Riccati equation proposed by Marmarou for cases 2 and 3 we approximate the Dirac distribution by one of its many continuous functions $\delta(t) = lim_{\in \to 0}\delta_{\in}(t)$, solve the corresponding sequence of

Riccati equations with continuous coefficients for $P_\epsilon(t)$ using the same change of variable as in [2] and the integrating factor method and then the limit $P(t) = lim_{\in \to 0} P_\in(t)$ is the solution to the original Riccati equation. This is the approach we will also use to solve Eq. 26.2 in cases 2 and 3.

We denote for simplicity by $\tilde{V} = \pm V$ and approximate the Dirac distribution by $\delta_\in(t) = \frac{1}{2\sqrt{\pi}\sqrt{\in}} e^{-\frac{t^2}{(4\in)}}$. We solve now the following sequence of fractional Riccati equations:

$$D^\alpha P + \frac{K}{R}P^2 - K\left(\tilde{V}\frac{1}{2\sqrt{\pi}\sqrt{\in}}e^{-\frac{t^2}{(4\in)}} + \frac{P_0}{R}\right)P = 0 \tag{26.5}$$

Equation 26.5 is a special case of the following general equation:

$$D^\alpha P(t) + \beta_1 P(t) + \beta_2 h(t)P(t) + \beta_3 f(P(t)) = g(t) \tag{26.6}$$

Equation 26.6 has not been investigated in [3], and thus we need to show that we can use the RAM modified decomposition method [3] to solve this equation for the initial condition $P(t_0) = P_0$. We use the fractional Taylor series representations $h(t) = \sum_{n=0}^{\infty} h_n (t-t_0)^{n\alpha}$, $g(t) = \sum_{n=0}^{\infty} g_n (t-t_0)^{n\alpha}$ (see [4] for the full representation of these series and their coefficients) and we look for a solution of the form $P(t) = \sum_{n=0}^{\infty} a_n (t-t_0)^{n\alpha}$.

By replacing the series representations of $h(t)$, $g(t)$, $P(t)$, and $D^\alpha((t-t_0)^{n\alpha}) = \frac{\Gamma(n\alpha+1)}{\Gamma(n\alpha-\alpha+1)}(t-t_0)^{(n-1)\alpha}$ into Eq. 26.6 and equating the coefficients of the terms with the same power, we get:

$$a_0 = P_0,\ a_{n+1} = \frac{\Gamma(n\alpha+1)}{\Gamma(n\alpha+\alpha+1)}(g_n - \beta_1 a_n - \beta_3 A_n - \beta_2 \sum_{k=0}^{n} a_k h_{n-k}),\ n = 0, 1, 2, \ldots$$

where the Adomian polynomials associated to the nonlinear term $f(P)$ are $A_0 = f(P_0)$, $A_1 = P_1 \frac{df(P_0)}{dP_0}$, $A_2 = P_2 \frac{df(P_0)}{dP_0} + \frac{P_1^2}{2}\frac{d^2 f(P_0)}{dP_0^2}$ .... with $P_n = a_n(t-t_0)^{n\alpha}$. The radius of convergence of the series solution for Eq. 26.6 remains the same as before. Thus, after performing some basic calculations, the series solution to Eq. 26.5 can be written as:

$$P_\in(t) = P_0 + \frac{K\tilde{V}P_0}{\Gamma(\alpha+1)}t^\alpha + \frac{K\tilde{V}P_0}{\Gamma(2\alpha+1)}(K\tilde{V} - \frac{KP_0}{R} + \Gamma(\alpha+1)h_1)\ t^{2\alpha} + \ldots \tag{26.7}$$

where $h_1 = \frac{1}{\Gamma(\alpha+1)\Gamma(1-\alpha)} \lim_{t\downarrow 0,\ \in\downarrow 0} \frac{-1}{4\in\sqrt{\pi}\sqrt{\in}} \int_0^t \frac{s\, e^{\frac{-s^2}{(4\in)}}}{(t-s)^\alpha} ds$ is the coefficient of the second term in the fractional Taylor series expansion of $h(t) = \frac{1}{2\sqrt{\pi}\sqrt{\in}} e^{-\frac{t^2}{(4\in)}}$. Once the CSF pressure is known, the ventricular CSF volume is found by integrating $\frac{dV}{dt} = \frac{1}{KP} D^\alpha P = I_f + \frac{1}{R}(P_0 - P)$ (from Eq. 26.2) with an initial condition $V(0) = V_0$.

26.3 Results

In our numerical simulations we used the following parameters found experimentally in [2] while investigating possible mechanisms for the onset of hydrocephalus in adult cats: $P_0 = P_d = 100$ [mmH$_2$O], $K = \frac{1}{0.4343}$ [mL^{-1}min$^{-\alpha}$], $R = 609$ [mmH$_2$O mL^{-1} min], $V_0 = 3$[mL], a constant infusion of rate $F = 0.02$ [mL min^{-1}] in case 1, and a bolus injection of $V = 0.02$[mL] in case 2. Given the duration of the experiments in [2] of 6–8 min, and the limitations imposed on our series solutions by their corresponding radii of convergence, we show our results for a time period of 5 min for the case of constant infusion, and for a period of up to 1 min for the case of bolus injection.

The solution given by formula (26.3) for different values of $\alpha < 1$ and the solution corresponding to $\alpha = 1$ given by formula (26.4) are plotted in Fig. 26.1a, while the corresponding variations of the ventricular CSF volume are shown in Fig. 26.1b. We notice that as α converges to 1 the corresponding pressures from formula (26.3) converge to the pressure given by formula (26.4). A similar behavior is seen in Fig. 26.1b for the ventricular CSF volume. As expected for the case of constant CSF infusion, the CSF volume increases in time. In addition, the initial slope of the CSF pressure decreases as α increases. During the very slow development of hydrocephalus when CSF accumulates in the ventricles due to say a constant

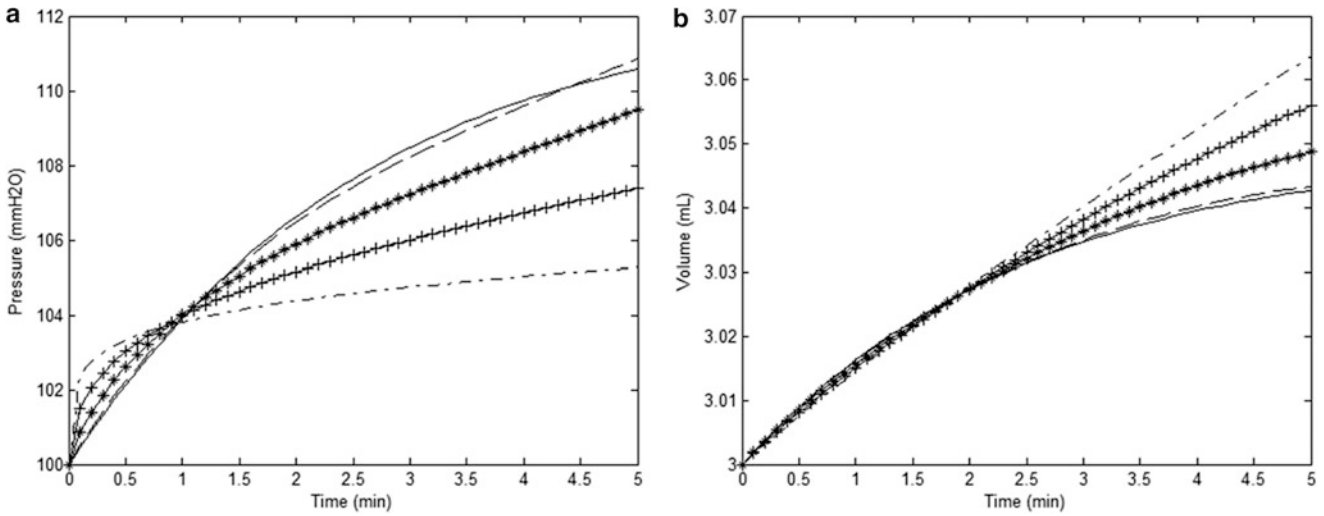

Fig. 26.1 The shapes of the CSF pressure (**a**) and ventricular CSF volume (**b**) in the case of constant CSF infusion for the following values of α: 0.25 (−.), 0.5 (+−), 0.75 (∗−), 0.95 (−−). The *solid line* corresponds to the solution given by formula (26.4)

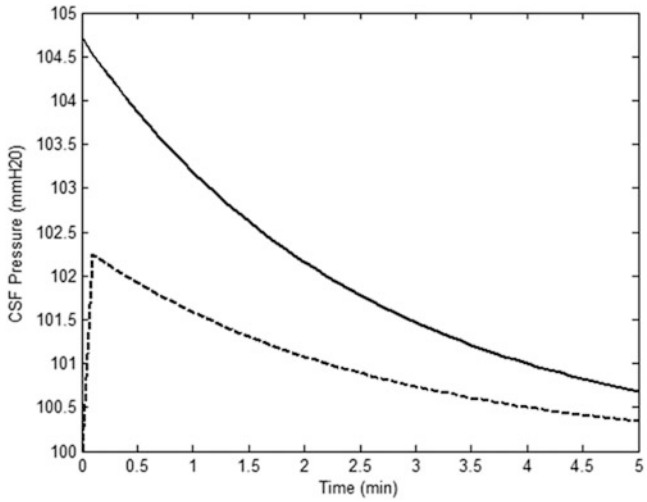

Fig. 26.2 In the case of bolus injection, the CSF pressure found in [2] is shown as a *solid line*, while the *dashed line* shows the CSF pressure calculated using a sequence of continuous functions to approximate the Dirac distribution

CSF infusion, the CSF pressure increases abruptly initially and then its increase slows down due to controllers such as special proteins in the brain that provide volume regulation and osmotic pressures. The shapes of the CSF pressure for $\alpha<0.5$ shown in Fig. 26.1a capture this physics of the CSF-brain interactions.

The results for the case of bolus injection are shown in Figs. 26.2, 26.3, and 26.4. In Fig.26.2 we plotted the CSF pressure as calculated in [2] and the CSF pressure we obtained using an approximation for the Dirac distribution. As expected, the two solutions do not agree on short times, although at long times they eventually coincide. In Figs. 26.3 and 26.4 we show the temporal variations of the CSF pressure as given by formula (26.7) and the corresponding ventricular CSF volumes for two sets of α: [0.05, 0.15, 0.25, 0.35] (Fig. 26.3) and [0.25, 0.5, 0.75, 0.95] (Fig. 26.4). While the CSF volume for each α is slightly decreasing as expected after a very small bolus injection (Figs. 26.3b and 26.4b), hinting to converge to the shape of the CSF volume obtained using the pressure calculated for an approximation of the Dirac distribution, the same cannot be said about the CSF pressure. While the initial slope of the pressure decreases as α increases (Figs. 26.3a and 26.4a), for $\alpha<0.5$ the pressure increases and then it reaches a steady state value (Fig. 26.3a), and as α approaches 1, the pressure given by formula (26.7) does not converge to the CSF pressure calculated using an approximation of the Dirac distribution (Fig. 26.4a). In our further work we plan to add more terms to formula (26.7) as well as to use Pad e′ approximants as in [3]

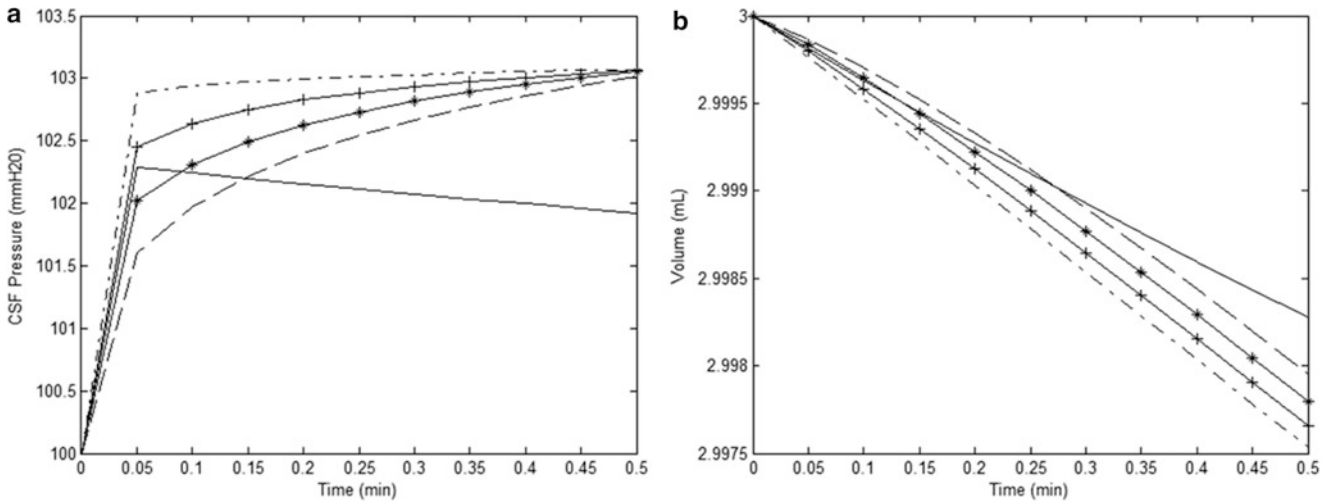

Fig. 26.3 The shapes of the CSF pressure (**a**) and ventricular CSF volume (**b**) in the case of bolus injection for the following values of α: 0.05 $(-.)$, 0.15 $(+-)$, 0.25 $(*-)$, 0.35 $(--)$. The *solid line* shows our approximate solutions to Marmarou's model in this case. The largest radius of convergence corresponds to $\alpha = 0.35$ and is given by $\rho_2 = 0.4754$

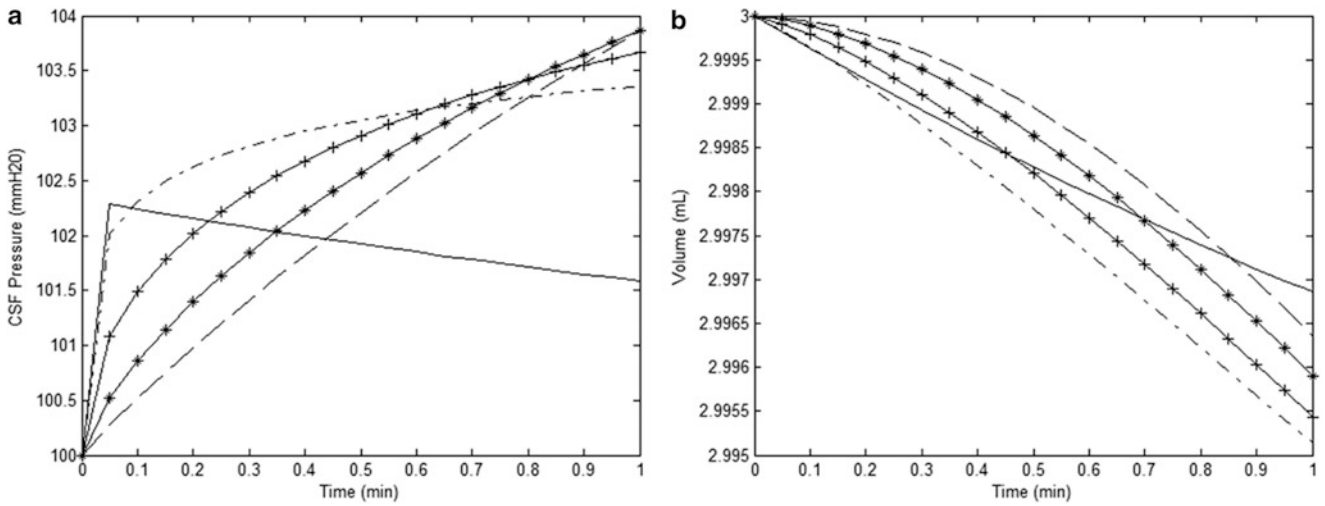

Fig. 26.4 The shapes of the CSF pressure (**a**) and ventricular CSF volume (**b**) in the case of bolus injection for the following values of α: 0.25 $(-.)$, 0.5 $(+-)$, 0.75 $(*-)$, 0.95 $(--)$. The *solid line* shows our approximate solutions to Marmarou's model in this case. The largest radius of convergence corresponds to $\alpha = 0.95$ and is given by $\rho_2 = 1.0983$

to get this expected convergence as α goes to 1. We will also implement better numerical solvers for the coefficients h_n, $n = 1, 2, \ldots$ of the fractional Taylor series of $h(t)$ needed in formula (26.7). It is important to notice that if after all these improvements we still see the same asymptotic behavior of the CSF pressure for $\alpha<0.5$ (Fig. 26.3a), we could hypothesize that at later times the CSF volume might start to increase and thus it could model the slow development of hydrocephalus. This means that a bolus injection of CSF could in fact cause hydrocephalus when the CSF-brain dynamics has been somehow compromised (by for instance damages of biochemical and/or biomechanical nature in the CSF[1] and/or the brain tissue). Thus, our fractional pressure-volume model appears to capture certain damaging processes happening at time scales of order $\alpha<0.5$ which could cause the onset of hydrocephalus either by constant infusion of CSF or by CSF bolus injection. A constant infusion of CSF is by now a known and accepted mechanism for hydrocephalus; however, *the bolus injection is a new and rather unexpected cause of hydrocephalus*. A deeper numerical analysis of our model as well as experiments are needed in order to truly say that this might be possible.

[1] We suspect that in hydrocephalus the CSF is a non-Newtonian fluid (while in healthy subjects it is already known that the CSF is Newtonian)

26.4 Conclusion

In this paper we presented a novel pressure-volume model for the CSF dynamics for studying hydrocephalus. We used fractional calculus and showed that our model is able to capture certain aspects of the CSF-brain interactions which have not been modeled before. Our results suggest that for a fractional order $\alpha<0.5$ both, a constant infusion of CSF and a bolus injection, are possible mechanisms for the onset of hydrocephalus.

References

1. Tuli S, Alshail E, Drake J (1999) Third ventriculostomy versus cerebrospinal fluid shunt as a first procedure in pediatric hydrocephalus. Pediatr Neurosurg 30(1):11–15
2. Marmarou A, Shulman K, Rosende RM (1978) A nonlinear analysis of the cerebrospinal fluid system and intracranial pressure dynamics. J Neurosurg 48:332–344
3. Duan J-S, Chaolu T, Rach R (2012) Solutions of the initial value problem for nonlinear fractional ordinary differential equations by the Rach-Adomian-Meyers modified decomposition solution. Appl Math Comp 218:8370–8392
4. Odibat ZM, Shawagfeh NT (2007) Generalized Taylor's formula. Appl Math Comp 186:286–293

Chapter 27
Site-Specific Diagnostic Evaluation of Hard Biological Tissues Using Solitary Waves

Jinkyu Yang, Sophia N. Sangiorgio, Sean L. Borkowski, Edward Ebramzadeh, and Chiara Daraio

Abstract We perform site-specific diagnostic evaluation of hard biological tissues via highly nonlinear solitary waves. Solitary waves are compact-supported tunable pulses with extremely high energy density, which can be efficiently formed in a chain of ordered granular particles defined as 1D granular crystals. We transmit a single pulse of solitary waves into specific areas of artificial biological systems via direct mechanical contact with a granular crystal sensor. We then record the solitary waves backscattered from a targeted bone area to assess its mechanical stiffness. By taking advantage of the coupling between nonlinear granular media and biological systems, we demonstrate that reflected solitary waves are highly sensitive to site-specific mechanical properties of hard biological tissues. The efficacy of the diagnostic approach is investigated by comparing the stiffness measurements with nominal elastic moduli of polyurethane foams that mimic osteoporotic bone. We also perform numerical investigations via a discrete element (DE) model, simulating propagation and attenuation of solitary waves at the interfaces. The site-specific evaluation technique via solitary waves has the potential for clinical applications, such as assisting appropriate intraoperative decision during joint replacement or spinal surgery for better surgical outcome.

Keywords Bone diagnostics • NDE • Solitary waves • Granular crystals

27.1 Introduction

According to the Surgeon General of the United States, osteoporosis affects approximately 10 million individuals over the age of 50 and is responsible for an estimated 1.5 million fractures annually in the US alone [1]. In elderly patients, hip fractures are often treated by performing a total hip arthroplasty (THA) operation, which replaces the joint with an artificial implant. The THA operation is well documented to have better long-term outcome with better bone quality [2]. Due to the aging population, spinal surgery is also becoming more popular. The implants in spinal surgery require adequate bone quality as they function by transmitting a large share of the loads through the posterior elements. Depending on the bone quality, different surgical procedures are often selected for improved long-term stability of implant. In particular, the site-specific mechanical properties of the posterior elements of the spine are therefore critical to the success of these surgeries [3–5].

The tools that are currently available for bone quality assessment include dual energy X-ray absorptiometry (DEXA), quantitative computerized tomography (qCT), and quantitative ultrasound (QUS). The most commonly used method, DEXA, is routinely used to screen for osteoporosis and osteopenia; however, this is a 2D quantification which averages bone mineral density (BMD) over relatively large geometric regions of interest. In addition to the lack of a direct

J. Yang (✉)
Mechanical Engineering Department, University of South Carolina, Columbia, SC 29208, USA

Graduate Aerospace Laboratories (GALCIT), California Institute of Technology, Pasadena, CA 91125, USA
e-mail: jkyang@gmail.com

S.N. Sangiorgio • S.L. Borkowski • E. Ebramzadeh
J. Vernon Luck, MD Orthopaedic Research Center, Los Angeles Orthopaedic Hospital, Los Angeles, CA 90007, USA

C. Daraio
Graduate Aerospace Laboratories (GALCIT), California Institute of Technology, Pasadena, CA 91125, USA

F. Barthelat et al. (eds.), *Mechanics of Biological Systems and Materials, Volume 4*,
Conference Proceedings of the Society for Experimental Mechanics Series,
DOI 10.1007/978-3-319-00777-9_27,

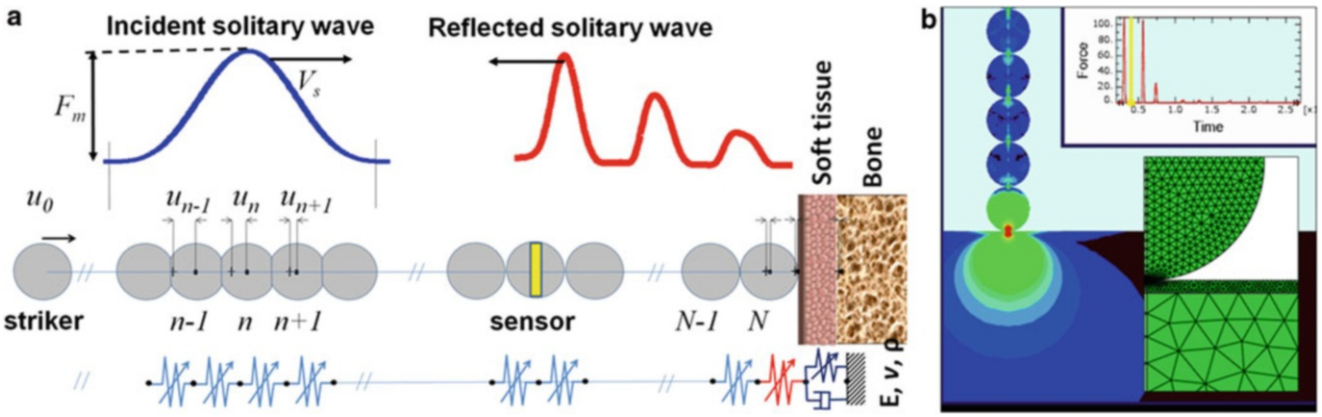

Fig. 27.1 (**a**) Schematic diagram showing the formation of compact-supported solitary pulses (width: ~5 particle diameters in a uniform 1D Hertzian chain). The *bottom* spring-mass system represents a discrete element model. (**b**) FEM results showing the interaction of HNSWs with bone. The *upper inset* shows incident and reflected solitary wave profile, while the *bottom inset* shows FEM mesh of multi-layered bone structures

measurement of bone quality and its relation to fracture, the DEXA scan also requires scored analysis performed by a radiologist [6]. On the other hand, pQCT can provide the bone mineral content as a function of 3D location within the bone, providing a finer mapping of the distribution of bone mineral content. However, pQCT requires a large machine with multiple X-rays, exposing patients to heavy dose of radiation. QUS is conventionally used to complement other methods due to its relative inaccuracy. Each of these technologies provides unique information and is widely used clinically for diagnosis as well as surgical planning and prognostication. However, none is capable of providing comprehensive, site-specific properties of bone in-vivo and in-situ to assist with surgical decision making.

In this work, we investigate a new diagnostic method for site-specific evaluation of hard biological tissues via highly nonlinear solitary waves (HNSWs). HNSWs are compact-supported lumps of energy that are formed as an outcome of balanced dispersive and nonlinear effects [7, 8]. We use HNSWs as novel information carriers to assess mechanical properties of bone structures in highly localized target areas. We generate a single pulse of HNSW in an ordered chain of spherical particles under nonlinear Hertzian contact, also defined as a 1D granular crystal (Fig. 27.1a) [7, 8]. We transmit a single pulse of HNSWs into an inspection spot of hard biological tissues via direct mechanical contact, so that the injected HNSW interacts with highly localized microstructures of bone. By measuring the reflected HNSWs via an instrumented sensor particle embedded in the chain, we obtain the site-specific mechanical properties of anisotropic and nonhomogeneous bone in a fast and reliable manner.

27.2 Numerical Approach

We use a discrete element method to simulate the coupling mechanism between the granular crystal and the hard biological systems. In a monodispersed chain of spheres, the particle interactions are regulated by the Hertzian contact law expressed as $F \propto \delta^{3/2}$ where F is force and δ is approach between particles. The equation of motion of such a nonlinear spring-type spherical lattice can be expressed as:

$$m\,\ddot{u}_n = A_n\left[u_{n-1}-u_n\right]_+^{3/2} - A_{n+1}\left[u_n-u_{n+1}\right]_+^{3/2},$$
$$A_n \equiv \begin{cases} A|_c = E\sqrt{2R}/3\,(1-\nu^2) & n \in \{1,\ \ldots, N\} \\ A|_w = \frac{4\sqrt{R}}{3}\left(\frac{1-\nu^2}{E}+\frac{1-\nu_w^2}{E_w}\right)^{-1} & n = N+1 \end{cases} \tag{27.1}$$

where m is the mass of the bead, and u_n is the displacement of the given particle from its equilibrium position (Fig. 27.1a) [7]. The coefficient of the nonlinear interaction A_n is a function of Young's modulus E, Poisson's ratio ν, and radius R of the granular element. The bracket $[s]_+$ takes only positive values and returns 0 if $s < 0$. Upon external impact applied to no or

weakly compressed granular system, Nesterenko derived an analytical solution of Eq. 27.1 in terms of strain field under the long-wave approximation [7]:

$$\xi = \frac{\partial u}{\partial x} = \xi_0 \cos^4\left(\frac{\sqrt{10}}{10R}(x - V_s t)\right), \text{ where } \xi_0 = \left[5\pi\rho(1-\nu^2)V_s^2/8E\right]^2, \quad |x - V_s t| \le \frac{5\pi R}{\sqrt{10}} \tag{27.2}$$

This expression represents a single impulse of compact waveform produced in the chain, which mathematically describes an impulse of incident solitary waves (see the blue curve in Fig. 27.1a). Here, ξ_0 is the maximum strain with ρ and V_s denoting the particle density and the solitary wave velocity determined by the chain configuration and striker impact condition. When incident solitary waves reach the interface with the biological system, they are backscattered and disintegrated into a chain of solitary waves, which are affected by the biological system's mechanical properties (see the red curve in Fig. 27.1a). For the direct interactions with hard biological tissues, such behavior is governed by the coefficient of the nonlinear spring in the chain $A|_w$ in Eq. 27.1, which is a function of the elastic modulus (E_w) and the Poisson's ratio (υ_w) of the biological system. In the spring-mass model, $A|_w$ corresponds to the nonlinear spring placed between the last particle in the chain and the half-spaced biological system. Given the DE model, we can numerically calculate the propagation and backscattering of the solitary waves by solving Eq. 27.1 using the ordinary differential equation solvers in MATLAB. For the accurate modeling of biological systems, numerical analysis can be conducted based on FE model using Abaqus. Figure 27.1b shows an example of FE simulation for the interactions of solitary waves with a layered biological system. More details on FE approach can be found in [9].

27.3 Verification via Polyurethane Foams

The preliminary investigation was performed using seven different samples of rigid polyurethane foam (Pacific Research Laboratories, Inc., Vashon, Washington) to simulate clinical bone quality ranging from healthy to severely osteoporotic according to clinical criteria (Fig. 27.2). Each artificial cancellous bone sample was cut into a 50×50×50 mm block, and the material properties of seven specimens are listed in Table 27.1. We obtained five measurements of reflected HNSWs using

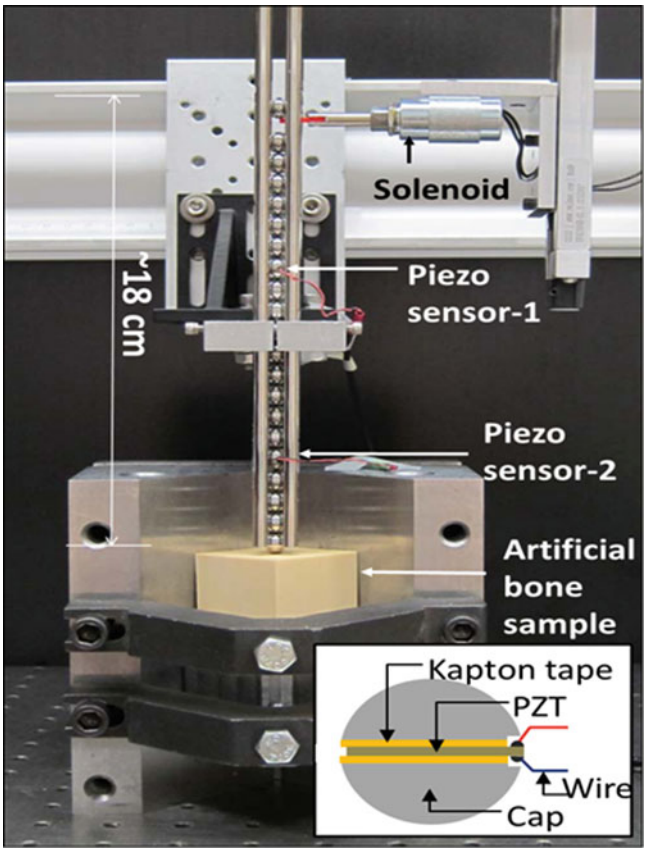

Fig. 27.2 Experimental setup of artificial bone testing using specimens in Table 27.1. Inset shows a schematic of an instrumented sensor particle

Table 27.1 Specifications of artificial cancellous bone samples [11]

Sample	Density [g/cc]	Strength [MPa]	Elastic modulus [MPa]	Osteoporotic categorization
1	0.08	1.0	32	High risk of fracture
2	0.16	2.2	58	Osteoporotic
3	0.24	4.9	123	Healthy
4	0.32	8.4	210	Healthy
5	0.48	18	445	Healthy
6	0.64	31	759	Healthy
7	0.80	48	1,148	Healthy

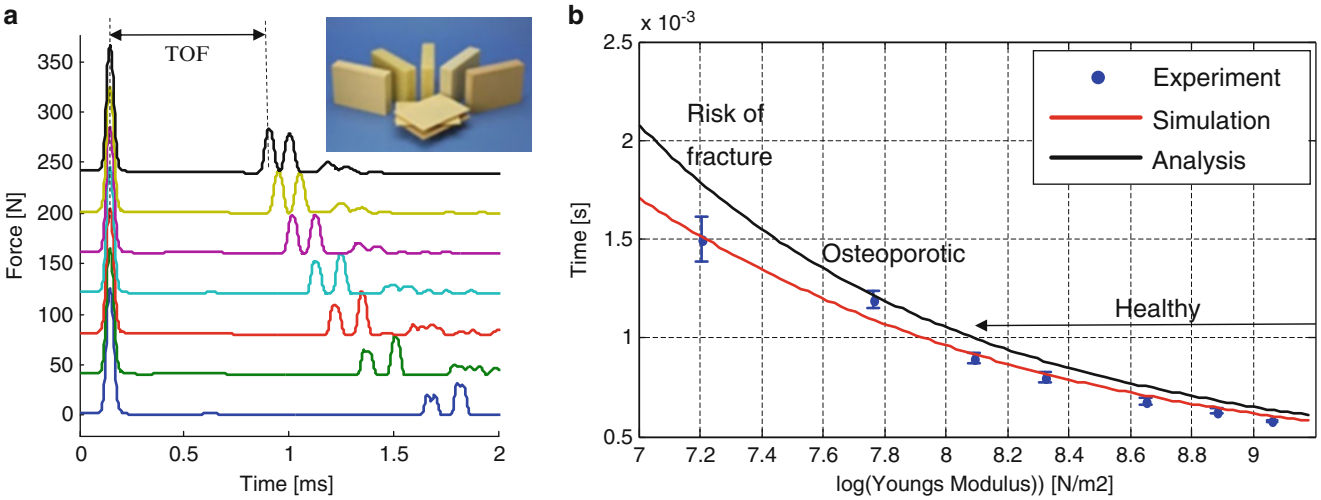

Fig. 27.3 Solitary wave interaction with artificially fabricated bone-like materials (**a**) Experimental force profiles of solitary waves in response to different specimens. (**b**) Quantified *TOF* as a function of polyurethane foam's elastic moduli

instrumented particles inserted in the granular chain [10]. The experimental data were analyzed in relation to the known properties of the synthetic foam, and were then compared to the numerical results obtained from the DE model.

Figure 27.3a reports the experimental results obtained from the interaction of HNSWs with synthetic bone. Here the signals obtained from the different bone materials are shifted vertically to ease visual comparison. The first impulse evident in the plots corresponds to the arrival of the incident solitary wave in the sensor site (in the seventh bead in the chain). The subsequent impulses represent the arrival of reflected solitary waves after the incoming impulse interacted with the polyurethane foam specimens. We observe a dramatic difference in the time of arrival of the reflected waves, by comparing results obtained from the different foam samples. In particular, the HNSW interaction with the more osteoporotic specimens results in longer delays in the arrival of the reflected solitary waves to the instrumented sensor than that of the healthier specimens. The delay time between incident and reflected waves is represented by time of flight (*TOF*) as marked in Fig. 27.3a. The dependence of *TOF* values on the synthetic bone's elastic modulus is shown in Fig. 27.3b based on analytical [12], numerical, and experimental approaches. It is evident that the *TOF* of the primary solitary waves exhibit strong dependence on the elastic modulus of synthetic bone. According to the experimental results, the *TOF* in the osteoporotic samples increases significantly in comparison to the healthy samples. It is notable that the reflected solitary waves vary their *TOF* on the order of milliseconds. This is in sharp contrast to the order-of-microsecond wave travelling time in the conventional ultrasound-based method (e.g., pitch-catch scheme in QUS) [13]. The higher responsiveness of the HNSWs can significantly enhance the sensitivity and reliability of the proposed highly nonlinear diagnostic method over QUS.

27.4 Verification via Artificial Bone Samples

As the next step, we conducted tests using five samples of artificial femurs (Pacific Research Laboratories, Inc., Vashon, Washington). We evaluated site-specific stiffness in terms of elastic moduli at 12 locations for each artificial femur (Fig. 27.4a). In each location, five repetitive tests were performed to acquire the mean *TOF* of the primary reflected solitary waves. Based on the numerical relationship between the *TOF* and elastic moduli developed by the DE model and verified by

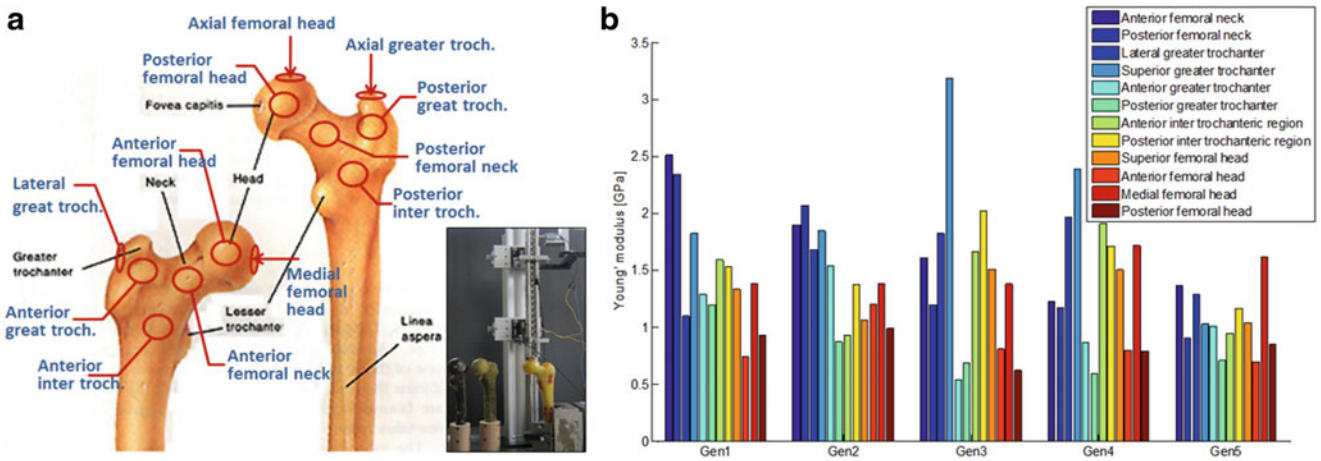

Fig. 27.4 (**a**) Schematic diagram of human femur with 12 measurement locations for the HNSW-based evaluation in anterior (*left*) and posterior (*right*) views (femur image source: Google image). Inset shows a digital photo of artificial femur testing via granular crystal sensor/actuator. (**b**) Site-specific elastic moduli measured from different generations of artificial femur samples

the polyurethane foams, the local stiffness at different locations of the proximal femur was calculated. Figure 27.4b shows various distributions of stiffness in different inspection spots. The measured stiffness values are in the range of artificial femur's stiffness, which is composed of epoxy and polyurethane layers simulating cortical and trabecular bone. This demonstrates the capability of the HNSW method to evaluate site-specific stiffness of localized bone regions.

27.5 Conclusions

We investigated the feasibility of a 1D granular crystal as a combined sensor and actuator suite to assess localized stiffness of hard biological tissues. The granular crystal sensor generated a single pulse of highly nonlinear solitary waves (HNSWs), which showed remarkable sensitivity to the mechanical stiffness of the region under inspection. We demonstrated how HNSWs respond to the mechanical stiffness of inspection media using a discrete element (DE) model. To validate the approach, we employed an artificial bone made of polyurethane and epoxy. The results were promising, showing the potential of the HNSW-based diagnostic method for biomedical purposes. Further details on this research, including cadaveric femur testing and the comparison with the conventional DEXA method, are described in the authors' recent publication [14].

References

1. Crowninshield RD, Rosenberg AG, Sporer SM (2006) Changing demographics of patients with total joint replacement. Clin Orthop Relat Res 443:266–272
2. Nixon M et al (2007) Does bone quality predict loosening of cemented total hip replacements? J Bone Joint Surg Br 89(10):1303–1308
3. Kurtz SM et al (2007) Future clinical and economic impact of revision total hip and knee arthroplasty. J Bone Joint Surg Am 89(Suppl 3):144–151
4. Kurtz SM et al (2009) Future young patient demand for primary and revision joint replacement: national projections from 2010 to 2030. Clin Orthop Relat Res 467(10):2606–2612
5. Deyo RA, Mirza SK (2006) Trends and variations in the use of spine surgery. Clin Orthop Relat Res 443:139–146
6. Hernandez CJ, Keaveny TM (2006) A biomechanical perspective on bone quality. Bone 39(6):1173–1181
7. Nesterenko VF (2001) Dynamics of heterogeneous materials. Springer, New York
8. Sen S et al (2008) Solitary waves in the granular chain. Phys Rep 462(2):21–66
9. Ni X et al (2012) Monitoring the hydration of cement using highly nonlinear solitary waves. NDT&E Int 52:76–85
10. Daraio C et al (2005) Strongly nonlinear waves in a chain of Teflon beads. Phys Rev E 72(1):016603
11. http://www.sawbones.com/products/bio/testblocks/solidfoam.aspx
12. Yang J et al (2011) Interaction of highly nonlinear solitary waves with linear elastic media. Phys Rev E 83:046606
13. Glüer CC, Wu CY, Genant HK (1993) Broadband ultrasound attenuation signals depend on trabecular orientation: an in vitro study. Osteoporos Int 3(4):185–191
14. Yang J et al (2012) Site-specific quantification of bone quality using highly nonlinear solitary waves. J Biomech Eng 134(10):101001–101008